



THE UNIVERSITY OF  
**WAIKATO**  
*Te Whare Wānanga o Waikato*

Research Commons

<http://researchcommons.waikato.ac.nz/>

## Research Commons at the University of Waikato

### Copyright Statement:

The digital copy of this thesis is protected by the Copyright Act 1994 (New Zealand).

The thesis may be consulted by you, provided you comply with the provisions of the Act and the following conditions of use:

- Any use you make of these documents or images must be for research or private study purposes only, and you may not make them available to any other person.
- Authors control the copyright of their thesis. You will recognise the author's right to be identified as the author of the thesis, and due acknowledgement will be made to the author where appropriate.
- You will obtain the author's permission before publishing any material from the thesis.

**Investigation of surge propagation in transient voltage surge  
suppressors and experimental verification**

A thesis submitted in fulfilment of the requirements for the degree

of

**Doctor of Philosophy**

in Electronics Engineering

at

**The University of Waikato**

by

**Sisira James**



THE UNIVERSITY OF  
**WAIKATO**  
*Te Whare Wānanga o Waikato*

2014



## Abstract

---

An on-going question in the field of surge protection study is how to predict incipient failure of power electronics in the event of a short time, high voltage, and high energy transient surge propagation. The work presented in this thesis addresses the above question by investigating how a high voltage transient surge, whose duration is in the microseconds range, will propagate through the two-level transient voltage suppressor system that is intended to protect sophisticated electronics situated close to the service entrance of a building. In this work the energy patterns relevant to the individual components of the system are evaluated using numerical methods and some of the results are also compared with those obtained using SPICE simulations. Although several mathematical models for surge protection components are discussed in the literature and some device specific ones are provided by manufacturers, there is no evidence to show that a complete analysis, using any such model, has been performed to predict the energy absorptions and associated time lags between the components in a TVSS.

Numerical simulation techniques using MATLAB are used to estimate the energy absorption and associated time delays in relation to the propagated transient surge, in individual components of a transient voltage surge suppressor. This study develops mathematical models for particular nonlinear transient surge absorbing elements, specifically for the metal oxide varistor and transient voltage suppressor diode, formulates the state equations which are used to numerically simulate several instances of the transient voltage surge suppressor system, and presents simulation results. All results are validated experimentally using a lightning surge simulator. The outcomes established using the two approaches indicate that the theoretical energy calculations are within 10% of the experimental validations for the metal oxide varistor, which is the main energy absorbing element in the system. The remaining energy distributions in the line-filter components and the transient voltage suppressor diode, which are at least 10 times smaller, are all within 20% of the experimental results. The times at which, the metal oxide varistor and the transient voltage suppressor diode switches to heavy conduction mode are also simulated accurately.



## **Dedication**

---

To my family.....Champa, Aseka and Pasan



## Acknowledgements

---

I am indebted to my primary supervisor Nihal Kularatna for his support, patience and encouragement throughout. I would also like to thank my co-supervisor Alistair Steyn-Ross who has imparted his knowledge on a wide range of matters that made my research possible. Much is owed to my co-supervisor Rainer Kunemeyer for his helpful ideas, guidance and enthusiasm. It has been wonderful working with you all.

It was my co-supervisor Alistair Steyn-Ross who suggested the use of Laplace transform method for the study of surge propagation in linear circuits and the use of numerical methods in the case of highly nonlinear circuits such as surge protector devices. He guided me in developing Laplace based analysis for the first loop of the lightning surge simulator equivalent circuit and in developing the state equations for the situation where a circuit containing a charged capacitor had to drive a highly nonlinear metal oxide varistor model. The preliminary computer code that was developed into code given in appendices A.1, A.3, B.3 and C.1 were also provided by him.

Many thanks to Jonathan Scott, Micheal Cree, Sadhana Talele, Adrian Dorrington and Howell Round who have been happy to help whenever the need arose. My sincere thanks also go to technical staff Stewart Finlay, Viking Zhou and Ian Honey, administrator Mary Dalbeth, computer support staff David Nichols and Ai Phing Wood for their continuous assistance throughout this work.

Thank you also to science librarian Cheryl Ward who has helped me in finding specific literature and also helped me in numerous ways in compiling this thesis.

University of Waikato is acknowledged for granting me a Doctoral Scholarship which helped me complete this work comfortably.

Thank you to my friends Hilary, Mohantha, Chandana, Udayangani and Ruwan for the support given to me and my family in settling down comfortably in Hamilton at the start of this endeavour. Finally, I would like to thank my family, Champa, Aseka and Pasan for supporting me in every way imaginable through some difficult times.



# Table of Contents

---

Abstract .....	iii
Dedication .....	v
Acknowledgements .....	vii
Table of Contents .....	ix
List of Figures .....	xv
List of Tables.....	xxi
List of symbols and abbreviations.....	xxiii
Chapter 1 : Introduction .....	1
1.1 Overture.....	1
1.2 Objective .....	2
1.3 Structure of the thesis .....	4
1.4 List of publications arising from the work in the thesis .....	6
Chapter 2 : Surge protection of power electronics.....	9
2.1 Introduction .....	9
2.2 Power line disturbances.....	11
2.2.1 RMS voltage fluctuations .....	12
2.2.2 Transient surges .....	13
2.2.3 Electrical noise .....	13
2.2.4 Harmonics.....	14
2.2.5 Modes of transients and noise .....	14
2.2.5.1 Differential Mode (Normal Mode or Transverse Mode) .....	15
2.2.5.2 Common Mode Signals.....	15
2.3 Power quality issues .....	16
2.3.1 Current state of a typical electronic load .....	16
2.3.2 Development of DC Power Supplies.....	18
2.4 Surge protection and surge absorbent devices.....	19
2.4.1 Practical Devices Used in Surge Protection Circuits.....	20
2.4.1.1 Metal Oxide Varistors .....	21
2.4.1.2 TVS diodes and thyristors.....	24

2.4.1.3	Gas Discharge Tubes .....	29
2.4.2	Levels of surge protection.....	31
2.4.2.1	Primary Protection.....	32
2.4.2.2	Secondary Protection.....	32
2.4.2.3	Board-level protection .....	32
2.5	Surge protection standards and practices.....	32
2.5.1	External sources of transient activity .....	33
2.5.2	Internal sources of transient Activity .....	34
2.5.3	Transient energy.....	34
2.5.4	Transient Protection Standards .....	34
2.5.4.1	IEEE C62.41: Location categories .....	35
2.5.4.2	Surge voltage waveforms .....	37
2.5.4.3	Underwriters Laboratories UL 1449 .....	38
2.6	Circuit concepts used for surge protection .....	39
Chapter 3 : Analytical and Numerical techniques for solving transient equations .....		43
3.1	Limitation of Laplace transform method .....	44
3.2	Euler’s method.....	45
3.2.1	Application of Euler method: LCR circuit driven by a charged capacitor .....	46
3.2.2	A better way of obtaining an impulse response .....	49
3.3	Runge-Kutta (RK) approximation methods.....	51
3.3.1	Application of RK4 method: LCR circuit driven by a charged capacitor .....	54
3.4	Variable step-size routines.....	55
3.4.1	ODE solvers for stiff problems .....	57
3.4.2	Improvements to the MATLAB code containing stiff ODE solvers .....	58
3.5	A comparison with available system simulation software.....	59
3.6	Chapter summary .....	60
Chapter 4 : Surge-absorbent device characterization .....		63
4.1	Introduction.....	63
4.2	MOV Characterization.....	64
4.2.1	Measuring set-up.....	64

4.2.2	Waveforms obtained and their analysis .....	66
4.2.2.1	Leakage region analysis .....	67
4.2.2.2	Normal varistor operation region observations.....	70
4.2.3	Approximation of the coefficient of nonlinearity “ $\alpha$ ” .....	74
4.2.4	Accurate measurement of leakage region currents.....	75
4.2.5	A varistor <i>I-V</i> characteristic for leakage and normal regions of operation .....	76
4.2.6	Development of a mathematical model for the varistor .....	78
4.2.7	Verification of the model for the varistor by simulation and validation .....	79
4.2.8	Study of varistor conductance, power and energy during a surge propagation .....	83
4.2.9	Study of an MOV’s industrial characterization that uses a logarithmic-term model .....	85
4.3	TVS diode characterization .....	89
4.3.1	Waveforms obtained and their analysis .....	91
4.3.2	A TVS diode (1.5KE170CA) <i>I-V</i> characteristic for leakage and normal regions of operation.....	93
4.3.3	Complete mathematical model for the TVS diode .....	95
4.4	Comparison of transient suppressor models.....	96
Chapter 5 : Investigation of surge propagation in linear systems .....		99
5.1	Analysis of LSS responses using Laplace methods .....	99
5.1.1	Laplace Solution for 1.2/50 $\mu$ s open-circuit voltage and its validations.....	100
5.1.2	Comparison of Laplace solutions with numerical simulation .....	105
5.1.3	Laplace solution for 8/20 $\mu$ s short-circuit current validated with experimental data from the LSS .....	107
5.2	Investigation of surge propagation through an MOV in the off state.....	109
5.3	Investigation of surge propagation in assumed fixed states of the MOV.....	112
5.4	Chapter summary .....	117
Chapter 6 : Investigation of surge propagation through a TVSS system.....		119
6.1	Introduction .....	119

6.2	Investigation of surge propagation through an MOV (1 <sup>st</sup> stage of the TVSS) .....	120
6.2.1	Simulation using the power-law model of an MOV .....	121
6.2.2	SPICE based simulation using a manufacturer supplied model of an MOV and comparison. ....	126
6.3	Investigation of surge propagation through two stages of the TVSS (MOV and LC line-filter).....	128
6.4	Investigation of surge propagation through a complete 2-wire category A/B TVSS .....	136
Chapter 7 : Conclusions and Recommendations .....		143
7.1	General conclusions .....	143
7.1.1	Nonlinear device modelling .....	143
7.1.2	Describing the problem with state equations and solving.....	144
7.1.3	Validation of the numerical simulations .....	144
7.2	Recommendations.....	145
7.2.1	Surge propagation conditions.....	145
7.2.2	Equivalent circuits used .....	146
7.2.3	Investigation of surge propagation in downstream electronics.....	146
References .....		147
Appendices .....		155
Appendix A: MATLAB code used for Chapter 3 .....		155
A.1	Euler simulation of LCR circuit driven by a charged capacitor .....	155
A.2	Improved Euler simulation (using initial conditions that arise from the impulse input) of LCR circuit driven by a charged capacitor .....	157
A.3	rk4fixed: General-purpose 4 <sup>th</sup> -order Runge-Kutta ODE used by simulation listed in Appendix A.4 .....	159
A.4	RK4 simulation of LCR circuit driven by a charged capacitor.....	161
A.5	ode45 simulation of LCR circuit driven by a charged capacitor .....	163
Appendix B: MATLAB code used in the compilation of Chapter 4.....		165
B.1	Calculation of the slope ( $\alpha$ ) and intercept ( $\log k$ ) of the “off” and “on” models for the varistor 275L40C.....	165

B.2	Development of the combined model for the MOV 275L40C.....	166
B.3	Verification of the combined model developed for the MOV 275L40C .....	168
Appendix C: Development of state equations and the MATLAB code used for the work presented in Chapter 5.....		
C.1	Laplace solution for the open-circuit voltage of the LSS validated with a SPICE simulation.....	171
C.2	SPICE input file to trace the open-circuit voltage of the LSS .....	173
C.3	Laplace solution for the open-circuit voltage of the LSS validated with numerical simulations based on Euler and RK4 method.....	174
C.4	Development of state equations (5-13) - (5-17) for the MOV “off” state driven by the LSS.....	176
C.5	Numerical simulation of the “off” state current in a MOV validated with a SPICE based simulation.....	180
C.6	Development of state equations (5-18) - (5-23) for the assumed fixed states of the MOV driven by the LSS.....	182
C.7	Numerical simulation of an assumed fixed state of an MOV validated with a SPICE based simulation.....	186
Appendix D: Development of state equations and the MATLAB code used for the work presented in Chapter 6.....		
D.1	Development of state equations(6-2) - (6-7) for an MOV driven by the LSS .....	188
D.2	Numerical simulation and validations of an MOV (1 <sup>st</sup> stage of an TVSS/SPD) driven by an LSS.....	192
D.3	PSpice source file for simulating an MOV (1 <sup>st</sup> stage of a TVSS) driven by an LSS .....	196
D.4	Development of state equations (6-9) - (6-15) for a 2-stage (MOV followed by a line-filter) TVSS driven by an LSS .....	198
D.5	Numerical simulation and validations of a 2-stage (MOV and a line-filter) TVSS/SPD driven by an LSS.....	202

D.6	Development of state equations (6-18) - (6-25) for a 3-stage (MOV followed by a line-filter and a TVS diode) TVSS driven by an LSS .....	207
D.7	Numerical simulation and validations of a 3-stage (MOV followed by a line-filter and a TVS diode) TVSS/SPD driven by an LSS .....	210
Appendix E: Transient analysis in linear networks by Laplace methods; some examples .....		215
E.1	Series RC circuit with a biexponential input voltage.....	215
E.2	RLC circuit driven by a charged capacitor .....	218
E.3	An occurrence of the unit impulse function; discharging of an initially charged capacitor .....	219
E.4	MATLAB symbolic toolbox.....	221
Appendix F: A provisionally accepted journal paper to be published in the IET Power Electronics journal.....		223

## List of Figures

---

Figure 2-1: Examples of disturbances on a 230V RMS, 50 Hz utility AC power supply: (a) RMS voltage fluctuations; (b) transients and noise superimposed on the waveform; (c) ideal waveform and its frequency spectrum .....	12
Figure 2-2: (a) Differential and common modes; (b) common-mode signal coupling towards secondary side due to coupling capacitance .....	15
Figure 2-3 Developments of integrated circuits and processor families: (a) Moore's law based progress of ICs; (b) development of processors and their power supply requirements; (c) processor speed, power consumption, and equivalent impedance .....	17
Figure 2-4: Comparison of linear power supplies and modern SMPS: (a) Simple linear power supply with an isolation transformer; (b) modern off-the-line switching power supply .....	18
Figure 2-5: Transient superimposed on the AC-input waveform with its effects.....	20
Figure 2-6: Metal oxide varistor characteristic and equivalent circuits: (a) V-I characteristic; (b) generalized equivalent circuit; (c) simplified cases under leakage and conduction .....	22
Figure 2-7: Comparison of clamping type transient protection devices: (a) ideal case; (b) zinc-oxide varistor; (c) TVS zener diode .....	25
Figure 2-8: An example of a TVS diode: (a) device behaviour and data sheet parameters; (b) pulse power absorption capability versus pulse width; (c) test pulse used; (d) typical application circuit and voltage at protected load due to device capacitance and lead inductance .....	27
Figure 2-9: An example of a thyristor breakover device (a) device behaviour and data sheet parameters (b) pulse power absorption capability versus pulse width (c) test pulse used (d) typical application circuit in telecommunication plant with series current limiting device .....	29
Figure 2-10: Facility-wide protection solution: a cascade (or 2-stage) approach; (a) Example of two-stage TVSS protection. (b) Achievable performance levels with single and two-stage protection .....	31
Figure 2-11: A typical lightning current waveform .....	33
Figure 2-12: Building location categories and types for IEEE C62.41 and UL 1449 .....	37

Figure 2-13: IEC 61000-4-5 combination wave (a) Open-circuit voltage (b) Short-circuit current.....	38
Figure 2-14: The 100 kHz ring wave.....	38
Figure 2-15: Line-to-line and line-to-ground transient overvoltage protection circuit with noise filter (can be designed for C62.41 location categories A and B) .....	40
Figure 3-1: Euler method: Approximation of the curve $y(t)$ by a polygon whose first side is tangent to the curve at $t_0$ .....	46
Figure 3-2: (a) RLC circuit driven by a charged capacitor (b) Laplace transformed network for the circuit in (a).....	47
Figure 3-3:(a) Euler simulation of the loop current compared with the theoretical result (b) Error between the simulation and theoretical results.....	49
Figure 3-4: (a) Euler simulation of the loop current compared with the theoretical result (b) Error between the simulation and theoretical results.....	51
Figure 3-5: (a) RK4 simulation of the loop current compared with the theoretical result (b) Error between the simulation and theoretical results (in mA).....	55
Figure 3-6: (a) ode45 simulation of the loop current compared with the theoretical result (b) Time-step changed dynamically by the ode45 integrator during the simulation .....	57
Figure 4-1 : A two-wire Category-B protection unit with two levels of protection .....	63
Figure 4-2: Circuit diagram for the measurement of the MOV voltage and current; impulse source is a lightning surge simulator (LSS) and a four-channel oscilloscope was used for measurements.....	65
Figure 4-3: Waveform of 1.2/50 $\mu$ s open-circuit voltage (waveform definition according to IEC 60060-1) .....	65
Figure 4-4: Waveform of 8/20 $\mu$ s short-circuit current (waveform definition according to IEC 60060-1) .....	66
Figure 4-5: Typical varistor characteristic showing different regions of operation .....	67
Figure 4-6: Leakage region varistor current produced by a low voltage impulse .....	67

Figure 4-7: The equivalent circuits required to analyse the working of the circuit of Fig. 5-2 for low voltage impulses .....	68
Figure 4-8: Combined equivalent of the measuring circuit shown in Fig.5-2 for the leakage region of the varistor .....	68
Figure 4-9: Mechanical dimensions of radial lead varistors used .....	69
Figure 4-10: Measured voltage across and the current through a varistor in the normal operation region. The LSS was set to deliver a surge of 1 kV. ....	70
Figure 4-11: Associated dynamic I-V curve for traces shown in Figure 4-10.....	71
Figure 4-12: <i>I-V</i> graph of a MOV illustrating symbols and definitions (see Table 4-2).....	72
Figure 4-13: Linear and log-log <i>I-V</i> plots for the varistor 275L40C .....	75
Figure 4-14: Circuit for measuring MOV voltage and current in the leakage region of operation. ....	76
Figure 4-15: <i>I-V</i> plots that show the leakage and normal regions of operation for a 275L40C varistor; (a) linear plot (b) log-log plot .....	77
Figure 4-16: Development of a combined model for the leakage and normal regions of operations for a varistor .....	79
Figure 4-17: The circuit used for an initial verification of the model developed for the varistor. ....	80
Figure 4-18: Illustration to show the solving of Eq. (4-11) to find the value of $I_m$ for $V_i = 800V$ .....	82
Figure 4-19: Simulation results for the circuit of Figure 4-17 along with experimental validation using an LSS: (a) $V_i$ vs. $V_L$ (b) $V_i$ vs. $I_m$ and (c) $V_i$ vs. $I_L$ .....	82
Figure 4-20: Characterization of the varistor conductance, power dissipation and energy absorption during the propagation of a transient .....	84
Figure 4-21: The effect of changing the coefficient $B1$ , on the <i>I-V</i> characteristic of the MOV .....	86
Figure 4-22: The effect of changing the coefficient $B2$ , on the <i>I-V</i> characteristic of the MOV .....	87
Figure 4-23: The effect of changing the coefficient $B4$ , on the <i>I-V</i> characteristic of the MOV .....	88

Figure 4-24: Typical $I$ - $V$ curve characteristics for a bidirectional TVS diode .....	90
Figure 4-25: Voltage across and the current through a TVS diode operated by an impulse input.....	92
Figure 4-26: Associated dynamic $I$ - $V$ curve for traces shown in Figure 4-25 for the TVS diode 1.5KE400CA .....	93
Figure 4-27: Linear and log $V$ - $I$ plots that show the leakage and normal regions of operation for a 1.5KE170CA TVS diode. ....	94
Figure 4-28: Development of a combined model for the “off” and “on” regions of a TVS diode.....	95
Figure 4-29: Varistor and TVS diode $I$ - $V$ characteristics drawn on log-log graph for comparison of the degrees of nonlinearity .....	96
Figure 5-1: The LSS equivalent circuit for finding the 1.2/50 $\mu$ s open-circuit voltage (Noise Laboratory Co., Ltd., Japan) .....	100
Figure 5-2: Transformed network for the circuit in Figure 5-1 .....	101
Figure 5-3: Laplace solution for the open-circuit voltage of the LSS validated with a SPICE simulation.....	103
Figure 5-4: Laplace solution for the open-circuit voltage of the LSS validated with the experimental result from the LSS .....	104
Figure 5-5: Semi-log plots for the curves shown in Figure 5-4.....	105
Figure 5-6: <code>rk4fixed</code> solver based validations of Laplace solutions with $\Delta t=10$ ps (a) LSS open-circuit voltage (b) short-circuit current.....	107
Figure 5-7: (a) Laplace solution for the short-circuit current of the LSS validated with the experimental result from the LSS. (b) Error between the Laplace solution and its validation. ....	108
Figure 5-8: (a) Laplace solution and its validation of Figure 5-7(a) changed for better comparison by minor changes to LSS circuit values. (b) Maximum error has reduced by about 40% compared to Figure 5-7(b).....	109
Figure 5-9: MOV “off” state driven by the LSS (Combined equivalent circuit) .....	110
Figure 5-10: (a) Numerical simulation of the “off” state current in a MOV validated with a SPICE based simulation; (b) variation in the time step during the simulation; $V_{C1}(0+) = 100 V$ .....	112
Figure 5-11: The $I$ - $V$ characteristic for the 275L40C varistor with a selection of operating points. ....	113

Figure 5-12: Fixed MOV states driven by transients from the LSS .....	113
Figure 5-13: Numerical simulation of assumed fixed states of the MOV validated with SPICE based simulations (a) $R_m = 34 \text{ M}\Omega$ (b) $R_m = 300 \Omega$ (c) $R_m = 7 \Omega$ .....	116
Figure 6-1: A 2-wire Category B protection unit with two levels of protection.....	120
Figure 6-2: LSS driving the first stage of a category B protection unit.....	120
Figure 6-3: Overall equivalent circuit for the set up shown in Figure 6-2.....	121
Figure 6-4: Numerical simulation and validations for the first stage (MOV) of a TVSS (a) MOV current and voltage (b) Power variation for the MOV (c) Energy absorption in the MOV .....	123
Figure 6-5: The phase plot (MOV current vs. MOV voltage) for the simulation and validation plots shown in Figure 6-4(a).....	124
Figure 6-6: The phase plot of the improved simulation compared with initial simulation and validation plots shown earlier in Figure 6-5.....	125
Figure 6-7: Improved numerical simulations and validations for the (a) MOV current and voltage (b) Energy absorption in the MOV.....	125
Figure 6-8: Schematic representation of Figure 6-2 used to develop the SPICE source file. ....	126
Figure 6-9: SPICE and MATLAB simulations compared with the validations for the first stage (MOV) of a TVSS (a) MOV current and (b) MOV voltage .....	127
Figure 6-10: SPICE and MATLAB simulations of Figure 6-9 made to coincide by changing $\alpha_2$ from 20.5306 to 20.4006 (a) MOV current and (b) MOV voltage.....	128
Figure 6-11: LSS driving the first two stages of a category B protection unit .....	129
Figure 6-12: Overall equivalent circuit for the setup shown in Figure 6-11.....	129
Figure 6-13: Numerical simulation and validations for the MOV of the TVSS (a) MOV voltage (b) MOV current (c) Power variation in the MOV (d) Energy absorption in the MOV .....	132
Figure 6-14: Numerical simulation and validations for the capacitor $C_f$ of the TVSS (a) capacitor current (b) capacitor voltage (b) Power variation in the capacitor (c) Energy absorption in the capacitor.....	134

Figure 6-15: Numerical simulation and validations for the inductor $L_f$ of the TVSS (a) Inductor current (b) Inductor voltage (b) Power variation in the inductor (c) Energy absorption in the inductor.....	135
Figure 6-16: LSS driving a complete 3-stage category A/B protection unit. The protection unit is shown in the shaded area. ....	136
Figure 6-17: MOV and TVS diode models used to redraw the circuit of Figure 6-16.....	137
Figure 6-18: Numerical simulation and validations for the MOV of the TVSS (a) MOV voltage (b) MOV current (b) Power variation for the MOV (c) Energy absorption in the MOV.....	141
Figure 6-19: Numerical simulation and validations for the TVS diode of the TVSS (a) TVS diode voltage (b) TVS diode current (c) Power variation in the TVS diode (d) Energy absorption in the TVS diode .....	142

## List of Tables

---

Table 2-1: Comparison of TVS devices .....	30
Table 2-2: IEEE C62.41 Location categories, frequency of occurrences and surge waveforms .....	37
Table 3-1: Some of the ODE solvers supplied by MATLAB .....	55
Table 4-1: Matching the right MOV with a particular application .....	64
Table 4-2: Description of terms and letter symbols used in defining a varistor .....	73
Table 4-3: Voltage and current readings obtained to characterize a 275L40C varistor.....	74
Table 4-4: Calculated values of $\alpha$ with percentage uncertainties.....	75
Table 4-5: Voltage and current readings obtained to characterize the leakage and normal regions of operation of a 275L40C varistor .....	77
Table 4-6: Experimental data obtained from testing the circuit of Fig. 5.17.....	83
Table 4-7: Parameters used for the basic varistor model .....	85
Table 4-8: Samples from a TVS diode product selection table .....	90
Table 4-9: Voltage and current readings obtained to characterize the leakage and normal regions of operation of a 1.5KE170CA TVS diode .....	94
Table 5-1: Parameters for the Noiseken LSS-6110.....	100



## List of symbols and abbreviations

---

A	Ampere
AC	Alternating current
ANSI	American national standards institute
BJT	Bipolar junction transistor
CM	Common-mode
CSV	Comma-separated values
DC	Direct current
DE	Differential equation
DM	Differential-mode
DUT	Device under test
EMI	Electromagnetic interference
EMP	Electro-magnetic pulses
ESD	Electrostatic discharge
FCC	Federal communications commission
FT	Fourier transform
GB	Giga byte
GDT	Gas discharge tube
HBM	Human body model
HV	High Voltage
IC	Integrated circuit

IEC	International electrotechnical commission
IEEE	Institute of electrical and electronics engineers
IGBT	Insulated-gate bipolar transistor
ITRS	International Technology Roadmap for Semiconductors
J	Joules
k	Kilo
KVL	Kirchoff's voltage law
LSI	Large-scale integration
LSS	Lightning surge simulator
$\mu$	micro
MM	Machine model
MOSFET	Metal-oxide semiconductor field-effect transistor
MOV	Metal oxide varistor
ODE	Ordinary differential equation
PBX	Private branch exchange
PC	Personal computer
PCC	Point of common coupling
RAM	Random access memory
RFI	Radio frequency interference
RMS	Root mean square
RK	Runge-Kutta
RK4	Fourth-order Runge-Kutta

s	Second
SMPC	Switched-mode power converter
SMPS	Switched-mode power supply
SPD	Surge protective device
SPICE	Simulation Program with Integrated Circuit Emphasis
SoC	System on a chip
TPMOV	Thermally protected MOV
TVS	Transient voltage suppressor
TVSD	Transient voltage suppressor diode
TVSS	Transient voltage surge suppressor
UL	Underwriters laboratories
ULSI	Ultra large scale integration
UPS	Uninterruptible power supply
V	Volt
W	Watt



# Chapter 1: Introduction

---

## 1.1 Overture

Modern semiconductor technology is vulnerable to power surges such as lightning and switching transients. Due to this fact, my chief supervisor, Nihal Kularatna had developed an interest to study the transient propagation phenomena within power electronic conversion interfaces. Based on this, a PhD research on “Investigation of surge propagation in transient voltage surge suppressors and experimental verification” was suggested.

A surge voltage, which can be described as an increase in voltage significantly above the designated level in the flow of electricity, boosts the electrical charge at some point in power lines. This causes an increase in the electrical potential energy, which can increase the current flowing in the supply lines. In today’s system of electricity distribution, surge voltages and surge currents occurring in low-voltage ac power circuits are an unavoidable occurrence. The some warm parts of the world (E.g. Democratic Republic of the Congo, Sri Lanka), the most common source of voltage surges is lightning [1].

Surge voltages can be extremely damaging to electronic systems, and can take two major forms, switching-induced or lightning-induced [2, 3].

Switching-induced surges/transients are associated with:

- a) major power system switching disturbances, such as capacitor bank switching or inductive load (motors, transformers) switching;
- b) minor switching activity near the instrumentation, or load changes in the power distribution system;
- c) resonating circuits associated with switching devices, such as thyristors;
- d) system faults, such as short circuits and arcing to the local earthing system

Mechanisms by which lightning induces surge voltages include:

- a) direct lightning strike to an external (outdoor) circuit, injecting high currents;

- b) indirect lightning strike that induces voltages/currents on the conductors outside and/or inside a building;
- c) high local earth terminal potential rise due to currents resulting from nearby direct-to-earth discharges coupling into the common earth paths of the installation.

Transient Voltage Surge Suppressors (TVSSs) or Surge Protection Devices (SPDs) are designed to protect electronic equipment from power surges. In most systems, the switched-mode or linear power supply as well as the electronic load are protected by the TVSS. With all the complex components that make up processor-based electronic loads, a surge or high voltage (HV) spike can inflict heavy damage to the system. Hence transient suppression plays an essential role in electronic system protection.

In most surge protectors, nonlinear electronic components divert the extra energy brought in by a surge voltage. Two different technologies based on the type of operation are commonly used: “crowbar type” SPD and “voltage-limiting type” SPD. A crowbar type SPD will either use a gas discharge tube (GDT) or a transient voltage suppressor (TVS) thyristor as the protective component, while a voltage-limiting SPD will use a metal-oxide varistor (MOV) or a back-to-back TVS diode. The surge absorbent components of an SPD have a variable highly nonlinear resistance that is dependent on voltage. When the voltage exceeds a threshold, the resistance is lowered to divert the energy of the surge.

Some SPDs also use transient voltage suppressor (TVS) diodes for a second level of protection. Numerical modelling of nonlinear devices, such as MOVs and TVS diodes, for fast transient impulses will help us investigate surge propagation through TVSSs. Such an investigation will be beneficial to predict energy absorption and incipient failure of TVSSs. Computer simulation using MATLAB offers a viable approach to such a study.

## **1.2 Objective**

The goal of this research is to develop numerical simulation techniques to study transient propagation phenomena within a TVSS. Specifically, we aim to predict the energy absorptions and associated time lags of the various linear and

nonlinear components that make up the surge suppression interface. Such a detailed predictive approach has not been undertaken elsewhere.

Motivation for this work is based on the predictions of the International Technology Roadmap for Semiconductors (ITRS) [4]. Microelectronic processors have proliferated into a wide range of equipment from automated industrial assembly lines and hospital diagnostic systems to sophisticated computer systems; these ultra-large-scale integrated (ULSI) circuits have progressed towards advanced system-on-chip concepts with feature size dropping towards 22 nm. Direct-off-line switch mode power supplies (SMPSs) that sit between the utility AC and processor-based equipment also carry complex circuitry. Both the power supply and the processor-based load are prone to damage by fast transient impulses such as lightning. Hence an end-to-end approach on transient propagation studies from the utility AC to final DC rails is of utmost importance. The TVSS studied in this work sits at the front end of such a chain to provide transient-free AC to downstream electronics.

Although system transients can be analysed using Laplace transforms in the case of electric circuits containing linear components, its application becomes unwieldy for circuits containing nonlinear device models. In this thesis mathematical models will be developed for the various nonlinear components used within a TVSS, and these models will be embedded in a set of state equations for the protection circuit. The state equations will then be solved numerically using the specialized ordinary differential equation (ODE) solvers available within MATLAB.

Theoretical predictions will be compared with experimental measurements obtained with the use of a Lightning Surge Simulator (LSS), the Noiseken LSS 6110. This simulator is designed for surge immunity testing, and conforms to IEC publication 61000-4-5 and IEEE/ANSI C62.41 standards [2, 3].

The magnitude of the expected surge stress depends on the location of the equipment to be protected. The IEEE/ANSI C62.41 standard proposes three location categories, A, B and C, for low voltage AC power lines [5]. Categories A and B are located within the building and category C locations are found outside and at the service entrance. Category A locations receive their power after more

than 60 feet of wiring run from the main power service entrance, with frequent exposure to comparatively low energy surges. Category B locations are close to the power service entrance, with greater exposure to infrequent, high energy surges originating outside the building. Although the TVSS design that we will be investigating can be used in both location categories A and B, we will limit our investigations to location category B. The Noiseken LSS 6110 is a combination wave (hybrid) generator [2] capable of generating an output required for category B testing. It can generate open-circuit voltages up to 6.6 kV and short-circuit currents up to 3.3 kA.

### **1.3 Structure of the thesis**

In **Chapter 1**, I have briefly presented the types of voltage surges and surge protector device technologies commonly used. **Chapter 2**, which is the first part of the literature review, summarizes a book chapter by Nihal Kularatna; areas on surge protection, surge absorbent devices and surge protection standards and practices which are important to this thesis have been expanded in this discussion. Analytical and numerical methods used in this work, are presented in **Chapter 3**.

My original contribution to the thesis is reported in the next three results oriented chapters; this includes mathematical model development, and theoretical analysis using Laplace and numerical methods with experimental validation. The mathematical models required for representing the highly nonlinear surge absorbent devices are developed in **Chapter 4**. **Chapter 5** investigates surge propagation through linear circuits by using Laplace methods. The lightning surge simulator which is used for experimental validation of the numerical simulations is also analysed in this chapter. **Chapter 6** investigates numerically how a surge propagates through a complete two-level transient voltage suppressor system. Energy absorptions and associated time lags for the individual components of the system are highlighted. The conclusion and recommendations are presented in **Chapter 7**.

#### **Thesis outline**

**Chapter 1: Introduction.** The general background of power surges and surge protection devices is given and the objectives of this study listed. Also briefed are

the types of power surges and SPD technologies commonly used and the outline of the thesis.

**Chapter 2: Surge protection of power electronics.** Here we present a literature survey describing transient surge disturbances, power quality issues, surge protection and surge absorbent devices, protection standards and practices, and circuit concepts used for surge protection. We show the standard surge voltage waveforms output by the LSS and used for experimental testing.

**Chapter 3: Analytical and Numerical techniques for solving transient equations.** The advantage of using Laplace transforms for the analysis of transient propagation in linear circuits is stated, and the limitations of Laplace methods for the case of circuits containing highly nonlinear elements are briefly explained. Methods available to numerically simulate a problem that can be represented by a set of ordinary differential equations (ODEs) are discussed. These methods are appropriate even when the DEs are nonlinear as is the case for a typical SPD. The discussion starts with the Euler method and progresses to the more accurate Runge-Kutta (RK) methods used by the variable-step ODE solvers built into MATLAB. The usefulness of stiff ODE solvers is explored and methods available to improve their performance are studied. Other system simulation software such as SPICE derivatives are compared with the MATLAB based state equation solution adopted in this thesis.

**Chapter 4: Surge-absorbent device characterization.** The mathematical models required to accurately represent the highly nonlinear surge absorbent devices are studied here. MOVs are characterized in order to find the model parameters for a recommended model based on device physics. The same characterization is extended to TVS diodes with reasonable success. The MOV industrial characterization is studied using a second basic model adapted for SPICE-based simulations by some manufacturers.

**Chapter 5: Investigation of surge propagation in linear systems.** The usefulness of Laplace transforms for the analysis of transient propagation in linear circuits is brought to light by using it to study the generation of the surge voltage by the LSS, which can be represented by a purely linear equivalent circuit. Numerical simulations using MATLAB as well as SPICE based simulations are

performed to validate the Laplace analysis. This chapter also explores improvements to numerical simulations using MATLAB by its use to study the “off” state of the MOV and also certain fixed states corresponding to three different operating points in its characteristic.

**Chapter 6: Investigation of surge propagation through a TVSS system.** Here we investigate numerically how a surge propagates through a complete two-level TVSS containing two nonlinear surge absorbent components and four linear components. Energy absorptions and associated time lags for the various linear and nonlinear components that make up the TVSS are highlighted. All simulated results for voltage, current, power and energy in individual components of the TVSS are validated against experimental data obtained by surging a prototype circuit using the LSS.

**Chapter 7: Conclusion and future developments.** The main conclusions in the development of numerical techniques to analyze the surge propagation in a class B TVSS unit are summarized here. Among the recommendations made for future research, use of alternative models for the surge absorbent electronic components and more accurate representation of the test setup are discussed. It is also suggested that the methodologies presented in the thesis be extended to include powered testing of the TVSS. The chapter concludes with the proposal of extending numerical techniques developed in this project to investigate propagation of transients in downstream electronics such as a switched mode power converter (SMPC) or an uninterruptible power supply (UPS).

## **1.4 List of publications arising from the work in the thesis**

### **Peer-reviewed conference papers**

- S. James, N. Kularatna, A. Steyn-Ross, and R. Kunnemeyer, "Numerical simulation of surge protection circuits and experimental verification using a lightning surge simulator," in *IECON 2012 - 38th Annual Conference on IEEE Industrial Electronics Society*, Montreal, Canada, pp. 615-620.
- S. James, N. Kularatna, A. Steyn-Ross, and R. Kunnemeyer, "Modeling of surge protection circuits for the study of transient propagation in power conversion interfaces," in *ENZCON 2011 – 18th Electronics New Zealand Conference*, Palmerston North, New Zealand, pp. 113-117.

- S. James, N. Kularatna, A. Steyn-Ross, A. Pandey, R. Kunemeyer, and D. Tantrigoda, "Investigation of failure patterns of desktop computer power supplies using a lightning surge simulator and the generation of a database for a comprehensive surge propagation study," in *IECON 2010 - 36th Annual Conference on IEEE Industrial Electronics Society*, Phoenix, USA, pp. 1275-1280.

### **Journal papers**

N. Kularatna, J. Fernando, A. Pandey, and S. James, "Surge Capability Testing of Supercapacitor Families Using a Lightning Surge Simulator," *Industrial Electronics, IEEE Transactions on*, vol. 58, pp. 4942-4949



## Chapter 2: Surge protection of power electronics

---

### 2.1 Introduction

Important areas relevant to background of the work done in the project such as “transient surge disturbances”, “surge protection and surge absorbent devices”, and “surge protection standards and practices” have been explained in detail using material from a book chapter [6] by the author’s supervisor. There is additional material here in the discussion of surge protection devices such as metal oxide varistors (MOVs) and transient voltage suppressor (TVS) diodes that have been used extensively in both analytical and experimental work for the thesis. State of the art in relation to modeling individual protection components is discussed. This is important for the work presented since a 2-level TVSS will be modeled and analyzed with the use of appropriate models for the surge protection components. The benefit of using the chosen models is also outlined.

A clear understanding of the difference between root mean square (RMS) voltage fluctuations and short-term high voltage (HV) transients is provided in Section 2.2. Investigation of surge propagation in this thesis is confined to the later type of transient disturbances.

By the turn of the century, around 75% of the power generated was processed by power electronics. In modern semiconductor technology, where ultra large scale integrated (ULSI) circuits are progressing towards system on a chip (SoC) concepts, the feature size is reaching sub 25 nm levels [4, 7, 8] and they are powered by DC power rails as low as 1.2 to 0.8 V. These two trends have made demands within the power conversion interface complex. Compact ultra-low DC voltage sources with energy backup, fast transient response and power management have become mandatory in powering modern electronics. Uninterruptible power supplies and advanced power conditioning with surge protection have become essential in providing clean and reliable AC power.

The proliferation of microelectronic processors in a wide range of equipment from automated industrial assembly lines to hospital diagnostic systems, has increased the vulnerability of such electronic systems to power line disturbances [9]. This is mainly because they bring together the high-energy power line and sensitive low-power integrated circuits controlling power semiconductors in the conversion interfaces such as DC-DC converters. The term *power conditioning* is used to describe a broad class of products designed to improve or assure the quality of the AC voltage connected to sensitive microelectronic loads. With the advent of “direct-off-line” switch mode power supplies using sensitive electronic primary control circuits, the need for input AC power-line transient surge protection has become more universally recognized [5].

Utilities realize that different types of customers require different levels of reliability, and make every effort to supply disturbance-free power. However, natural phenomena such as lightning transients make it impossible to provide disturbance-free power all the time. In addition to these external disturbances, sources within buildings, such as switching of heavy inductive equipment loads, poor wiring, overloaded circuits, and inadequate grounding, can cause electrical disturbances. Many of these power disturbances, particularly the transient surges, can be harmful to sensitive electronic loads supplied with low voltage DC power. Power disturbances can alter or destroy data and sometimes cause equipment damage which may, in turn, result in loss of production, scheduling conflicts, lost orders, and accounting problems.

There are specialized components and well-designed protection systems that can prevent these undesirable disturbances reaching the sensitive electronic loads. Protective systems range from those providing minimal protection to those that construct a new power source such as a uninterruptible power supply (UPS) for critical loads, converting the standard “utility grade power”, which may be adequate for most equipment, into “electronic grade power” required by many critical loads. This chapter discusses the protection methods against transients and surges in power conversion systems required for electronic systems demanding higher reliability.

Treatment will also discuss characterization of surges affecting electronic circuits powered by low DC voltages derived from low-voltage (1000V and less) AC power.

## **2.2 Power line disturbances**

In a single- or three-phase utility power supply, commercial power companies are expected to supply AC power at a nominal RMS voltage with a percentage tolerance such as  $\pm 6\%$  with limited amounts of harmonics as per applicable standards. However, the practical utility grade power supply carries many unwanted RMS voltage disturbances, harmonics, noise and transients. Figure 2-1(a) and Figure 2-1(b) depict the RMS voltage disturbances and transients and noise respectively. Figure 2-1(c) shows the ideal waveform of a 50 Hz, 230V RMS power supply and its corresponding frequency spectrum.

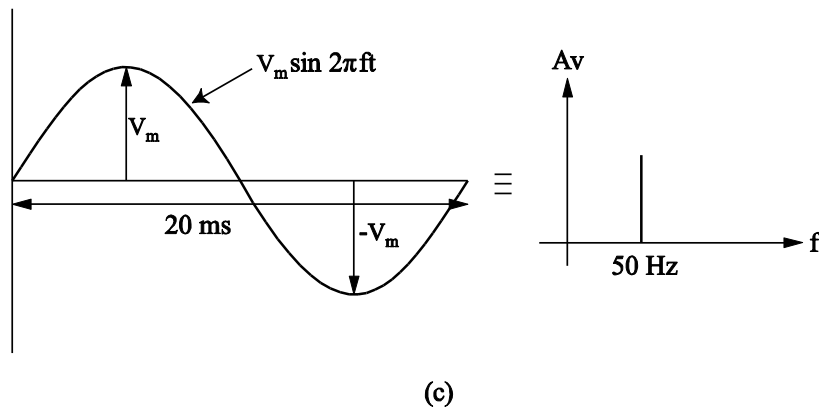
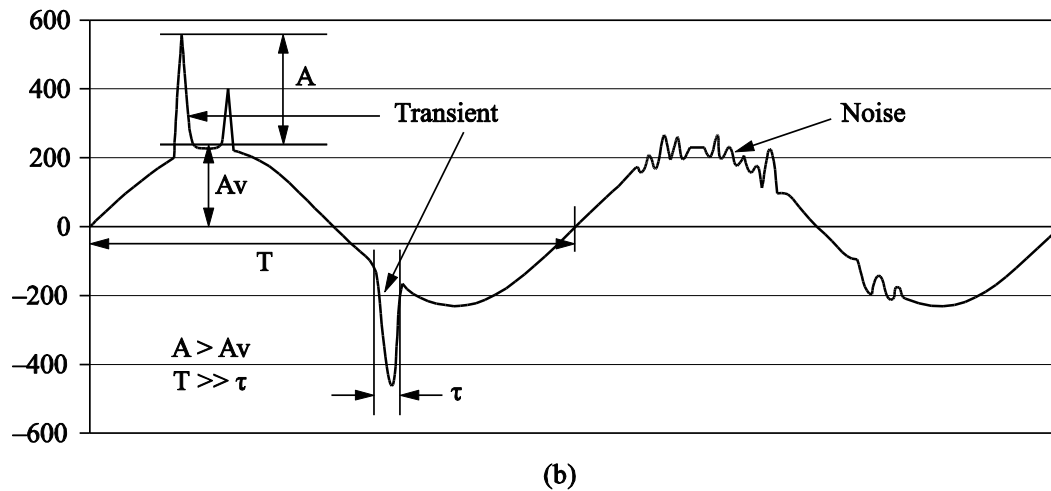
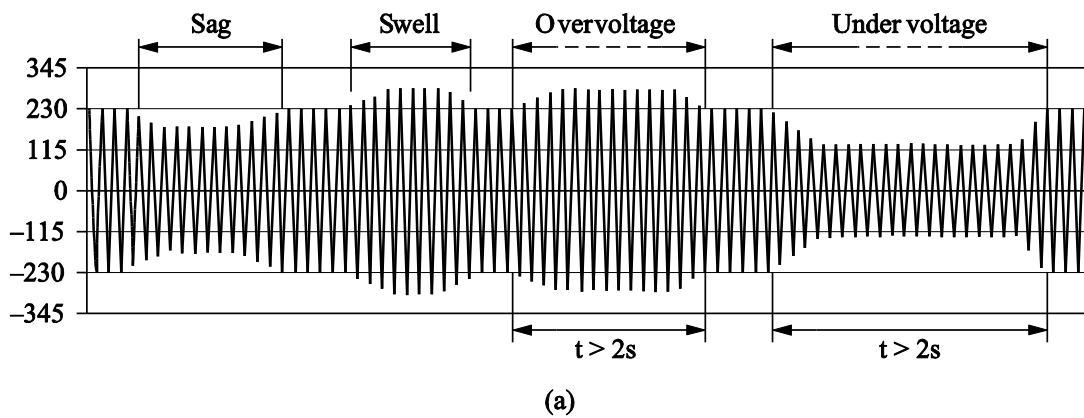


Figure 2-1: Examples of disturbances on a 230V RMS, 50 Hz utility AC power supply: (a) RMS voltage fluctuations; (b) transients and noise superimposed on the waveform; (c) ideal waveform and its frequency spectrum [6]

## 2.2.1 RMS voltage fluctuations

Voltage surges are voltage increases which typically last from about 15 milliseconds to one-half of a second. A surge that lasts more than two seconds is typically referred to as an *overvoltage*. Voltage sags are undervoltage conditions,

which also last from 15 milliseconds to one-half of a second. Voltage sag that lasts for more than two seconds is typically referred to as an *undervoltage*.

### **2.2.2 Transient surges**

Surge voltages occurring in low-voltage ac power circuits originate from two major sources, system switching transients and direct or indirect lightning effects on the power system [10].

As depicted in Figure 2-1(b) voltage transients are sharp, very brief spikes in the supply waveform. These sudden increases in voltage are commonly caused by the on and off switching of heavy loads such as air conditioners, electric power tools, machinery and elevators. Lightning transients can cause even larger spikes. Although they usually last less than 200 microseconds, these spikes, positive or negative, in the range from about 180% of the AC peak value to over 6 kV can be dangerous to unprotected equipment. These high magnitude sudden voltage variations can wipe out stored data, alter data in progress, and cause fatal electronic hardware damage.

### **2.2.3 Electrical noise**

Electrical noise is high-frequency interference which can vary in frequency from 7000Hz to over 50 MHz. Noise can be transmitted and picked up by a power cord acting as an antenna or it can be carried through the power line. These disturbances can be radio frequency interference (RFI) from radio, TV, cellular and microwave transmission, radar, arc welding and distant lightning. Noise can also be caused by electromagnetic interference (EMI) produced by heaters, air conditioners, electric typewriters, coffee makers, and other thermostat-controlled or motor-operated devices.

Although generally non-destructive, electrical noise can sometimes pass through a power supply as if it were a signal and wipe out stored data or cause erroneous data output. Problems result when microelectronic circuitry is invaded by transient, high-frequency voltages collectively called “line noise”, which can be grouped into one of two categories: normal mode or common mode (described in Section 2.2.5).

#### **2.2.4 Harmonics**

Harmonic distortions are usually caused by the use of nonlinear loads by the end users of electricity. Nonlinear loads, a vast majority of which are loads with power electronic devices, draw current in a non-sinusoidal manner. With the increased use of such devices in consumer loads, the presence of distortions in current and voltage waveforms have become a frequent occurrence today. It is quite common to have a flattened-top sine wave with these nonlinear loads such as computer power supplies, UPS rectifiers or even energy saving lamps. The ultimate result is that the terminal voltage at the consumer end will be a non-sinusoidal waveform with a great deal of harmonics.

#### **2.2.5 Modes of transients and noise**

The noise and transients sources superimposed on the utility voltage can come in two different forms, namely common mode and differential mode. Differential mode is sometimes referred to as normal-mode or transverse-mode. In tackling surge protection in power electronic systems it is very important to deal with both cases. Figure 2-2(a) illustrates the two cases.

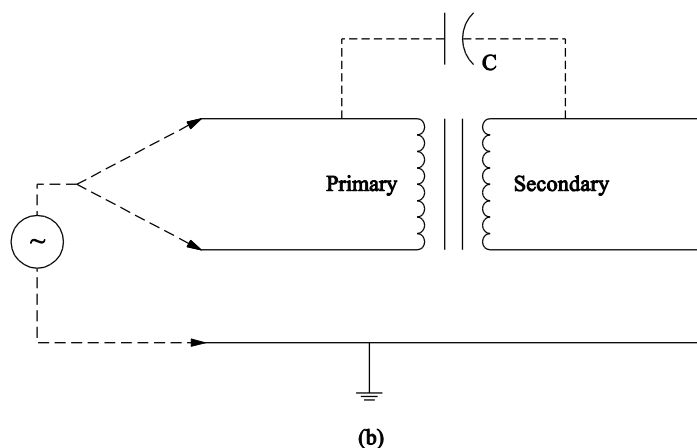
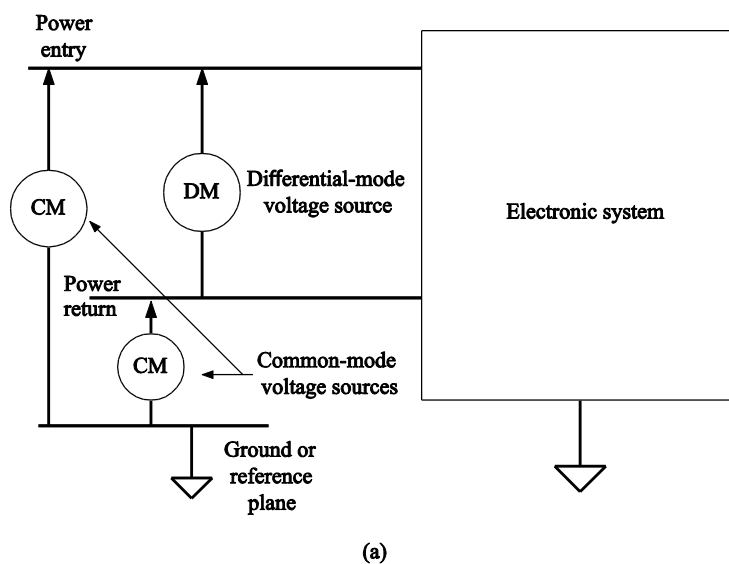


Figure 2-2: (a) Differential and common modes; (b) common-mode signal coupling towards secondary side due to coupling capacitance

### 2.2.5.1 Differential Mode (Normal Mode or Transverse Mode)

As the name implies differential mode signals appear between the live wire and the accompanying neutral wire in the case of an AC supply input. Similarly for a DC power input it appears between the positive or negative rail and its return current path. These two lines represent the normal path of power through the electric circuits, which gives any normal-mode signal route into sensitive components.

### 2.2.5.2 Common Mode Signals

Common-mode signals are voltage differentials that appear between the ground and either of the two supply lines. Common-mode (CM) transients are most often the cause of disruption, because digital logic or analog signals are either directly

or capacitively tied to the safety ground as a zero-voltage data reference point for semiconductors. As a result, transient CM voltage differences as small as 0.5V can cause that reference point to shift, momentarily “confusing” the semiconductor chips. Figure 2-2 (b) indicates the possibility of transferring common mode signals due to interwinding capacitances in a transformer with electrical isolation. If the transformer winding process is focused on reducing interwinding capacitances, an isolation transformer will reduce noise and transients coupled towards the load. However, manufacturing isolation transformers with high common-mode isolation properties can be expensive.

## **2.3 Power quality issues**

### **2.3.1 Current state of a typical electronic load**

After the invention of the transistor in 1947, followed by the development of integrated circuit concepts in the mid-1950s, an exponential growth of integrated circuits occurred following Moore’s law [11]. Moore's law is the observation that, over the history of computing hardware, the number of transistors on integrated circuits doubles approximately every two years. While silicon (Si) and gallium arsenide (GaAs) progressed on similar paths, newer compound semiconductor materials such as silicon-germanium (SiGe) were also gradually introduced to cater for high-frequency requirements of commercial electronic systems.

With integrated circuits gradually progressing towards SoC concepts with massively increased transistor count, the feature size of the transistors was gradually dropping towards less than 0.1 $\mu$ m. For example, the company Intel announced a 22 nm microprocessor in 2011 [12]. Figure 2-3(a) indicates the Moore’s law-based general progress of integrated circuits (ICs), while the DC rail voltages are dropping towards sub-1 V levels. With the equivalent noise levels increasing within the complex ICs, dropping of the logic voltage levels makes the scenario even more complex [13, 14]. Figure 2-3(b) indicates the development of processors similar to the Intel family, and their power supply requirements. Figure 2-3(c) indicates the scenario in terms of clock speed, power consumption and most importantly the equivalent impedance of the processor load. With the processor equivalent impedance

dropping below 1 mΩ and the DC rail voltages coming down to sub-1 V levels, a transient surge voltage appearing on the power supply rails could create disastrous consequences.

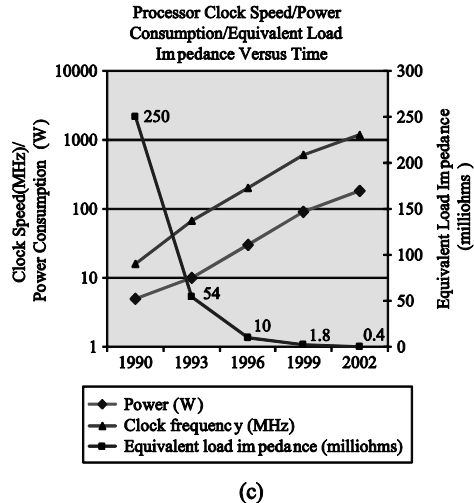
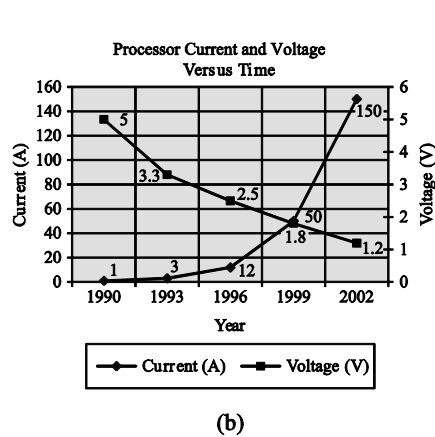
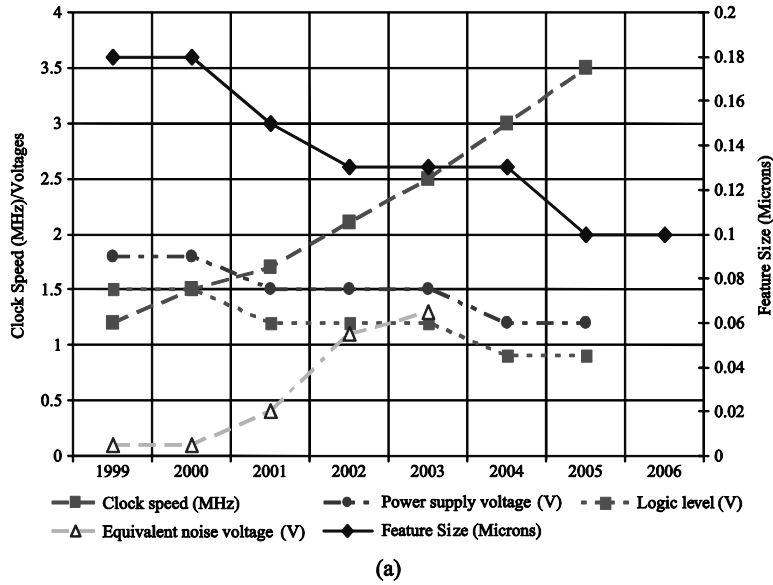


Figure 2-3 Developments of integrated circuits and processor families: (a) Moore's law based progress of ICs; (b) development of processors and their power supply requirements; (c) processor speed, power consumption, and equivalent impedance

In summary this situation creates a challenge to the maintenance of power quality in order to maintain signal integrity in complex processor based electronic loads; chip designers, as well as the power supply designers, are required to pay adequate attention to this situation for reliable product design. Protection against transients and surges therefore is of paramount interest.

### 2.3.2 Development of DC Power Supplies

During the 1970s and early 1980s most DC supplies were linear types as depicted in Figure 2-4(a). These simple linear power supplies were based on a step-down transformer which had the advantage of suppressing high voltage differential or common mode transients. Particularly dangerous common-mode transients were easily suppressed by a reasonably well-designed input transformer with galvanic isolation between the windings and with low inter-winding capacitances.

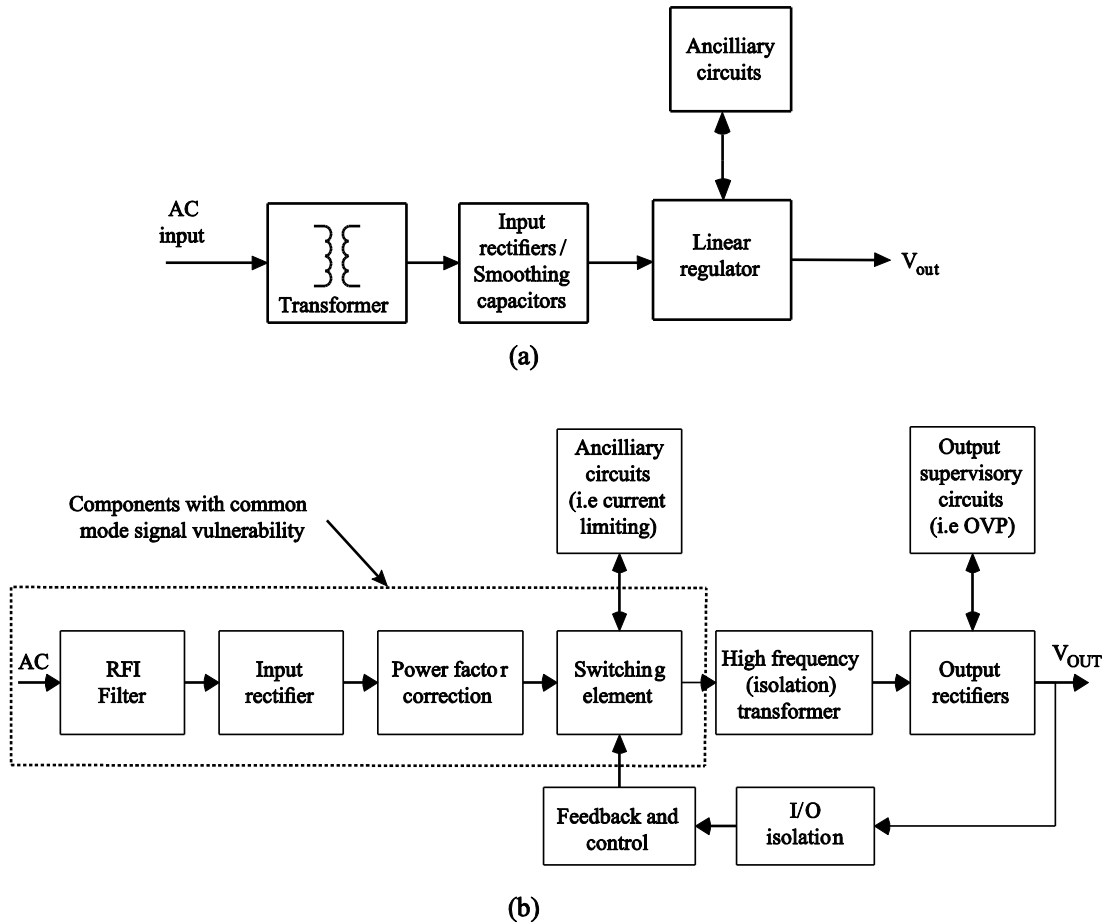


Figure 2-4: Comparison of linear power supplies and modern SMPS: (a) Simple linear power supply with an isolation transformer; (b) modern off-the-line switching power supply

Figure 2-4(b) shows the situation of modern SMPS systems designed based on power semiconductors such as BJTs, MOSFETS or IGBTs where higher VA-rated units carry a power factor correction block as well. In these units the essential (regulatory) condition of ground isolation, for minimizing safety issues, is maintained only by the high-frequency switching transformer, which becomes an integral part of

the DC-DC converter stage [15, 16]. It is important to note that the input bulk DC rail is the result of direct rectification of 230V/50 Hz or 120V/60 Hz input source, creating an unregulated DC rail of 320V DC or 165 VDC respectively. All circuit blocks, from the AC input up to the DC-DC converter stage of the complex modern direct-off-the-line SMPS systems, are vulnerable to directly coupled common-mode transients. Hence well-designed surge protection circuits are necessary, particularly for the components shown within the dotted lines of Figure 2-4(b).

## **2.4 Surge protection and surge absorbent devices**

Transient surges are usually unpredictable and statistical in nature. It is not possible to stop them totally but, in planning engineering facilities, every effort must be made to minimize their effects. Transients that either get induced, or enter directly can cause disastrous effects on various end user circuits. Protection of circuits against transients is based on two main principles: (a) limiting the amplitude of the surge at each component to a safe value, and (b) diverting the surge currents through protection-specific components. Figure 2-5 shows what a circuit designer is expected to consider, when protecting a system against a surge superimposed on 230 V/50 Hz supply input. The voltage transient shown in the figure, which might represent a lightning strike, exists only for about 100  $\mu$ s, compared to the 20-ms period AC cycle. In the design of the basic power conversion system, designers often disregard the possibility of these superimposed signals, and assume that the input utility source is a sine wave as per specifications considered in the project. In general, the possibility of surge damage is related to the height of the surge, and the duration of the surge. As indicated in Figure 2-5, if the transient amplitude is between 400-600 V, the basic circuit blocks are still considered to be safe. When the spike amplitude is within 600-900 V, degradation of performance or temporary errors could be expected, while values above this can cause permanent faults.

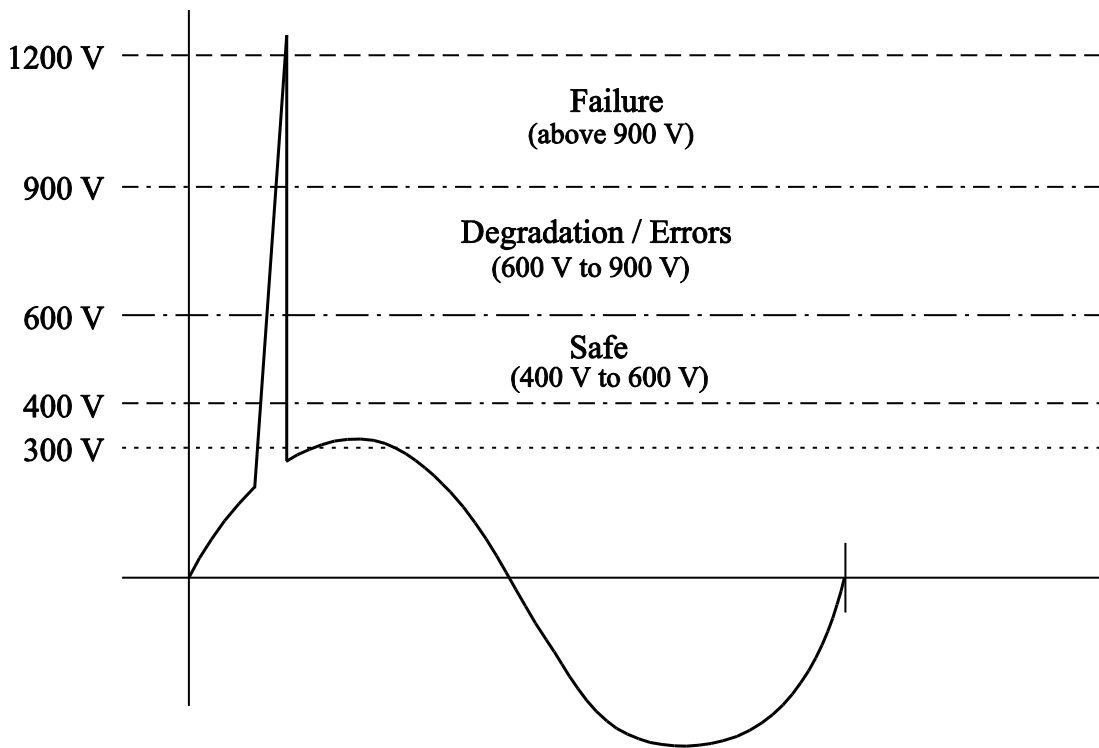


Figure 2-5: Transient superimposed on the AC-input waveform with its effects

### 2.4.1 Practical Devices Used in Surge Protection Circuits

In developing surge protection circuits, the designer has to ensure that: (1) surge arrester stages do not alter the normal operation of the power conversion circuit, and (2) components used for surge absorption, diversion or attenuation should be able withstand the surge. Reliability of the surge protection system is also important, since a very high level surge might destroy the surge arrester components.

Diverting a transient can be accomplished with a voltage-clamping device or with a crowbar device that switch into a very low impedance mode to short circuit the transient. The designs of these two types, as well as their operation and application are different [17]. In designing practical surge arrester circuits, these nonlinear devices are combined with inductors, and capacitors.

A voltage clamping device has variable impedance depending on the current flowing through the device or on the voltage across its terminals. These devices exhibit a nonlinear impedance characteristic, that is Ohm's law applicable, but the equation has a variable  $R$ . The variation of the impedance is monotonic; in other

words, it does not contain discontinuities unlike a crowbar device, which exhibits a turn-on action [18].

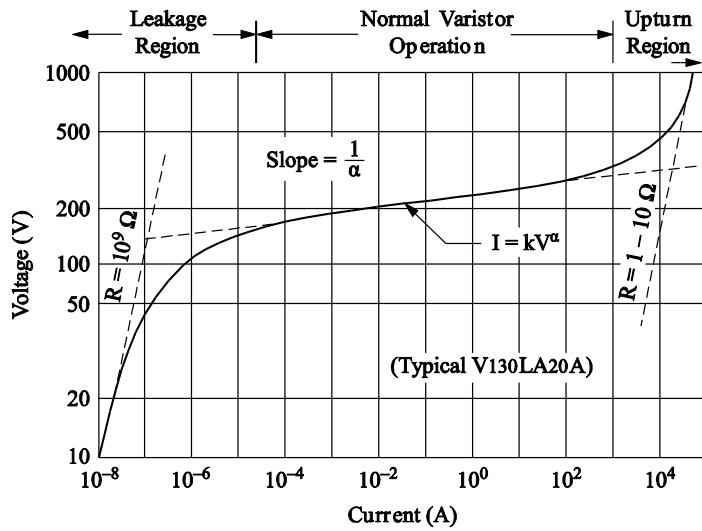
The most common semiconductor nonlinear devices used are metal oxide varistors (MOVs), thyristors and avalanche-type back-to-back zener diodes. Gas discharge tubes (GDTs) are also used in some systems. MOVs and avalanche type back-to-back zener diodes are voltage-clamping devices whereas thyristors and gas discharge tubes are classified as “crowbar” devices.

#### **2.4.1.1 Metal Oxide Varistors**

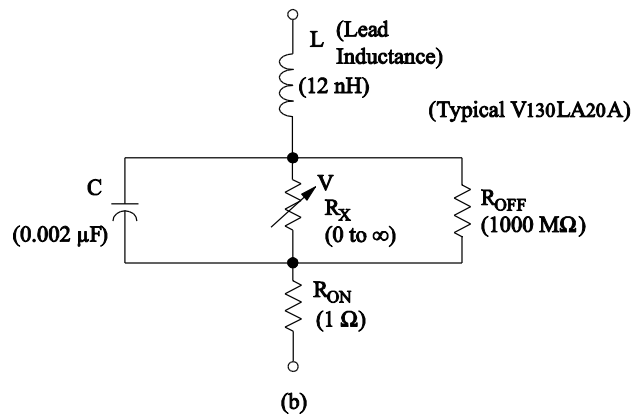
MOVs are zinc-oxide (ZnO) based ceramic semiconductor devices with highly nonlinear current-voltage characteristics similar to back-to-back zener diodes [19]. They are typically formed into a disc shape. The structure of the body consists of a matrix of conductive ZnO grains separated by grain boundaries providing p–n junction semiconductor characteristics. Each inter-granular boundary displays a rectifying action and presents a specific voltage barrier. When these conduct, they form a low ohmic path to absorb surge energy [20].

Figure 2-6 (a) shows a typical  $V-I$  characteristic of an MOV. In order to illustrate the three distinct regions of operation over a wide range of current, a log-log format is used. The basic electrical model for the varistor that could relate to all three regions of operation is shown in Figure 2-6(b) [21]. At low currents the  $V-I$  curve approaches a linear ohmic relationship and shows a significant temperature dependence. Under this condition the MOV is in a very high resistance mode approaching about  $1\text{G}\Omega$  or higher. Under this near open-circuit condition, the nonlinear resistance  $R_X$  in Figure 2-6(b) can be ignored, as  $R_{\text{OFF}}$  value in parallel will dominate. The resulting equivalent applicable to the leakage region is shown in Figure 2-6(c).  $R_{\text{OFF}}$  value is dependent on the temperature, but remains in the range of 10 to  $1000\text{M}\Omega$ . It also depends on the frequency in an inversely proportional manner. In the normal varistor operation region or in the conduction mode the value of  $R_X$  becomes many orders of magnitudes less than  $R_{\text{OFF}}$ . The effect of this is for the MOV to absorb much of the transient energy. The equivalent circuit applicable to normal varistor operation is also shown in Figure 2-6(c). At high currents, approaching the maximum rating, the nonlinear resistance is in a low resistance mode that

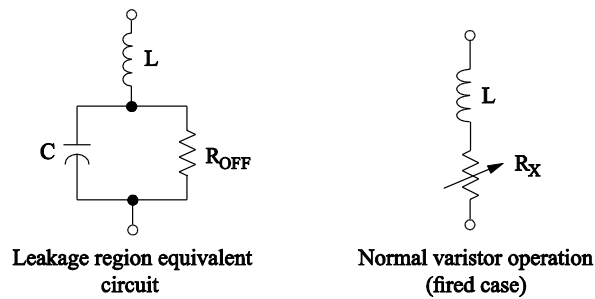
approximates a short circuit. This is represented by  $R_{ON}$  which is the bulk resistance of the zinc oxide grains and would be in the range 1 – 10  $\Omega$  [21].



(a)



(b)



(c)

Figure 2-6: Metal oxide varistor characteristic and equivalent circuits: (a) V-I characteristic; (b) generalized equivalent circuit; (c) simplified cases under leakage and conduction [21]

In the state of the art in MOV modelling, different mathematical models are used for the nonlinear resistance  $R_X$ , which plays the major role in surge absorption

by the varistor [21, 22]. Two different relationships that govern the operation of this nonlinear resistance are given by Eqs (2-1) and (2-2):

$$i(v) = kv^\alpha \quad (2-1)$$

$$\log(v) = B_1 + B_2 \log_{10}(i) + B_3 e^{-\log_{10}(i)} + B_4 e^{\log_{10}(i)} \quad (2-2)$$

where  $i$  is the current through and  $v$  is the voltage across the varistor. The parameters  $k$  and  $\alpha$  of Eq.(2-1) and parameters  $B_1, B_2, B_3$  and  $B_4$  of Eq. (2-2) are unique to each varistor type.

The power-law representation given in Eq. (2-1) which represents the MOV's nonlinear resistance in its 'normal varistor operation' region [19, 21, 23] was chosen to model the MOV in this work; almost all of the surge energies, which is of interest to the work done here, are transferred when the MOV operates in this region. The parameters  $k$  and  $\alpha$  of Eq. (2-1) can be experimentally found by curve-fitting for any available MOV as shown in Chapter 4;  $k$  is dependent on the device geometry and the exponent  $\alpha$  defines the degree of nonlinearity in the resistance characteristic and can be controlled by selection of materials and the manufacturing process. High  $\alpha$  implies a stronger clamping action. For zinc-oxide technology, typical  $\alpha$  values lie in the range of 15 to 30.

Mathematically more complex, highly nonlinear log representation given by Eq. (2-2) represents the MOV's nonlinear resistance from a few  $\mu\text{A}$  (leakage region) to tens of kA [22]. As shown in Chapter 6, modelling of the leakage region can be ignored for the energies to be estimated in this work. The significance of right hand side (RHS) coefficients, of Eq. (2-2) is provided in Section 4.2.9, where the characterization of a MOV based on the model of Eq.(2-2) is studied. A weakness of this representation would be the difficulty in estimating the coefficients by a suitable curve-fit for an off-the-shelf MOV. Varistor manufacturers such as *Littelfuse* have provided SPICE (Simulation Program with Integrated Circuit Emphasis) based models, for some of the varistors manufactured by them; in these models the

nonlinearity of the MOV characteristic has been represented by extended versions of Eq (2-2), with up to six terms [24].

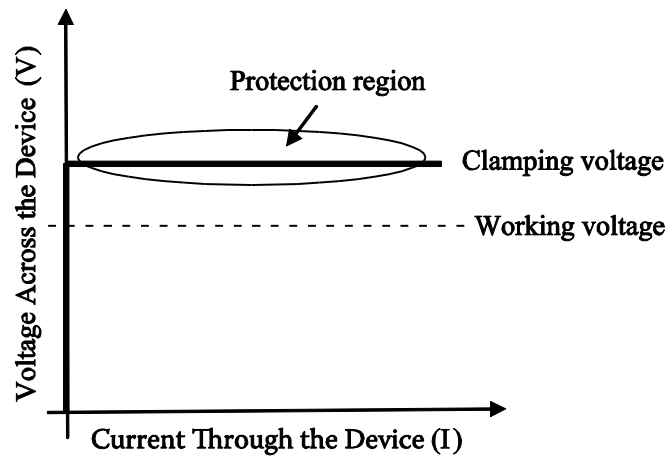
High transient energy absorbent capability is achieved by increasing the size of the disc. Typical diameters range from 3 to 20 mm. MOVs turn on in a few nanoseconds and have high clamping voltages, ranging from approximately 30V to 1.5kV. Figure 2-7 compares the behaviour of an MOV with an ideal clamping device, and with a TVS zener diode. Application guidelines on MOVs are given in [25, 26]. Basic theory of operation of ZnO varistors can be found in [19, 27].

Subjecting an MOV to continuous abnormal voltage conditions, rather than short-duration transients, may cause the MOV to go into thermal runaway, resulting in overheating, smoke and possible fire. To prevent this condition, many modern MOVs include an internal thermal fuse or a thermal cutoff device. Some even extend this capability with an internal indicator that provides a logic output if the device's thermal protection is engaged [28]. An overview comparison of thermally protected MOVs (TPMOV) with traditional MOVs is provided in [29]. These TPMOVs are useful in occasions where continuous AC line overvoltages could occur.

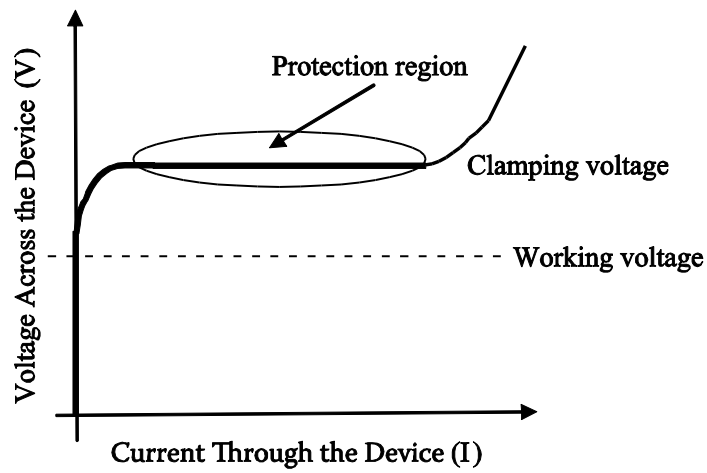
#### **2.4.1.2 TVS diodes and thyristors**

TVS diodes and TVS thyristors are two basic types of p-n junction devices available for transient surge protection. Both types are available as back-to-back devices (bidirectional devices) suitable for protection against positive or negative surges appearing at power or signal entry inputs. The TVS diode is a clamping device which suppresses all voltages above its breakdown voltage whereas the TVS thyristor is a crowbar device which switches on when overvoltages rise up to the break-over voltage [30].

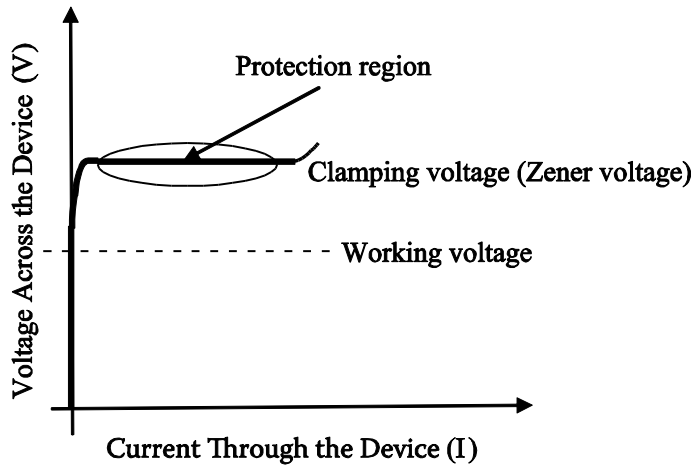
Silicon rectifier technology, designed for transient suppression, has improved the performance of regulator-type zener diodes to provide TVS diodes. The major advantage of these diodes is their very effective clamping, which comes closest to an ideal constant voltage clamp [17].



(a)



(b)



(c)

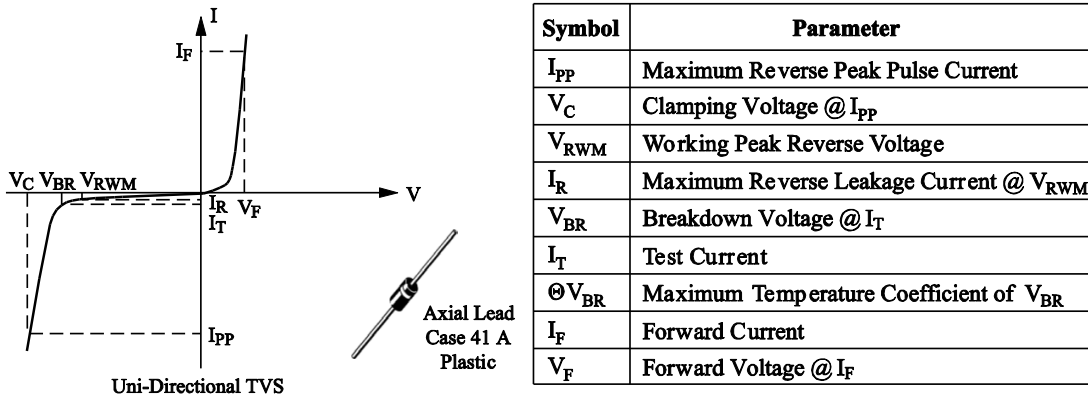
Figure 2-7: Comparison of clamping type transient protection devices: (a) ideal case; (b) zinc-oxide varistor; (c) TVS zener diode

Figure 2-8 provides an example of a commercial TVS diode device manufactured by ON Semiconductor [31]. As shown in Figure 2-8(a), the  $V-I$  characteristic curve of the TVS diode is similar to that of a zener diode. Unlike zener diodes, TVS diodes are specifically designed to clamp transient surge pulses, rather than regulate a relatively stable voltage. Like all clamping devices, it automatically resets when the transient drops below the breakdown voltage, but absorbs much more of the transient energy internally than a similarly rated TVS thyristor device. A large cross sectional area is employed for a TVS diode junction, allowing it to conduct high transient currents. These diodes respond almost instantaneously to transient events. Their clamping voltage (which is the voltage measured across the device terminals when the device is fired, and a peak pulse current is flowing through the device) ranges from a few volts to a few hundred volts.

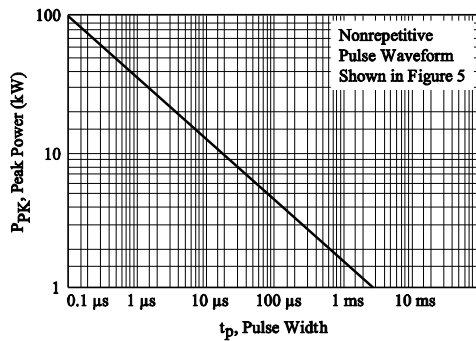
A TVS diode can respond to transients faster than other transient protection components such as MOVs and GDTs. Clamping occurs in picoseconds. The fast response time of the TVS diodes means that any voltage overshoot, as shown in Figure 2-8(d), is primarily due to lead inductance. Bi-directional TVS diodes available from several manufacturers have symmetrical response in both positive and negative regions and offer similar clamping to both positive and negative surges. They come in axial leaded and surface mount packages. Datasheet terminology for silicon TVS devices and design calculations are discussed in [32].

When individual excessive surges occur beyond the rating of the TVS diode, it can fail like any other stressed semiconductor component. For the TVS diode, this primarily involves peak pulse power ( $P_{PP}$ ) and/or peak pulse current ( $I_{PP}$ ). The basic form of failure mechanism is attributable to excessive heat in the active p-n junction of the silicon element [33].

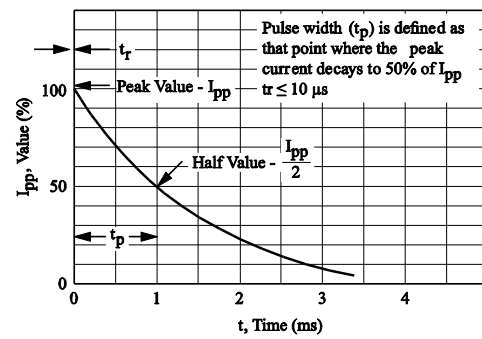
A TVS diode macro-model offering greater accuracy than a standard diode SPICE model is discussed in [34].



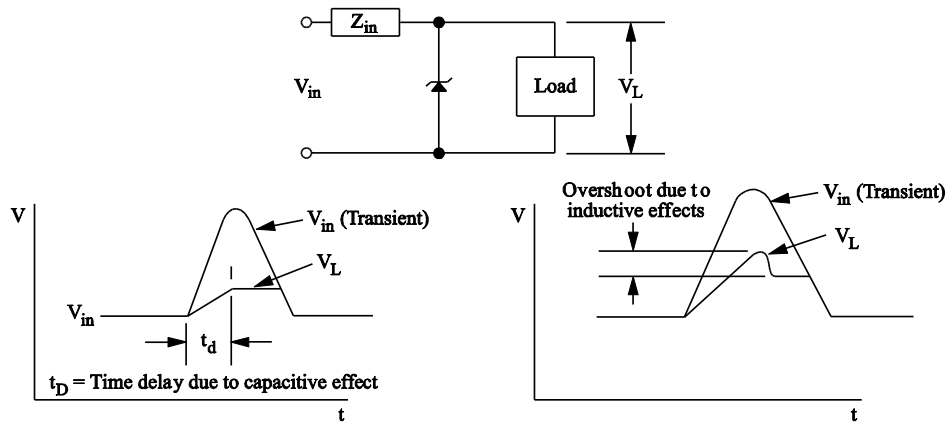
(a)



(b)



(c)



(d)

Figure 2-8: An example of a TVS diode: (a) device behaviour and data sheet parameters; (b) pulse power absorption capability versus pulse width; (c) test pulse used; (d) typical application circuit and voltage at protected load due to device capacitance and lead inductance [31]

TVS thyristors are solid state devices constructed with four alternating layers of p-type and n-type material. The advantage of this device is its low on-state voltage after triggering which provides much higher current capability for a relatively small

chip size compared to a clamp device. TVS thyristors are used extensively in surge protection of communication equipment for the reasons given next.

Because communication equipment with large-scale integrated (LSI) circuits is very sensitive to surges, its surge protection devices are required to have a high-speed response and a high surge capability. These devices are also be required to have low capacitance to reduce transmission losses in high-speed wideband transmission systems. Conventional lightning surge protectors, with a GDT, resistors and ceramic varistors, cannot be used in high-speed transmission systems because they cause excessive transmission loss. TVS thyristors have been used for surge protection because of their high per-unit area surge capability. This characteristic enables reduction of device size and hence also its capacitance and transmission loss [35].

TVS thyristors are avalanche triggered components and protect sensitive loads by switching to a low on-state of a few volts, thus providing a “crowbar” effect with high current capability. Transition to on-state is initiated at the maximum breakover voltage of the device. Once the TVS thyristors is in the on-state, the current through the device must be interrupted or drop below minimum holding current to restore to nonconduction after the transient has subsided. They are normally not used for protection across DC power or low impedance voltage sources because they may not restore to non-conduction. A TVS diode would be a better choice for such applications.

The surge current capability of a TVS thyristor is determined by structure as well as size. Operating voltage levels begin at 12V and are available in several increments up through several hundred volts. They do not wear out, but when electrically overstressed fail as a short-circuit [36]. Figure 2-9 provides an example of a commercial device from ON Semiconductor, with a typical telecommunication outside-plant protection circuit [37].

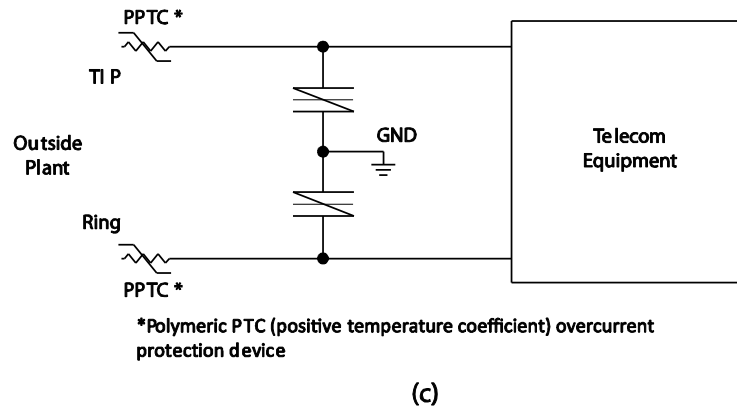
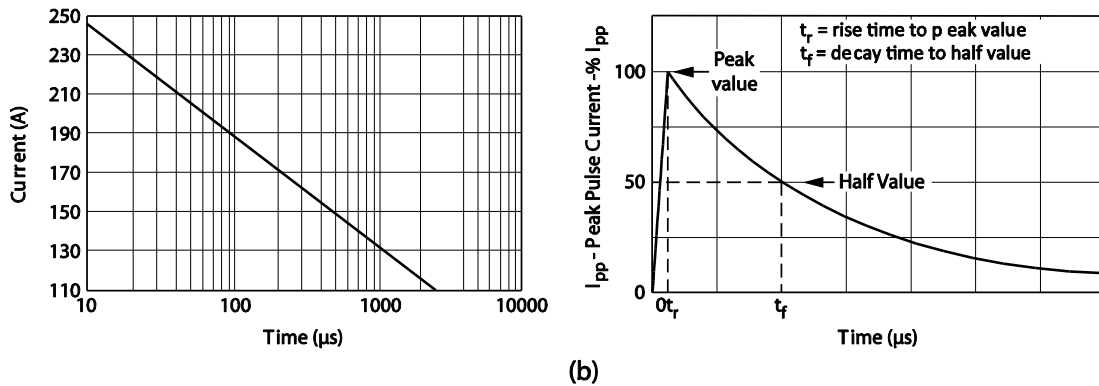
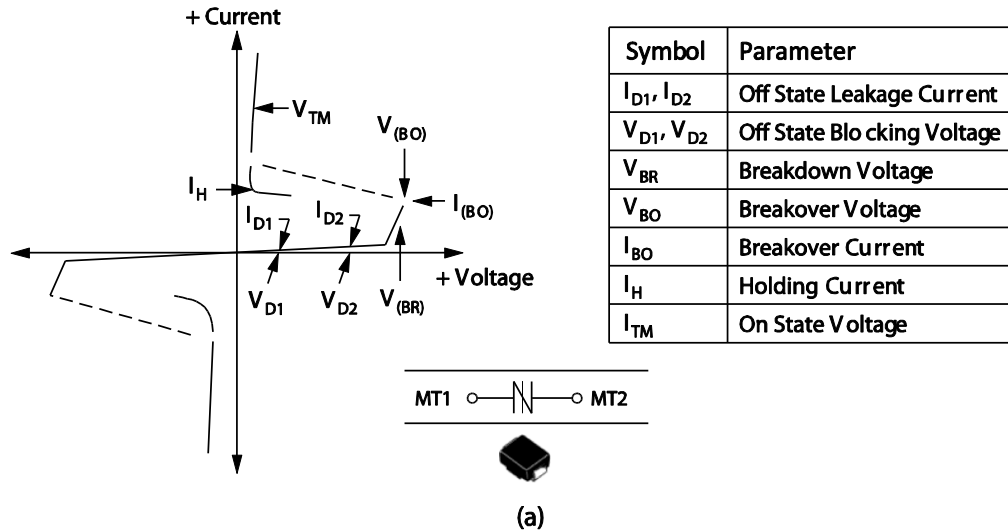


Figure 2-9: An example of a thyristor breakover device (a) device behaviour and data sheet parameters (b) pulse power absorption capability versus pulse width (c) test pulse used (d) typical application circuit in telecommunication plant with series current limiting device [37]

### 2.4.1.3 Gas Discharge Tubes

Gas discharge tubes (GDTs, or simply gas tubes) are devices that employ an internal inert gas that ionizes and conducts during a transient event. Because the internal gas requires time to ionize, gas tubes can take several microseconds to turn

on or “fire.” In fact, the reaction time, and firing voltage are dependent on the slope of the transient front. A circuit protected by a gas tube arrester will typically see overshoot voltages ranging from a few hundred volts to several thousand volts.

The GDT uses specially designed electrodes fitted inside a tube filled with one or more gases under pressure. They are rugged, relatively inexpensive, and have a small shunt capacitance; therefore, they do not limit the bandwidth of high frequency circuits as much as other nonlinear components [38]

GDTs have extremely high pulse ratings for their size. They are designed for use over a broad voltage spectrum. Impulse striking (firing) voltages typically start at 500V; these firing voltages are too high to protect microchips but GDTs can be used in conjunction with TVS diodes to provide effective multi-kilo ampere, low clamping level for 5V signal lines [39]. They are used in telecom network interface device boxes and central office switching gears to provide protection from lightning and alternating current power cross faults on the telecom network [40].

Table 2-1: Comparison of TVS devices [41]

Suppression element	Advantages	Disadvantages	Expected Life
Gas tube	Very high current-handling capability Low capacitance High insulation resistance	Very high firing voltage Finite life cycle Slow response times Non-restoring under DC	Limited
MOV	High current-handling capability Broad current spectrum Broad voltage spectrum	Gradual degradation High clamping voltage High capacitance	Degrades
TVS diode	Low clamping voltage Does not degrade Broad voltage spectrum Extremely fast response time	Limited surge current rating High capacitance for low-voltage types	Long
TVS thyristor	Does not degrade Fast response time High current-handling capability	Non-restoring under DC Narrow voltage range Turn-off delay time	Long

Table 2-1 compares the characteristics of the most widely used TVS devices. References [41, 42] provide more details.

## 2.4.2 Levels of surge protection

As recommended by the IEEE [43], surge protective devices (SPDs), also known as transient voltage suppressor systems (TVSSs), should be coordinated in a staged or cascaded approach. The starting point is at the service entrance. With primary protection, the first surge diversion occurs at the service entrance, and then any residual voltage can be dealt with by a second TVSS at the power panel of the computer room, or other critical load as shown in Figure 2-10(a). This two-stage approach will reduce 20,000 volt induced lightning surges well under 330 volts peak as recommended by the IEEE [44].

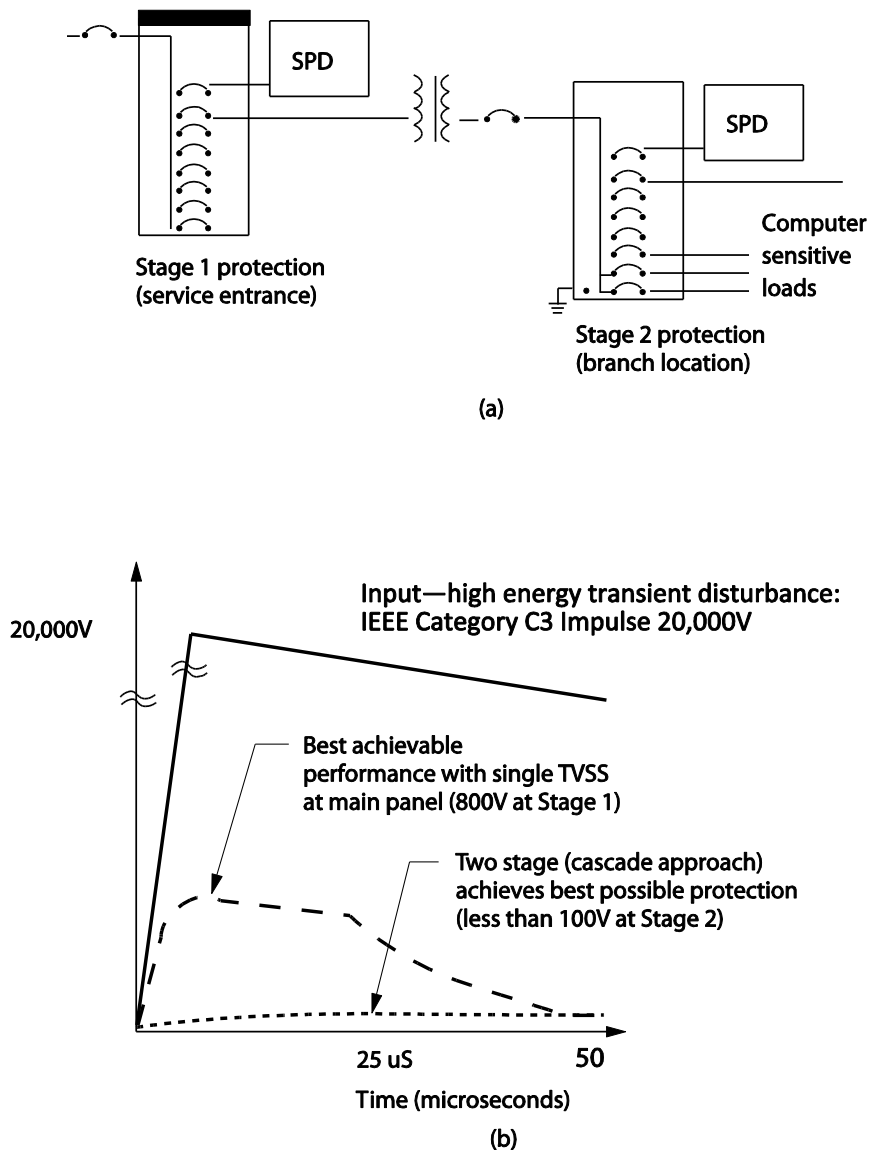


Figure 2-10: Facility-wide protection solution: a cascade (or 2-stage) approach; (a) Example of two-stage TVSS protection. (b) Achievable performance levels with single and two-stage protection [44].

Stages applicable to TVSS protection may be divided into three categories: (a) primary protection, (b) secondary protection, and (c) board-level protection.

#### **2.4.2.1 Primary Protection**

Primary protection applies to power lines and data lines exposed to an outdoor environment, service entry, and AC distribution panels (stage 1 in Figure 2-10(a)). For a typical lightning impulse of 20,000V, the best achievable clamping would be about 800V. Transient currents can range from tens to hundreds of kiloamperes at the service entrance.

#### **2.4.2.2 Secondary Protection**

Secondary protection (stage 2 in Figure 2-10(a)) is for equipment inputs, including power from long-branch circuits, internal data lines, PBX, wall sockets, and lines that have primary protection at a significant distance from the equipment. With the application of both primary and secondary protection best possible protection (less than 100 V) is achieved. Transient voltages at this stage can exceed several kilovolts with transient currents ranging from several hundred to several thousand amperes.

#### **2.4.2.3 Board-level protection**

Board-level protection is usually internal to the equipment; it is for protection against residual transient from earlier stages of protection, system-generated transients, and Electro Static Discharge (ESD). Transients at this level range from tens of volts to several thousand volts with currents usually in the tens of amperes.

### **2.5 Surge protection standards and practices**

Transients that get induced on the equipment inputs could be due to several different reasons, such as (a) inductive switching (b) lightning (c) electrostatic discharge and (d) electro-magnetic pulses (EMPs). All these are very unpredictable random occurrences. Electrostatic discharge may occur due to build-up of static charge on the human body with voltages as high as 20,000 V. These can generate transients with rise times as fast as 2 kV/ns. Electromagnetic pulses due to nuclear activities where gamma rays can be released could cause transients with rise times

with 5 kV/ns, while lightning activity-related transients can generate signals with rise times around 600 V/ns [45].

Due to the statistical nature of transient voltages, many useful guidelines are provided by the standards and practices available for designers. Transient activity can be generated by external sources and internal sources.

### 2.5.1 External sources of transient activity

Power companies have no control over transients induced by lightning or high-power switching at substation levels. Figure 2-11 illustrates the very high current levels that correspond to large energy content of a typical lightning waveform. Currents from a direct or indirect strike may enter conductors of a suspended cable or enter a buried cable by ground currents. Either way, the surge will propagate through the cable in the form of a bidirectional travelling wave starting from the point of origin. Severity of impact to the end user is directly proportional to the proximity of the lightning strike. If the facility is at a 10 to 20 pole distance from the strike, little harm will occur, since the surge current will have been dissipated by the utility ground system. Such is not the case where the strike is much closer. In this case, the residual current can migrate through the facility's service equipment and cause severe damage. Other externally generated transients result from switching in nearby industrial complexes which can send transients back into the power line, causing damage to equipment. EMPs are another rare case of external transient activity.

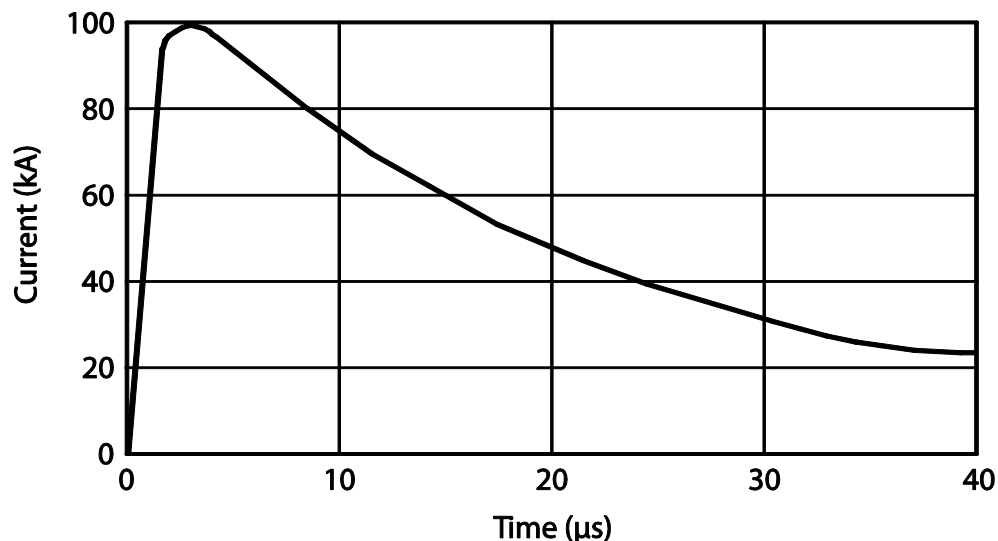


Figure 2-11: A typical lightning current waveform [6]

## 2.5.2 Internal sources of transient Activity

Internally-generated transients result from switching within the facility. Any time the flow of inductive current is altered, such as in the simple act of turning a motor off, transient activity can result in an “inductive kick”. Another common example of this phenomenon is the voltage transient generated by turning off a fluorescent light with a magnetic choke.

## 2.5.3 Transient energy

The energy of a transient waveform may be readily calculated for transients that are internal to the circuit, such as those caused by inductive switching. Transients external to the circuit are more difficult to quantify.

The energy absorbed by the suppression element may be calculated as,

$$E = \int_0^{\tau} vi \, dt \quad (2-3)$$

where,

$E$  = energy in joules

$v$  = instantaneous voltage across the suppression element in volts

$i$  = instantaneous current through the suppression element in amperes

$\tau$  = impulse duration

## 2.5.4 Transient Protection Standards

Committees such as ANSI, IEEE, and IEC have defined standards for transient waveshapes based on the threat environment.

European or IEC transient standards include:

- IEC 61000-4-2 Electromagnetic compatibility (EMC): Testing and measurement techniques – Electrostatic discharge (ESD)
- IEC 61000-4-4 Electromagnetic compatibility: Testing and measurement techniques - Electrical fast transient/burst immunity test

- IEC 61000-4-5 Electromagnetic compatibility: Testing and measurement techniques – Surge immunity test

US transient standards include:

- ANSI/IEEE C62.41: IEEE recommended practice on characterization of surges in low-voltage (1000 V and less) AC power circuits
- FCC Part 68 for telecommunication lines
- UL 1449, and various military standards

IEC 61000-4-5 and ANSI/IEEE C62.41 are central to the work done in this project and they address the most severe transient conditions on both power and data lines. These are transients caused by lightning strikes and by switching. Lightning transients may result from a direct strike or induced voltages and currents due to an indirect strike. Switching transients may be the result of power system switching, load changes in power distribution systems, or short-circuit fault conditions.

The IEC 61000-4-5 standard defines a transient entry point and a set of installation conditions [46]. The transient is defined in terms of a generator producing a given waveform and having a specified open circuit voltage and source impedance.

Measurements carried out by the IEEE over a number of years have demonstrated, on a statistical basis, the likely frequency of occurrence, typical amplitudes, and waveshapes to be expected in various locations as a result of artificial and naturally occurring electrical phenomena. These findings are published in IEEE C62.41. The work outlined in the IEC 61000-4-5 and the ANSI/IEEE 62.41 standards provides the basis for the design of AC powerline transient SPDs.

#### **2.5.4.1 IEEE C62.41: Location categories**

In general terms, the surge stress to be expected depends on the location of the equipment to be protected. When equipment is inside a building, the stress depends on the distance from the electrical service entrance to the equipment location, the size and length of connection wires, and the complexity of the branch circuits [5].

The purpose of the standard IEEE C62.41 is to provide information on the surge environment and offer recommendations to interested parties involved in developing test and application standards related to SPDs as well as recommendations to equipment designers and users [3].

IEEE C62.41 identifies location categories within a building, described as A1, A2, A3, B1, B2, and B3 for surge locations. The “A” and “B” location prefixes represent wiring run distances within a building, the “1,” “2,” and “3,” suffixes represent surge severity. “A” category locations receive their power after more than 60 ft. of wiring run from the main power service entrance, with frequent exposure to comparatively low-energy surges.

External surges will be of a lesser threat in “A” locations than “B” locations due to the impedance protection provided by the inductance of the building wiring in “A” locations. IEEE specifies a low energy “ring wave” surge waveform for the “A” locations. “B” category locations are within a building, close to the power service entrance, with greater exposure to infrequent, high energy surges originating outside the building. The “B” location category surges can be caused by lightning, power outages due to storms, and normal utility switching functions. A “combination wave” with high surge energy is specified by IEEE for these “B” locations.

“1,” “2,” and “3” denote low, medium, and high exposures respectively, in terms of the number and severity of surges, with “1” being the least severe and “3” being the most severe. A “B3” location, therefore, would have the highest exposure to surge energy, while a “A1” location would have the lowest incidence of surge energy.

Table 2-2 shows possible annual surge magnitudes, frequency of occurrences, and surge waveform as extracted from the IEEE C62.41 Standard. Figure 2-12 depicts the building locations as given in the standards IEEE C62.41 and UL 1449. IEEE C62.41 details are available in [3, 47]. The standard UL 1449 is discussed in the next section.

Table 2-2: IEEE C62.41 Location categories, frequency of occurrences and surge waveforms

IEEE LOCATION CATEGORY	IEEE EXPOSURE	2,000 V, 70 A Ringwave Surges (.63 Joules)	4,000 V, 130 A Ringwave Surges (2.34 Joules)	6,000 V, 200 A Ringwave Surges (5.4 Joules)
A1	Low	0	0	0
A2	Medium	50	5	1
A3	High	1,000	300	90
		2,000 V, 1,000 A Combination Wave Surges (9 Joules)	4,000 V, 2,000 A Combination Wave Surges (36 Joules)	6,000 V, 3,000 A Combination Wave Surges (81 Joules)
B1	Low	0	0	0
B2	Medium	50	5	1
B3	High	1,000	300	90

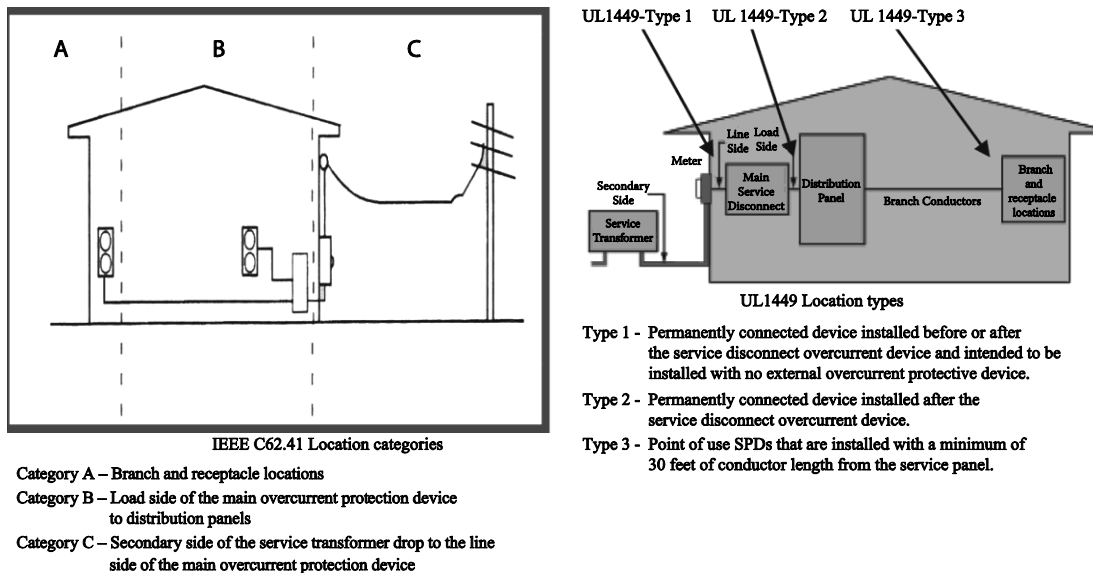


Figure 2-12: Building location categories and types for IEEE C62.41 and UL 1449

### 2.5.4.2 Surge voltage waveforms

The IEC 61000-4-5 standard specifies a *combination wave* consisting of two waveforms which are shown in Figure 2-13: the 1.2/50  $\mu$ s open-circuit voltage waveform and the 8/20  $\mu$ s short-circuit current waveform. These impulse waveforms

are defined by their rise times and half-amplitude duration. For example, an 8/20  $\mu\text{s}$  impulse current would have an 8  $\mu\text{s}$  rise time from 10 percent of the peak current to 90 percent of the peak current. The 20  $\mu\text{s}$  decay time is measured between half amplitude points.

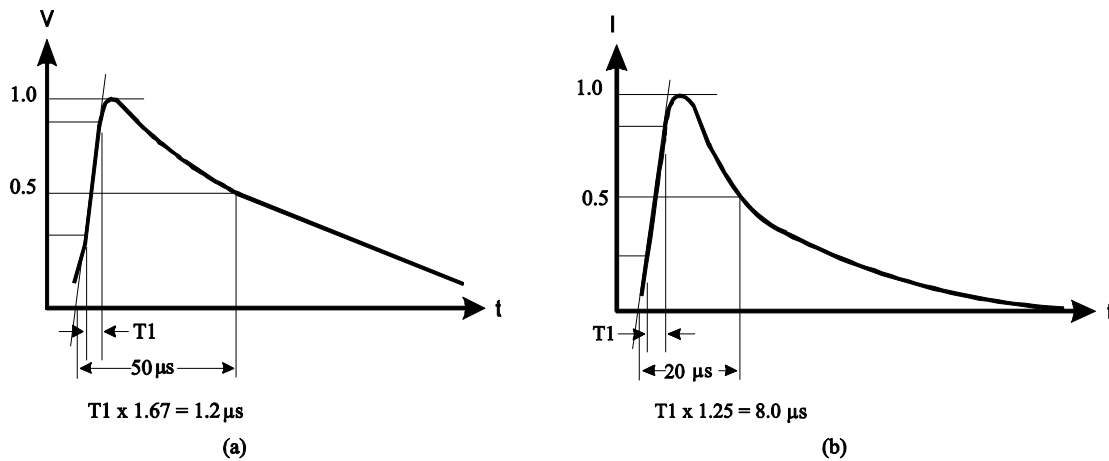


Figure 2-13: IEC 61000-4-5 combination wave (a) Open-circuit voltage (b) Short-circuit current

The combination wave shown in Figure 2-13 is also defined in ANSI/IEEE C62.41 along with another standard waveform, which is the 100 kHz ring wave shown in Figure 2-14. The location categories to which these two standard waves are applicable are indicated in Table 2-2.

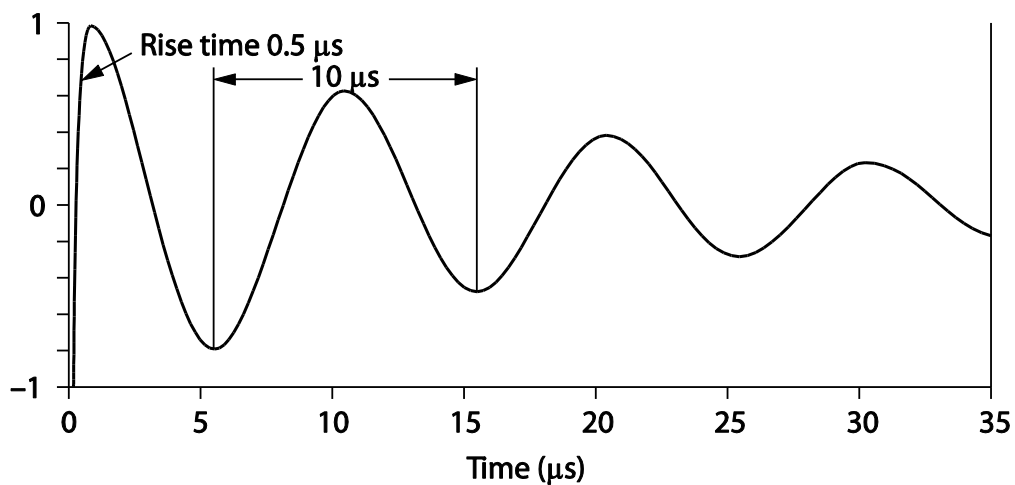


Figure 2-14: The 100 kHz ring wave

### 2.5.4.3 Underwriters Laboratories UL 1449

About two decades ago, Underwriters Laboratories (UL) established a uniform TVSS rating system by creating UL Standard 1449-1987. Although

somewhat limited, it was the first step toward establishing benchmarks to compare transient voltage suppressor system (TVSS) products. The standard has been revised twice in the past few years. UL 1449 3<sup>rd</sup> edition completely supersedes preceding editions. This edition has become an American National Standard (ANSI) and is aligned with other North American surge standards including IEEE C62.41 [48]. The term for surge protectors has been changed from TVSS to Surge protective device (SPD) in the 3<sup>rd</sup> edition. Underwriters Laboratories established specific test criteria to determine the ability of a SPD product to stop the travel of a transient voltage surge into protected equipment. The 3<sup>rd</sup> edition gives three designations to SPDs depending on where in the electrical distribution system the device is connected. A description of these designations is given in Figure 2-12. The correspondence of these designations to C62.41 location categories can also be seen in this figure.

Clamping voltage tests under UL 1449 2<sup>nd</sup> edition were conducted at 500 A, 6 kV. The tests in the 3<sup>rd</sup> edition are done at 3 kA, 6 kV, which delivers six times more surge energy resulting in higher clamping voltages. The voltage available is in a 1.2x50 $\mu$ s waveform and the current is available in an 8x20 $\mu$ s waveform.

The new title of UL 1449 in the 3<sup>rd</sup> edition is, “UL Standard for Safety for Surge Protective Devices, UL 1449”. In addition to location descriptions of Types 1 to 3, there is also a Type 4 which applies to individual components used in all location categories. More details pertaining to this standard can be found in [49, 50].

## **2.6 Circuit concepts used for surge protection**

In general practical circuits developed for surge protection are based on three basic concepts: (1) design the protection circuit separately as an add-on block to the base circuit; (2) attenuate the incoming transient using passive series-connected high-impedances, or shunt the surge currents via passive low-impedance circuits (which act as filters for high-frequency components of the surge); (3) use nonlinear devices such as GDTs, MOVs, TVS diodes or TVS thyristors to divert the surge currents and absorb the transient energy.

Figure 2-15 shows an SPD which is designed to protect against both common and differential mode transients. The combination of line filter and transient suppressor components in this SPD makes it suitable for use in both C62.41 location categories A and B. When designed for category B locations larger components will have to be selected for the transient suppressor components [5]. Inductors  $L_1$  and  $L_2$  and capacitors  $C_1$  through  $C_4$  form the noise filter network.  $M_1$  to  $M_3$  are MOVs which will enter their firing or conduction mode when the transient exceeds the threshold voltage limit thus providing the first level of protection. For very short lived high-voltage transients, the clamping action of the varistors, together with the voltage dropped across the series inductance, holds off the majority of the transient voltage from the output.

For more extended stress conditions, the current in  $L_1$  and  $L_2$  will increase to the point where the output capacitors  $C_2$  through  $C_4$  are charged to a voltage at which TVS diodes  $T_2$  through  $T_4$  are brought into conduction. These diodes prevent the output voltage from exceeding their rated clamp values for all stress currents up to the failure point of the diodes.

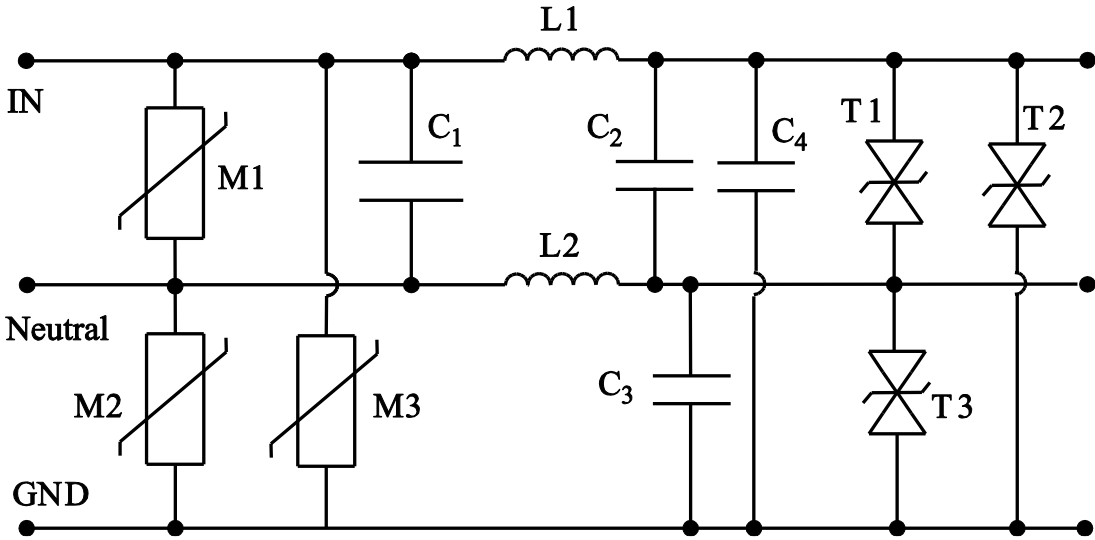


Figure 2-15: Line-to-line and line-to-ground transient overvoltage protection circuit with noise filter (can be designed for C62.41 location categories A and B)

This SPD also prevents voltage transients generated within the driven equipment from feeding back into the supply line. This can be an important advantage when several pieces of equipment in a system are connected to the same supply.

A simplified 2-wire version of this versatile SPD design is considered in this project. The power-law model outlined in section 2.4.1.1 was used to model the nonlinear resistances of the MOV employed for the first level of protection and the TVSD employed for the second level of protection. Simulations and prediction of power and energy transfers to all its components are presented in Chapter 6. There is no evidence in the literature to suggest that such an analysis has been done, using suitable models for the nonlinear surge protection components.

Several other SPD circuit concepts are discussed in [5, 6].



## **Chapter 3: Analytical and Numerical techniques for solving transient equations**

---

Although the TVSS that is investigated in the thesis is nonlinear, the analysis of transient propagation in linear systems is important for this project for several reasons. First, significant parts of the overall circuit we need to analyse are linear. Second, the exact solutions available for the behaviour of linear systems through standard techniques allow us to analyse the linear parts easily. Third, the validations of the simulations for the linear parts of our circuits can be performed using standard techniques. Fourth, the nonlinear differential equations (DEs) that we need to formulate in order to simulate the nonlinear systems become an extension of the linear DEs for the linear portions of the overall system.

In this thesis, the Laplace transform method, which is a standard technique for solving linear differential and integrodifferential equations, is used to analyse the linear circuits relevant to the project. These equations in electrical engineering can arise from the presence of reactive components such as capacitors and inductors. Laplace transform method is, in many circumstances, simpler and more convenient to use than the other classical methods of solving ordinary DEs. Areas of this method relevant to the study of this thesis have been included in Appendix E.

Power electronic circuits such as the ones we will be investigating consist of nonlinear devices and therefore would give rise to nonlinear differential equations. In general, nonlinear DEs cannot be solved analytically by a method such as Laplace transforms. This limitation of the Laplace transform is highlighted in Section 3.1.

Until the 1960s, practical ways of solving nonlinear problems involved graphical and experimental approaches. Since that time, computer simulation has become a powerful tool in solving nonlinear problems. In order to predict power dissipation and energy absorption in the Transient Voltage Surge Suppressors (TVSS), this project resorted to computer simulation of the circuits that contain them. The use of numerical simulation successfully for this investigation of transient surge propagation in a power electronics interface has made this project a unique one.

The major portion of the remainder of this chapter looks at methods adopted in numerical simulation of DEs. We will start our study with the straightforward Euler's method and proceed to more complex and more accurate Runge-Kutta methods [51]. Standard and special purpose Ordinary Differential Equation (ODE) solvers that are supplied with MATLAB, are discussed in Section 3.4. Effective use of these variable time-step solvers is also discussed here, as we will be using them extensively for our simulation studies.

Section 3.5 looks at circuit simulation software such as SPICE derivatives, which are also suitable for transient propagation studies under certain conditions; the discussion compares them to the simulation of relevant DEs through MATLAB coding that is employed in this project. Advantages of the method used in this thesis over that of widely used simulation software are also outlined here.

### **3.1 Limitation of Laplace transform method**

As mentioned earlier in section 2.4.1.1, the circuits we analyse in this thesis contain nonlinear devices such as MOVs which can be represented by the power law relationship of Eq. (2-1), which is repeated here.

$$i(v) = kv^\alpha$$

where  $k$  is a constant dependent on the device geometry and  $\alpha$  defines the degree of nonlinearity of the characteristic. For MOVs the value of  $\alpha$  can be in the range of 15-30 and evaluation of this parameter for several MOVs in Chapter 4 yielded values in this range.

The techniques that have been developed for Laplace transforms will not be able to analyse a circuit containing such highly nonlinear elements symbolically. Although a numerical solution would be possible, it will be more straightforward to solve the state equations that describe the system directly using numeric techniques as we have done in this thesis.

## 3.2 Euler's method

The simplest numerical method for the solution of initial value problems is Euler's method [52]. In order to generate an update rule for Euler's method, we will expand  $y(t + \Delta t)$  using the Taylor series.

$$y(t + \Delta t) = y(t) + \Delta t \frac{dy}{dt} + \frac{(\Delta t)^2}{2!} \frac{d^2y}{dt^2} + \frac{(\Delta t)^3}{3!} \frac{d^3y}{dt^3} + \dots \quad (3-1)$$

For small values of  $\Delta t$ , the higher powers  $(\Delta t)^2$ ,  $(\Delta t)^3$ , ... in Eq. (3-1) will be very small. This suggests the following *Euler approximation* for  $y(t + \Delta t)$ , which ignores quadratic and higher order terms in Eq.(3-1):

$$y(t + \Delta t) \approx y(t) + \Delta t \frac{dy}{dt} \quad (3-2)$$

Adopting the shorthand notation  $t \equiv n\Delta t$ ,  $y(t) \equiv y_n$ ,  $y(t + \Delta t) \equiv y_{n+1}$ , Eq. (3-2) can be written as

$$y_{n+1} \approx y_n + \Delta t \left( \frac{dy}{dt} \right)_n \quad (3-3)$$

The subscript  $n$  on  $(dy/dt)$  indicates that the derivative is to be evaluated at time  $t = n\Delta t$ . The *Euler updating rule* given below can be arrived at by substituting for the derivative from the differential equation(3-1):

$$y_{n+1} \approx y_n + \Delta t \cdot F(y_n, t_n) \quad (3-4)$$

The initial condition  $y(t_0) = y_0$  is used to start the calculation and then the updating rule given by Eq. (3-4) is applied iteratively to go forward in time:

$$y_1 \approx y_0 + \Delta t \cdot F(y_0, t_0)$$

$$y_2 \approx y_1 + \Delta t \cdot F(y_1, t_1)$$

$$y_3 \approx y_2 + \Delta t \cdot F(y_2, t_2)$$

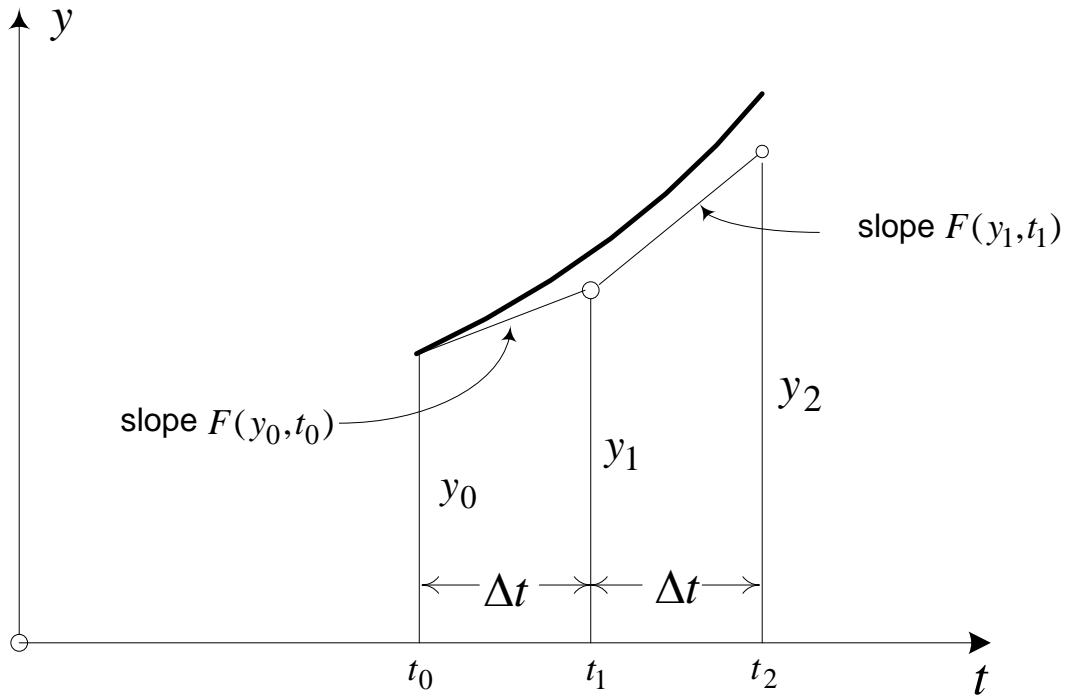


Figure 3-1: Euler method: Approximation of the curve  $y(t)$  by a polygon whose first side is tangent to the curve at  $t_0$

The Euler method is illustrated in Figure 3-1. Geometrically it is an approximation of the curve of  $y(t)$  by a polygon whose first side is tangent to the curve at  $t_0$ . The method is called a first-order method, because in Eq. (3-2) we take only the constant term and the term containing the first power of  $\Delta t$ . The truncation error per step is of order  $(\Delta t)^2$ . The practical value of the Euler method is limited, but since it is simple, it helps us to understand the more accurate methods that are presented in this chapter.

### 3.2.1 Application of Euler method: LCR circuit driven by a charged capacitor

In this section we will apply Euler's method to the LCR circuit shown in Figure 3-2, which is driven by a charged capacitor. This circuit, which is identical to the first loop of the LSS equivalent circuit, is solved using Laplace methods in Appendix E.2. Here we will have an opportunity to compare simulation results from the Euler method with the solution obtained by the Laplace method. From waveform drawn with the Laplace solution, we see that the two time constants for the loop current are approximately  $0.4 \mu\text{s}$  and  $70 \mu\text{s}$ . We need to choose our increment  $\Delta t$  to

be a small fraction of the smaller time constant to adequately sample the exponential evolutions.

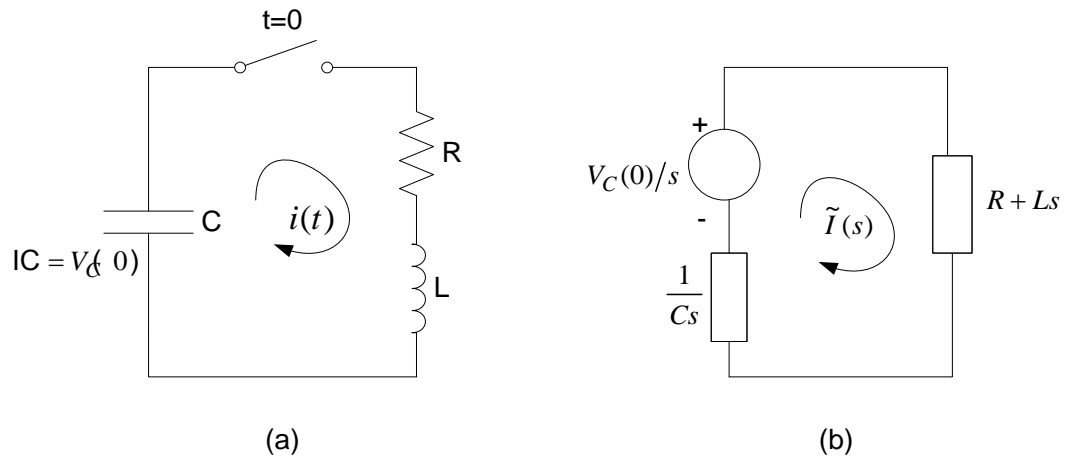


Figure 3-2: (a) RLC circuit driven by a charged capacitor (b) Laplace transformed network for the circuit in (a)

For the transformed network,

$$\frac{V_C(0)}{s} = I(s) \left( \frac{1}{sC} + R + sL \right)$$

$$(1 + sCR + s^2CL)I(s) = CV_C(0) \quad (3-5)$$

Assuming  $i(0) = i'(0) = 0$ , and taking the inverse Laplace transform of Eq. (3-5)

$$CL \frac{d^2i}{dt^2} + CR \frac{di}{dt} + i = CV_C(0)\delta(t) \quad (3-6)$$

Eq. (3-6) can be rewritten as

$$\frac{d^2i}{dt^2} + \frac{R}{L} \frac{di}{dt} + \frac{1}{LC} i = \frac{V_C(0)}{L} \delta(t) \quad (3-7)$$

The RHS of Eq. (3-7) is the forcing function of this DE and has the Dirac delta  $\delta(t)$  as a result of the discharging capacitor. For the purposes of this simulation

this Dirac delta function can be replaced by the Kronecker delta [51] and the forcing function can be represented as

$$\frac{V_C(0)}{L}\delta(t) \rightarrow \frac{V_C(0)}{L} \frac{1}{\Delta t} \delta_{1,n} \quad (3-8)$$

where  $\delta(t)$  is constrained by the identity  $\int_{-\infty}^{\infty} \delta(t)dt = 1$  and the Kronecker delta is identified as

$$\delta_{ij} = \begin{cases} 0 & \text{if } i \neq j \\ 1 & \text{if } i = j \end{cases} \quad (3-9)$$

In order to solve the second-order DE Eq. (3-7) numerically, we must recast it into normal form: a system with two interacting DEs.

Let

$$\frac{di}{dt} = j \quad (3-10)$$

Then Eq. (3-7) will reduce to

$$\frac{dj}{dt} = -\frac{R}{L}j - \frac{1}{LC}i + \frac{V_C(0)}{L}\delta(t) \quad (3-11)$$

By using Eqs. (3-4), (3-10) and (3-11) the following Euler update equations can be written

$$i(n+1) = i(n) + \Delta t \cdot j(n) \quad (3-12)$$

$$j(n+1) = j(n) + \Delta t \cdot \left( -\frac{R}{L}j(n) - \frac{1}{LC}i(n) \right) + \frac{V_C(0)}{L} \delta_{1,n} \quad (3-13)$$

For the simulation, we have chosen the increment  $\Delta t$  to be much smaller than two time constants associated with the Laplace solution, which are approximately  $0.4 \mu\text{s}$  and  $70 \mu\text{s}$ . The Matlab code `RLC_simulations_4_methods` given in Appendix A.1 tests the simulation for  $\Delta t$  values of  $0.125 \mu\text{s}$ , where an explicit approximation has been used for the delta-function. A comparison of the simulation

with that of the Laplace solution is shown in Figure 3-3(a). The error which is prominent within the first microsecond is shown in Figure 3-3(b).

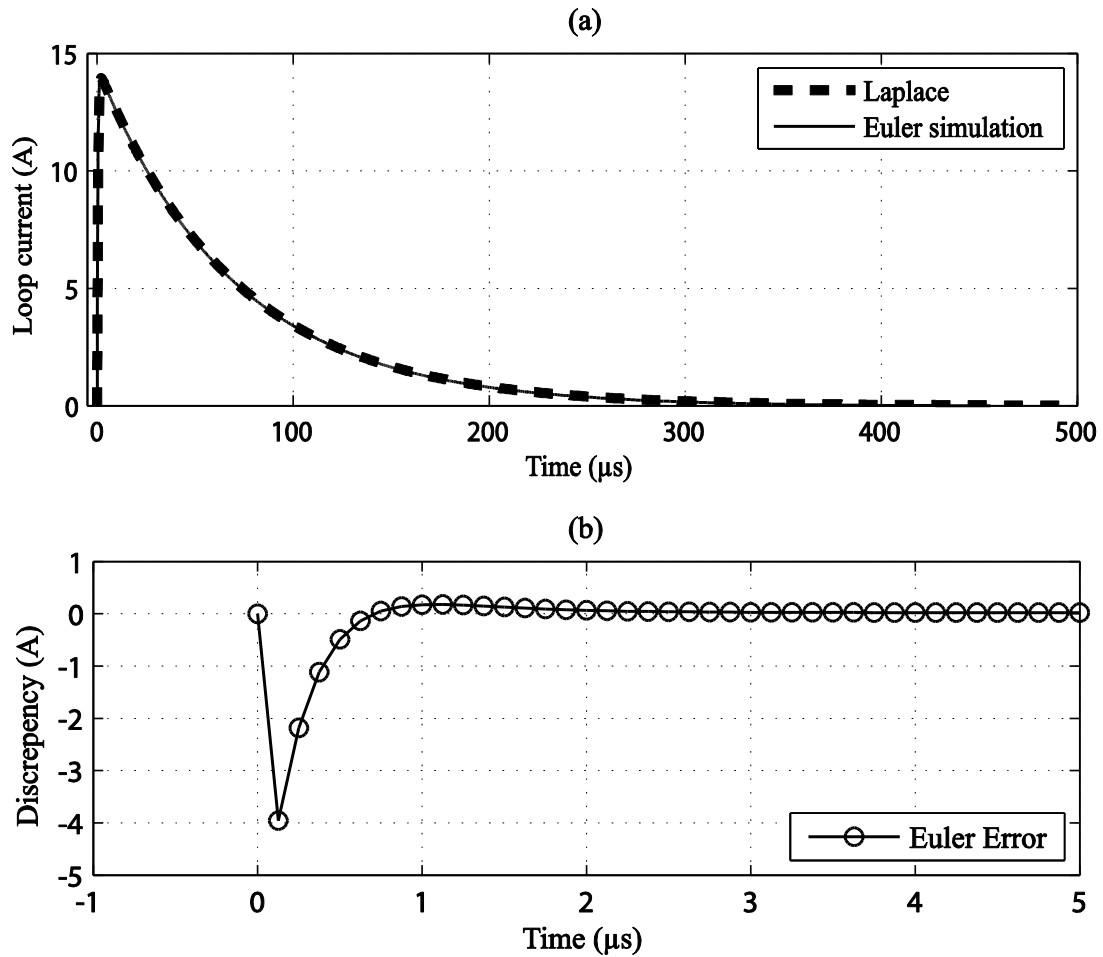


Figure 3-3:(a) Euler simulation of the loop current compared with the theoretical result (b) Error between the simulation and theoretical results

Although this simulation result looks satisfactory for the short duration transients we will be looking at, the simulation results can be improved by obtaining an impulse response as outlined in the following section.

### 3.2.2 A better way of obtaining an impulse response

An impulse response can be obtained by using initial conditions that arise from the impulse input [53]. This approach allows the zero time duration of the impulse to be correctly modelled, rather than using it as an input signal as in the previous section.

The following proof demonstrates this by considering the differential equation (3-11) which has a delta function as an input signal:

Integrating Eq.(3-11) gives,

$$j(t) = -\frac{R}{L} \int j(t)dt - \frac{1}{LC} \int i(t)dt + \frac{V_c(0)}{L} \int \delta(t)dt \quad (3-14)$$

This simplifies to

$$j(t) = -\frac{R}{L} \int j(t)dt - \frac{1}{LC} \int i(t)dt + \frac{V_c(0)}{L} \quad (3-15)$$

Here we are interested in determining the value of  $j(t)$  at  $t = 0$ , i.e., the initial conditions that arise from the impulse input. Assume that from  $t = -\infty$  to  $t = 0$ ,  $j(t) = i(t) = 0$ . The result is that the two integrals in Eq.(3-15) can be evaluated from 0 to time  $t$ . Since we are interested in the initial condition at  $t = 0$ , this leaves the two integrals to be evaluated from  $t = 0$  to  $t = 0$ . The result is

$$-\frac{R}{L} \int_0^0 j(t)dt = \frac{1}{LC} \int_0^0 i(t)dt = 0 \quad (3-16)$$

and from Eq. (3-15)

$$j(t = 0) = \frac{V_c(0)}{L} \quad (3-17)$$

This shows that an impulse response can be obtained by using the initial condition that arise from the impulse input, and making the input itself equal to zero. A general form of this proof applicable to any system that can be represented by the general state-space representation is available in [53].

Now we will simulate the same loop current of the RLC circuit of section 3.2.1 and see how this improved Euler simulation compares with the true solution. Again the MATLAB code `RLC_simulations_4_methods` given in Appendix A.2 tests this simulation for a  $\Delta t$  value of  $0.125 \mu s$  with the `switch` statement set to 2. A comparison of the simulation with that of the Laplace solution is shown in Figure 3-4(a) and the error between these two is shown in Figure 3-4(b). We see that

the maximum error which was minus 4 amperes in Figure 3-3(b) has reduced to a positive 1 ampere in Figure 3-4(b).

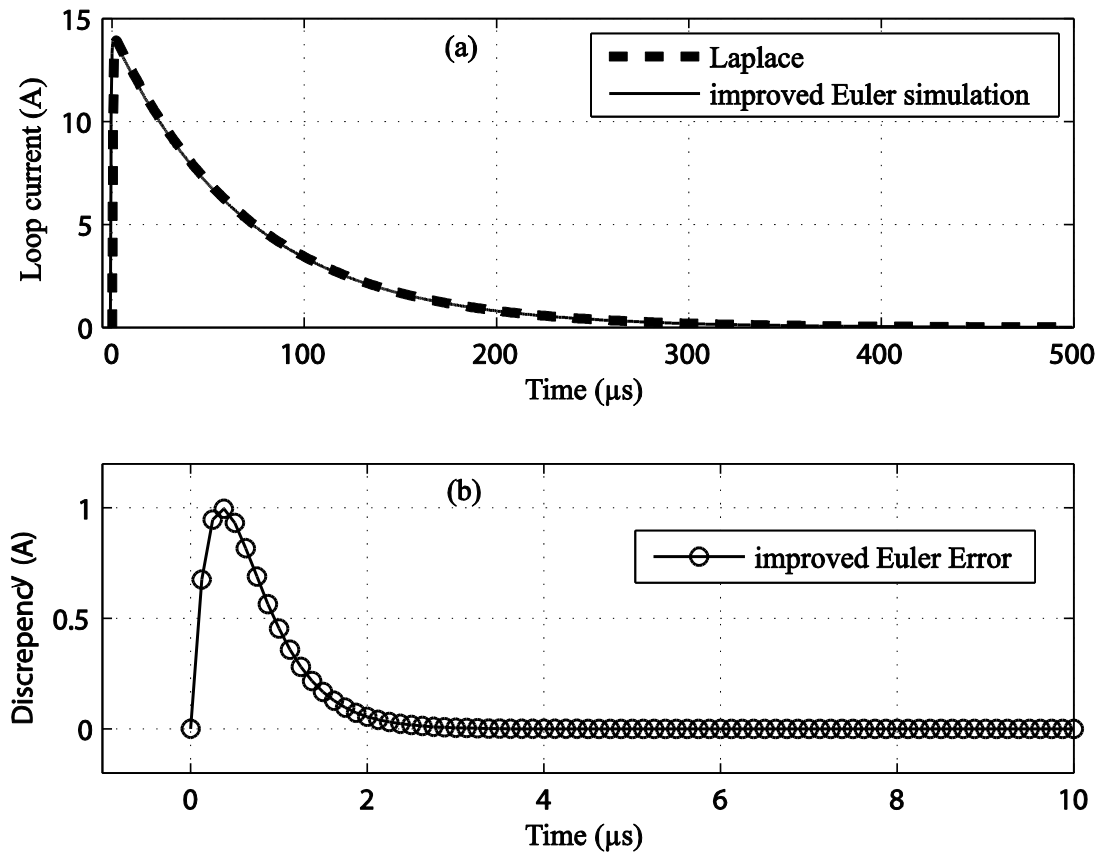


Figure 3-4: (a) Euler simulation of the loop current compared with the theoretical result (b) Error between the simulation and theoretical results

As it is a good programming practice to keep the differential equations separated from the DE solver, we have implemented this next for the present Euler method in the same MATLAB code `RLC_simulations_4_methods` with the switch statement set to 3. The same programming technique will be retained when we test the more accurate Fourth-order Runge-Kutta simulation in the next section.

### 3.3 Runge-Kutta (RK) approximation methods

As we have already seen in the previous section, the Euler method retains only the linear term of the Taylor series expansion. Hence, it does not produce accurate results unless the step size  $\Delta t$  is rather small. Runge-Kutta (RK) approximation methods retain more terms in the Taylor expansion and this results in

better accuracy for a given step size. Also in RK methods the function  $F[y(t), t]$  is evaluated several times for values of  $t$  between  $t_n$  and  $t_{n+1}$  and then the values of  $y$  are obtained by adding linear combinations of the values of  $F$  to  $y_n$ . The actual step is taken using another linear combination of the function values [52].

The order of an RK method is the exponent of the largest power of time step  $\Delta t$  that can be matched. For example, the second-order RK algorithm has a truncation error  $O[(\Delta t)^3]$  since the Taylor-series for  $y(t + \Delta t)$  gets truncated at the quadratic term.

The second-order RK updating rule is given by

$$y_{n+1} \approx y_n + \frac{\Delta t}{2}(K_1 + K_2) \quad (3-18)$$

where  $K_1 = F_n$  and  $K_2 = F(y_n + \Delta t.F_n)$ . Here, the RK forward step takes the average of two estimates of the gradient:  $K_1$  is the gradient at the present time  $t_n$ , and  $K_2$  is the estimated gradient after making an Euler step of  $\Delta t$  into the future.

We can construct third-, fourth- and fifth- order RK algorithms by extending the Taylor series to higher orders. The classical RK method is the fourth-order RK (RK4) and is derived by retaining terms in the Taylor series polynomial up to  $(\Delta t)^4$ , which reduces the local truncation error to  $O[(\Delta t)^5]$ .

The RK4 formula is:

$$y_{n+1} \approx y_n + \frac{\Delta t}{6}(K_1 + 2K_2 + 2K_3 + K_4) \quad (3-19)$$

where

$$\begin{aligned} K_1 &= F(y_n, t_n), & K_2 &= F\left(y_n + \frac{1}{2}\Delta t K_1, t_n + \frac{1}{2}\Delta t\right), \\ K_3 &= F\left(y_n + \frac{1}{2}\Delta t K_2, t_n + \frac{1}{2}\Delta t\right), & K_4 &= F(y_n + \Delta t K_3, t_n + \Delta t) \end{aligned}$$

Again in line with good programming practices, we will keep the differential equation separated from the RK4 ODE solver. The code `rk4fixed` (Appendix A.3) that we will be using is a general purpose fourth-order Runge-Kutta ODE solver that uses a step-size  $\Delta t$  that is fixed by the user. RK4 solver is accessed by calling a function of the form

```
[t_out, X_out] = rk4fixed(@FUN, tspan, y0, flag, params);
```

where the arguments are given by

@FUN	a handle to the ODE function which returns a vector of rates of change
tspan	a vector of regularly spaced time-values that determines the integration start-time ( <code>tspan(1)</code> ), stop-time ( <code>tspan(end)</code> ) and the time-step ( <code>dt=tspan(2)-tspan(1)</code> )
y0	is the initial condition from which integration proceeds
flag	is a string that allows the ODE function to respond in different ways—we won't be using <code>flag</code> so we will treat it as a place holder
params	is a vector containing a list of parameters that need to be communicated to the ODE function

### 3.3.1 Application of RK4 method: LCR circuit driven by a charged capacitor

In order to check the improved accuracy of the classical RK method over the Euler methods, we will simulate the same loop current of the RLC circuit of section 3.2.1 and see how this simulation compares with the true solution. Again the MATLAB code `RLC_simulations_4_methods` given in Appendix A.3 tests this simulation for the same  $\Delta t$  value of  $0.125 \mu\text{s}$  with the `switch` statement set to 4.

Equations (3-10) and (3-11) define the state equations for the LCR circuit driven by a charged capacitor. We have encoded them into the MATLAB function `RLC_dot`. The impulse response resulting from the delta function in Eq.(3-11) has been taken care of by the initial condition given in Eq. (3-17).

The function `RLC_dot` takes four arguments: the current time `t` (scalar); the current state `x` (a two-component column-vector); a string constant named `flag` (not used here; required for compatibility with the suite of MATLAB ODE solvers); and a row vector `params` (not used here; usually contains the coefficients of the state equations). In our case the coefficients have been supplied at the beginning of the code. To solve the ODE, we specify the initial conditions and the time-span over which the integration is to proceed, then pass these values, along with the name of the function that contains the ODE definition to the `RK4fixed` solver.

A comparison of the simulation with that of the Laplace solution is shown in Figure 3-5(a) and the error between these two is shown in Figure 3-5(b). We see that the maximum error which was 1 ampere in Figure 3-4(b) has reduced by more than 1000 times to a value less than 1 mA in Figure 3-5(b).

The classical RK method demonstrated above does not provide an error estimate. The variable step routines presented in the next section provides an error estimate and can be more efficient.

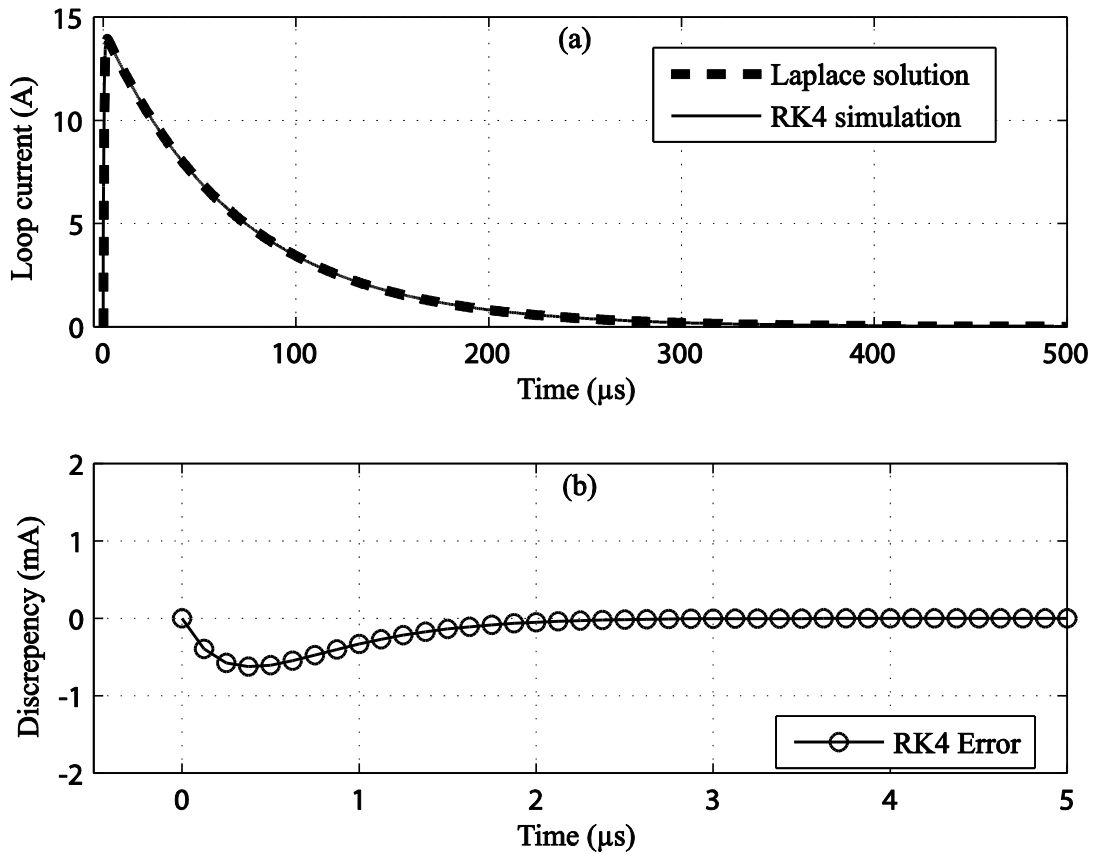


Figure 3-5: (a) RK4 simulation of the loop current compared with the theoretical result (b) Error between the simulation and theoretical results (in mA)

### 3.4 Variable step-size routines

Adaptive ODE solvers supplied with MATLAB, such as the ones shown in Table 3-1 [54], can continuously estimate the local error in the solution and, if necessary, modify the time-step to ensure that a specified level of accuracy is maintained.

Table 3-1: Some of the ODE solvers supplied by MATLAB [54]

Solver	Implicit / Explicit	Accuracy
ode45	Explicit	4 <sup>th</sup> order, medium accuracy
ode23	Explicit	2 <sup>nd</sup> /3 <sup>rd</sup> order, low accuracy
ode113	Explicit	13 <sup>th</sup> order, very accurate
ode15s	Implicit	Anything from 1 <sup>st</sup> -5 <sup>th</sup> order
ode23s	Implicit	Low accuracy (but may be more stable than ode15s)
ode23tb	Implicit	Low accuracy (but may be more stable than ode15s)

Names of the ODE solvers provided by MATLAB are of the form `odennxx`, where digits `nn` indicates the order of the underlying method and a non-empty `xx` indicates some special characteristic of the method [52]. If the error estimate is obtained by comparing formulas with different order, the digits `nn` indicate these orders. For example, `ode23` uses 2<sup>nd</sup> and 3<sup>rd</sup> order RK formulas for medium accuracy and `ode45` uses a 4<sup>th</sup> and 5<sup>th</sup> order pair for higher accuracy [55].

We can demonstrate the `ode45` solution to the LCR circuit problem by making a couple of changes to the MATLAB code written for the RK4 solution (see code `RLC_circuit_simulation_ode45` in Appendix A.5). The time span is now a two-element vector giving the start and stop times for the integration. During the simulation, the time-step will be selected automatically and changed dynamically by the `ode45` integrator in order to keep the estimated error at every step below the default settings of 0.1 % (relative error) and  $1 \times 10^6$  (absolute error).

Figure 3-6(b) demonstrates that the `ode45` integrator dynamically changes the time-step during the course of the simulation of the LCR circuit loop current, which is shown in Figure 3-6(b) for the first 20  $\mu\text{s}$ . The  $\Delta t$  values used to plot Figure 3-6(b) were extracted with the help of MATLAB's `diff` function. Automatic step size RK algorithms, such as `ode45`, take larger steps where the solution is more slowly changing. Since `ode45` uses higher order formulas, it usually takes fewer integration steps and gives a solution more rapidly [55].

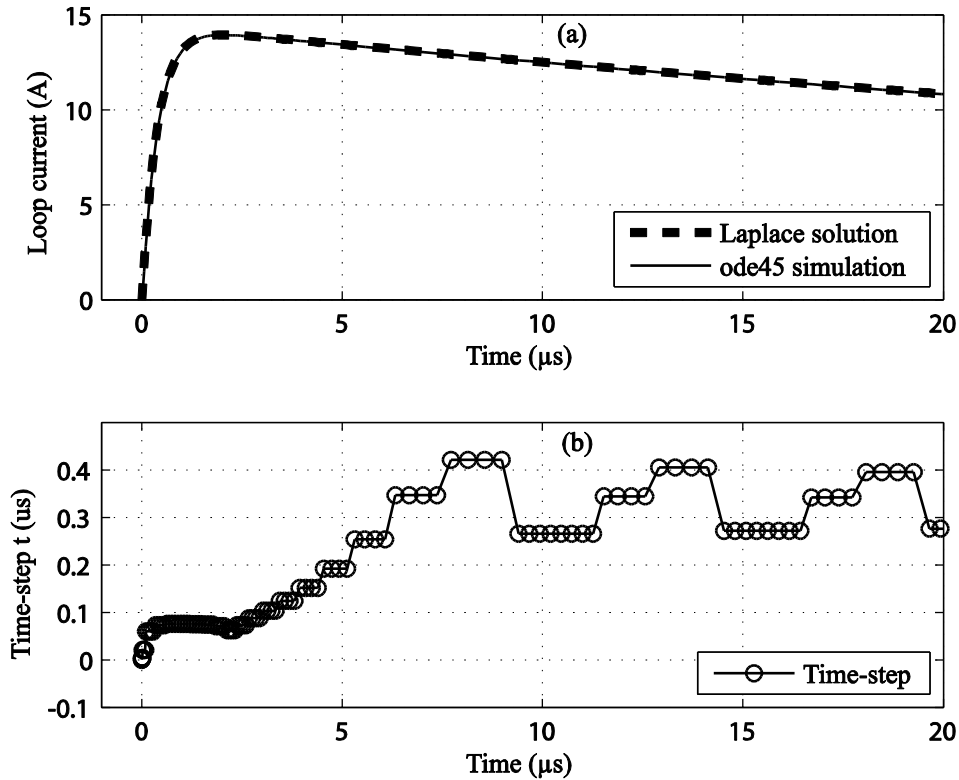


Figure 3-6: (a) ode45 simulation of the loop current compared with the theoretical result (b) Time-step changed dynamically by the ode45 integrator during the simulation

### 3.4.1 ODE solvers for stiff problems

A problem is stiff if the solution being sought varies slowly, but there are nearby solutions that vary rapidly, so the numerical method must take small steps to obtain satisfactory results [52].

Although ode45 is an efficient solver, it can become unstable with stiff systems. This instability will manifest itself by the solver taking shorter and shorter time steps to compensate. The solution will either take a long time, or the time step will be reduced to the point where machine precision causes the routine to fail [54].

A solver such as ode15s can be used if the problem is found to be stiff. A stiff problem will consist of several processes, at least one of which will have a very small time constant. If the problem is represented by the general form  $\dot{\mathbf{x}} = \mathbf{Ax} + \mathbf{Bu}$ , an idea of the stiffness of the problem can be obtained by the examination of the eigenvalues of matrix A [54].

### 3.4.2 Improvements to the MATLAB code containing stiff ODE solvers

Let us assume that the problem at hand can be represented by the following set of DEs

$$\frac{d}{dt} \begin{bmatrix} x_1 \\ x_2 \\ \vdots \\ x_n \end{bmatrix} = \begin{bmatrix} f_1(x_1, x_2, x_3, \dots, x_n) \\ f_2(x_1, x_2, x_3, \dots, x_n) \\ \vdots \\ f_n(x_1, x_2, x_3, \dots, x_n) \end{bmatrix}$$

The above set of DEs in turn can be represented by

$$\frac{dx}{dt} = f(\underline{x})$$

MATLAB ODE solvers which consist of implicit routines such as `ode15s` will solve the set of linear or nonlinear equations, defined by  $F(\underline{x})$  at each time step, and for this it will require the Jacobian of  $F(\underline{x})$  [54]. In this case the Jacobian is an  $n$ -by- $n$  matrix of partial derivatives:

$$J = \begin{bmatrix} \frac{\partial f_1}{\partial x_1} & \frac{\partial f_1}{\partial x_2} & \dots & \frac{\partial f_1}{\partial x_n} \\ \frac{\partial f_2}{\partial x_1} & \frac{\partial f_2}{\partial x_2} & \dots & \frac{\partial f_2}{\partial x_n} \\ \vdots & \vdots & \dots & \vdots \\ \frac{\partial f_n}{\partial x_1} & \frac{\partial f_n}{\partial x_2} & \dots & \frac{\partial f_n}{\partial x_n} \end{bmatrix}$$

If no information on the Jacobian is provided, the solver will be forced to estimate the Jacobian numerically. This difficulty can be overcome by using any one of the following options.

1. *Supply a routine which will return the Jacobian, or supply the Jacobian if it is a constant.*

This can be done by setting the ‘Jacobian’ option in the `odeset` structure to the matrix or function name. Generally, this is the most computationally efficient option [54].

The following example code illustrates the setting up of the ‘Jacobian’ options for a constant Jacobian

```
J = [1, -2; ...  
     4, 6900];  
Options=odeset('RelTol', 1e-5, 'Stats', 'on', 'Jac', J);
```

## 2. *Supply a Jacobian pattern*

By supplying a Jacobian pattern, the routine is able to avoid calls to the rate of change function. A Jacobian pattern is a sparse matrix of zeros and ones. The ones appear where the Jacobian is nonzero.

### 3.5 A comparison with available system simulation software

SPICE (*Simulation Program with Integrated Circuit Emphasis*) is a general-purpose, analog electronic circuit simulator; for comparison and validation purposes, the work in this thesis employed PSpice, which is a prominent commercial version of SPICE available from Cadence Design Systems. PSpice models for certain surge protection components are available from manufacturers and it becomes a useful simulation package when matching components are used in TVSSs under investigation. Almost identical results were obtained by such simulation compared with MATLAB based simulations of this project, as depicted in Section 6.2.2.

PSCAD/EMTDC is a popular power system simulation transient simulation package; although the surge protection components such as low-voltage (under 1000 V) MOVs and TVS diodes are not represented in the model library of this software, it has provision for the creation of a model for a nonlinear device with a known characteristic, making it a candidate for simulations similar to the ones undertaken in this project.

The advantages of the MATLAB-based approach followed in this project over the software packages discussed above are

- (a) The exposed DEs defining the system and their solution provide more insight into the working of the system

(b) Provides a good understanding of how circuit analysis techniques and mathematical techniques of solving a set of nonlinear DEs together make up a good software tool for the simulation of nonlinear power electronic interfaces.

(c) The value of the approach is enhanced, since suitable models can be quickly found for off-the-shelf surge protection components by experiment, when popular software based models are not readily available.

### 3.6 Chapter summary

This chapter has investigated the numerical simulation techniques available to solve nonlinear DEs. Generally there will not be any analytical solution for these nonlinear DEs. Due to the presence of nonlinear electronic components in power electronic interfaces such as SPDs, we will have to solve a set of nonlinear DEs in order to investigate surge propagation through them. The following computer simulation techniques were discussed here.

- Euler's method, which retains only the *linear* term in the Taylor series expansion. The step size  $\Delta t$  needs to be rather small for accurate results
- Runge-Kutta (RK) approximation methods, which retains more terms in the Taylor expansion. Higher the order of the RK method better would be the accuracy.
- Variable step-size routines which are provided by MATLAB. These adaptive ODE solvers monitor the local error in the solution continuously and, if necessary, modify the time-step to ensure that a specified level of accuracy is maintained.

Due to the stiff nature of the problems dealt within this project, we found variable step-size routines provided by MATLAB, such as `ode15s` and the `ode23t` to be the most suitable ones for the project.

In Chapter 4, we will characterize the nonlinear devices used in SPDs that are to be investigated for surge propagation. This characterization will lead to suitable

nonlinear models that would result in a set of nonlinear DEs, which are to be solved using some of the techniques outlined here.

Chapter is concluded with a discussion of popular circuit simulation software packages and the advantages of the approach taken up by this thesis.



## Chapter 4: Surge-absorbent device characterization

---

### 4.1 Introduction

In Chapter 2 we discussed four different types of practical devices used in surge protection circuits: metal oxide varistors (MOVs), gas discharge tubes (GDTs), transient voltage suppressor diodes (TVS diodes) and transient voltage suppressor thyristors (TVS thyristors). Except GDTs the others are solid-state devices. In the same chapter we also saw the use of some of these devices in category-A and category-B protection units. We will be investigating surge propagation using a category-B protection unit similar to the one shown in Figure 4-1, which is a two-wire version of a category-A protection unit with larger protection devices to handle the larger transients anticipated for category-B. This circuit uses a metal oxide varistor for the first level of protection and a TVS diode for the second level of protection. For a comprehensive investigation of surge propagation through this circuit, it is necessary that we characterize the nonlinear devices and obtain suitable mathematical models to be used in our numerical simulations. The work done in the development of the relevant models for the MOV and the TVS diode are presented in this chapter.

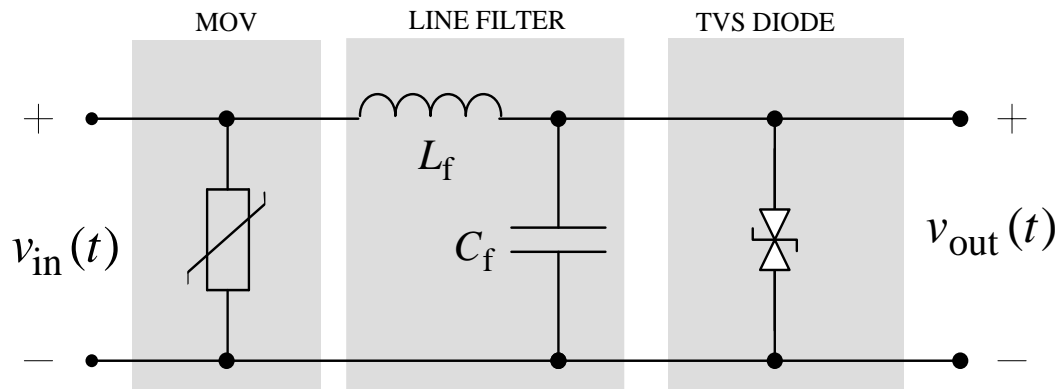


Figure 4-1 : A two-wire Category-B protection unit with two levels of protection

## 4.2 MOV Characterization

MOV manufacturers such as *Littelfuse* offer different types of MOV products, each one to suit a particular environment. A sample set of MOVs from their product line is given in Table 4-1 [25].

Table 4-1: Matching the right MOV with a particular application

VOLTAGE (V)	ENERGY (J)	PACKAGING AND OTHER CONSIDERATIONS	PREFERRED SERIES
AC APPLICATIONS			
130-1000	11-360	Through-hole mounting Low/Medium AC power line	LA “C” III UltraMOV
130-750	270-1050	High-energy applications Shock/Vibration environment	DA HA, HB NA DB
DC APPLICATIONS			
4-460	0.1-35	Through-hole mounting Automotive and low voltage applications	ZA

For our initial characterization experiments, we selected the devices 275L40C, 20V275 and V271HA32 from the “C” III, UltraMOV and HA series respectively. Each one of these devices is rated to operate at a maximum system RMS voltage of 275 V.

### 4.2.1 Measuring set-up

The measuring circuit diagram for obtaining the  $V-I$  characteristics of the MOV is shown in Figure 4-2. The NoiseKen LSS-6110 lightning surge simulator was used as an impulse source.

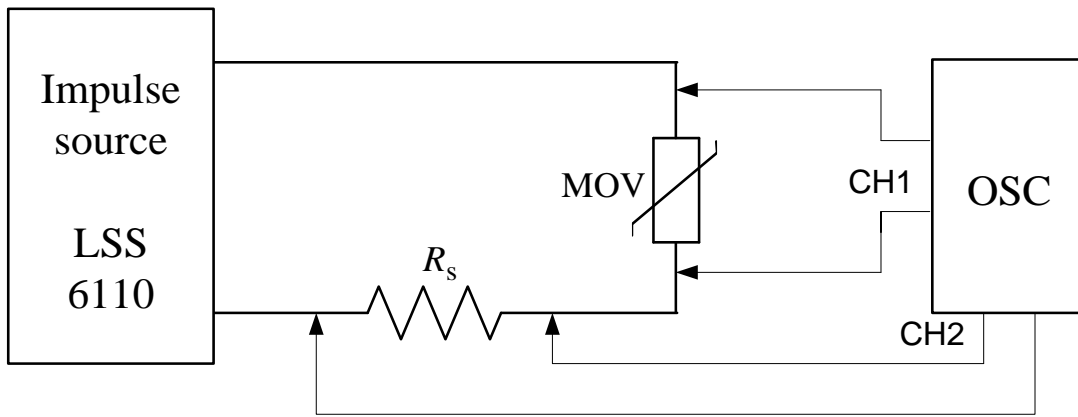


Figure 4-2: Circuit diagram for the measurement of the MOV voltage and current; impulse source is a lightning surge simulator (LSS) and a four-channel oscilloscope was used for measurements

The NoiseKen simulator is a combination wave generator (CWG) or hybrid generator that can provide a 1.2/50  $\mu\text{s}$  impulse voltage in an open circuit (1.2  $\mu\text{s}$  correspond to the *front time* and the 50  $\mu\text{s}$  correspond to the *time to half-value* as depicted Figure 4-3) and an 8/20  $\mu\text{s}$  impulse current in a short circuit (8  $\mu\text{s}$  correspond to the *front time* and the 20  $\mu\text{s}$  correspond to the *time to half-value* as depicted Figure 4-4). Both these waveforms conform to IEC publications 61000-4-5 [2] and 60060-1 [56] and the IEEE publication C62.41.2 [57].

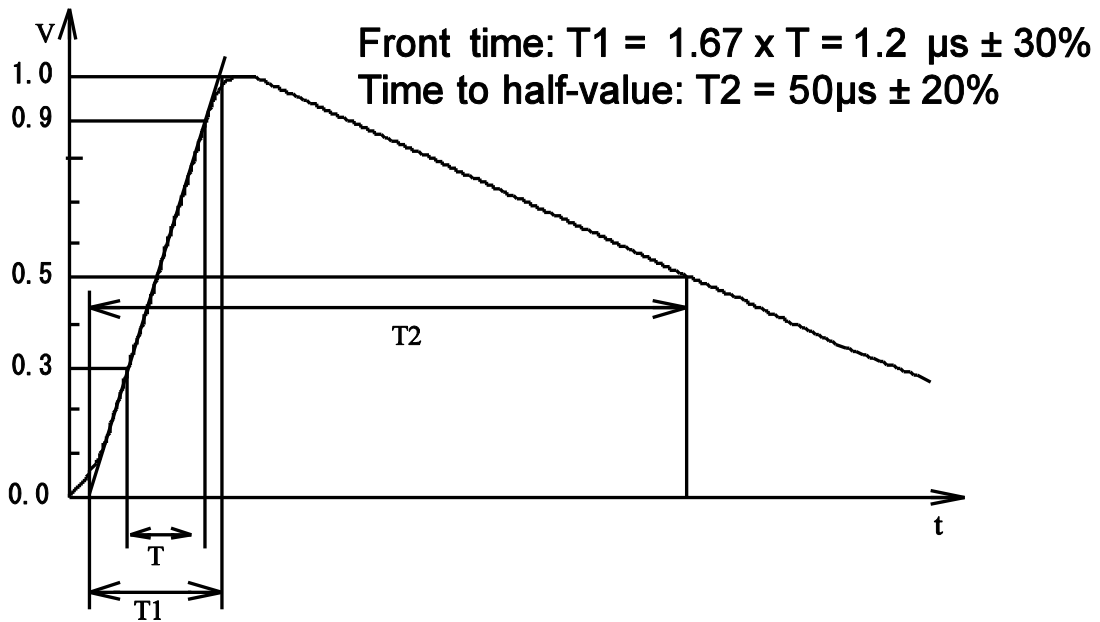


Figure 4-3: Waveform of 1.2/50  $\mu\text{s}$  open-circuit voltage (waveform definition according to IEC 60060-1)

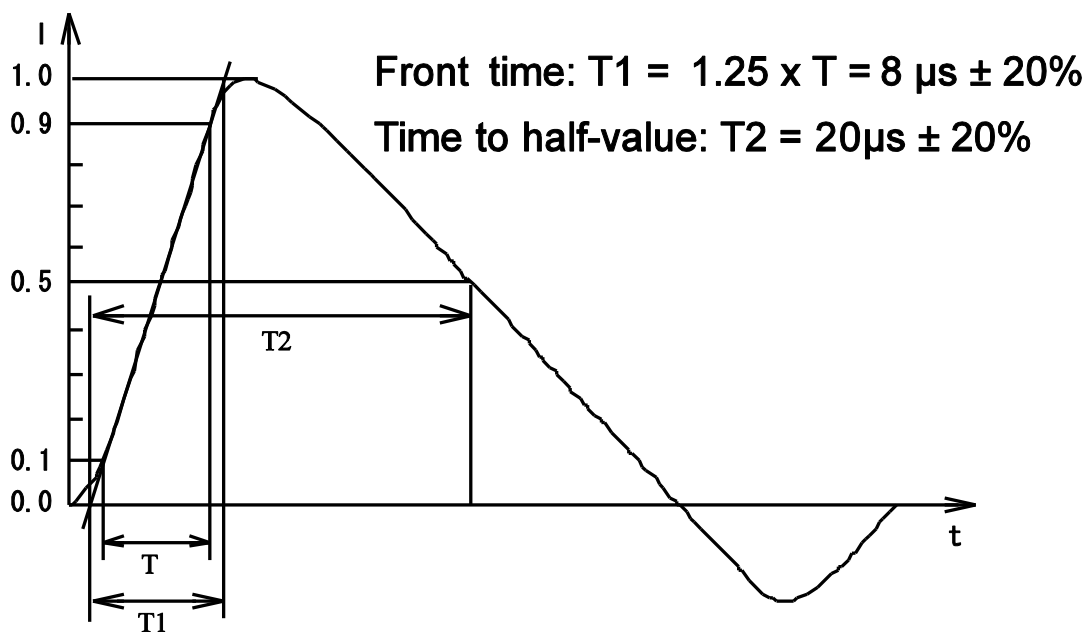


Figure 4-4: Waveform of 8/20  $\mu\text{s}$  short-circuit current (waveform definition according to IEC 60060-1)

The charging voltage of the impulse generator can be adjusted in 100 V steps from 0.1 kV to 6.6 kV.

The voltages were recorded with a Tektronix TPS2024 oscilloscope at a sampling rate of 2 GS/s. Tektronix P5120 1 kV 20X (frequency bandwidth 200 MHz) and P6015A 40 kV 1000X (frequency bandwidth 75 MHz) high voltage probes were used for voltage measurements.

Out of the MOVs characterized, the types 275L40C and the 20V275 had diameters of 20 mm. The third type V271HA32 had a diameter of 32 mm. All three types had a steady-state maximum AC voltage of 275 V. A series of pulses with different voltage amplitudes were applied to each one of the varistors.

#### 4.2.2 Waveforms obtained and their analysis

Measurements described in the previous section fall into two distinct categories; *leakage* region and the *normal varistor operation* region as depicted in Figure 4-5.

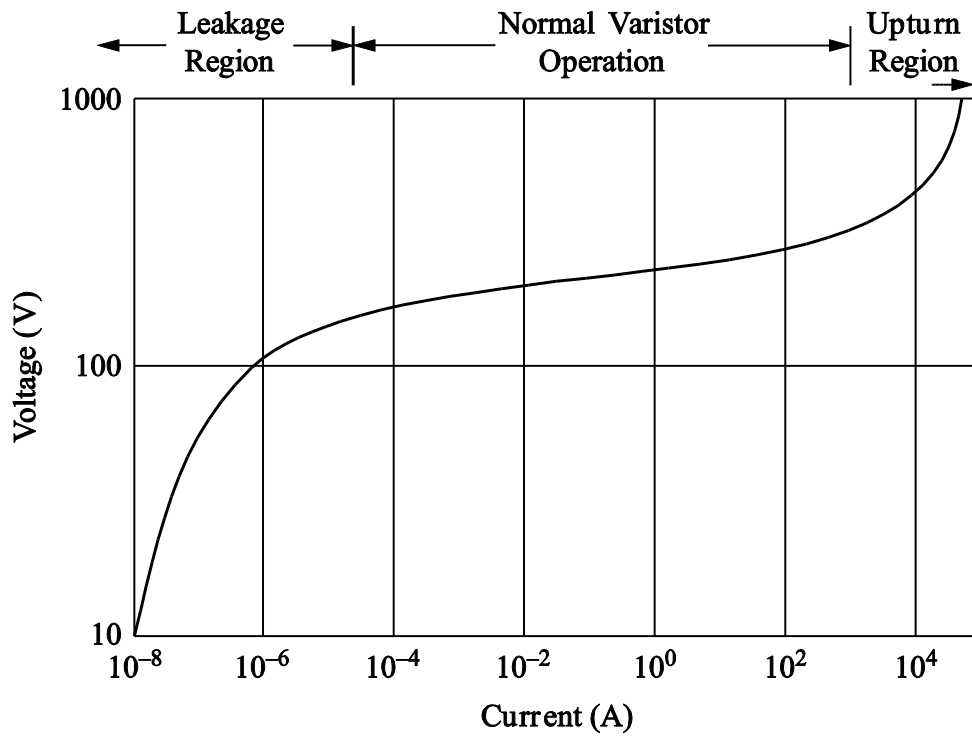


Figure 4-5: Typical varistor characteristic showing different regions of operation

#### 4.2.2.1 Leakage region analysis

All the tested varistors operated in the leakage region for low impulse voltages ranging from 100 - 500 V. All of them turned on beyond 500 V. A typical varistor current waveform obtained in this region of operation is shown in Figure 4-6.

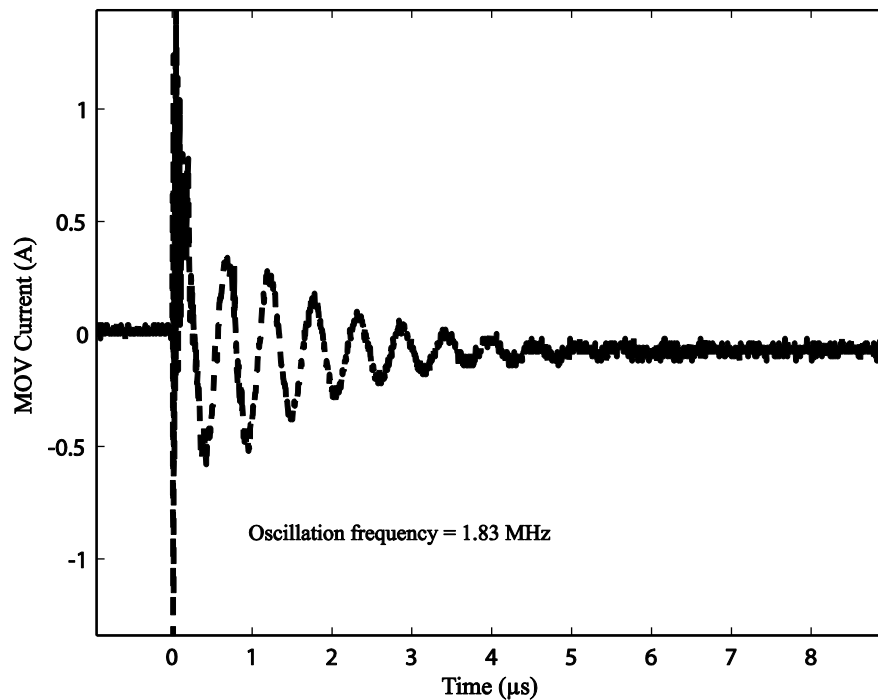


Figure 4-6: Leakage region varistor current produced by a low voltage impulse

In order to find an explanation for the resonance in the above current waveform we consider the MOV equivalent circuit in the leakage region shown in Figure 4-7(a) as well as the equivalent circuit of the impulse generator LSS-6110 shown in Figure 4-7(b).

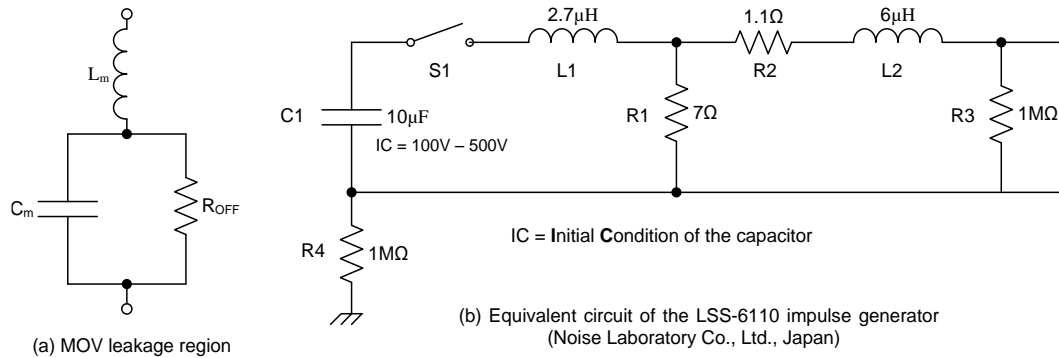


Figure 4-7: The equivalent circuits required to analyse the working of the circuit of Fig. 5-2 for low voltage impulses

The combined equivalent circuit of Figure 4-8 drawn for the measuring circuit of Figure 4-2 disregards  $R_{OFF}$  as it approaches  $10^9 \Omega$  in the leakage region. The following paragraphs discuss the values of  $C_m$  and  $L_m$  used for the analysis of this circuit.

Typical capacitance value  $C_m$  for a 20V275 *UltraMOV* series varistor is available from the datasheet as 900 pF [58]. Since the bulk region of the varistor acts as a dielectric, the device capacitance depends on its area and varies inversely with its thickness. Hence the capacitance of the varistor is a function of its voltage and energy ratings. The voltage rating is determined by device thickness, and the energy rating is directly proportional to volume [59].

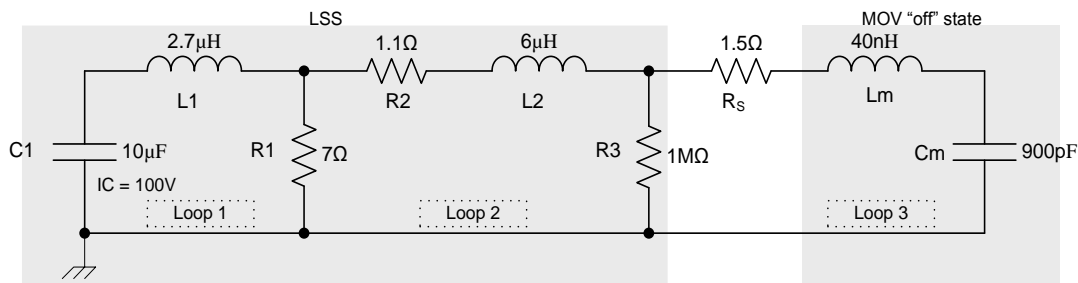
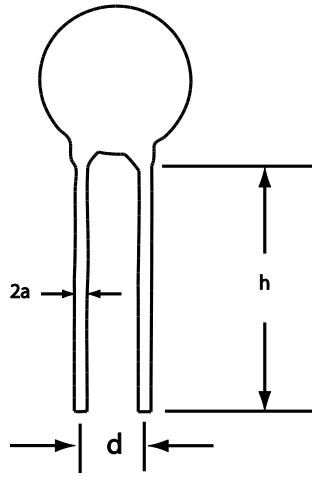


Figure 4-8: Combined equivalent of the measuring circuit shown in Fig.5-2 for the leakage region of the varistor

$L_m$  the lead inductance of the MOV, which is not explicitly given in the datasheet, can be calculated using the mechanical dimensions given in Figure 4-9 which have been taken from the respective datasheets.



Varistor model	275L40C	20V275
$h$	25.4	25.4
$2a$	0.76 (min) 0.86(max)	0.76 (min) 0.86(max)
$d$	6.5 (min) 8.5 (max)	9 (min) 11(max)

Note: Measurements in mm

Figure 4-9: Mechanical dimensions of radial lead varistors used [58, 60]

Lead inductance  $L_m$ , which is the *self* inductance of a pair of parallel wires, is given by [61]

$$L_m = \frac{\mu_0 h}{\pi} \ln \frac{d - a}{a} \quad (4-1)$$

where  $h$ ,  $d$  and  $a$  are illustrated in Figure 4-9. Multiplication by the symbol  $\mu_0$ , which denotes the relative permeability of free space ( $4\pi \times 10^{-7}$  H/m), gives the result in henries. The lead inductances calculated, using the average values of  $d$  and  $a$ , gives 32.2 nH for the 20V275 varistor and 29.9 nH for the 275L40C varistor.

A qualitative analysis of the measuring circuit tells us that the loop-3 current is almost equal to loop-2 current due to the high resistance of  $R_3$  and therefore the ringing seen in the loop 3 current is mainly due to the combined inductance of  $L_2$  and  $L_m$  resonating with  $C_m$ . This resonant frequency, which is sensitive mainly to  $L_2$ ,  $L_m$  and  $C_m$  is calculated as 2.15 MHz using equation (4-2) which is given below.

$$f_{r3} = \frac{1}{2\pi\sqrt{(L_2 + L_m)C_m}} \quad (4-2)$$

The observed value of approximately 1.83 MHz is fairly close to the calculated figure of 2.15 MHz. It must be noted that very small inductance and capacitance values associated with the cables and setup have been ignored in this calculation.

As expected the rate of decay in the ringing waveform is sensitive to both  $R_2$  and  $R_5$ . This was verified by simulating the circuit given in Figure 4-8 using a SPICE simulator.

#### 4.2.2.2 Normal varistor operation region observations

When the impulse voltage exceeds 600 V, the tested varistors tend to move from the *leakage* region to the *normal operation* region. Typical varistor current and voltage waveforms obtained in this region of operation are shown in Figure 4-10.

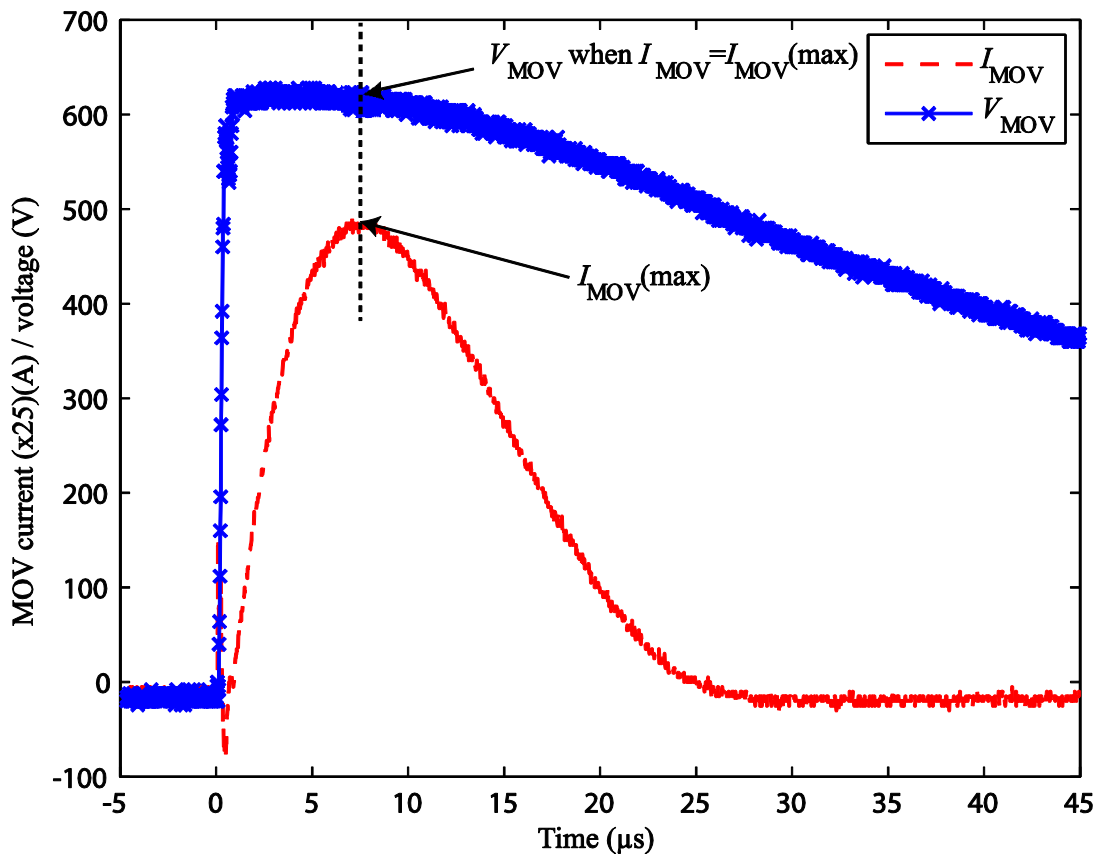


Figure 4-10: Measured voltage across and the current through a varistor in the normal operation region. The LSS was set to deliver a surge of 1 kV.

In Figure 4-10 measured voltage and current waveshapes for the varistor 275L40C are shown. The LSS was set to output a 700 V surge. It is observed that the voltage peak occurs before the current peak. This tells us that the varistor during conduction is not purely resistive.

Waveshapes similar to the ones shown in Figure 4-10 were obtained for the other two types of tested varistors as well. The time delay between the voltage and current peaks was observed in all measurements taken in the normal operation region of the varistors. The difference in this delay for different samples of the same type of varistor was found to be negligible. Figure 4-11 shows the associated dynamic  $I$ - $V$  curve for traces shown on Figure 4-10. If we are to simulate the varistor in its normal region of operation we will have to develop a varistor model capable of reproducing the major features displayed by the curves in Figure 4-10 and Figure 4-11.

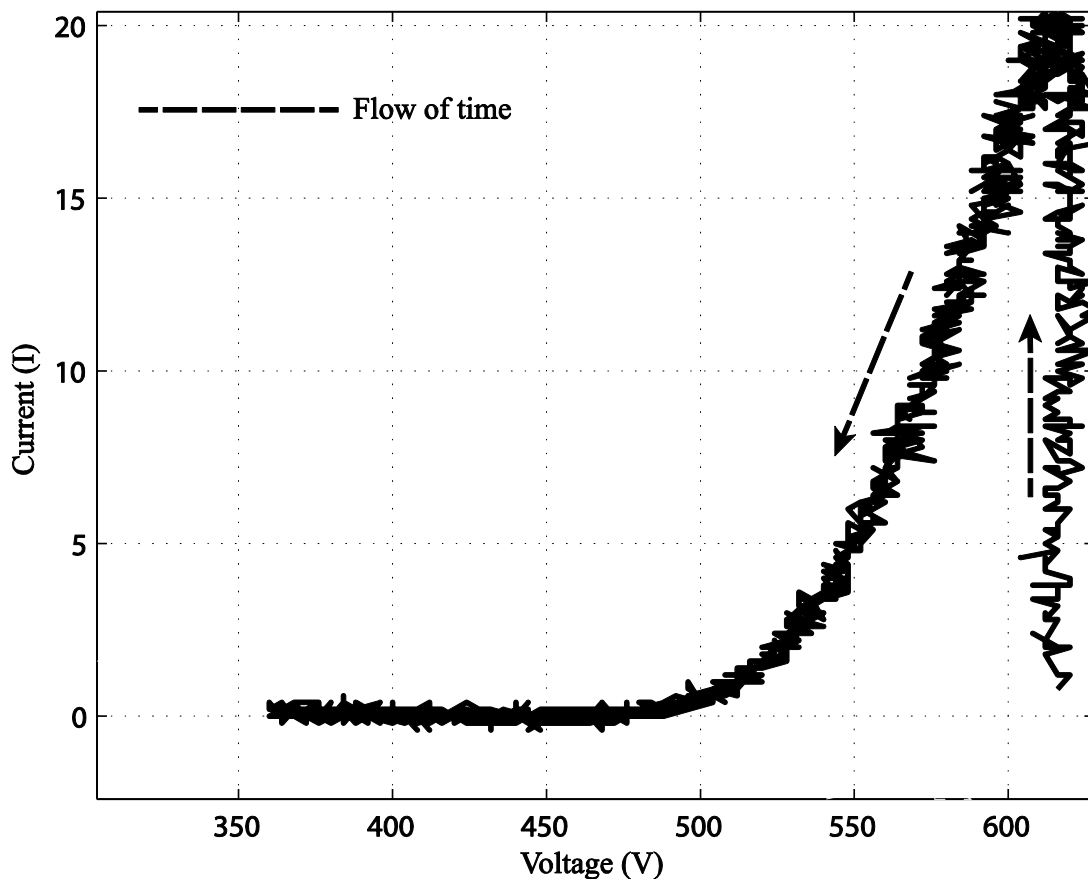


Figure 4-11: Associated dynamic  $I$ - $V$  curve for traces shown in Figure 4-10

Figure 4-10 and Figure 4-11 clearly show that when the voltage exceeds a certain threshold (around 620 V in this case), the current increases extremely fast.

Although the current starts to decrease after reaching a maximum, this decrease follows a different more gradual path with the disappearing surge voltage. This phenomenon gives rise to a hysteresis loop in the V-I characteristic of a varistor. If a very accurate model of MOV dynamics is needed, then this phenomenon will have to be taken into account [22, 62-64].

Most application notes and international standards which discuss varistor characteristics ignore this hysteresis phenomenon and present an idealized *I-V* characteristic which is a slight variation of the one shown in Figure 4-5, where the upturn region is usually omitted and the axes interchanged as shown in Figure 4-12 [21, 65]. Some of the important definitions indicated in Figure 4-12 and Table 4-2 will be discussed in the following sections where we will characterize several individual varistors.

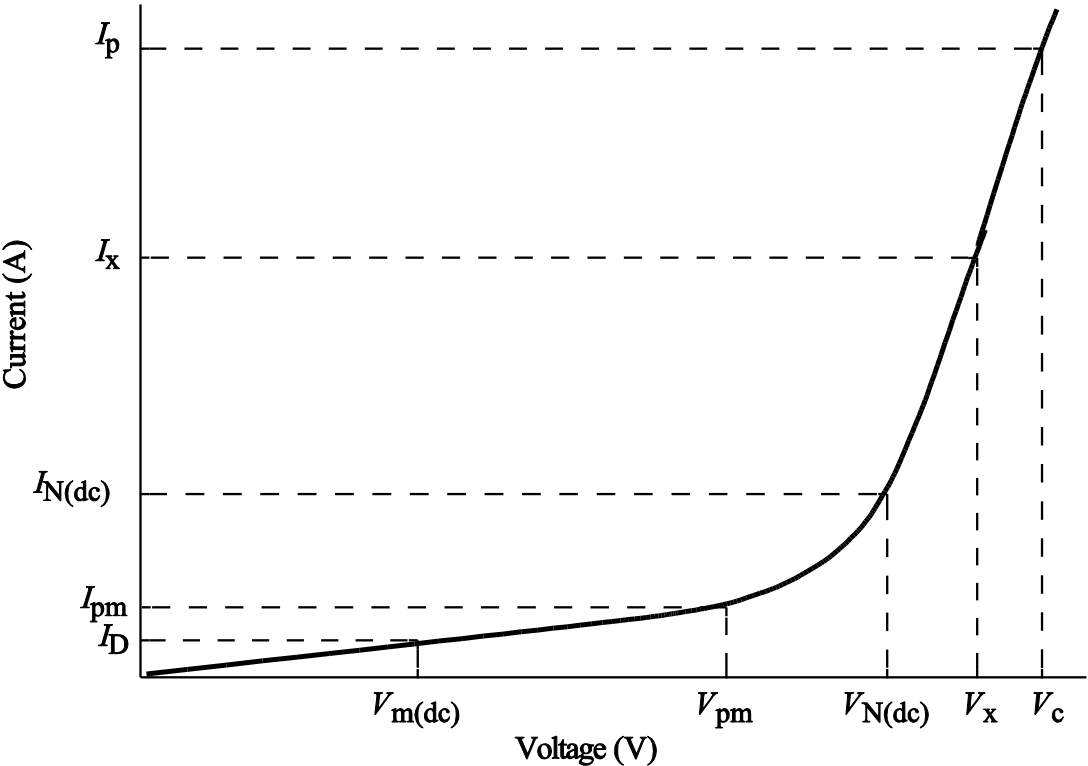


Figure 4-12: *I-V* graph of a MOV illustrating symbols and definitions (see Table 4-2)

Table 4-2: Description of terms and letter symbols used in defining a varistor

Terms and descriptions	Symbol
<b>Clamping voltage.</b> Peak voltage across the varistor measured under conditions of a specified peak pulse current and specified waveform.	$V_C$
<b>Rated DC voltage (varistor).</b> Maximum continuous DC voltage which may be applied.	$V_{m(dc)}$
<b>DC standby current (varistor).</b> Varistor current measured at rated voltage, $V_{M(DC)}$	$I_D$
<b>Nominal varistor voltage.</b> Voltage across the varistor measured at a specified pulsed dc current, $I_{N(DC)}$ , of specific duration. $I_{N(DC)}$ is specified by the varistor manufacturer.	$V_{N(dc)}$
<b>Rated recurrent peak voltage (varistor).</b> Maximum recurrent peak voltage which may be applied for a specified duty cycle and waveform.	$V_{pm}$
<b>Varistor voltage.</b> Voltage across the varistor measured at a given current, $I_X$	$V_X$

The most important property of a varistor is its nonlinear  $I$ - $V$  characteristic in the normal operation region. As indicated in references [19, 21, 23], this property can be expressed by the equation  $I = KV^\alpha$ , where  $\alpha \gg 1$  is the coefficient of non-linearity. The following argument tells us that  $\alpha$  can be determined graphically if the  $I$ - $V$  characteristic of a varistor is drawn as a log plot. Assume that MOV current follows a power-law function of MOV voltage:

$$I = KV^\alpha \quad (4-3)$$

Taking the logarithm of both sides of Eq. (4-3)

$$\log I = \log K + \alpha \log V \quad (4-4)$$

Since Eq. (4-4) is comparable to the equation of a straight line,  $y = mx + c$ , the normal operation region of the varistor should appear as a straight line in a log plot of its characteristic. The coefficient of nonlinearity  $\alpha$  is given by the slope of this line.

### 4.2.3 Approximation of the coefficient of nonlinearity “ $\alpha$ ”

Table 4-3 shows the voltage and current values obtained for the characterization of the above varistor by using the measuring set-up described in Section 4.2.1 and the wave shapes described in Section 4.2.2. In order to obtain these values, surge voltages from 100 V to 2 kV (in 100 V steps) were applied to the test circuit. The varistor current was calculated by measuring the voltage across the high wattage 1  $\Omega$  resistor connected in series with the varistor. In the leakage region of operation (0 V to 500 V) the current is recorded as 0 V due to the negligibly small values obtained.

Table 4-3: Voltage and current readings obtained to characterize a 275L40C varistor

$V_{MOV}$ (V)	$I_{MOV}$ (A)						
98	0.0	584	1.4	664	60.8	704	136.0
197	0.0	620	10.2	668	76.8	708	152.0
300	0.0	632	22.2	692	91.2	712	166.0
400	0.0	636	34.8	688	105.6	716	184.0
500	0.0	656	48.8	696	120.8	724	196.0

Figure 4-13 shows the linear and log-log  $I$ - $V$  plots done using the values recorded in Table 4-3.

It follows from Eq. (4-4) that the coefficient of nonlinearity  $\alpha$  can be determined from the log  $I$ - $V$  plot by using the following equation:

$$\alpha = \frac{\log I_2 - \log I_1}{\log V_2 - \log V_1} = \frac{\log(I_2/I_1)}{\log(V_2/V_1)} \quad (4-5)$$

where  $(V_2, I_2)$  and  $(V_1, I_1)$  are two suitably chosen points on the log  $V$ - $I$  plot. The chosen points are shown in Figure 4-13 for the log-log plot of varistor 275L40C. The calculated value of  $\alpha$  works out to be 23.94. Depending on the points chosen for the above calculation of  $\alpha$ , we see a deviation of  $\pm 10\%$ . The values of  $\alpha$  obtained for all the tested varistor types are summarized in Table 4-4.

Table 4-4: Calculated values of  $\alpha$  with percentage uncertainties

Device	Type	Exponent $\alpha_2$
MOV	275L40C	$23.94 \pm 10\%$
MOV	20V275	$20.18 \pm 8\%$
MOV	V271HA32	$16.9 \pm 10\%$

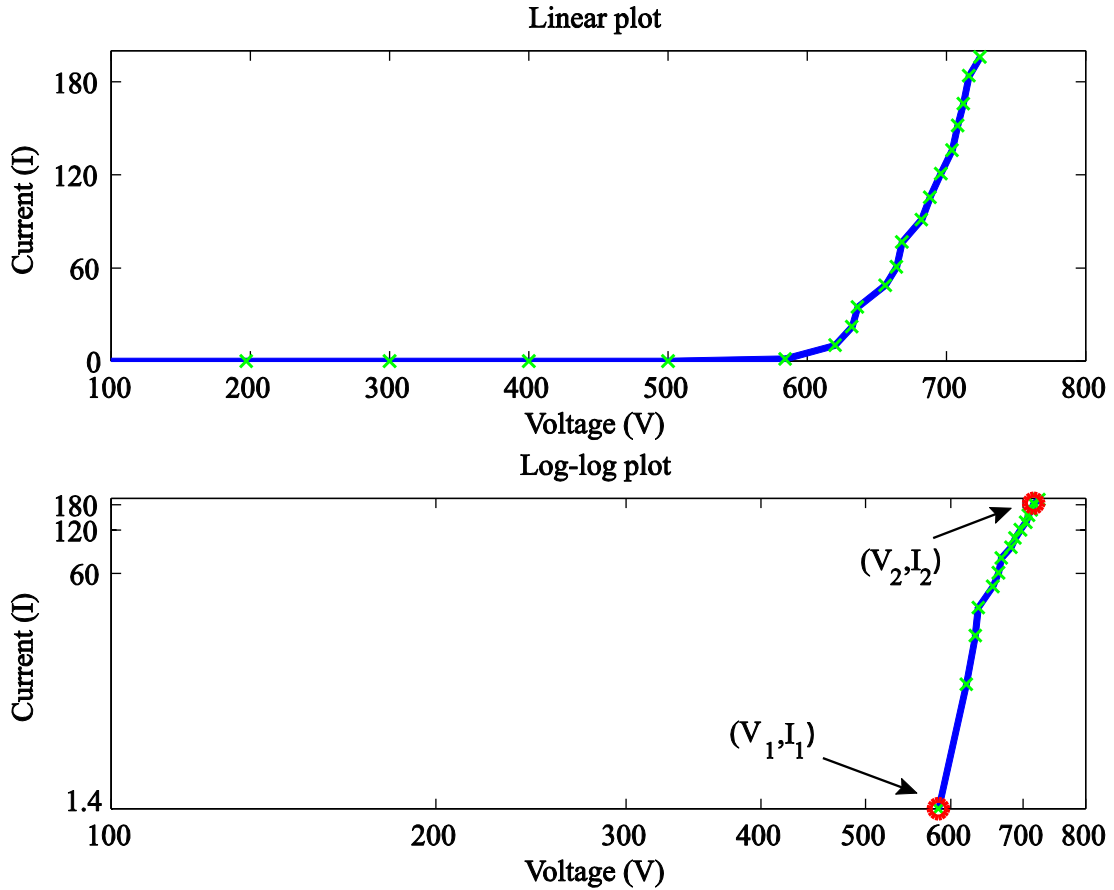


Figure 4-13: Linear and log-log  $I$ - $V$  plots for the varistor 275L40C

#### 4.2.4 Accurate measurement of leakage region currents

As we know now the measuring set-up shown in Figure 4-2 is not able to provide accurate measurements of the small currents ( $<1$  mA) resulting from voltages applicable for the leakage region of the varistor. This range of voltages can be approximately up to the  $V_{N(DC)}$  value, which is specified as 473V for the 275L40C varistor [60].

The measuring set-up shown in Figure 4-14 can be used to characterize the leakage region of the varistor. Here the impulse generator has been replaced by a Glassman HV regulated DC power supply EW5R120 as the source. This supply is

capable of 0 – 5 kV continuous output voltage and 0-120 mA output current. A Fluke 19 digital voltmeter was used for measuring the voltages. As the varistors have low average power dissipations,  $R_s$  must be chosen to limit the current to a safe value. For example, for a Littelfuse C-III 20 mm varistor, the average power dissipation should not exceed 1W.

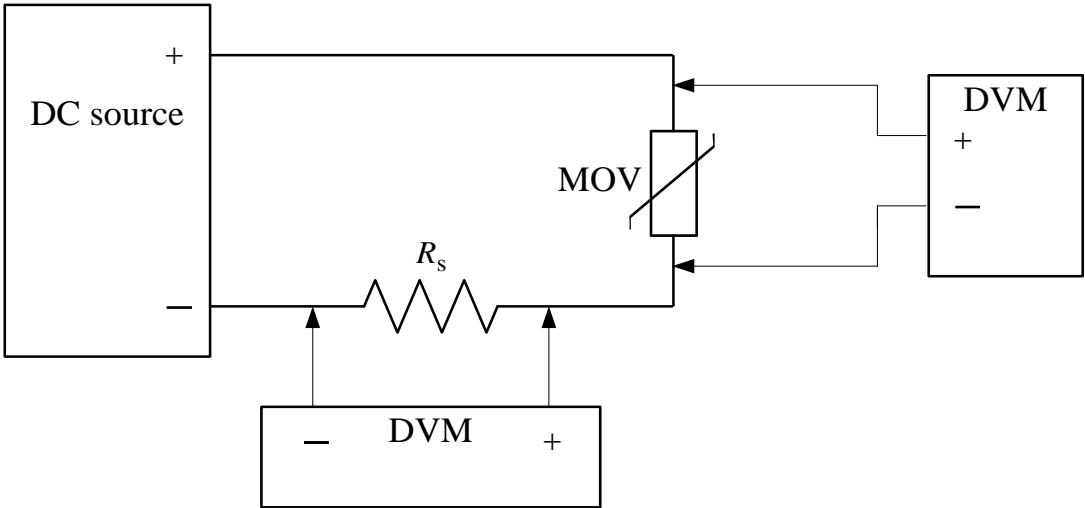


Figure 4-14: Circuit for measuring MOV voltage and current in the leakage region of operation.

**4.2.5 A varistor *I-V* characteristic for leakage and normal regions of operation**

The varistor voltage and current values in Table 4-5 were obtained by using the measuring set ups shown in Figure 4-2 and Figure 4-14 separately in order obtain a complete *I-V* characteristic to cover both the leakage as well as the normal region of operation. The device under test (DUT) was a 275L40C varistor.

Table 4-5: Voltage and current readings obtained to characterize the leakage and normal regions of operation of a 275L40C varistor

Source	$V_{MOV}$	$I_{MOV}$	Source	$V_{MOV}$	$I_{MOV}$
DC	100.3	1.5E-07	DC	461	4.16E-03
DC	199.4	1.1E-06	DC	462	4.7E-03
DC	300.3	8.8E-06	DC	464	5.3E-03
DC	397	4.1E-05	Impulse	600	2
DC	446	7.2E-04	Impulse	640	21
DC	452	1.9E-03	Impulse	660	46
DC	457	3.0E-03	Impulse	680	72
DC	458	3.5E-03	Impulse	700	104

The varistor voltage at 1mA DC test current is specified as variable from 389V to 473V in the datasheet [60]. The data in Table 4-5 confirms this. Figure 4-15 shows the linear and log  $I$ - $V$  plots done using the values recorded in Table 4-5.

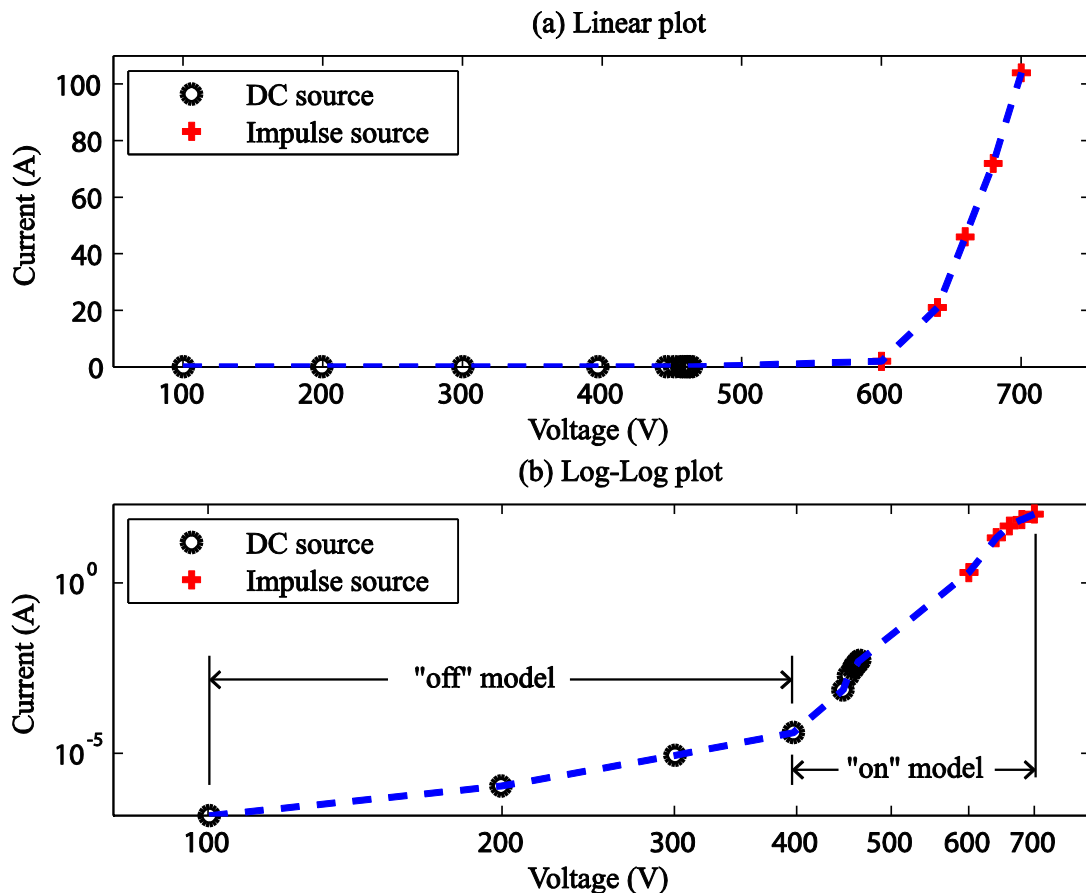


Figure 4-15:  $I$ - $V$  plots that show the leakage and normal regions of operation for a 275L40C varistor; (a) linear plot (b) log-log plot

The log plot in Figure 4-15 is approximately piecewise linear and could be modelled by using a power law expression, such as the one given in Eq. (4-3), for

each of the linear portions. Let the leakage region indicated as the “off” model in the figure be represented by  $K_1V^{\alpha_1}$  and the normal region indicated as the “on” model in the figure be represented by  $K_2V^{\alpha_2}$ .

#### 4.2.6 Development of a mathematical model for the varistor

In order to get an estimation of the parameters for the “off” and “on” models we will use the MATLAB command `polyfit(x, y, n)` to return the coefficients of our single degree polynomial in descending order. The single degree polynomial in our case would be

$$\log I = \alpha \log V + \log K \quad (4-6)$$

Hence `polyfit` would return the values for  $\alpha$  (slope) and  $\log K$  (intercept) for the straight line given by Eq (4-6).

In order to illustrate the development of a combined model for the leakage and normal regions of operation for a varistor, the data points of Table 4-5 are used again in the log-log plot of Figure 4-16. The positioning of the straight line segments in Figure 4-16, represented by  $I = K_1V^{\alpha_1}$  and  $I = K_2V^{\alpha_2}$ , was done with the following values obtained from appropriate curve fitting using `polyfit` for the tested 275L40C varistor (see Appendix B.1 for MATLAB code).

$$K_1 = 9.3231 \times 10^{-16}, \alpha_1 = 4.0413 \quad (\text{“off” model parameters})$$

$$K_2 = 3.5040 \times 10^{-73}, \alpha_2 = 26.2396 \quad (\text{“on” model parameters})$$

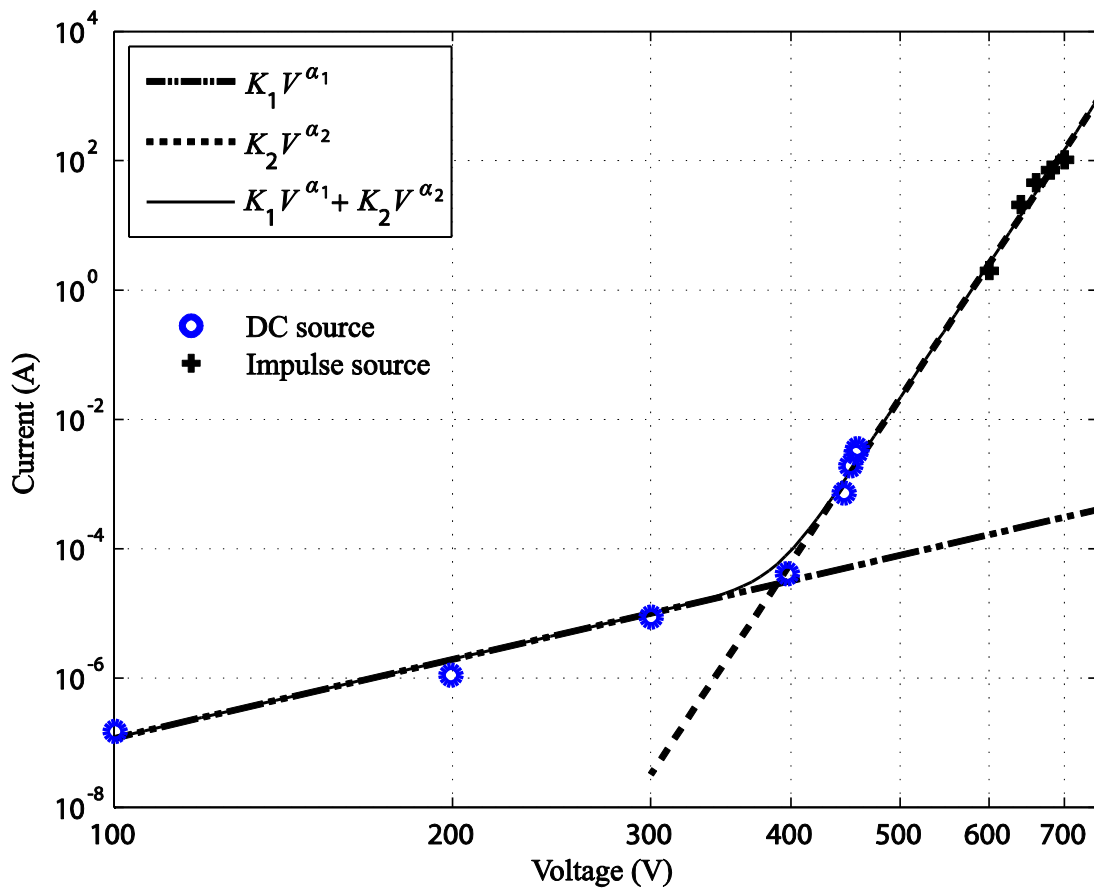


Figure 4-16: Development of a combined model for the leakage and normal regions of operations for a varistor

The curve for the combined model  $I = K_1V^{\alpha_1} + K_2V^{\alpha_2}$  is shown in Figure 4-16 (see Appendix B.2 for MATLAB code) along with its two straight line component segments. In the following section we will verify the validity of this model.

#### 4.2.7 Verification of the model for the varistor by simulation and validation

The following circuit (Figure 4-17) was chosen to verify the mathematical model developed for the varistor in the previous section. In this circuit a set of DC voltages ranging from 20 to 1200 V is applied to the input and the resulting varistor current and voltage are simulated along with the load current. An experimental validation is subsequently performed by taking maximum values resulting from surging the circuit using an LSS.

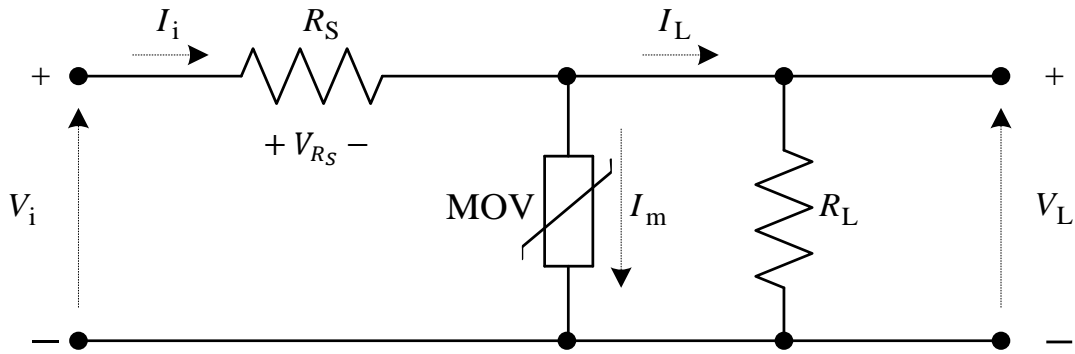


Figure 4-17: The circuit used for an initial verification of the model developed for the varistor.

Now we will formulate an equation for the input current  $I_i$ , and get MATLAB code to solve for  $I_i$  by finding the roots of this equation. Once  $I_i$  is known, the remaining unknowns can be found by the equations listed below, for each value of  $V_i$ , within the range of interest.

By applying Kirchoff's voltage law (KVL), we have

$$V_L = I_L R_L = (I_i - I_m) R_L = V_i - I_i R_S \quad (4-7)$$

The varistor current  $I_m$  represented by the model developed in the previous section is given by :

$$I_m = K_1 V_L^{\alpha_1} + K_2 V_L^{\alpha_2} \quad (4-8)$$

Hence  $I_m$  can be defined as a function of  $V_L$  and therefore

$$I_m = f(V_L) = f(V_i - I_i R_S) \quad (4-9)$$

Substitution of Eq. (4-9) in Eq. (4-7) results in,

$$[I_i - f(V_i - I_i R_S)] R_L = V_i - I_i R_S \quad (4-10)$$

Rearranging Eq. (4-9) gives

$$[I_i(R_L + R_S) - V_i]/R_L - f(V_i - I_i R_S) = 0 \quad (4-11)$$

We see that the only unknown in Eq.(4-11) is  $I_i$ . For each input voltage value, this equation is solved to find the corresponding value of  $I_i$ . This is done by finding the range of values the equation would take for a given span of values for  $I_i$ . Since the required value of  $I_i$  is given by the roots of the equation, it can be found by locating the value of  $I_i$  at the zero crossing point of the equation curve. This is illustrated in Figure 4-18 for a sample input voltage of 800 V. MATLAB command `fzero` that uses the bisection iteration method was used in the calculation of  $I_i$  and the code used is listed in Appendix B.3.

The simulations done with the help of the above solution are shown in Figure 4-19, where the circuit resistances were set to  $R_S = 1 \Omega$  and  $R_L = 1 \text{ k}\Omega$ . As expected, when the input voltage exceeds the MOV's threshold voltage almost all of the input current is carried by the MOV. In order to validate these simulations and check the suitability of the developed varistor model, an experimental validation was performed by surging the circuit with the LSS. The data collected for this validation are given in Table 4-6 (the shaded cell values were calculated) and the points are plotted in Figure 4-19. It can be clearly seen that the simulation and the experimental results compare well. We are now convinced that we can experiment with this model to investigate transient propagation through surge protection circuitry, which is the primary task of this research project.

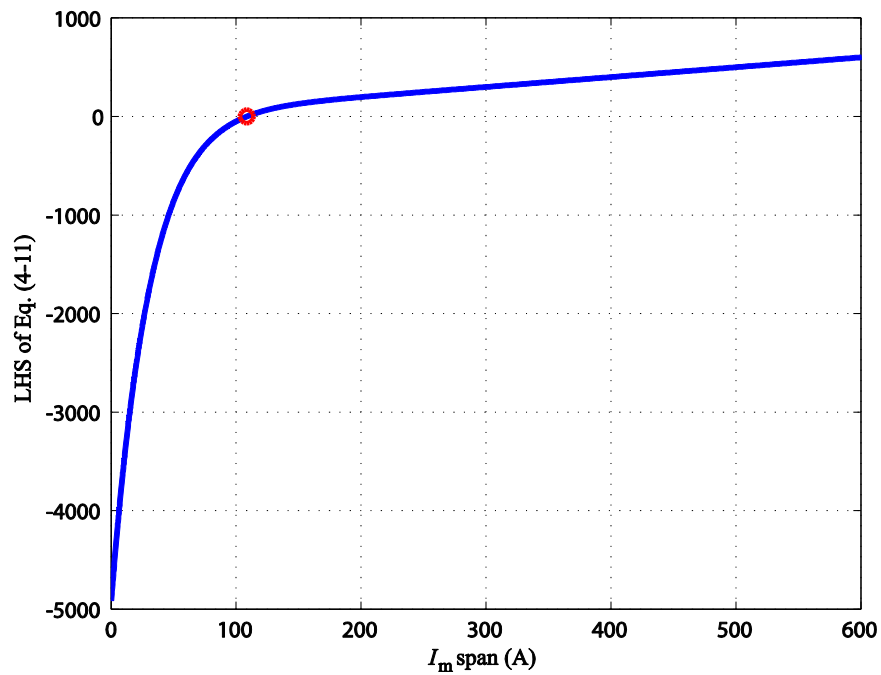


Figure 4-18: Illustration to show the solving of Eq. (4-11) to find the value of  $I_m$  for  $V_i = 800V$

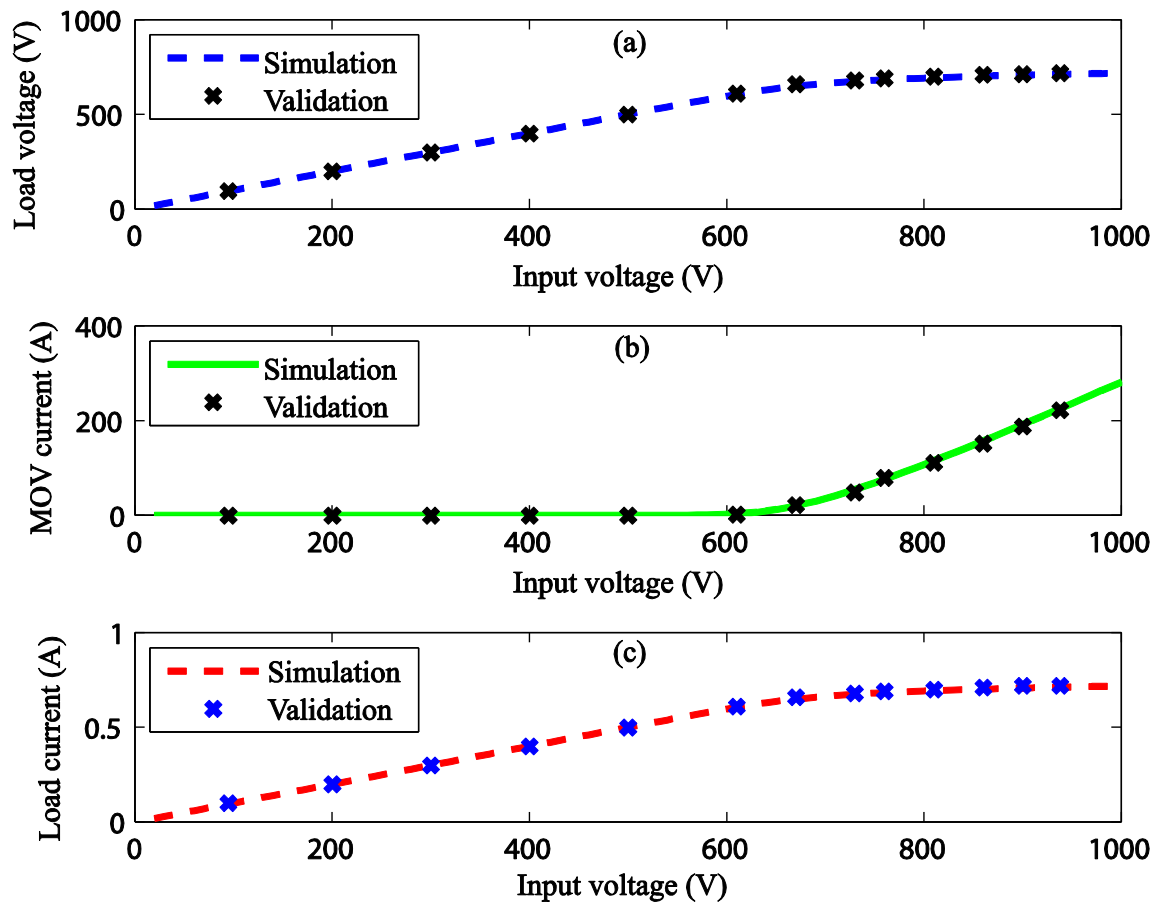


Figure 4-19: Simulation results for the circuit of Figure 4-17 along with experimental validation using an LSS: (a)  $V_i$  vs.  $V_L$  (b)  $V_i$  vs.  $I_m$  and (c)  $V_i$  vs.  $I_L$

Table 4-6: Experimental data obtained from testing the circuit of Fig. 5.17.

$V_i$ (V)	$V_{R_S}$ (V)*	$I_{R_S} = V_{R_S}/R_S$ (A)	$V_L$ (V)	$I_L = V_L/R_L$ (mA)	$I_m = V_{R_S} - I_L$ (A)
95	Very small		95		
200	Very small		200		
300	Very small		300		
400	Very small		400		
500	Very small		500		
610	2	2	610	610	1.5
670	22	22	660	660	21.5
730	49	49	680	680	48.5
760	79	79	690	690	78.5
810	111	111	700	700	110.5
860	152	152	710	710	151.5
900	188	188	713	713	187.5
938	222	222	718	718	221.5

Note: \* Very small values indicated accordingly are not accurately measurable.  
Shaded values were calculated

#### 4.2.8 Study of varistor conductance, power and energy during a surge propagation

Once the varistor voltage  $v(t)$  and current  $i(t)$  variations with respect to time are known, it is possible to study the conductance, power and energy variations due to the following relationships.

$$\text{Conductance} = G(t) = I(t)/V(t) \quad (4-12)$$

$$\text{Power} = P(t) = V(t) \cdot I(t) \quad (4-13)$$

$$\text{Energy} = E = \int P(t)dt = \int V(t) \cdot I(t)dt \quad (4-14)$$

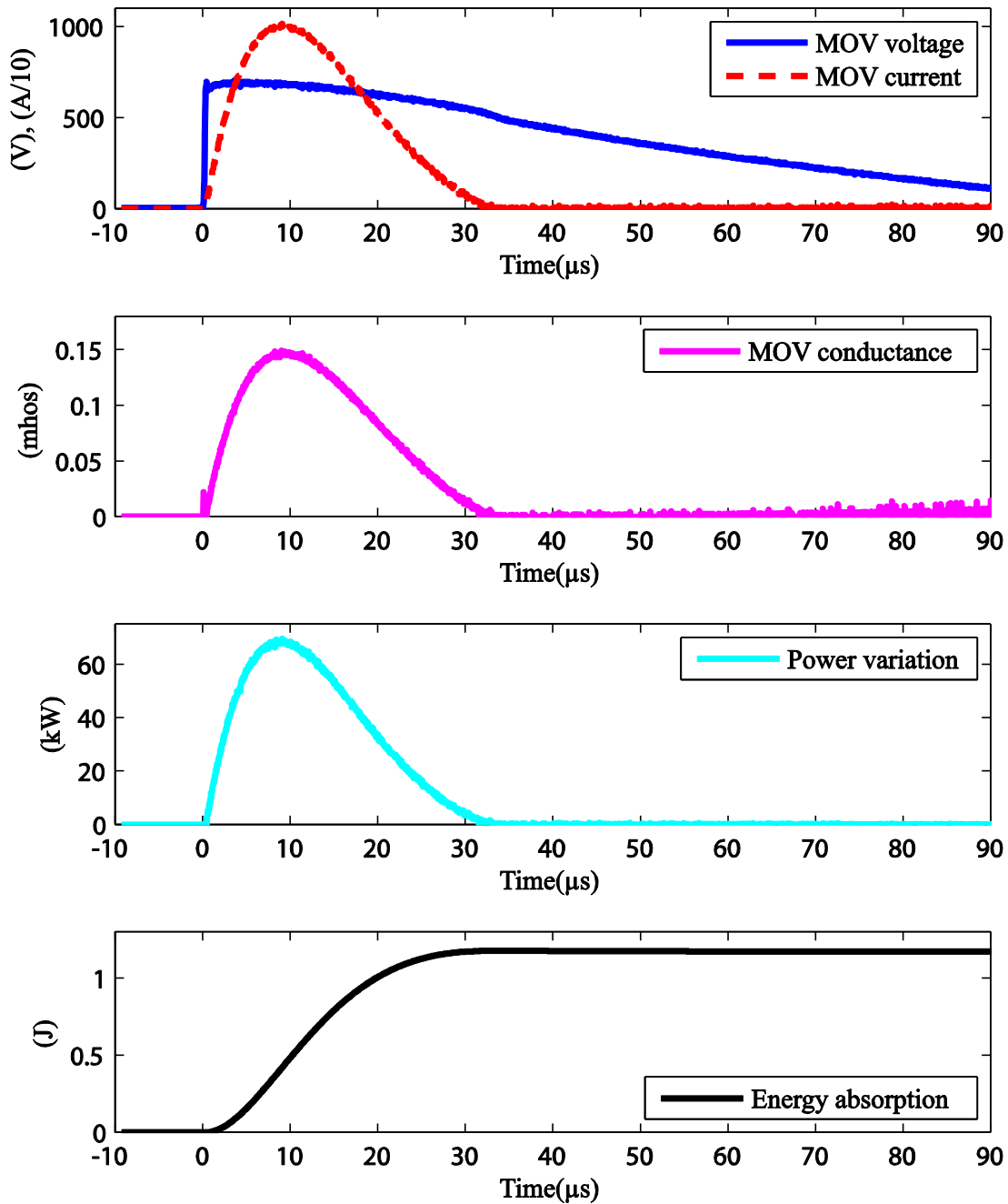


Figure 4-20: Characterization of the varistor conductance, power dissipation and energy absorption during the propagation of a transient

In Section 4.2.2.2, we saw the varistor voltage and current waveshapes during the propagation of a typical transient through it. These variations can be used to study the varistor conductance, power and energy variations as illustrated in Figure 4-20.

Detailed observations of the conductance plot (Figure 4-20) indicate that the conductance follows the pattern of the MOV current, due to the small drop in the

MOV voltage. When the conduction is at its peak, the resistance of the MOV drops to a very low value which is close to  $7 \Omega$ .

Figure 4-20 also shows the instantaneous power variations for the varistor and this curve too tends to follow the shape of the varistor current, again since the varistor voltages stays almost constant during conduction. The last plot in Figure 4-20 gives an idea as to the total energy absorbed by the varistor at the end of the transient. Obtaining this curve by experiment is important for this project as we will be using it for validating the simulated energy plots that we will be investigating in Chapter 7. Among others, the study of energy absorption by simulation is important in predicting device failure.

#### 4.2.9 Study of an MOV's industrial characterization that uses a logarithmic-term model

As mentioned in Section 2.4.1.1, the SPICE-based industrial model of an MOV is based on a logarithmic-term model for the nonlinear resistance, which is an extension of the model given by Eq. (2-2). In order to understand the industrial characterization, we will study the characterization of the MOV in this section, using this logarithmic-term model

$$\log_{10}(v) = B_1 + B_2 \log_{10}(i) + B_3 e^{-\log_{10}(i)} + B_4 e^{\log_{10}(i)} \quad (4-15)$$

where  $i$  is the current through the varistor and  $v$  is the voltage across the varistor.

We will now use the following interpolation parameters given for the S20K250 varistor [22] to study the implication of each of the terms in Eq. (5-15) in shaping the  $V$ - $I$  characteristic of the MOV.

Table 4-7: Parameters used for the basic varistor model

Coefficient	Varistor S20K250
$B_1$	2.6830619
$B_2$	0.0261918
$B_3$	-0.0006173
$B_4$	0.0045183

First, let us first consider the effect of the coefficient  $B_1$  by setting  $B_2= B_3= B_4=0$ . Then, from Eq. (4-15), we have

$$\log_{10}(v) = B_1 = 2.6830619 \quad (4-16)$$

Taking antilogs, we get

$$v = 10^{2.6830619} = 482.016 \quad (4-17)$$

We see that the contribution of this term is a constant voltage offset independent of current. If we change  $B_1$ , first to 2.5830619 and then to 2.7830619, the respective values for  $v$  will be 482 V and 606 V. Careful examination of the plots around the cut-in points tells us that these voltage values correspond to the voltage across the device when the current is approximately 1 A. The effect of varying  $B_1$  on the  $I$ - $V$  characteristic of the MOV is shown in Figure 4-21.

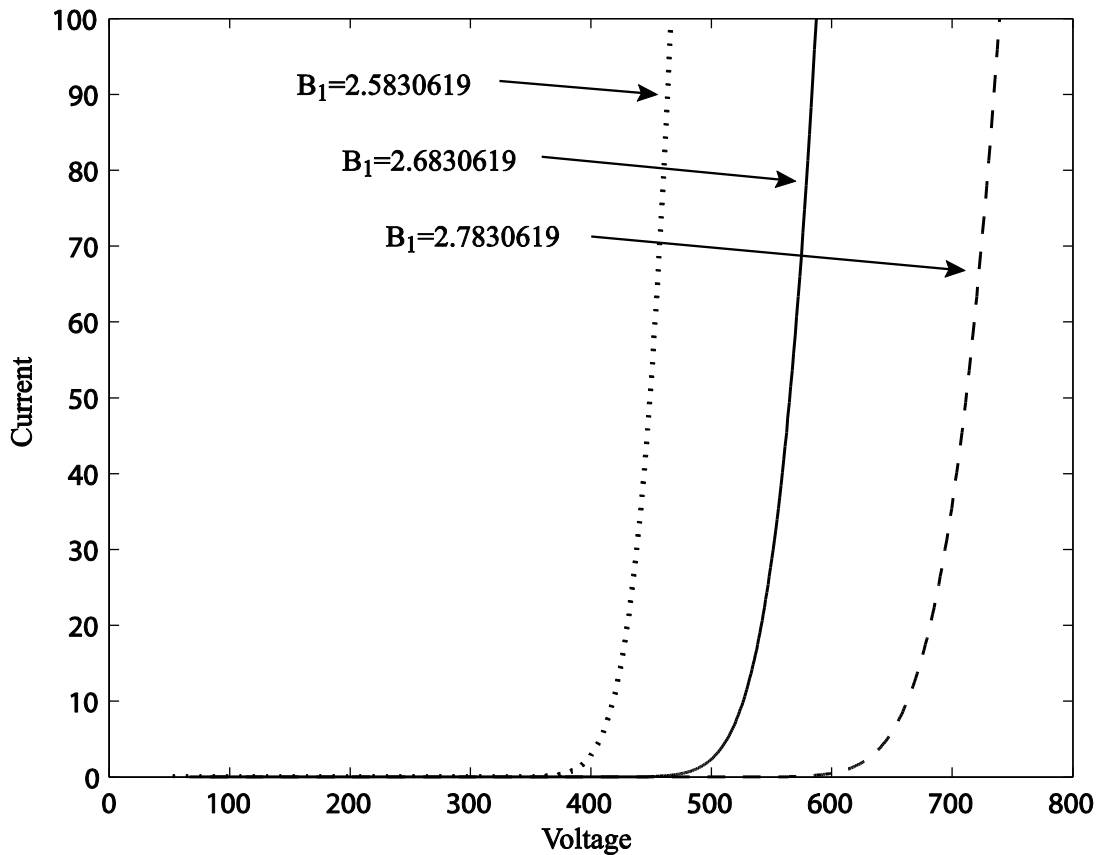


Figure 4-21: The effect of changing the coefficient  $B_1$ , on the  $I$ - $V$  characteristic of the MOV

Next, let us first consider the effect of the coefficient  $B_2$  on the characteristic. If we set  $B_1 = B_3 = B_4 = 0$ , then, from Eq. (4-15), we have

$$\log_{10}(v) = B_2 \log_{10}(i) = \log_{10}(i^{B_2}) \quad (4-18)$$

Taking antilogs, we get

$$v = i^{B_2} \quad \text{or} \quad i = v^{1/B_2} = v^{1/0.0261918} = v^{38.18} \quad (4-19)$$

Here we have a power-law relationship between the MOV current and the voltage, similar to the relationship given by Eq. (4-3). Our coefficient of nonlinearity  $\alpha$  in Eq. (4-3) is similar to the reciprocal of  $B_2$ .

The effect of varying  $B_2$  only on the  $I$ - $V$  characteristic of the MOV is shown in Figure 4-21.

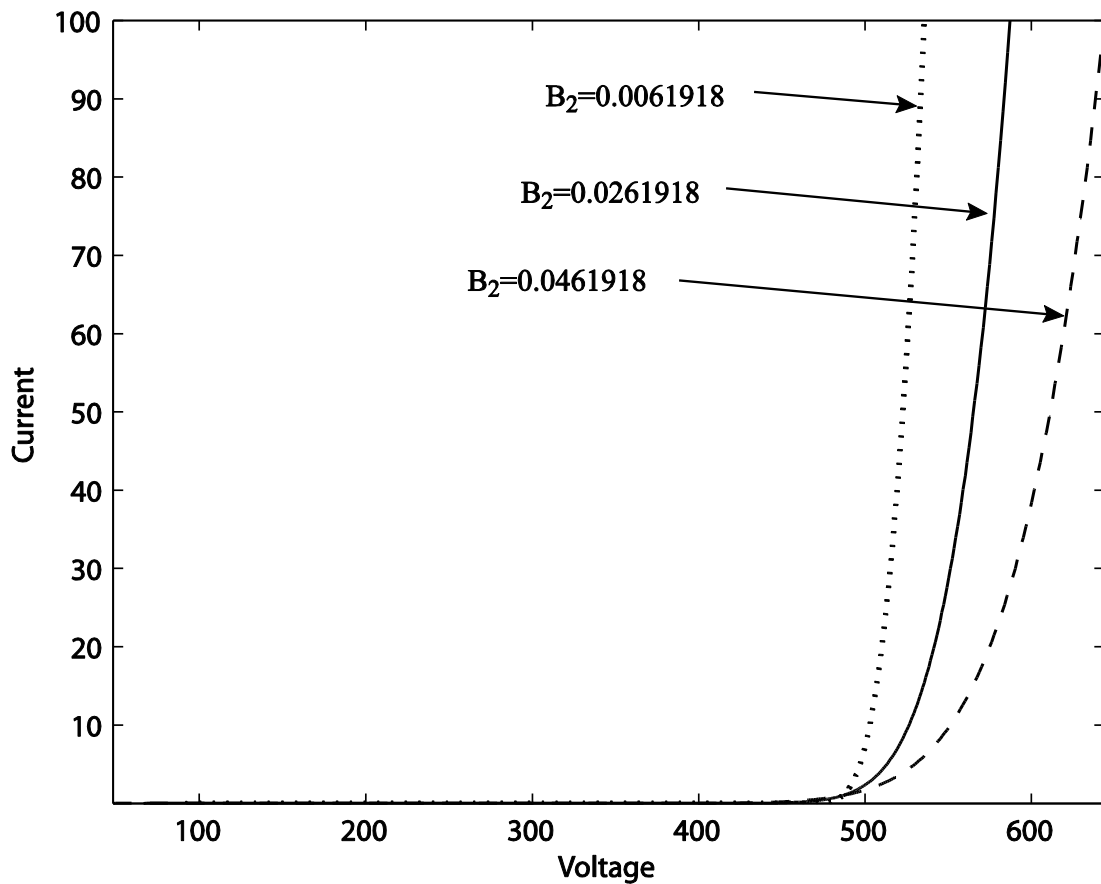


Figure 4-22: The effect of changing the coefficient  $B_2$ , on the  $I$ - $V$  characteristic of the MOV

We found that the coefficient  $B_3$  does change the “off” model which can be easily seen by studying a log-log plot of the  $I$ - $V$  characteristic, but has no effect on the shape of the “on” model characteristic of the varistor. As we are mostly interested in dissipated energies in individual components during the “on” time of the varistor, this coefficient will not play any useful role in the present study.

Now let us consider the effect of the last coefficient  $B_4$  on the characteristic. If we let  $B_1=B_2=B_3=0$ , then, from Eq. (4-15), we have

$$\log_{10}(v) = B_4 e^{\log_{10}(i)} \tag{4-20}$$

Taking antilog and using the log identity  $\log_a x / \log_a y = \log_y x$ , we can show that

$$v = 10^{B_4 i^{0.434}} \tag{4-21}$$

The complex term shown above also contributes to the degree of nonlinearity of the  $I$ - $V$  characteristic, in a way similar to the  $B_2$  term, as shown in Figure 4-23. The changes in the degree of nonlinearity can be finer in the case of  $B_4$ .

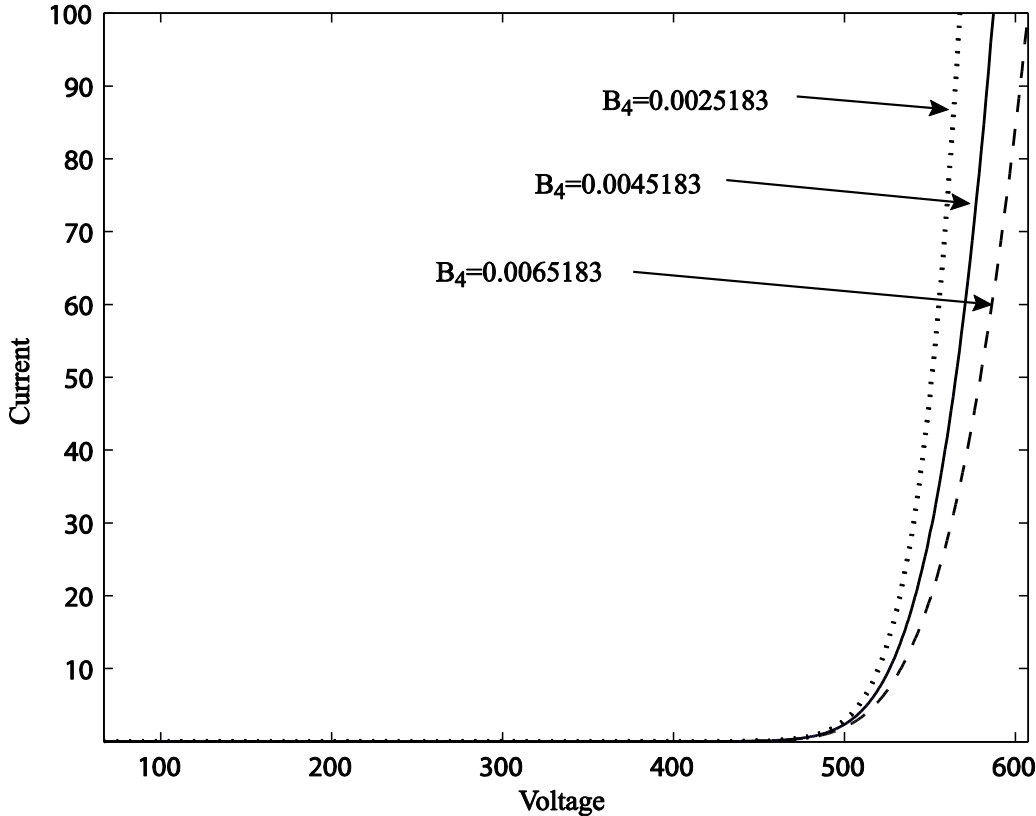


Figure 4-23: The effect of changing the coefficient  $B_4$ , on the  $I$ - $V$  characteristic of the MOV  
88

This study of the varistor model given by Eq. (4-15) shows us that the coefficients  $B_1$ ,  $B_2$  and  $B_4$  together can achieve a good curve fit for the  $I$ - $V$  characteristic of the varistor. We have already seen that a similar curve fit can be obtained by the coefficient  $k$  and the exponent  $\alpha$ , if we use the alternate model given by Eq. (4-3). In the numerical simulation work that we undertake for our investigation of surge propagation in Chapter 6, the simpler model given by Eq. (4-3) is preferred, as our interest is focused mainly on the energy distribution within the power electronics interface.

We also found that, the industrial characterization studied here does not account for the hysteresis effect discussed in Section 4.2.2.2, despite its complexity. A parallel-branch model where each branch contains a nonlinear resistance based on the model studied here is proposed in [22], to account for the hysteresis effect .

### 4.3 TVS diode characterization

Manufacturers such as *Littlefuse* offer a broad range of TVS diodes, including high peak pulse current and peak pulse power options up to 10 kA and 30 kW respectively. A sample set of TVS diodes from their product line is given in Table 4-8. They are available in both uni-directional (uni-polar) or bi-directional (bi-polar) diode circuit configurations.

For our experiments of characterization and model development, we selected the devices 1.5KE170CA and 1.5KE400CA from the 1.5KE series, which are bidirectional. This series includes matching unidirectional devices as well. Figure 4-24 illustrates a typical  $I$ - $V$  characteristic for a bidirectional TVS diode. Since the peak pulse power range is constant for all devices in the 1.5KE series, the devices with higher breakdown voltages ( $V_{BR}$ ) have lower peak pulse current ( $I_{PP}$ ) at the clamping voltage ( $V_C$ ).

Table 4-8: Some characteristics of samples from a TVS diode product selection table [66]

Series Name	Reverse Standoff Voltage ( $V_R$ )	Peak Pulse Power Range ( $P_{PP}$ )	Peak Pulse Current ( $I_{PP} \times 8 \times 20 \mu s$ )
Surface Mount – Standard Applications (400-5000W)			
SMAJ	5.0-440V	400W	NA
SMCJ	5.0-440V	1500W	NA
Axial leaded – Standard Applications (400-5000W)			
1.5KE	5.8-495V	1500W	NA
5KP	5.0-250	5000W	NA
Axial leaded – High Power			
30KPA	28.0-288V	30000W	NA
AK10	58-430V	NA	10000A
Automotive Applications			
SLD	10-24V	2200W based on $1 \mu s/150ms$ pulse	NA

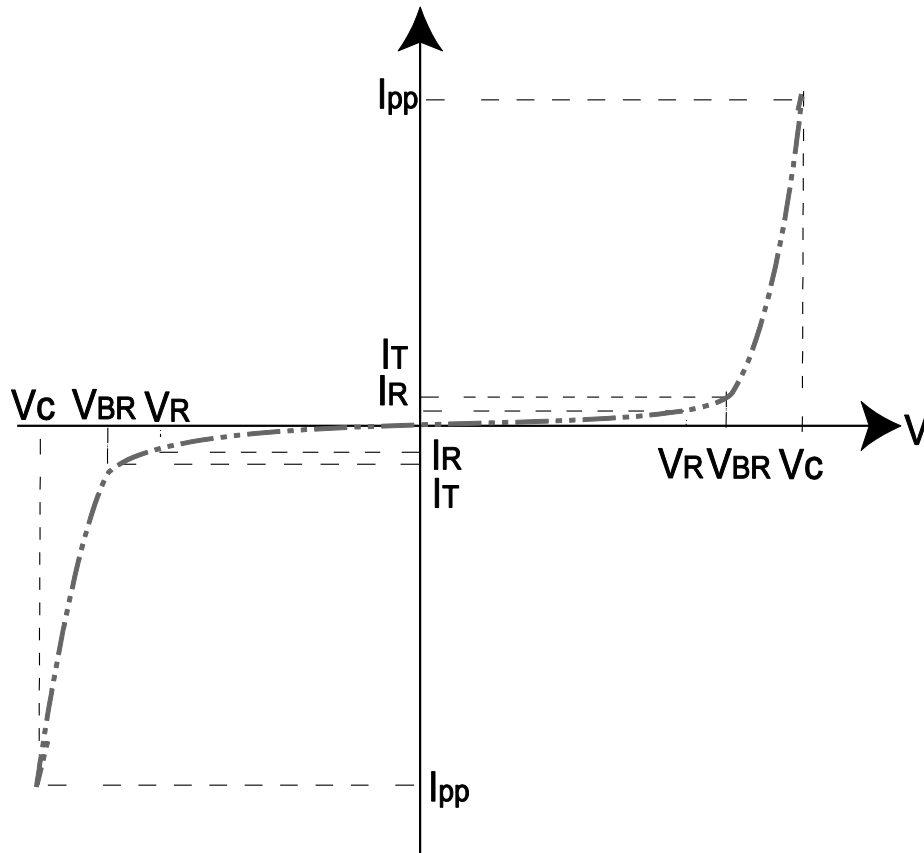


Figure 4-24: Typical I-V curve characteristics for a bidirectional TVS diode [67]

Terms and descriptions for the important symbols shown in Figure 4-24 are given below:

$V_R$     **Stand-off Voltage** – Maximum voltage that can be applied to the TVS without significant conduction.

$V_{BR}$     **Breakdown Voltage** measured at a specified DC test current typically 1mA.

$I_{PP}$     **Peak Pulse Current** – Identifies the maximum current the TVS diode can withstand without damage.

$V_C$     **Clamping Voltage** - This is the peak voltage that will appear across the TVS diode when subjected to a specified  $I_{PP}$  (peak impulse current).

$I_R$     **Reverse Leakage Current** – Current measured at  $V_R$ .

The measuring circuit diagram we used for obtaining the  $I$ - $V$  characteristics of the TVS diode is identical to the one shown in Figure 4-2. The Noiseken LSS-6110 lightning surge simulator was again used as an impulse source. A series of pulses with different voltage amplitudes were applied to each one of the TVS diodes tested.

#### **4.3.1 Waveforms obtained and their analysis**

The 1.5KE400CA TVS diode moves from a high impedance state to normal operation when the impulse voltage exceeds 500V because its breakdown voltage lies above 420V. Typical current and voltage waveforms obtained for this device in the region of normal operation are shown in Figure 4-25.

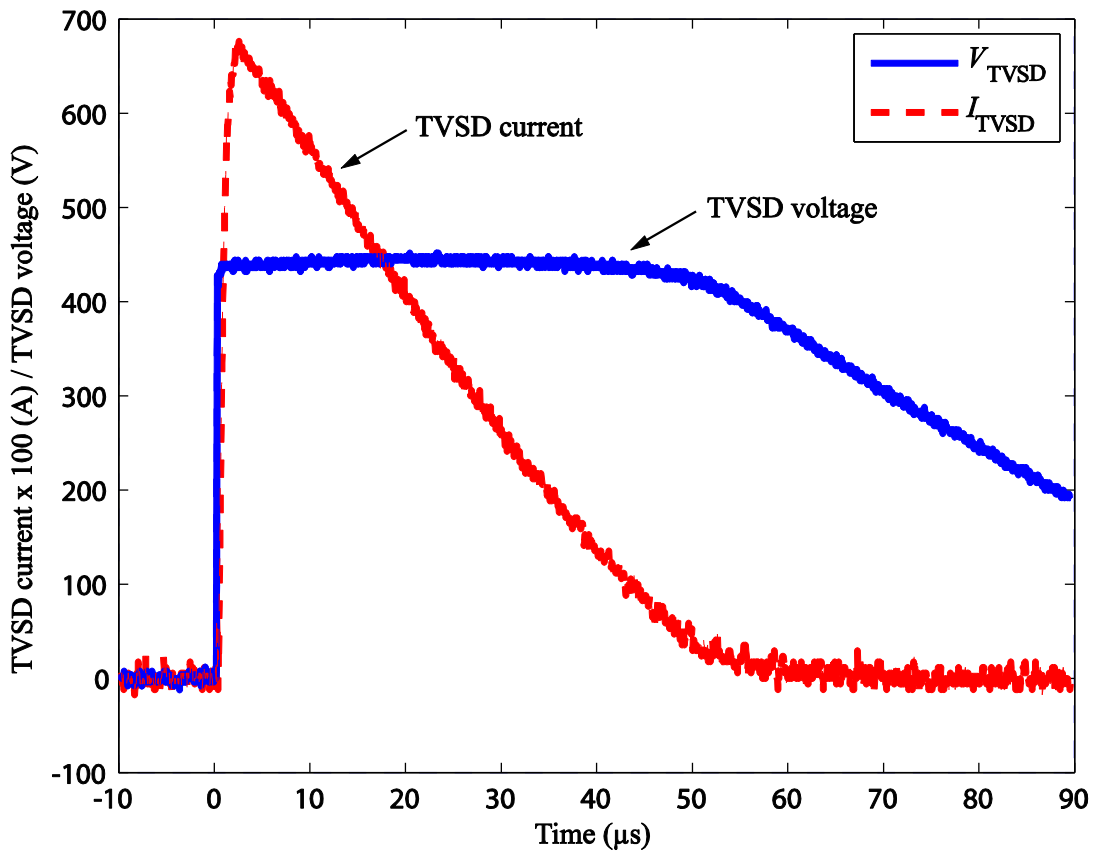


Figure 4-25: Voltage across and the current through a TVS diode operated by an impulse input

The waveforms shown in Figure 4-25 were obtained by setting the LSS to output an impulse of 900V. It is clearly seen that the *speed of response* of conduction in this TVS diode is far superior to that of the varistor tested earlier (Figure 4-10). In the case of the TVS diode, the current maximizes in approximately 2.5  $\mu\text{s}$ , compared to 7.5  $\mu\text{s}$  for the varistor. In spite of this difference, both devices are fast enough to respond to real world transient events [17].

The dynamic  $I$ - $V$  curve associated with the waveforms of Figure 4-25 is shown in Figure 4-26. Unlike in the case of the varistors investigated, we do not observe a significant hysteresis effect.

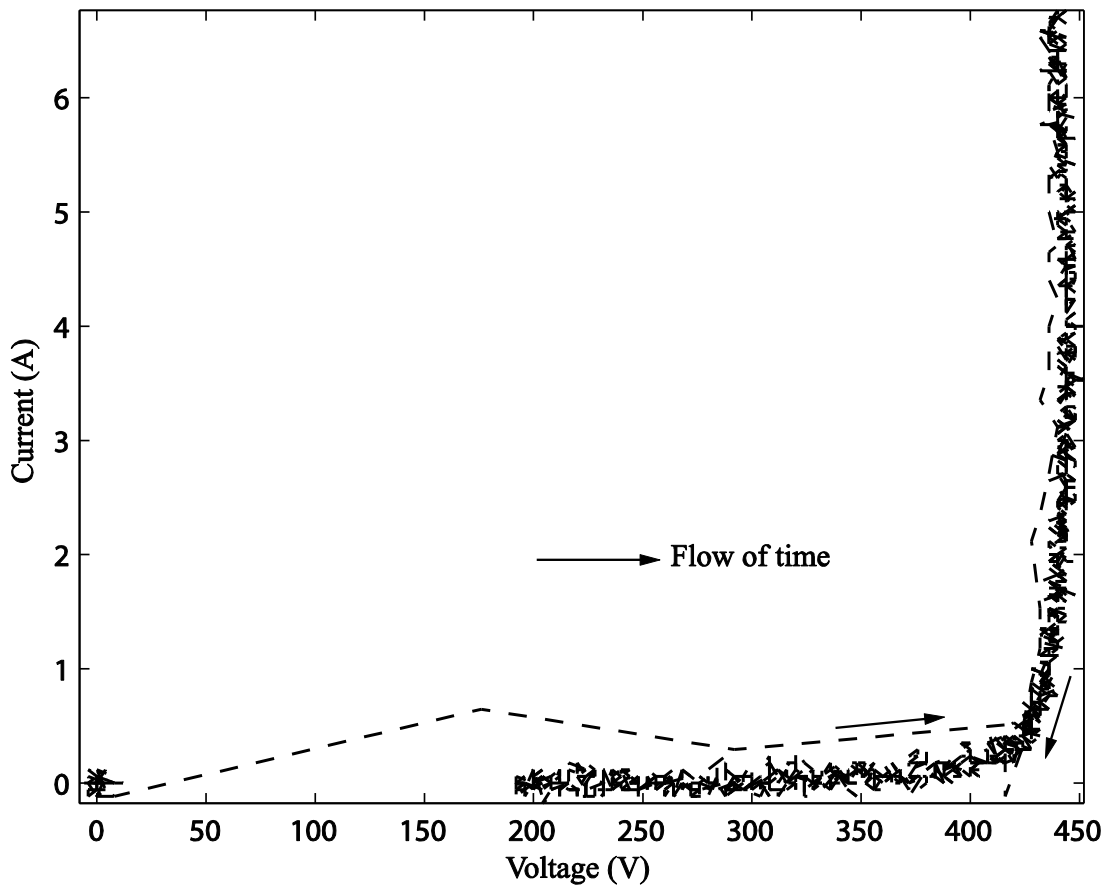


Figure 4-26: Associated dynamic I-V curve for traces shown in Figure 4-25 for the TVS diode 1.5KE400CA

### 4.3.2 A TVS diode (1.5KE170CA) I-V characteristic for leakage and normal regions of operation

The voltage and current values in Table 4-9 were obtained by testing a TVS diode using the measuring set ups shown earlier in Figure 4-2 and Figure 4-14. A 1.5KE170CA TVS diode was used as the device under test (DUT).

We note that the leakage current  $I_{RM} = 5\mu A @ V_{RM} = 145V$  specified in the datasheet [68] is very close to corresponding datapoints recorded in Table 4-9.

Table 4-9: Voltage and current readings obtained to characterize the leakage and normal regions of operation of a 1.5KE170CA TVS diode

Source	$V_{TVSD}$	$I_{TVSD}$	Source	$V_{TVSD}$	$I_{TVSD}$
DC	100.3	0.92E-06	DC	169.6	35.71E-06
DC	106.2	2.12E-06	DC	169.6	44.16E-06
DC	110.6	2.94E-06	DC	169.7	73.34E-06
DC	138.5	8.67E-06	DC	170	84.05E-06
DC	169.4	17.24E-06	Impulse (200V)	194	2.00
DC	169.5	26.93E-06	Impulse (300V)	208	23.10

Figure 4-27 shows the linear and log-log  $I$ - $V$  plots done using the values recorded in Table 4-9. The nearly straight-line segments of the log-log plot suggests piecewise modelling similar to the varistor modeling done in Sections 4.2.5 and 4.2.6. Again, the “off” model and the “on” model shown in the figure may be represented by  $K_1V^{\alpha_1}$  and  $K_2V^{\alpha_2}$  respectively. Calculation of the constants  $K_1$ ,  $K_2$ ,  $\alpha_1$ , and  $\alpha_2$  is illustrated in the following section.

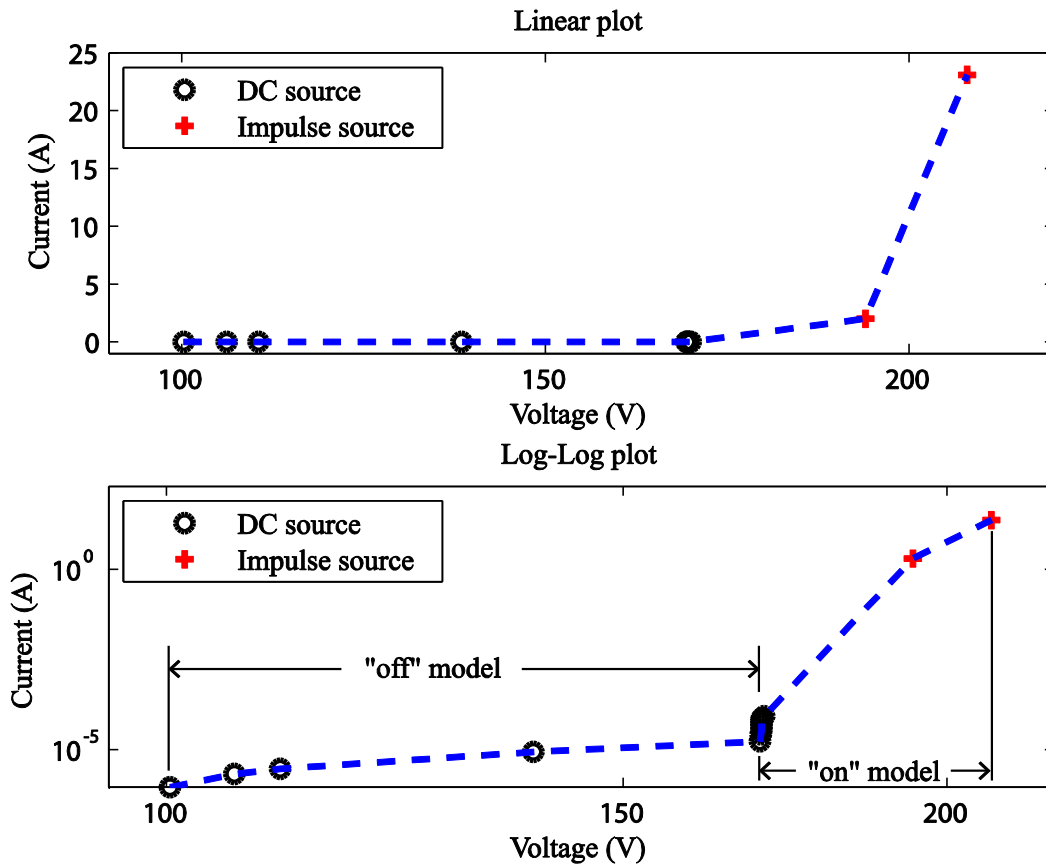


Figure 4-27: Linear and log V-I plots that show the leakage and normal regions of operation for a 1.5KE170CA TVS diode.

### 4.3.3 Complete mathematical model for the TVS diode

In order to develop a combined model for the “off” and “on” regions of the TVS diode, the data points of Table 4-9 are used again in the plot of Figure 4-28. The curve fitting exercise carried out here is very similar to the one done for the varistor, where the slope of the linear segments was found with the use of MATLAB’s polyfit command.

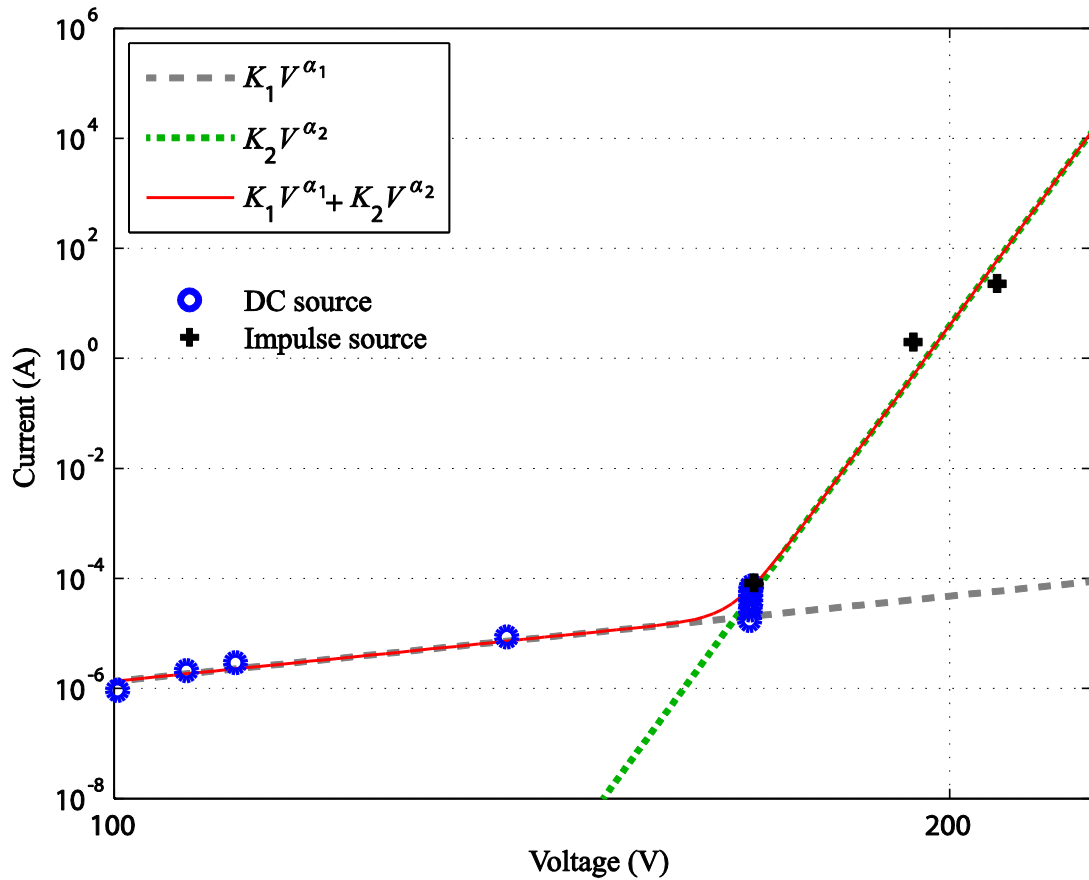


Figure 4-28: Development of a combined model for the “off” and “on” regions of a TVS diode.

The positioning of the straight line segments in Figure 4-28, represented by  $I = K_1V^{\alpha_1}$  and  $I = K_2V^{\alpha_2}$ , was done with the following values obtained from appropriate curve fitting using polyfit for the tested 1.5KE170CA TVS diode.

$$K_1 = 5.5217 \times 10^{-17}, \alpha_1 = 5.1561 \quad (\text{“off” model parameters})$$

$$K_2 = 9.8813 \times 10^{-159.1}, \alpha_2 = 68.8466 \quad (\text{“on” model parameters})$$

The curve for the combined model  $I = K_1V^{\alpha_1} + K_2V^{\alpha_2}$  was also developed earlier for the varistor and was shown in Figure 4-16. Hence MATLAB code similar to code given in Appendix B.2 can be used in this instance as well.

#### 4.4 Comparison of transient suppressor models

The models that we developed for the 275L40C varistor and the 1.5KE170CA TVS diode are displayed side-by-side in Figure 4-29 for comparison. Two important parameters, the degree of nonlinearity  $\alpha$ , and the leakage current can be easily compared using these plots.

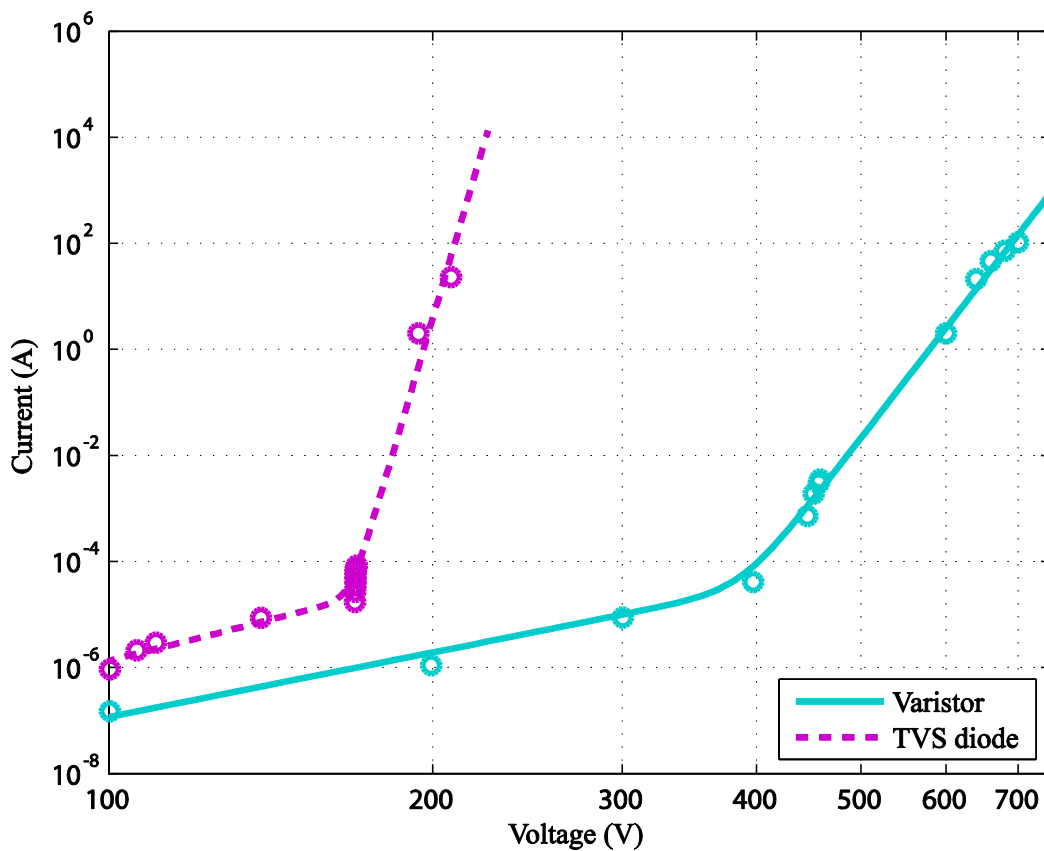


Figure 4-29: Varistor and TVS diode  $I$ - $V$  characteristics drawn on log-log graph for comparison of the degrees of nonlinearity

It can be seen that the “on” model alpha factor is much higher for the TVS diode than that of the varistor. For higher “on” model alpha factors, the voltage-current slope of the curve becomes very steep and approaches an almost constant voltage. High “on” model alphas are desirable for clamping applications that require operation over a wide range of currents [17].

Leakage current can be an area of misconception when comparing a varistor and a TVS diode. For example, we see from Figure 4-29, that the TVS diode leakage current is about 10 times higher at 100 V than the varistor. The leakage current of a TVS diode can be reduced by specifying a higher voltage device [17].



## Chapter 5: Investigation of surge propagation in linear systems

---

As mentioned in the beginning of Chapter 3, significant parts of the overall circuit to be analyzed are linear. In order to perform experimental validations for the investigations of transient propagation, a lightning surge simulator (LSS) will be used as the source of the transient. As seen in Sec. 4.2.2.1, the LSS equivalent circuit is a linear circuit with  $R$ ,  $L$ , and  $C$  elements. In addition, important surge protection devices such as varistors and Transient Voltage Suppressor (TVS) diodes also have linear circuit elements in their mathematical models. As a result, investigation of transient propagation through related linear circuitry would certainly be the way forward here in preparing for the inclusion of the nonlinear devices in Chapter 6 to complete our study.

Among standard methods available for the analysis of transient response in linear circuits, Laplace transforms stands out over other available methods. Investigations here, uses Laplace methods to study surge propagation through the linear circuits of interest to this project. The solutions obtained by the use of Laplace methods for the output responses of the LSS equivalent circuit will be verified with the experimentally obtained waveforms. Numerical simulation will also be used here for validation.

In sections 5.2 and 5.3 numerical simulations are used to study the behaviour of a Metal Oxide Varistor (MOV) driven by the LSS with the help of limited linear models for the MOV. These simulations will be validated using LTspice which is a SPICE (Simulation Program with Integrated Circuit Emphasis) based circuit simulation application.

### 5.1 Analysis of LSS responses using Laplace methods

Let us consider the Noiseken LSS 6110 equivalent circuit shown in Figure 5-1: We will be using this LSS for experimental validation of our investigations throughout this research.

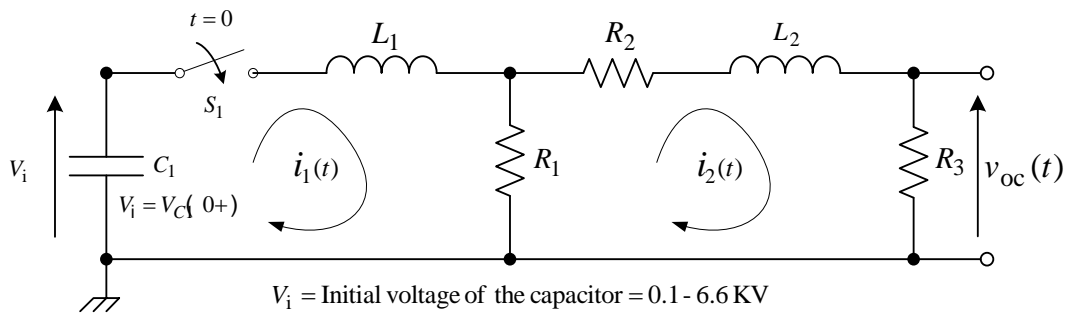


Figure 5-1: The LSS equivalent circuit for finding the 1.2/50  $\mu$ s open-circuit voltage (Noise Laboratory Co., Ltd., Japan)

Here we need to solve for the open-circuit voltage and the short-circuit current. In producing these waveforms the LSS behaves as a combination wave (hybrid) generator. The open-circuit voltage should match the 1.2/50  $\mu$ s waveform and the short-circuit current should match the 8/20  $\mu$ s waveform, both specified by the IEC 61000-4-5 standard.

### 5.1.1 Laplace Solution for 1.2/50 $\mu$ s open-circuit voltage and its validations

The capacitor  $C_1$  of the LSS (Figure 5-1) can be charged to any value from 100 V to 6.6 kV in 100 V steps. When switch  $S_1$ , a Mercury Relay Discharge Switch, is closed, the capacitor  $C_1$  discharges through the wave-shaping circuit to produce the required open-circuit voltage across  $R_3$ . In order to solve this 2-loop LSS circuit for the open-circuit voltage we will assume that the loop currents are  $i_1$  and  $i_2$ . In order to match the given standards, the model parameters given in Table 5-1 are specified by the manufacturer.

Table 5-1: Parameters for the Noiseken LSS-6110

Parameter	Value	Parameter	Value
$C_1$	10 $\mu$ F	$R_1$	7 $\Omega$
$L_1$	2.7 $\mu$ H	$R_2$	1.1 $\Omega$
$L_2$	6 $\mu$ H	$R_3$	1 M $\Omega$

The Laplace transformed network representation of Figure 5-1 is given in Figure 5-2.

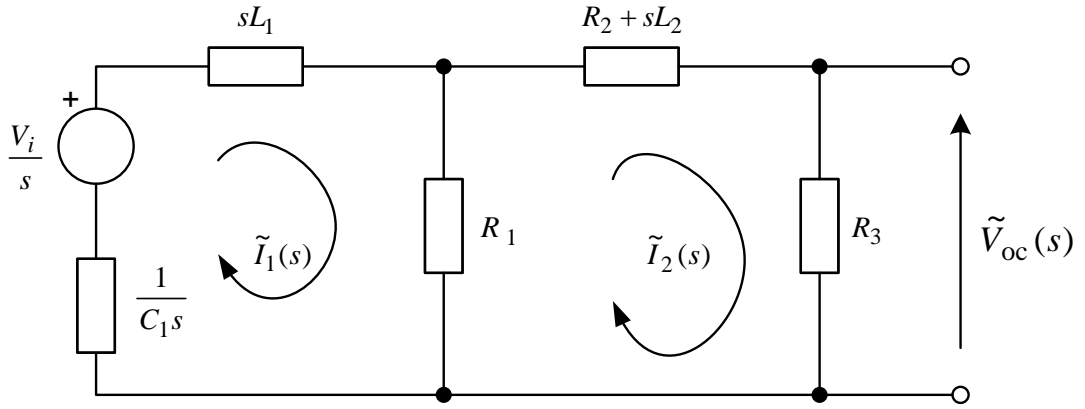


Figure 5-2: Transformed network for the circuit in Figure 5-1

The loop equations for the circuit shown in Figure 5-2 are given by

$$-\frac{V_i}{s} + \left(sL_1 + \frac{1}{sC_1}\right)\tilde{I}_1(s) + R_1[\tilde{I}_1(s) - \tilde{I}_2(s)] = 0 \quad (5-1)$$

$$R_1[\tilde{I}_2(s) - \tilde{I}_1(s)] + (R_2 + R_3 + sL_2)\tilde{I}_2(s) = 0 \quad (5-2)$$

Rearranging Eq. (5-1) and Eq. (5-2),

$$\tilde{I}_1(s) \left[ R_1 + sL_1 + \frac{1}{sC_1} \right] + \tilde{I}_2(s)[-R_1] = \frac{V_i}{s} \quad (5-3)$$

$$\tilde{I}_1(s)[-R_1] + \tilde{I}_2(s)[R_1 + R_2 + R_3 + sL_2] = 0 \quad (5-4)$$

Using Cramer's rule to solve for  $\tilde{I}_2$

$$\tilde{I}_2(s) = \frac{\begin{vmatrix} \left[ R_1 + sL_1 + \frac{1}{sC_1} \right] & \frac{V_i}{s} \\ -R_1 & 0 \end{vmatrix}}{\begin{vmatrix} \left[ R_1 + sL_1 + \frac{1}{sC_1} \right] & -R_1 \\ -R_1 & [R_1 + R_2 + R_3 + sL_2] \end{vmatrix}} \quad (5-5)$$

The fact that the determinant of a matrix  $A$  is denoted by  $|A|$  is used in Eq. (5-5).

Simplifying Eq. (5-5),

$$\tilde{I}_2(s) = \frac{R_1 \left( \frac{V_i}{s} \right)}{\left( R_1 + sL_1 + \frac{1}{sC_1} \right) (R_1 + R_2 + R_3 + sL_2) - R_1^2} \quad (5-6)$$

Further simplifying

$$\tilde{I}_2(s) = \frac{C_1 R_1 V_i}{(sC_1 R_1 + s^2 L_1 C_1 + 1)(R_1 + R_2 + R_3 + sL_2) - sC_1 R_1^2} \quad (5-7)$$

After expanding the denominator and rearranging, if we let

$$a_0 = C_1 R_1 V_i,$$

$$b_3 = L_1 L_2 C_1,$$

$$b_2 = C_1 R_1 L_2 + (R_1 + R_2 + R_3) L_1 C_1,$$

$$b_1 = (R_1 + R_2 + R_3) C_1 R_1 + L_2 - C_1 R_1^2, \text{ and}$$

$$b_0 = R_1 + R_2 + R_3$$

then Eq. (5-7) reduces to

$$I_2(s) = \frac{a_0}{b_3 s^3 + b_2 s^2 + b_1 s + b_0} \quad (5-8)$$

When the MATLAB Symbolic Toolbox command `ilaplace` is used to find the inverse Laplace transform of Eq. (5-8), we get

$$i_2(t) = a_0 \sum_{\alpha=\%1} \frac{e^{\alpha t}}{3b_3 \alpha^2 + 2b_2 \alpha + b_1} \quad (5-9)$$

where `%1` = roots of  $(b_3 s^3 + b_2 s^2 + b_1 s + b_0)$

The LSS output voltage is given by  $v_{oc}(t) = R_3 i_2(t)$ . The code written in MATLAB to find  $v_{oc}$  is given in Appendix C.1. This code also includes data generated by the SPICE simulation, which is used here to validate the Laplace solution. The resulting plots for an initial capacitor voltage of 1 kV are given in Figure 5-3. The SPICE implementation of the circuit in Figure 5-1, used for the validating simulation is given in Appendix C.2.

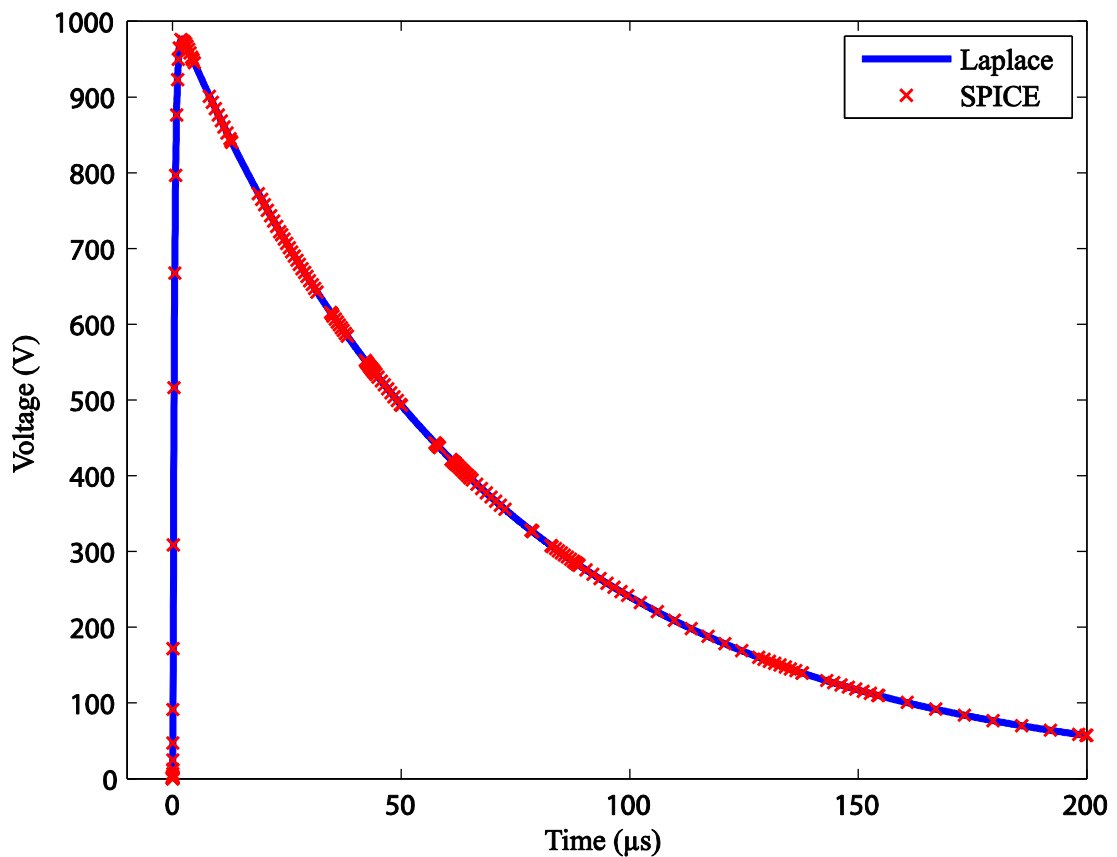


Figure 5-3: Laplace solution for the open-circuit voltage of the LSS validated with a SPICE simulation

We also found that the Laplace solution can be matched very well by numerical simulations using both Euler and RK4 methods.

In addition the Laplace solution of the short-circuit current was validated with the experimental result from the LSS. The Tektronix TPS2024 oscilloscope which was used to display the experimental waveforms captures the data by saving each of its input channels in a *comma-separated values* (CSV) file. All CSV files generated by a single display event can be combined into a single CSV file and this file was imported by MATLAB using the command `csvread` to produce the validation curve. Figure 5-4 shows the results obtained for the Laplace solution and the experimental result and the two curves match well during both rising and decaying parts of the surge.

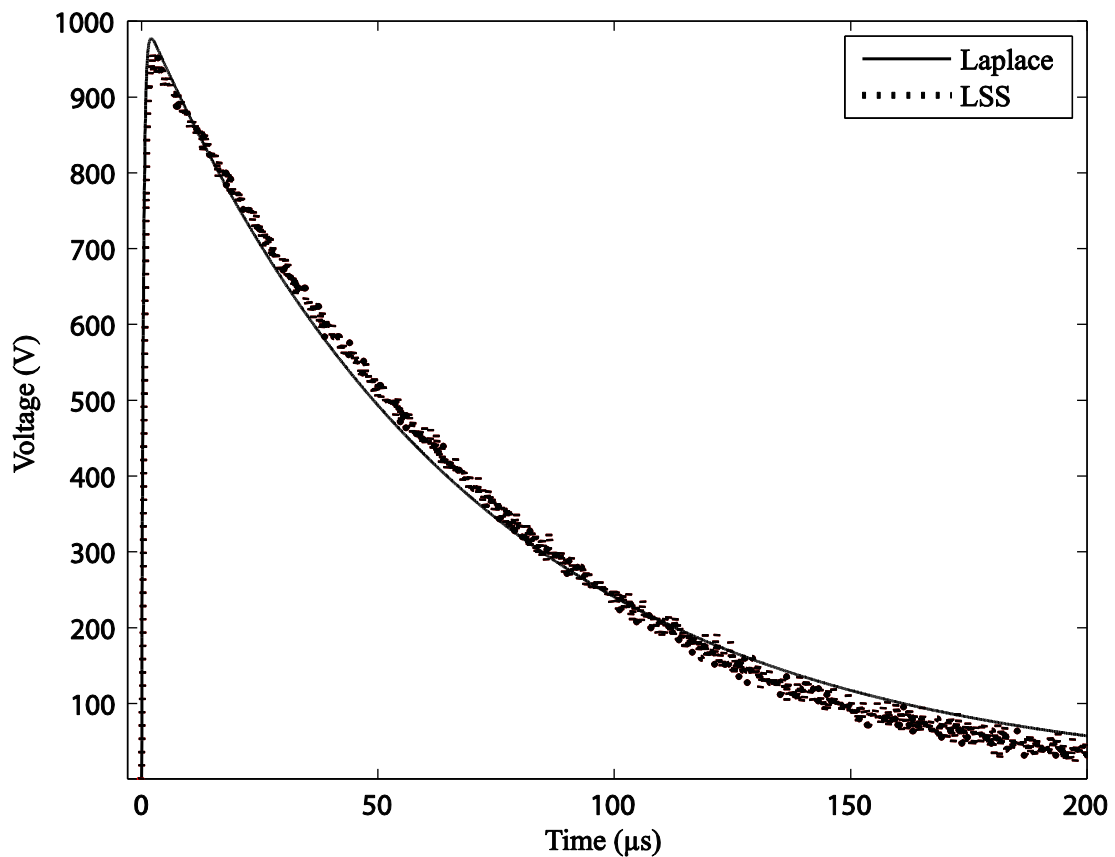


Figure 5-4: Laplace solution for the open-circuit voltage of the LSS validated with the experimental result from the LSS

In studying the above waveform generated by the circuit of Figure 5-1, we found it to be sensitive to the component values  $C_1$ ,  $L_1$  and  $R_1$  in the first loop, provided  $R_3$  was large. The very short rise-time was sensitive to the value of  $L_1$ . In order to understand the decaying part of the open-circuit voltage, we have plotted the curves again in Figure 6-5, but this time with voltage indicated by a log scale. The straight line seen for the decaying voltage suggests that only a single-time-constant circuit is dominant during this period in spite of the circuit having three reactive components. By changing the values of the reactive components it was found that the dominant time constant for the decaying portion is decided by the first loop component values of  $C_1$  and  $R_1$  ( $R_1 C_1$  time constant =  $70 \mu\text{s}$ ).

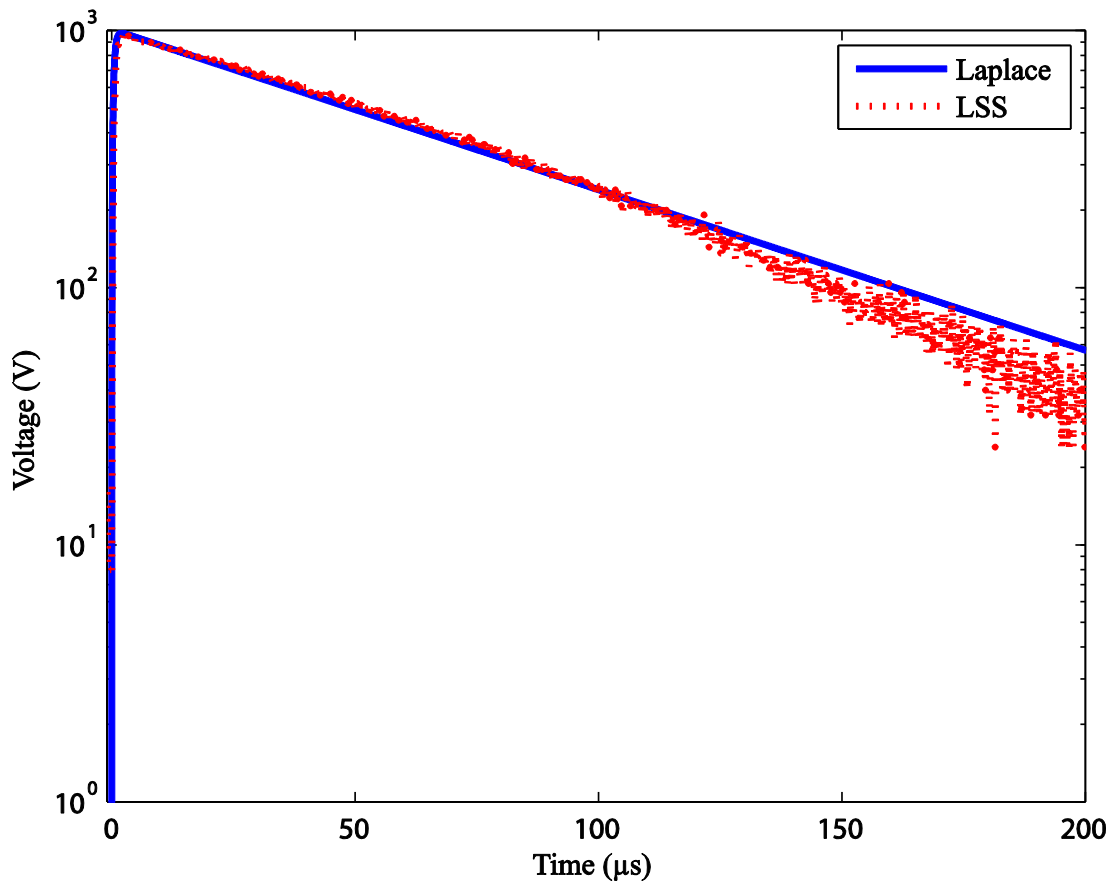


Figure 5-5: Semi-log plots for the curves shown in Figure 5-4

Here we see that the experimental curve deviates from the straight line (Laplace solution) after about 100  $\mu\text{s}$ . It was found that this deviation is not sensitive to any of the components in the LSS equivalent circuit and is thought to be due to some small stray reactive component values coming to play in the coupling circuit of the LSS. Further analysis of this variation was ignored with the expectation that this would not cause any significant changes to our future analysis. Modification of the equivalent circuit in order to eliminate this variation would be a useful exercise in a future research.

### 5.1.2 Comparison of Laplace solutions with numerical simulation

For reasons indicated in Section 3.1, we need to develop robust numerical simulation techniques to investigate transient propagation through nonlinear circuit elements.

For the LSS circuit shown in Figure 5-1 and Figure 5-2, the following network equations can be formulated as a system of coupled first-order equations which govern the dynamic behaviour of the network.

$$\frac{di_1}{dt} = j \quad (5-10)$$

$$\frac{dj}{dt} = -aj - (b - ac)i_1 - adi_2 + \frac{V_{C1}(0+)}{L} \delta(t) \quad (5-11)$$

$$\frac{di_2}{dt} = ci_1 - di_2 \quad (5-12)$$

where  $a = R_1/L_1$ ,  $b = 1/L_1C$ ,  $c = R_1/L_2$ , and  $d = R_1 + R_2 + R_3/L_2$

Again the impulse response that results from the delta function input in Eq. (5-11) can be taken care of by using the initial condition that arises from the impulse input, and making the input itself equal to zero. Hence the initial conditions would be  $i_1(0) = 0$ ,  $j(0) = V_{C1}(0+)/L$ , and  $i_2(0) = 0$ .

State equations (5-10)-(5-12) were included in a MATLAB program to be used by the Euler method and by the more accurate `rk4fixed` and `ode15s` DE solvers discussed in Chapter 3. The MATLAB code `LSS_OCV_Euler_RK4.m` used to simulate the open-circuit voltage is made available in Appendix C.3. Once the values of  $i_2$  is obtained open-circuit voltage can be determined by finding the voltage drop across the resistor  $R_3$ . A comparison of the RK4 based simulation with the Laplace solution of the open-circuit voltage is given in Figure 5-6(a).

The MATLAB based simulations were run on a Windows XP based Dell PC which had 3 GB of RAM. For the simulation of the extremely fast rising open-circuit voltage, `rk4fixed` simulation took as much as 17 minutes to simulate a 100  $\mu$ s waveform. The simpler less accurate Euler method carried out the same task in 20 seconds. Both methods worked satisfactorily for a step size ( $\Delta t$ ) of 10 ps. The variable step MATLAB ODE solver `ode15s` which is suitable to handle “stiff” problems produced satisfactory results in 30 seconds.

The LSS short-circuit current was also simulated using `rk4fixed` solver. When we short-circuit the output of the LSS in order to determine the short-circuit current we will be short circuiting the resistor  $R_3$ . Hence we could find  $i_2$  provided we substitute  $R_3 = 0$  at the beginning of all calculations. The same MATLAB code can be used simply by setting the value of  $R_3$  to zero. The simulation worked

satisfactorily with step sizes ranging from 100 ns to 10 ps. A comparison of the rk4fixed based simulation with the Laplace solution of the short-circuit current is given in Figure 5-6(b).

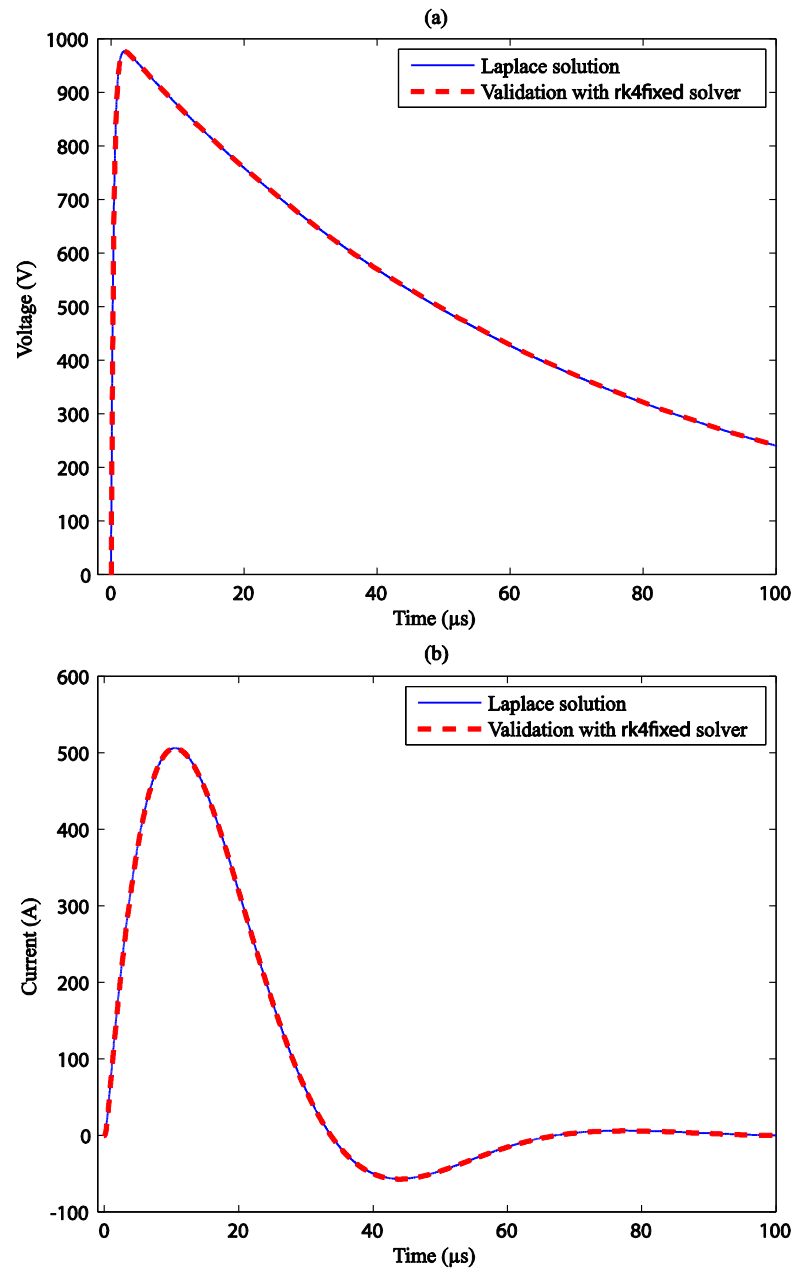


Figure 5-6: rk4fixed solver based validations of Laplace solutions with  $\Delta t=10$  ps (a) LSS open-circuit voltage (b) short-circuit current

### 5.1.3 Laplace solution for 8/20 $\mu\text{s}$ short-circuit current validated with experimental data from the LSS

Here we will validate the Laplace solution for the short-circuit current of the LSS with the experimental result from the LSS. The resulting short-circuit current for an initial capacitor voltage of 1 kV is shown in Figure 5-7(a) along with its validation obtained experimentally from the LSS.

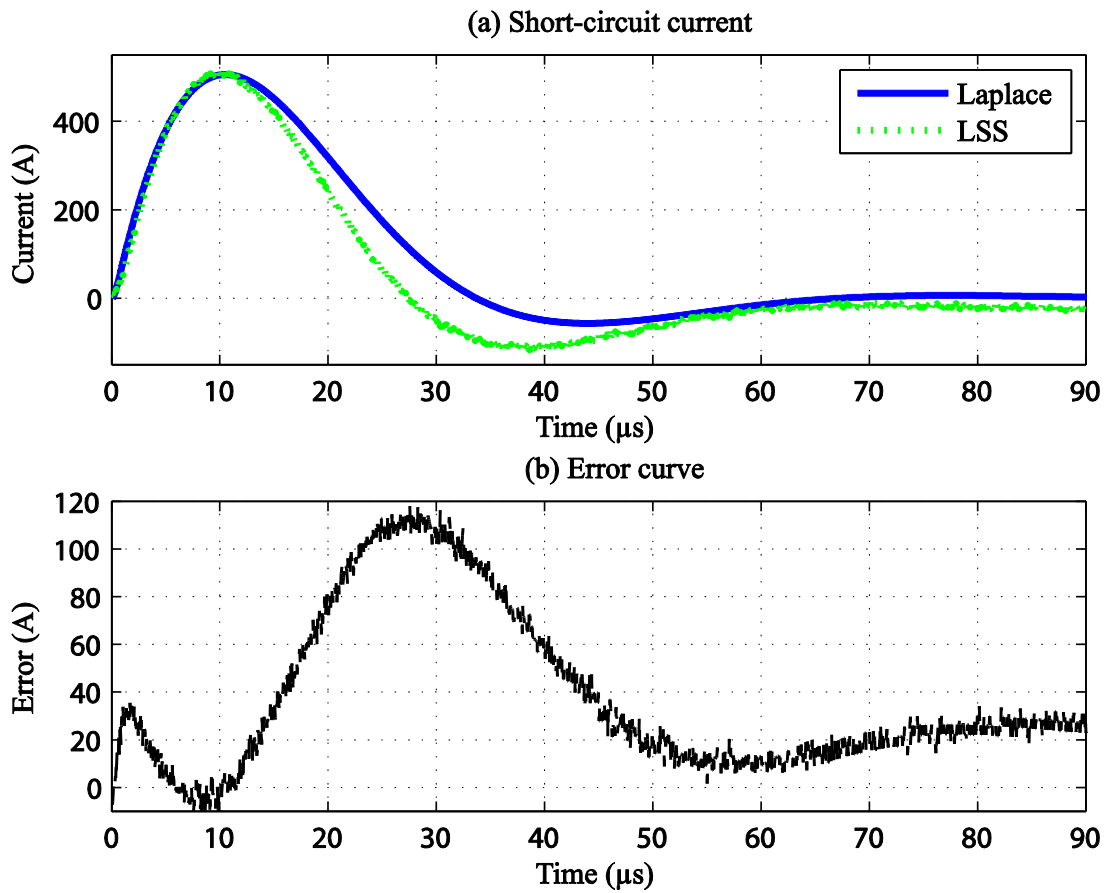


Figure 5-7: (a) Laplace solution for the short-circuit current of the LSS validated with the experimental result from the LSS. (b) Error between the Laplace solution and its validation.

Figure 5-7(b) shows the absolute error between the Laplace solution and the experimental validation. We found the area of maximum error to be sensitive in particular to the values of  $C_1$  and  $R_1$  and the short-circuit current curves of Figure 5-8 was obtained with the changed values of  $C_1 = 9.0 \mu\text{F}$  and  $L_1 = 2.0 \mu\text{H}$ . We see that the maximum error value has been reduced by about 40% in this case.

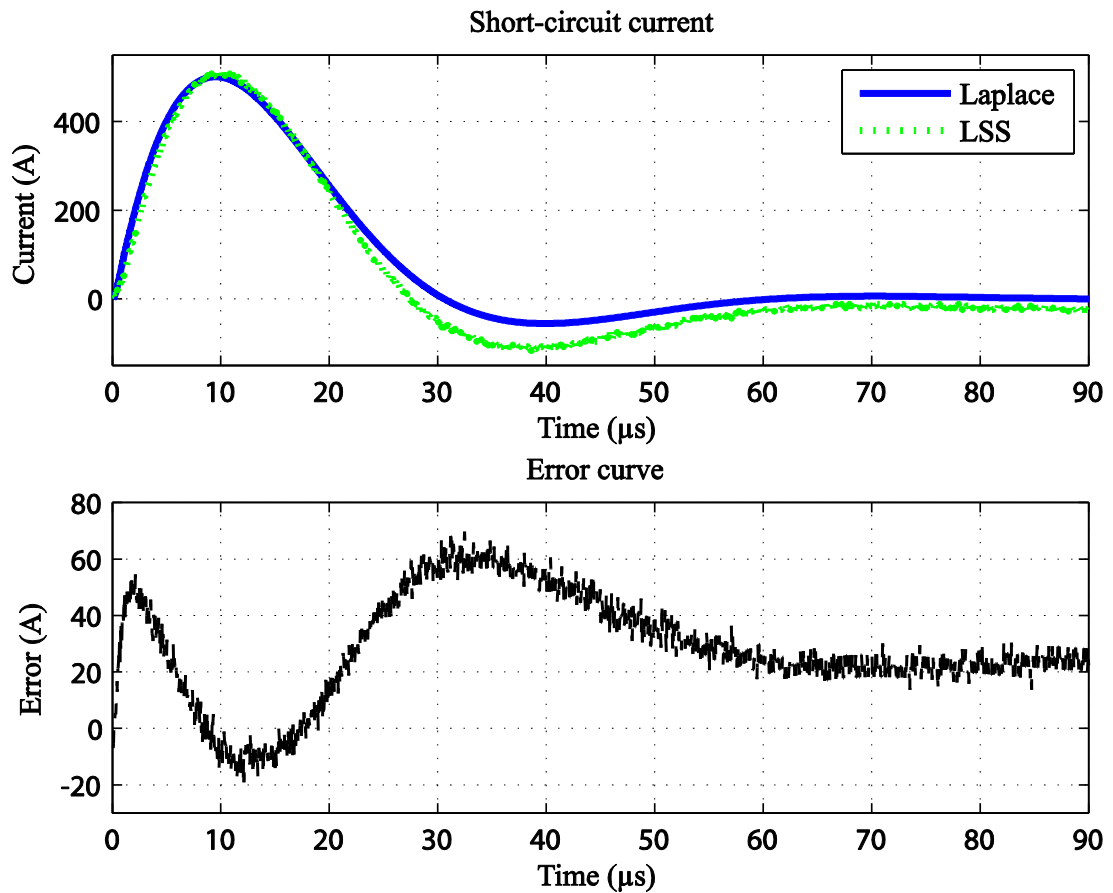


Figure 5-8: (a) Laplace solution and its validation of Figure 5-7(a) changed for better comparison by minor changes to LSS circuit values. (b) Maximum error has reduced by about 40% compared to Figure 5-7(b).

## 5.2 Investigation of surge propagation through an MOV in the off state

One of the goals in this project is to investigate surge propagation through a 2-wire version of a category B protection unit similar to the one shown in Figure 4-1. Such a unit will have larger protection devices to handle the larger transients anticipated for category B. At the front end of this circuit is an MOV to provide the first level of protection [5]. We have already seen in Chapter 4 that an MOV in the “off” state can be modelled by a purely linear circuit.

In order to build the complete equivalent circuit for this investigation we need to consider the MOV equivalent circuit for its leakage region which was presented in Figure 4-7(a) as well as the equivalent circuit of the Noiseken LSS impulse generator given in Figure 4-7(b). The combined circuit shown in Figure 5-9 disregards  $R_{\text{OFF}}$  of the MOV as it approaches  $10^9 \Omega$  in the leakage region.

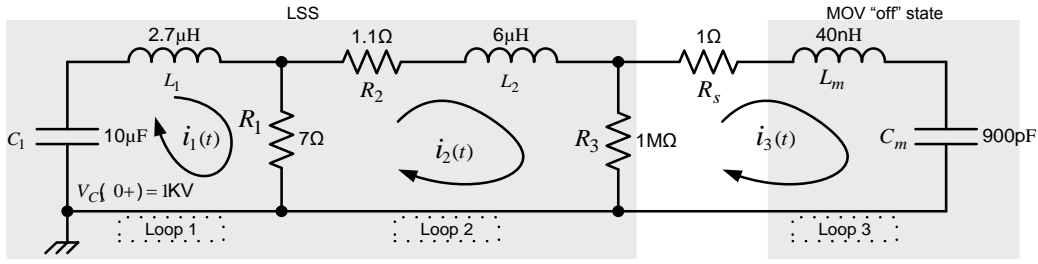


Figure 5-9: MOV “off” state driven by the LSS (Combined equivalent circuit)

In order to analyze  $i_3$ , the current through the MOV in its “off” state, we consider the loop currents of Figure 5-9. The state equations for the above circuit can be formulated as below by using five state variables: three currents and the time derivatives of the currents  $i_1$  and  $i_3$ , which are  $j_1$  and  $j_3$  respectively. A complete working to arrive at Eqs. (5-13) - (5-17) is shown in Appendix C.4.

$$\frac{di_1}{dt} = j_1 \quad (5-13)$$

$$\frac{dj_1}{dt} = -aj_1 - (b - ac)i_1 - adi_2 + aei_3 + \frac{V_{C1}(0+)}{L_1} \quad (5-14)$$

$$\frac{di_2}{dt} = ci_1 - di_2 + ei_3 \quad (5-15)$$

$$\frac{di_3}{dt} = j_3 \quad (5-16)$$

$$\frac{dj_3}{dt} = -fj_3 + cgi_1 - gdi_2 + (eg - h)i_3 \quad (5-17)$$

where  $a = R_1/L_1$ ,  $b = 1/L_1C_1$ ,  $c = R_1/L_2$ ,  $d = R_1 + R_2 + R_3/L_2$ ,  $e = R_3/L_2$ ,  $f = (R_3 + R_S)/L_m$ ,  $g = R_3/L_m$ , and  $h = 1/L_mC_m$ .

The initial conditions for solving the above circuit are.  $i_1(0) = 0$ ,  $j_1(0) = V_{C1}(0+)/L$ ,  $i_2(0) = i_3(0) = j_3(0) = 0$ , where  $V_{C1}(0+)$  is the initial voltage on the capacitor  $C_1$ .

The simulation plot for  $i_3$ , the MOV current in the “off” state is shown in Figure 5-10(a). It shows a high frequency oscillation at the start which decays rapidly. This simulation, for the component values shown in Figure 5-9, presented

a “stiff” problem to the MATLAB’s standard ODE solver `ode45`, as the above state equations represent several processes of which one has a very small time constant. When `ode45` is used the MATLAB application goes into a busy mode and fails to produce the required results within reasonable time. The difficulty was overcome by using `ode15s`, which is a stiff ODE solver provided by MATLAB. When `ode15s` is used, the Dell desktop PC mentioned earlier completes the simulation within 1s. The code used `LSS_MOV_three_loops_ode15s.m` is given in Appendix C.5.

As mentioned in Section 4.2.2.1 the ringing is due to the MOV capacitance resonating with the MOV lead inductance and the inductance  $L_2$  of the LSS equivalent circuit. A quantitative analysis tells us that most of this current flows through the external current-measuring resistance  $R_S$  and the LSS resistances  $R_1$  and  $R_2$ ; hence these resistances are primarily responsible for the decay in the resonance of the MOV current.

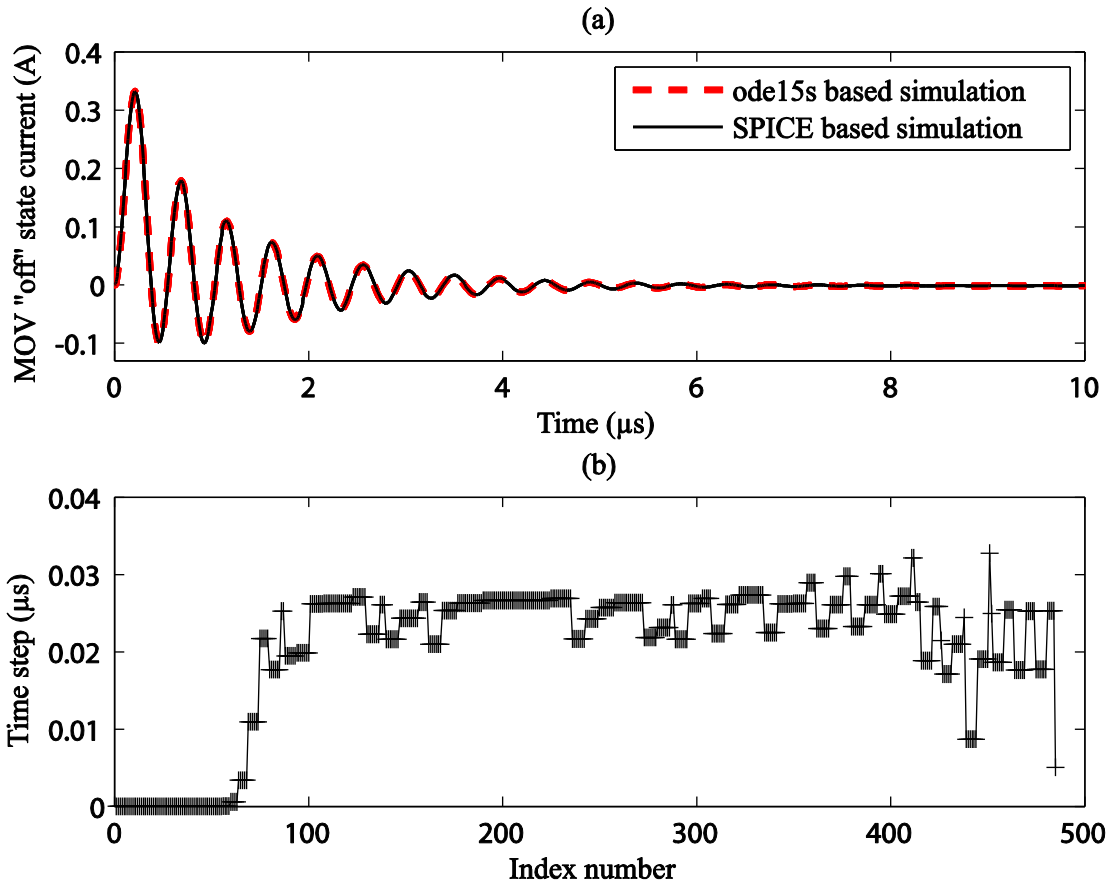


Figure 5-10: (a) Numerical simulation of the “off” state current in a MOV validated with a SPICE based simulation; (b) variation in the time step during the simulation;  $V_{C1}(0+) = 100\text{ V}$

### 5.3 Investigation of surge propagation in assumed fixed states of the MOV

In Section 4.2.2, we closely looked at the two main regions of operation of an MOV- viz. the leakage region and the normal operation region. Here we will study the propagation of a surge through an MOV assuming that it operates at a fixed point in its performance characteristic. Although it is unlikely to operate in such a situation, it would help us understand the behaviour of an MOV under stress using a linear model. The three operating points that we consider are shown in the  $I$ - $V$  characteristic of Figure 5-11 which we developed for the varistor 275L40C in Section 4.2.5. They correspond to points in the *leakage region* ( $34\text{ M}\Omega$ ), the *knee* ( $300\ \Omega$ ) and the *normal operation region* ( $7\ \Omega$ ) of the characteristic. Since the MOV’s nonlinear resistance is represented by a fixed resistance  $R_m$  at each of these points, the overall circuit analysed, shown in Figure 5-12, remains a linear circuit at each one of these operating points.

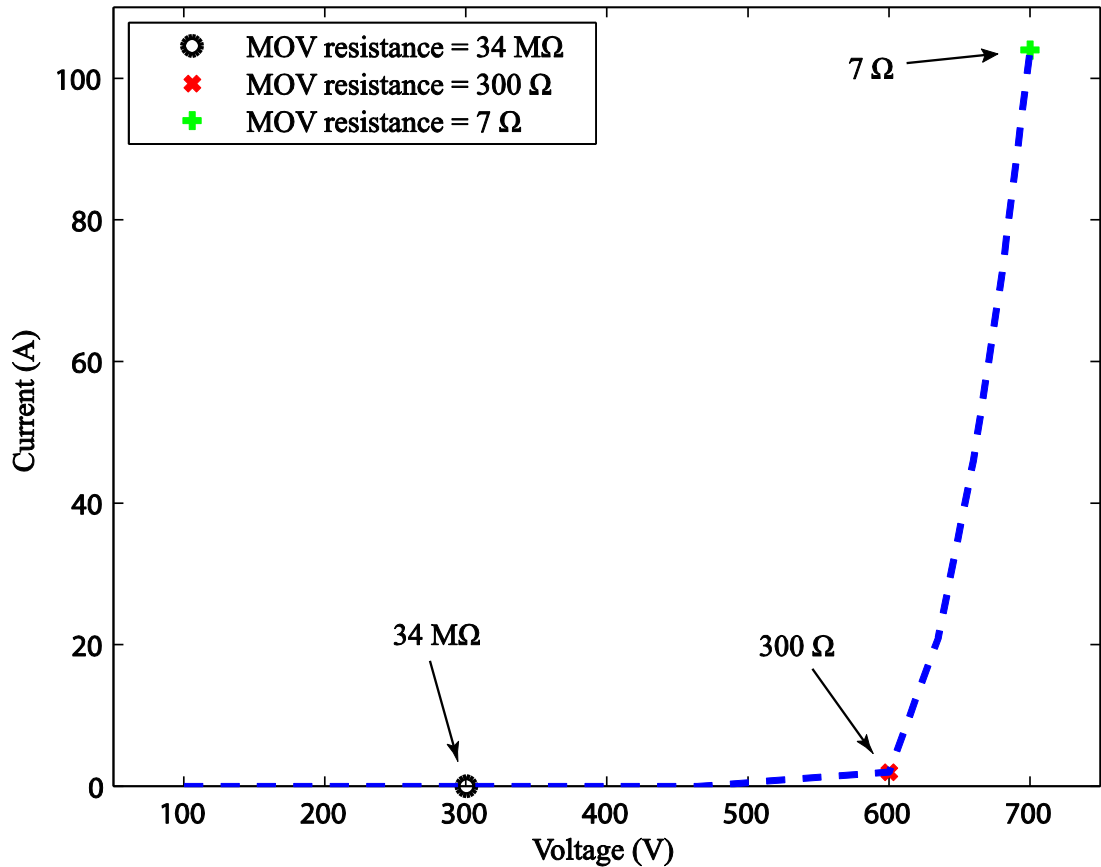


Figure 5-11: The  $I$ - $V$  characteristic for the 275L40C varistor with a selection of operating points.

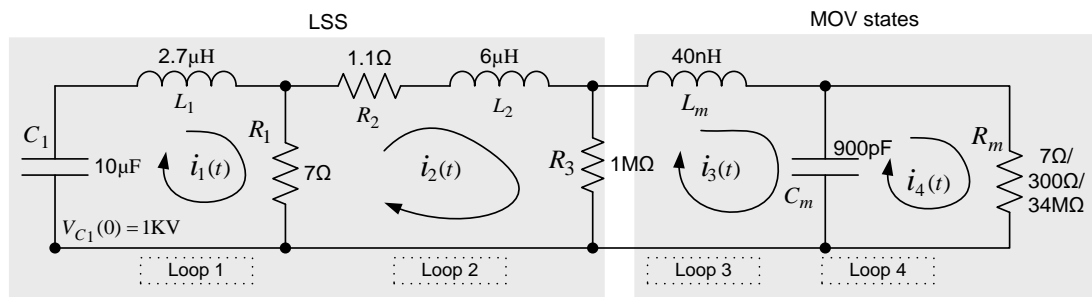


Figure 5-12: Fixed MOV states driven by transients from the LSS

In order to numerically simulate the above circuit and to study the current through the fixed states of the MOV, we have considered the four loop currents as shown in Figure 5-12. The state equations for the above circuit which are given below use six state variables; two of the loop equations being second-order DEs, were converted to normal form (a system with two interacting first-order DEs). The four loop currents and the time derivatives of the currents  $i_1$  and  $i_3$  are the state variables. The complete derivation of the state equations Eqs. (5-18) - (5-23) is included in Appendix C-6.

$$\frac{di_1}{dt} = j_1 \quad (5-18)$$

$$\frac{dj_1}{dt} = -aj_1 - (b - ac)i_1 - adi_2 + aei_3 + \frac{V_{c1}(0+)}{L_1} \cdot \delta(t) \quad (5-19)$$

$$\frac{di_2}{dt} = ci_1 - di_2 + ei_3 \quad (5-20)$$

$$\frac{di_3}{dt} = j_3 \quad (5-21)$$

$$\frac{dj_3}{dt} = -fj_3 + cgi_1 - gdi_2 + (eg - h)i_3 + hi_4 \quad (5-22)$$

$$\frac{di_4}{dt} = ki_3 - ki_4 \quad (5-23)$$

where  $a = R_1/L_1$ ,  $b = 1/L_1C$ ,  $c = R_1/L_2$ ,  $d = R_1 + R_2 + R_3/L_2$ ,  $e = R_3/L_2$ ,  $f = g = R_3/L_m$ ,  $h = 1/L_mC_m$ , and  $k = 1/C_mR_m$ .

The initial conditions for the simulation are  $i_1(0) = 0$ ,  $j_1(0) = V_{c1}(0+)/L$ ,  $i_2(0) = i_3(0) = j_3(0) = i_4(0) = 0$ , where  $V_{c1}(0+)$  is the initial voltage of the LSS capacitor or the amplitude of the surge voltage generated by the LSS.

In general ODE solvers have to solve the set of differential equations governing the problem for each time step during the simulation. As per our discussion in section 3.4.2, if the Jacobian matrix of the differential equations is not provided the efficiency and the accuracy of the simulation suffers. For the three cases studied, the accuracy of the simulations were restricted to the first 7 to 36  $\mu$ s, since the ODE solver had to calculate the Jacobian matrix of the differential equations, for each iteration of the simulation. When the Jacobian matrix was provided, long duration simulations were possible. A complete listing of the code used to simulate the  $R_m = 7 \Omega$  instance, `LSS_MOV_four_loops_Rm_7ohms.m` is given in Appendix C.7.

Figure 5-13 shows the simulations for the three cases mentioned. The simulation result for the leakage region ( $R_m = 34 \text{ M}\Omega$ ) is familiar to us from the

discussion in Section 4.2.2.1. The ringing is due to a resonating effect of  $L_2$ ,  $L_m$  and  $C_m$ , and it dies down due the resonating current flowing through  $R_1$  and  $R_2$ .

At the knee of the I-V characteristic ( $R_m = 300 \Omega$ ), significant current flows through the lowered MOV resistance: smaller ringing current flows for a shorter period of time. Figure 5-13(c) shows the simulation for the point ( $R_m = 7 \Omega$ ) which well into the normal operation region of the *I-V* curve of the MOV. No ringing is seen in this case. This tells us that the role played by the lead inductance and the capacitance of the MOV is negligible when the device is operating in its normal region of operation. Hence we will be able to omit one or both of these components from the MOV equivalent circuit during our investigations of surge propagation in Chapter 6.

All numerically simulated plots of Figure 5-13 were validated with SPICE based simulations using LTspice. It can be observed that the numerical simulations match very well with the validations.

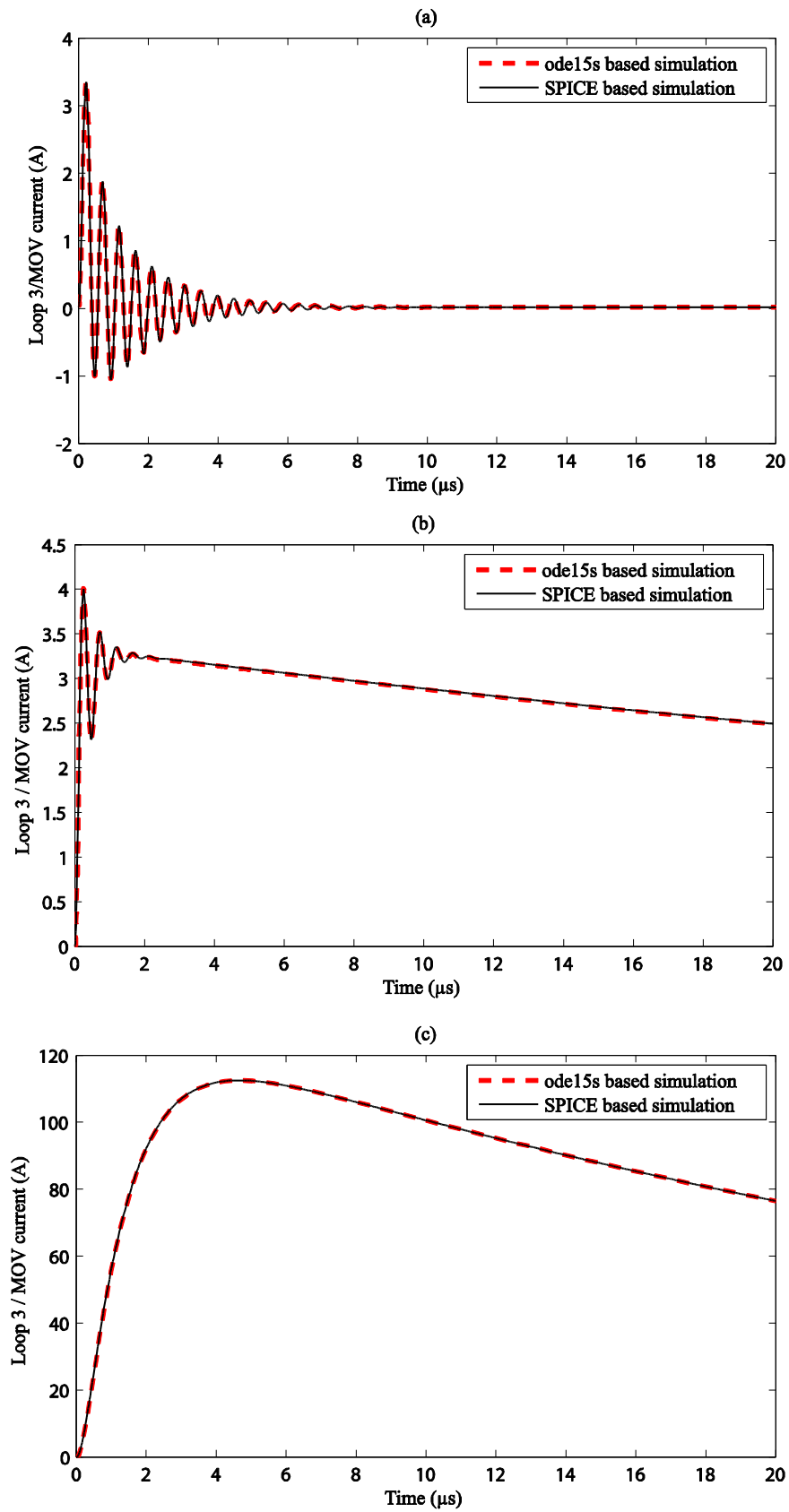


Figure 5-13: Numerical simulation of assumed fixed states of the MOV validated with SPICE based simulations (a)  $R_m = 34 \text{ M}\Omega$  (b)  $R_m = 300 \Omega$  (c)  $R_m = 7 \Omega$

## 5.4 Chapter summary

This chapter has investigated transient propagation through several purely linear circuits which are closely related to the nonlinear surge protection circuit that we intend investigating in this research. We started these investigations by analysing the LSS output waveforms using Laplace transforms and validating them using experimental data as well as numerical and SPICE simulations. Although the Laplace method is very useful in providing accurate results for these linear circuits we will not pursue with this method due to its limitations in handling circuits containing nonlinear device models such as a power-law based model of an MOV.

The numerical simulations that we used in this chapter, as the primary method as well as for validation purposes has helped us in a number of ways and will simplify our effort in our investigations of nonlinear circuits presented in Chapter 6.

Following points highlight the ways in which we were able to use alternative tools available in MATLAB or improve the MATLAB coding of our circuits for fast and accurate simulations.

- With the use of the MATLAB ODE solvers `ode15s` and `ode23t`, we were able to simulate circuits such as the one given in Section 5.2, where an off state model of an MOV was driven by the LSS. Due to the “stiff” nature of the problem the standard Matlab ODE solver `ode45` could not handle this problem.
- By supplying the Jacobian matrix to the MATLAB ODE solver we were able to simulate the circuit given in Section 5.3, where a given fixed state of the MOV was driven by the LSS. When the Jacobian was not included in the coding, only short duration simulations were possible.

With these improvements to our MATLAB based numerical simulations we are confident to move on to Chapter 6, where we will study the surge propagation through nonlinear surge protection circuitry. In this chapter we also saw the successful use of a SPICE simulator for simulating linear electric circuits. These SPICE simulations were useful in validating our numerical simulations. While

continuing our numerical simulations to study the behaviour of nonlinear protection circuitry to the occurrence of transients, we will also make an effort to study these circuits or similar alternate circuits using available SPICE models from the surge protection device manufacturers such as *Littelfuse*.

## Chapter 6: Investigation of surge propagation through a TVSS system

---

### 6.1 Introduction

In Chapter 4 we developed suitable mathematical models for the metal oxide varistor (MOV) and the transient voltage suppression (TVS) diode. The developed MOV model was validated successfully by using a variable DC source. The required numerical simulation techniques were tested on related linear circuits in Chapter 5 and the results were validated using SPICE simulations. These tested numerical simulation techniques will be made use of in this chapter to study the surge propagation through a class A/B protection unit with two different nonlinear surge protection components. The study will be limited to class B operation.

In Chapter 2, we looked at both category A and category B protection units, which are essentially Surge Protection Devices (SPDs) or Transient Voltage Suppressor Systems (TVSSs). They usually make up the front-end of modern power supplies. As discussed in Chapter 2, four different types of nonlinear devices are used in these circuits: Gas discharge tubes (GDTs), and three different types of solid-state devices: Metal oxide varistors (MOVs), Transient voltage suppression (TVS) diodes and TVS thyristors. The mathematical models developed for the MOV and the TVS diode will be valuable for developing the simulations that are to be performed in this chapter, as these components make up the 2-level protection in a class A/B protection unit.

The complete TVSS circuit that we will be investigating here was shown in Figure 4-1 and the same is presented here as Figure 6-1 for convenience. This circuit uses an MOV for the first level of protection and a TVS diode for the second level of protection. In order to investigate the propagation of a lightning surge through this circuit, it will be driven by the lightning surge simulator (LSS) Noiseken LSS 6110, whose equivalent circuit was presented and examined in Section 5.1. The MOV, the line filter and the TVS diode will be added in steps to make up the whole class B

protection unit during our surge propagation investigations. The resulting circuit at each step will be numerically simulated and validated, highlighting the power dissipation and energy absorption of each component. We will start our study in the next section by connecting an MOV, which usually provide the first level of protection in a class A/B protector.

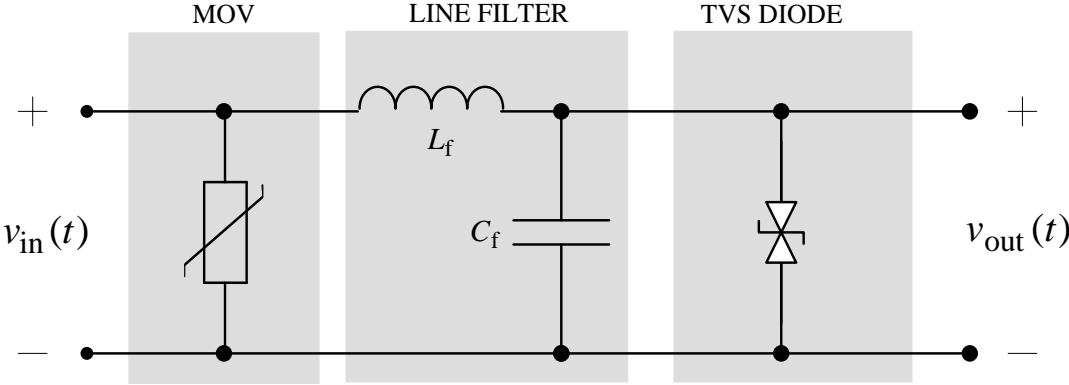


Figure 6-1: A 2-wire Category B protection unit with two levels of protection

**6.2 Investigation of surge propagation through an MOV (1<sup>st</sup> stage of the TVSS)**

The circuit under test in this case, shown in Figure 6-2 is simply a stand-alone MOV connected to the lightning surge simulator (LSS) output through a very low valued resistor; the resistor  $R_s$  is required to calculate the current through the MOV.

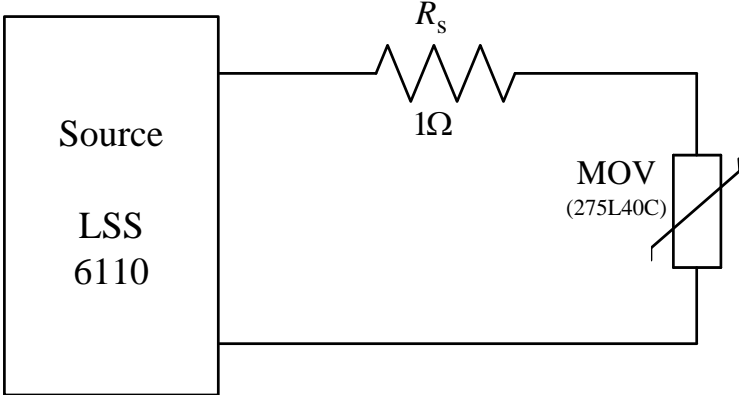


Figure 6-2: LSS driving the first stage of a category B protection unit

### 6.2.1 Simulation using the power-law model of an MOV

In order to develop the set of differential equations required to numerically simulate the above circuit we need to consider the equivalent circuit. Replacing the LSS and the MOV with their equivalent circuits gives us the overall circuit shown in Figure 6-3.

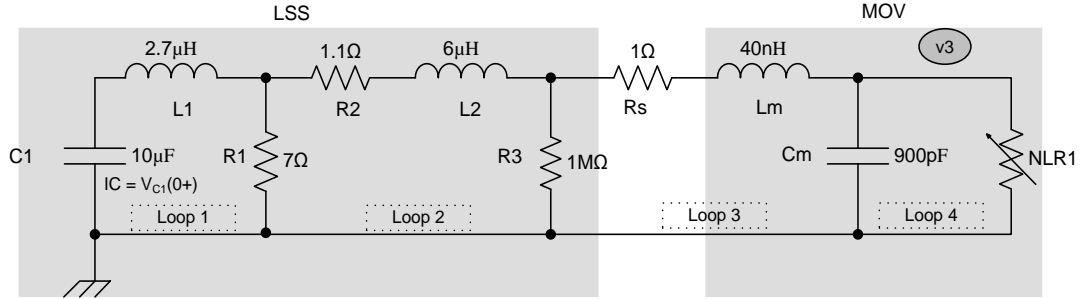


Figure 6-3: Overall equivalent circuit for the set up shown in Figure 6-2

We will consider four loop currents  $i_1, i_2, i_3$  and  $i_4$  for the loops shown in Figure 6-3. In addition we will have to consider the nodal voltage  $v_3$  across the nonlinear resistance  $NLR_1$ , as we will be using the following mathematical model for the MOV's nonlinear resistance, which was developed in Chapter 5.

$$i_4 = K_1 v_3^{\alpha_1} + K_2 v_3^{\alpha_2} \quad (6-1)$$

The set of state equations formulated for the above circuit is given next. The loop currents  $i_1, i_2$ , and  $i_3$ , the nodal voltage  $v_3$  and the derivatives of the loop currents  $i_1$  and  $i_3$  were selected to be the state variables. The complete derivation of the state equations Eqs. (6-2) - (6-7) is included in Appendix D-1.

$$\frac{di_1}{dt} = j_1 \quad (6-2)$$

$$\frac{dj_1}{dt} = (-a)j_1 - (b - ac)i_1 - (ad)i_2 + (ae)i_3 \quad (6-3)$$

$$\frac{di_2}{dt} = (c)i_1 - (d)i_2 + (e)i_3 \quad (6-4)$$

$$\frac{di_3}{dt} = j_3 \quad (6-5)$$

$$\frac{dj_3}{dt} = -(f)j_3 + (cg)i_1 - (dg)i_2 + (eg - h)i_3 + h(k_1v_3^{\alpha_1} + k_2v_3^{\alpha_2}) \quad (6-6)$$

$$\frac{dv_3}{dt} = k(i_3 - k_1v_3^{\alpha_1} - k_2v_3^{\alpha_2}) \quad (6-7)$$

where  $a = R_1/L_1$ ,  $b = 1/L_1C$ ,  $c = R_1/L_2$ ,  $d = (R_1 + R_2 + R_3)/L_2$ ,  $e = R_3/L_2$ ,  $f = (R_3 + R_S)/L_m$ ,  $g = R_3/L_m$ ,  $h = 1/L_mC_m$ , and  $k = 1/C_m$ .

The initial conditions for the simulation are  $i_1(0) = 0$ ,  $j_1(0) = V_c(0)/L$ ,  $i_2(0) = i_3(0) = j_3(0) = v_3(0) = 0$ . As before, the value given for  $j_1(0)$  results due to the initial voltage  $V_{C1}(0)$  of the capacitor  $C_1$ . A complete listing of the code used for the simulation `LSS_MOV_with_nonlinearR.m` is given in Appendix D.2. The values of  $K_1 = 9.3231 \times 10^{-16}$ ,  $\alpha_1 = 4.0413$ ,  $K_2 = 3.5040 \times 10^{-73}$  and  $\alpha_2 = 26.2396$  for the model of the *nonlinear resistance of the MOV* were obtained from Section 4.2.6 where a 274L40C MOV was considered.

In order to study the propagation of the surge through the MOV, we have presented the simulated current through the MOV along with the voltage across the device in Figure 6-4(a). We see that the simulations compare well with the validations with respect to both shape and magnitude in spite of the simulation current peaking slightly before the validation current. In Figure 6-4(b) and (c) we have shown the power variation and energy absorption of the MOV during the period of surge propagation. Simulation of the energy absorption in particular is very important as it would be able to predict the incipient failure of the device once the specified threshold is exceeded. Again we see that the curves compare well although we see a difference of 13% in Figure 6-4(c) between the simulation and the validation of the total energy absorbed by the MOV. It was also noted that making the term  $K_1v_3^{\alpha_1} = 0$  did not have any impact on the curves of Figure 6-4. This is not surprising as this term is responsible only for modelling of effects in the leakage region of the MOV. Ignoring this term in the model is justified, since the primary

goal of this project is to estimate the total energy absorption of each component of the protector unit, during the propagation of high-voltage transients such as lightning.

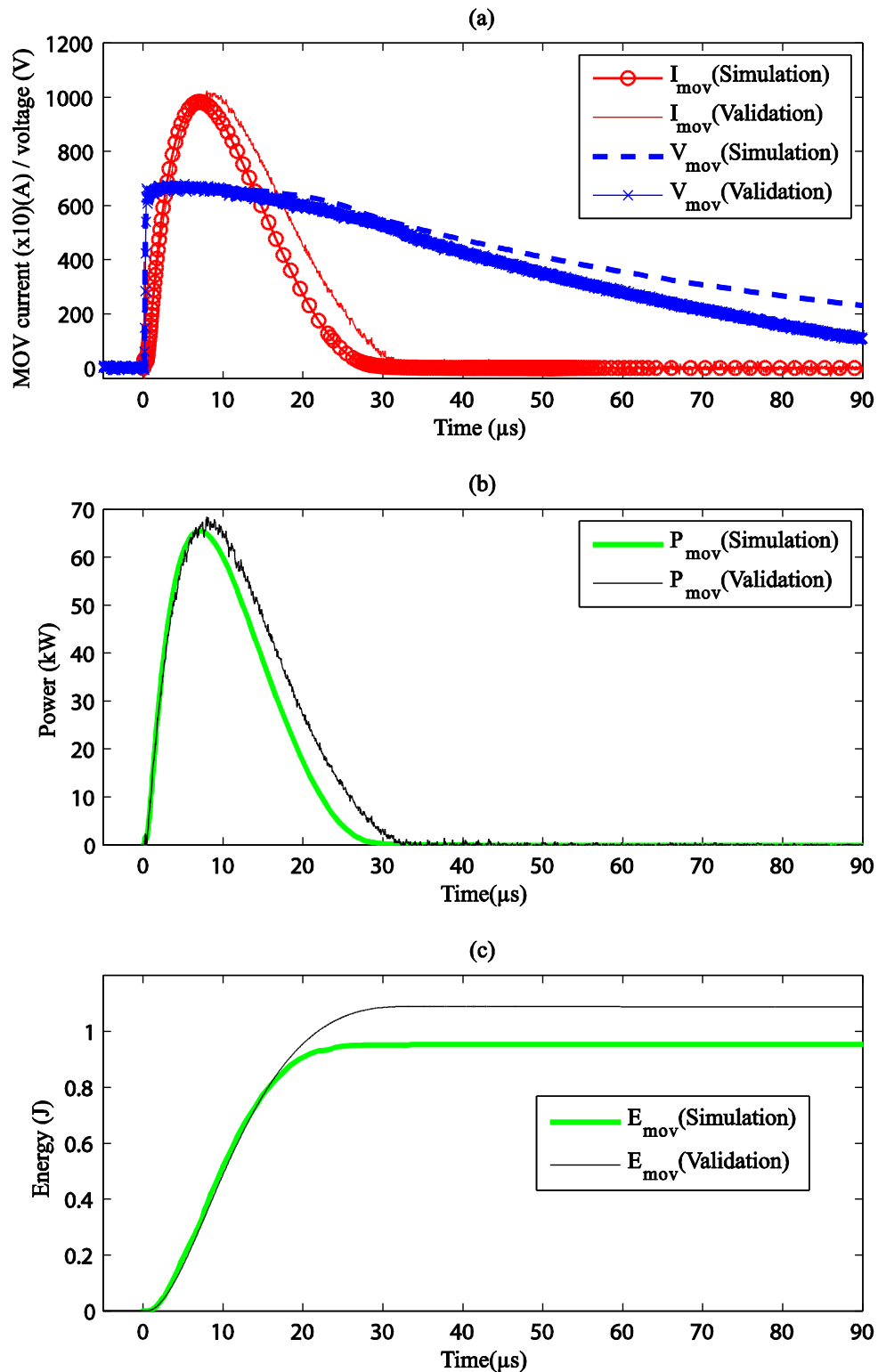


Figure 6-4: Numerical simulation and validations for the first stage (MOV) of a TVSS (a) MOV current and voltage (b) Power variation for the MOV (c) Energy absorption in the MOV

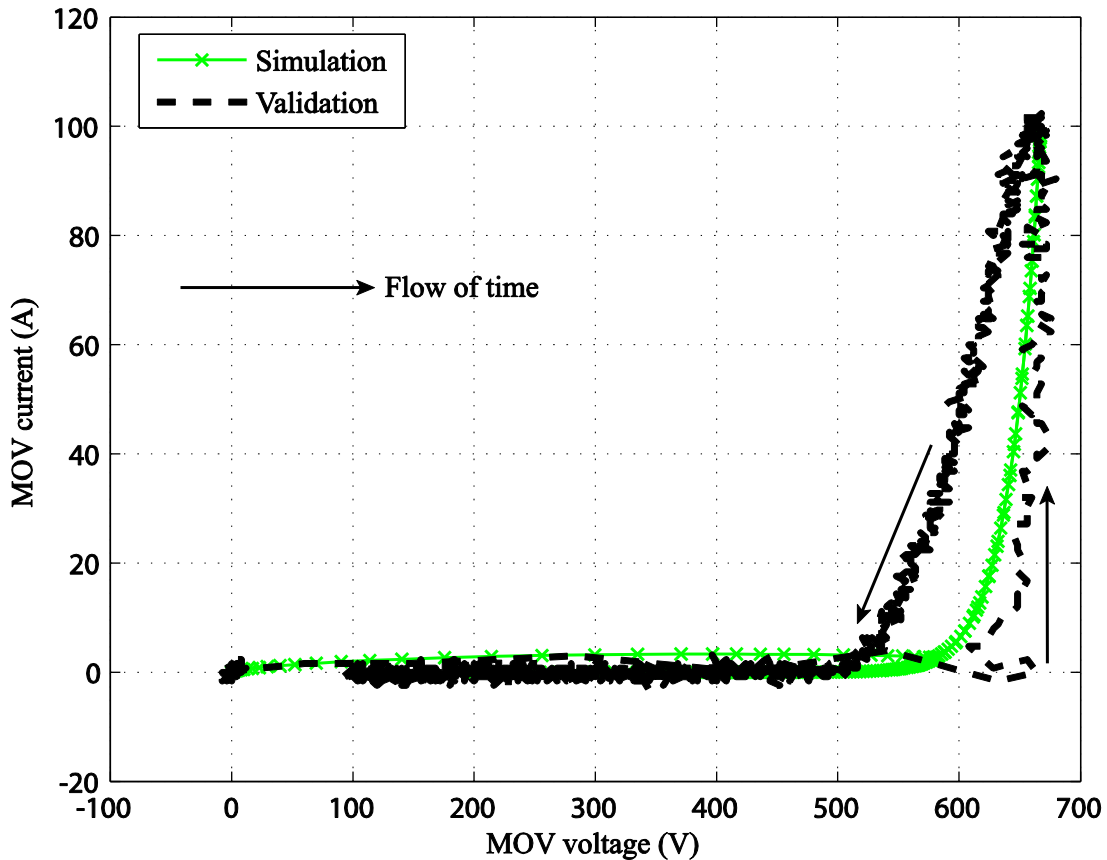


Figure 6-5: The phase plot (MOV current vs. MOV voltage) for the simulation and validation plots shown in Figure 6-4(a)

In order to understand the discrepancies between the simulations and the validations we will now look at the phase plots (MOV Current vs. MOV Voltage) for the simulation and validation curves of Figure 6-4(a). These are presented in Figure 6-5 and it can be seen that the current decrease in the validation curve follows a different more gradual path than the current increase path as per our discussion in Section 4.2.2.2. This phenomenon gives rise to a hysteresis loop in the phase plot of a varistor. The power-law model that we have adopted for the nonlinear resistance of the MOV does not take into account the hysteresis effects and hence, as anticipated, the phase plot for the simulation curve has the same upward and downward paths for the current within the hysteresis loop of the experimental plot. In spite of this discrepancy in the phase plots, we were able to reduce the error in the total energy absorption to 9% by slightly varying the parameters values of  $K_2$  and  $\alpha_2$  to  $K_2 = 2.4496 \times 10^{-50.15}$  and  $\alpha_2 = 18.3338$ . Figure 6-5 and Figure 6-6 highlight this improvement to the simulation. The simulation phase plot is now well centred within the hysteresis loop of the validating phase plot.

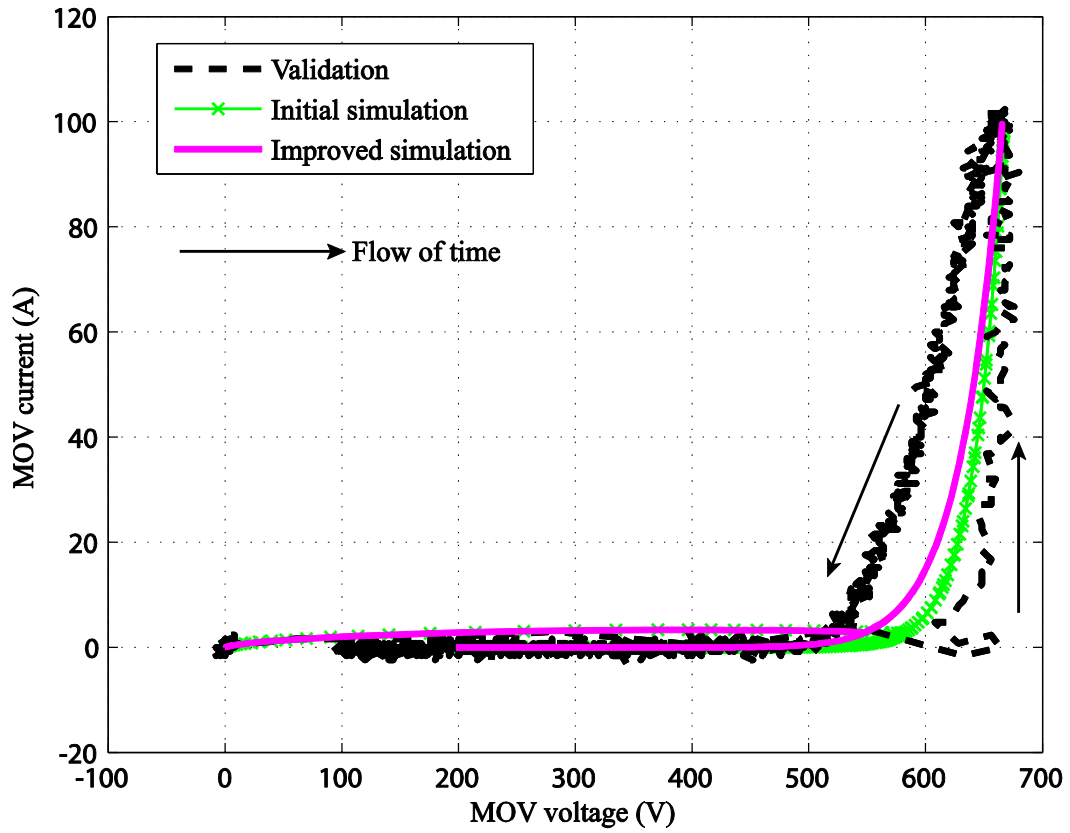


Figure 6-6: The phase plot of the improved simulation compared with initial simulation and validation plots shown earlier in Figure 6-5.

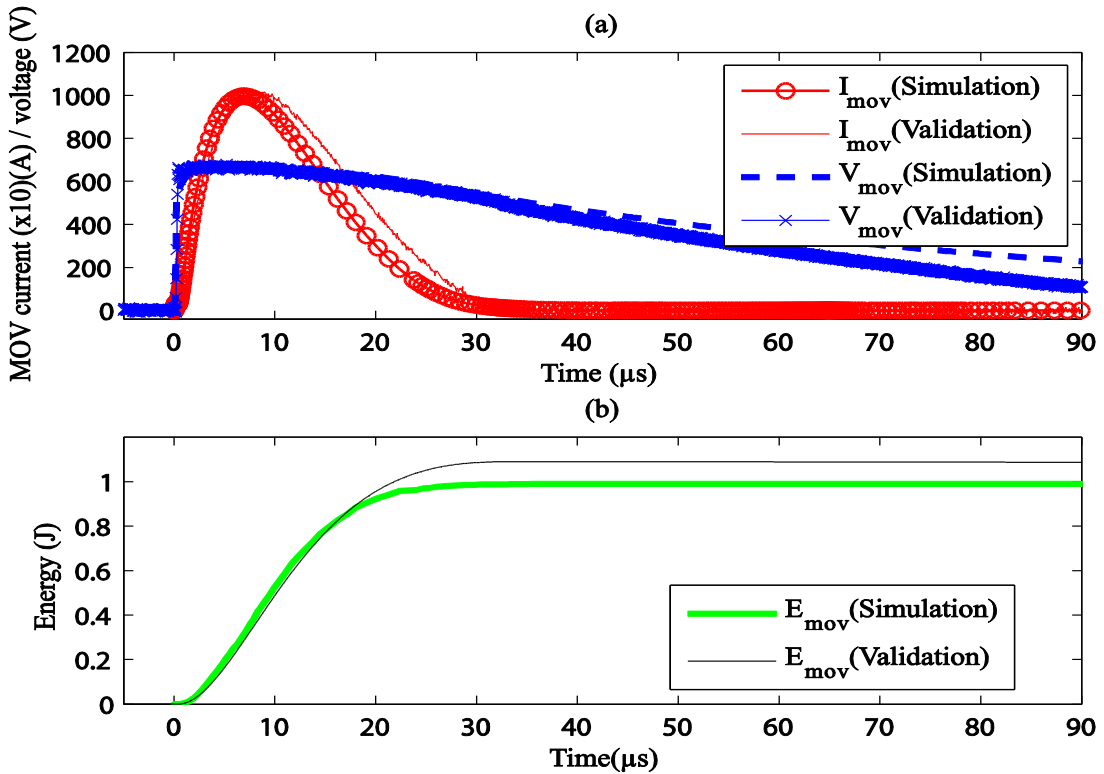


Figure 6-7: Improved numerical simulations and validations for the (a) MOV current and voltage (b) Energy absorption in the MOV

### 6.2.2 SPICE based simulation using a manufacturer supplied model of an MOV and comparison.

As mentioned in Chapter 2, the varistor manufacturers such as *Littelfuse* provide SPICE based models for some of their varistor families. Although we were unable to find any SPICE based model for the 275L40C varistor from the C-III varistor series, *Littelfuse* does provide a SPICE based model for the 20V275 varistor which belong to the *UltraMOV* series [24]. We will now use this model in a PSpice simulation of the circuit shown in Figure 6-2 with the MOV model 20V275 in place instead of the 275L40C.

Let us consider the schematic diagram given in Figure 6-8, which is a representation of Figure 6-2. The PSpice source file for the simulation is created using this schematic diagram and is given in Appendix D-3. The voltage source  $V_x = 0\text{ V}$  is introduced solely for the purpose of simulating the current through it, which is also the current flowing through the MOV.

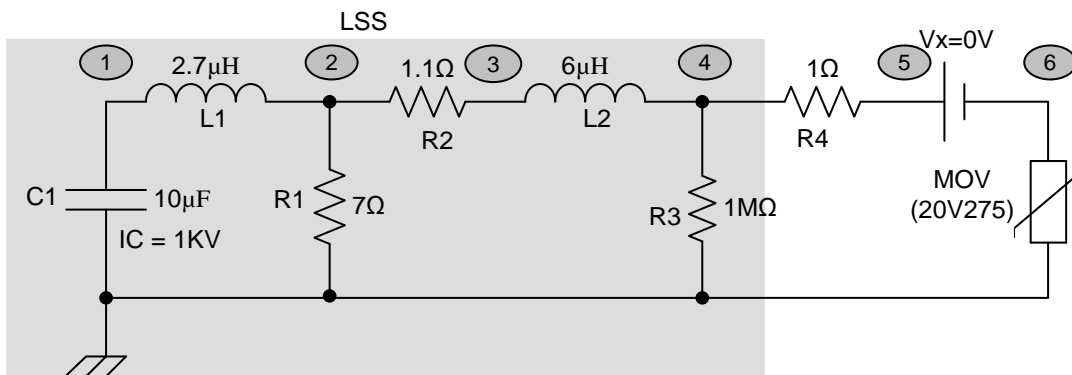


Figure 6-8: Schematic representation of Figure 6-2 used to develop the SPICE source file.

The MOV voltage and the current obtained from the PSpice simulation were compared with MATLAB based numerical simulation and also with experimental results. The MATLAB based numerical simulation was performed using the power-law based model for the varistor 20V275. An initial estimate of power-law model parameters resulted in the following;  $K_2 = 1.0794 \times 10^{-55}$  and  $\alpha_2 = 20.5306$  and the same were used in the simulation that generated the plots of Figure 6-9.

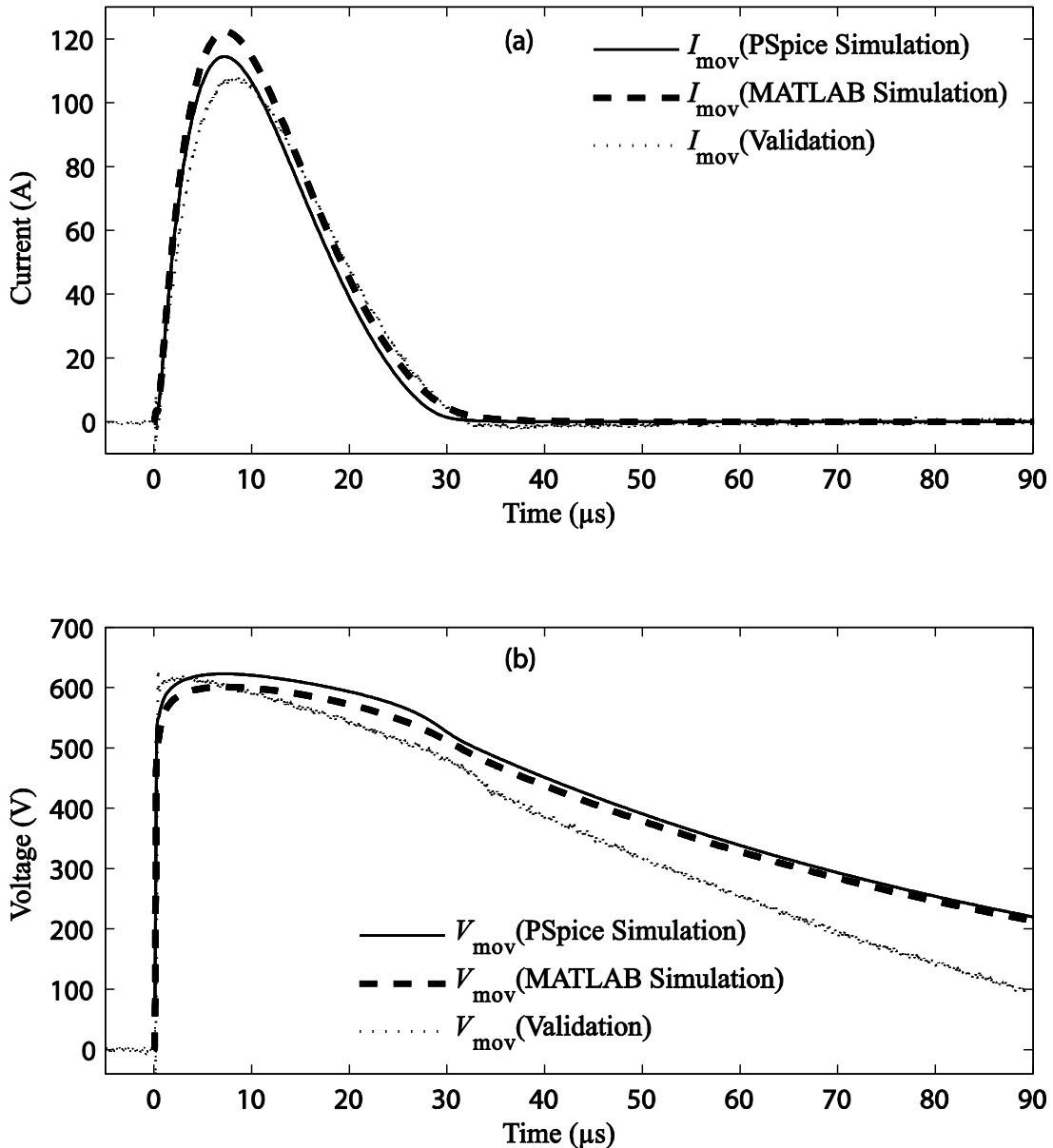


Figure 6-9: SPICE and MATLAB simulations compared with the validations for the first stage (MOV) of a TVSS (a) MOV current and (b) MOV voltage

We were able to minimize and almost eliminate the discrepancy between the PSpice and MATLAB simulations by marginally changing  $\alpha_2$  from 20.5306 to 20.4006. The resulting plots are shown in Figure 6-10.

It must be noted that the PSpice model for the MOV given by the manufacturer (seen in the PSpice source file in Appendix D-3) is much more complex mathematically than the power-law model that we have used for the Matlab simulation. In spite of this complexity, it too has failed to account for the hysteresis effect shown by MOVs, which was discussed in Section 4.2.2.2.

All simulations in the following sections will be done using MATLAB ODE solvers and suitable power-law models for the two nonlinear devices used; viz., the MOV and the TVS diode.

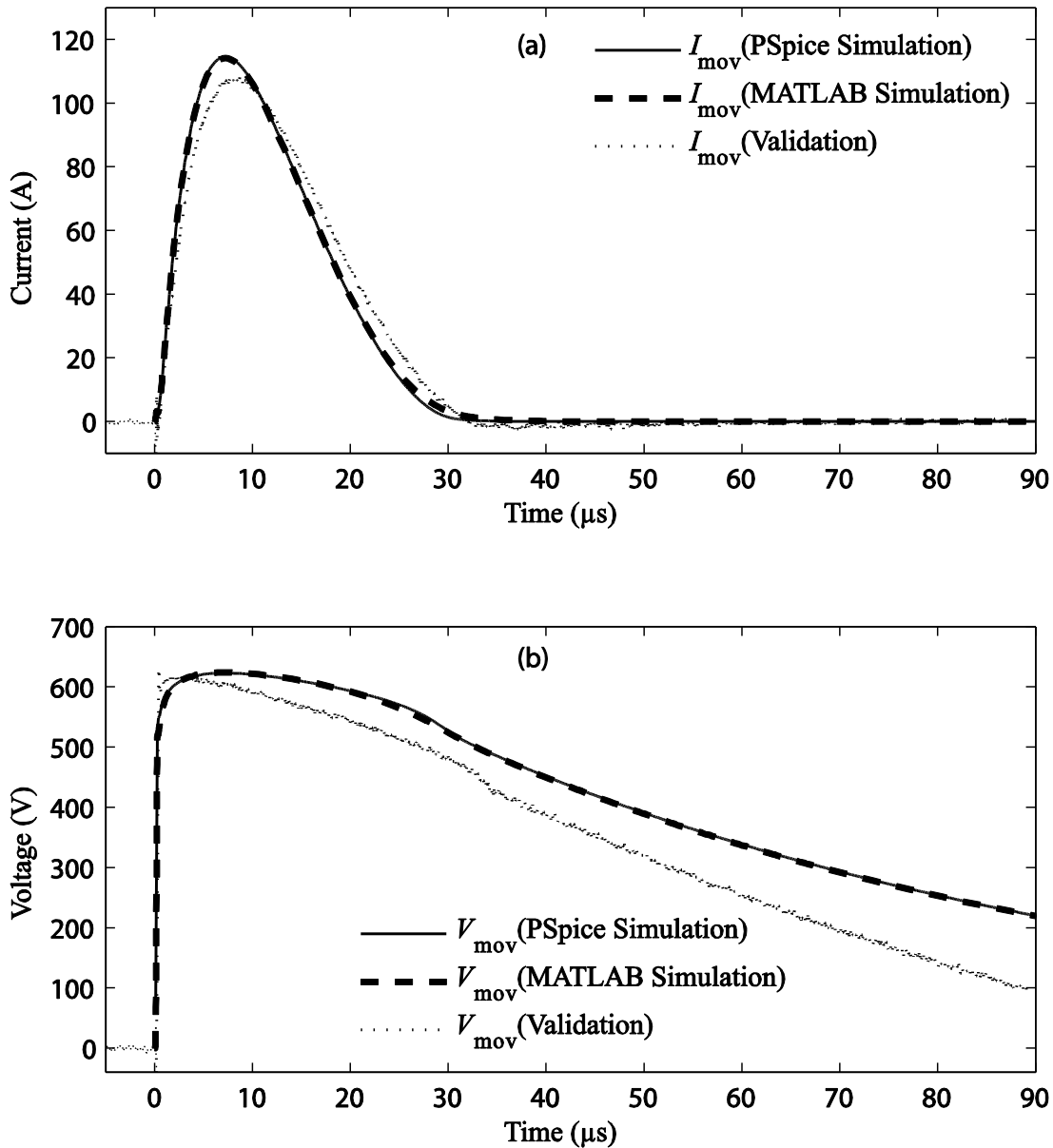


Figure 6-10: SPICE and MATLAB simulations of Figure 6-9 made to coincide by changing  $\alpha_2$  from 20.5306 to 20.4006 (a) MOV current and (b) MOV voltage

### 6.3 Investigation of surge propagation through two stages of the TVSS (MOV and LC line-filter)

Now that we have simulated the propagation of a transient through the first stage of a TVSS with sufficient accuracy, we will take this approach a step further to

numerically simulate the propagation of a transient through a TVSS consisting of two stages: an MOV and a line-filter. This setup is shown in Figure 6-11, where  $L_f$  and  $C_f$  make up the line-filter and the small resistance  $R_f$  is included for the purpose of current measurement.

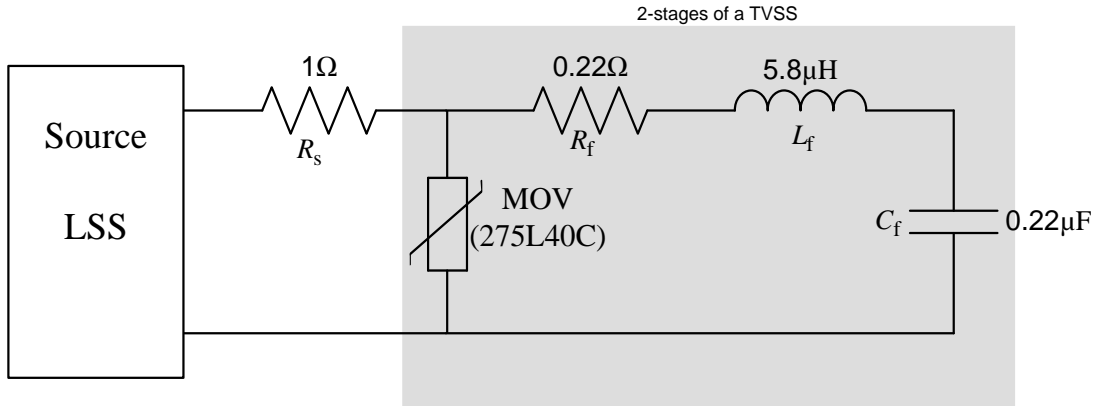


Figure 6-11: LSS driving the first two stages of a category B protection unit

We will now consider the complete equivalent circuit for the setup shown in Figure 6-11, in order to develop the set of differential equations required to numerically simulate the propagation of a HV transient through it. The complete equivalent circuit resulting from replacing the LSS and the MOV by their equivalent circuits is shown in Figure 6-12. The small lead inductance of the MOV, which plays an insignificant role in the normal operation of the MOV in its normal region of operation, has been left out of this simulation.

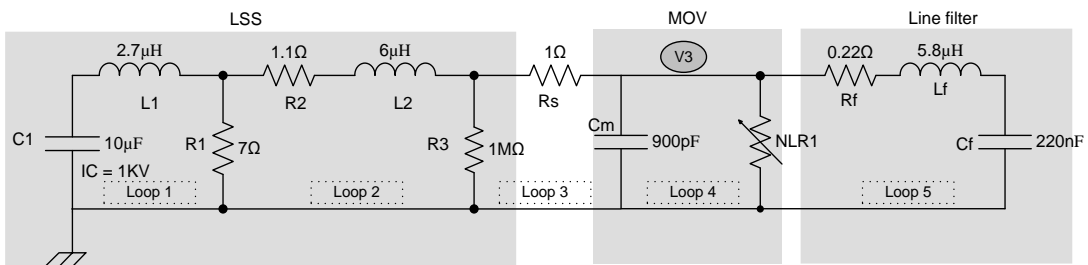


Figure 6-12: Overall equivalent circuit for the setup shown in Figure 6-11.

We will consider five loop currents  $i_1$ ,  $i_2$ ,  $i_3$ ,  $i_4$  and  $i_5$  for the loops shown in Figure 6-12. In addition we will have to consider the nodal voltage  $v_3$  across the nonlinear resistance  $NLR_1$ , as we will continue to use the same power-law based mathematical model for the MOV's nonlinear resistance which we had used in the

previous section. For the current and voltage variables shown in Figure 6-12, this mathematical model can be represented by

$$i_4 - i_5 = K_2 v_3^{\alpha_2} \quad (6-8)$$

The first power-law term  $K_1 v_3^{\alpha_1}$  has been ignored here due to the reasons mentioned in the previous section. We will now present the set of state equations formulated for the simulation of the above circuit. The loop currents  $i_1$ ,  $i_2$ ,  $i_3$  and  $i_5$  the nodal voltage  $v_3$  and the derivatives of the loop currents  $i_1$  and  $i_5$  were selected to be the state variables. The complete derivation of the state equations (6-9) - (6-15) is included in Appendix D-4.

$$\frac{di_1}{dt} = j_1 \quad (6-9)$$

$$\frac{dj_1}{dt} = -(a)j_1 - (b - ac)i_1 - (ad)i_2 + (ae)i_3 \quad (6-10)$$

$$\frac{di_2}{dt} = (c)i_1 - (d)i_2 + (e)i_3 \quad (6-11)$$

$$\frac{di_3}{dt} = (cf)i_1 - (df)i_2 + (ef - g)i_3 + (g)i_5 + (gk_2)v_3^{\alpha_2} \quad (6-12)$$

$$\frac{dv_3}{dt} = l(i_3 - i_5 - k_2 v_3^{\alpha_2}) \quad (6-13)$$

$$\frac{di_5}{dt} = j_5 \quad (6-14)$$

$$\frac{dj_5}{dt} = (h)i_3 - (h + k)i_5 - (hk_2)v_3^{\alpha_2} - (m)j_5 \quad (6-15)$$

where  $a = R_1/L_1$ ,  $b = 1/L_1 C_1$ ,  $c = R_1/L_2$ ,  $d = (R_1 + R_2 + R_3)/L_2$ ,  $e = R_3/L_2$ ,  $f = R_3/(R_3 + R_S)$ ,  $g = 1/C_m (R_3 + R_S)$ ,  $h = 1/L_f C_m$ ,  $k = 1/L_f C_f$ ,  $l = 1/C_m$  and  $m = R_f/L_f$ .

The initial conditions for the simulation are  $i_1(0) = 0, j_1(0) = V_{C1}(0+)/L, i_2(0) = i_3(0) = v_3(0) = i_5(0) = j_5(0) = 0$ . As before, the value given for  $j_1(0)$  results due to the initial voltage  $V_{C1}(0+)$  of the capacitor  $C_1$ . A complete listing of the code used for the simulation `LSS_MOV_LineFilter.m` is given in Appendix D.5. The values of  $K_2 = 2.4496 \times 10^{-50.15}$  and  $\alpha_2 = 18.3338$  for the model of the *nonlinear resistance of the 275L40C MOV* are taken from the improved model discussed in Section 6.2.

We will use the simulation to study the propagation of the transient through different components of the TVSS which will include a study of the total energy absorbed by each of the components with respect to time. This type of study would be helpful in determining the most vulnerable components of the system for failure in the event of a high energy transient.

First we will examine the behavior of the MOV during the surge propagation. The simulated voltage across the device along with the current through the MOV is presented in Figure 6-13(a) and Figure 6-13(b) respectively. We see that the simulations compare well with the validations with respect to both shape and magnitude in spite of the ringing in the simulations not being damped as much as the validations. In Figure 6-13 (b) and (c) we have shown the power variation and energy absorption of the MOV during the period of surge propagation. We see that most of the energy absorption peaks around the 30  $\mu$ s mark. Very good agreement is observed between the simulation and validation for the total energy absorbed by the MOV, in spite of the mismatch in the amplitudes of the ringing peaks in the instantaneous power curves of Figure 6-13(b). This is encouraging, especially since we have added two new components to the circuit under test.

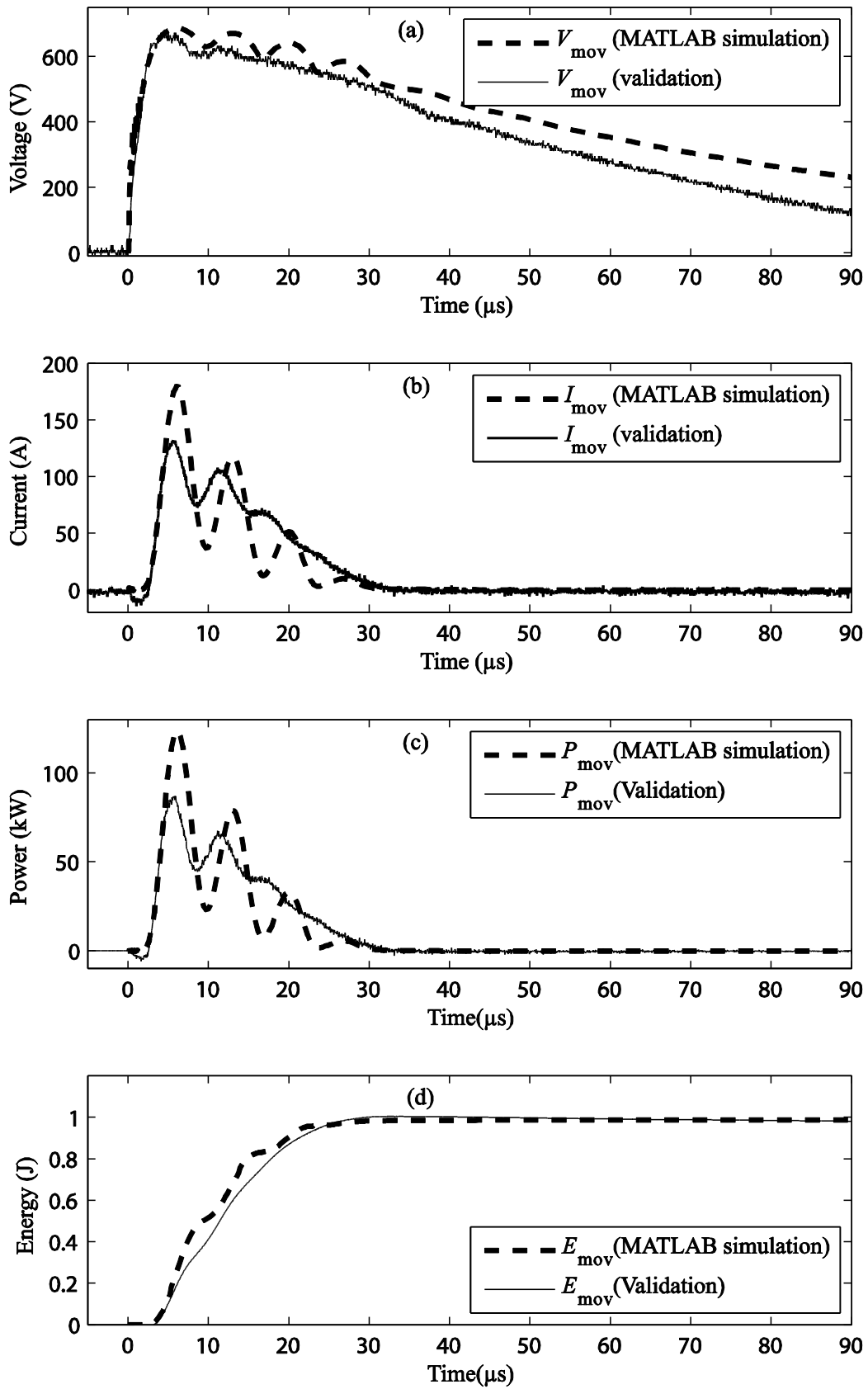


Figure 6-13: Numerical simulation and validations for the MOV of the TVSS (a) MOV voltage (b) MOV current (c) Power variation in the MOV (d) Energy absorption in the MOV

Now we will study how the same surge propagates through the capacitor  $C_f$  of the line filter. The simulated voltage across the capacitor and the current through this component is presented in Figure 6-14(a) and (b) respectively along with the experimental curves for a surge of 1 kV. Again we see that the simulations compare reasonably well with the validations with respect to both shape and magnitude in spite of the ringing in the simulations not being damped as much as the validations. In Figure 6-14 (c) and (d) we have shown the power variation and energy absorption in the capacitor  $C_f$  during the period of surge propagation. Approximately a 5% error is observed between the simulation and validation for the energy absorbed by the capacitor. We see that the resonance frequency ( $f_r = 1/2\pi\sqrt{L_f C_f} \approx 141$  kHz) in the simulation of capacitor current match with the resonance frequency of the line filter components  $L_f$  and  $C_f$ , whereas the experimental curves exhibit a frequency approximately 5% higher. We believe that parasitic capacitances and inductances present in the experimental setup due to connecting cables and proximity of components are responsible for this small deviation in frequency.

The maximum energy absorption in the capacitor takes place approximately after 4  $\mu$ s from the occurrence of the transient and we see that the maximum energy shown by the simulation at this point is about 20% higher than the experimental result. This energy, which is about 100 mJ, is much smaller than the energy absorbed by the MOV, which is in the range of 1 J.

Finally to complete our study of this circuit, we will look at how the surge propagates through the inductor  $L_f$  of the line filter in Figure 6-15. Again we see similar waveshapes although the peaks of ringing in the simulation tend to be higher than in the validating curves. The maximum energy absorption in the inductor can be noted in Figure 6-15(d) and takes place approximately 2.5  $\mu$ s after the occurrence of the surge. Although the maximum energy levels of the simulation and validation differ by about 25% the amount of energy absorbed in this case is even smaller and is in the range of 15-20 mJ.

The work done up to this point is summarized in a provisionally accepted journal paper, which is given in Appendix F.

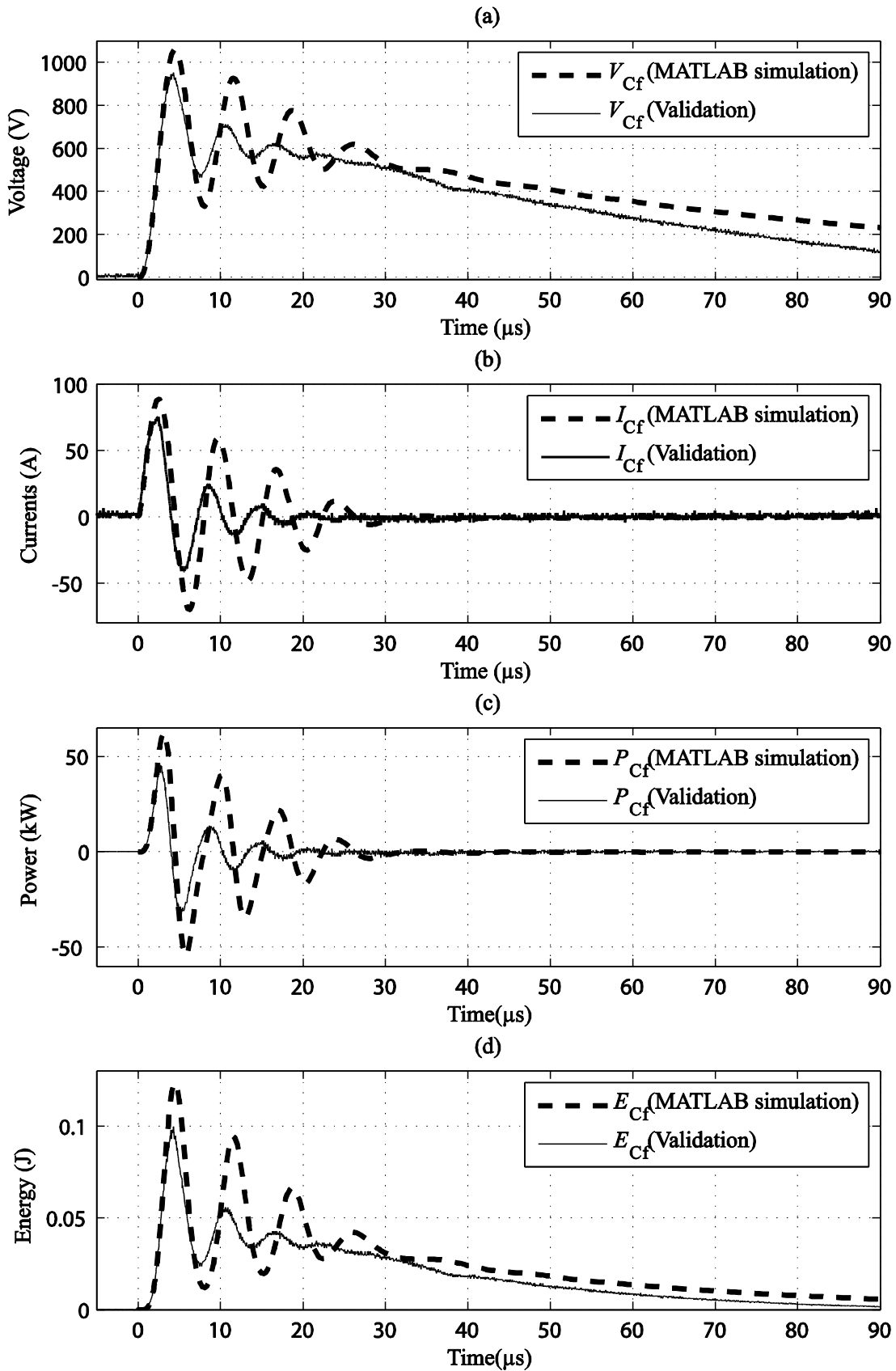


Figure 6-14: Numerical simulation and validations for the capacitor  $C_f$  of the TVSS (a) capacitor current (b) capacitor voltage (b) Power variation in the capacitor (c) Energy absorption in the capacitor

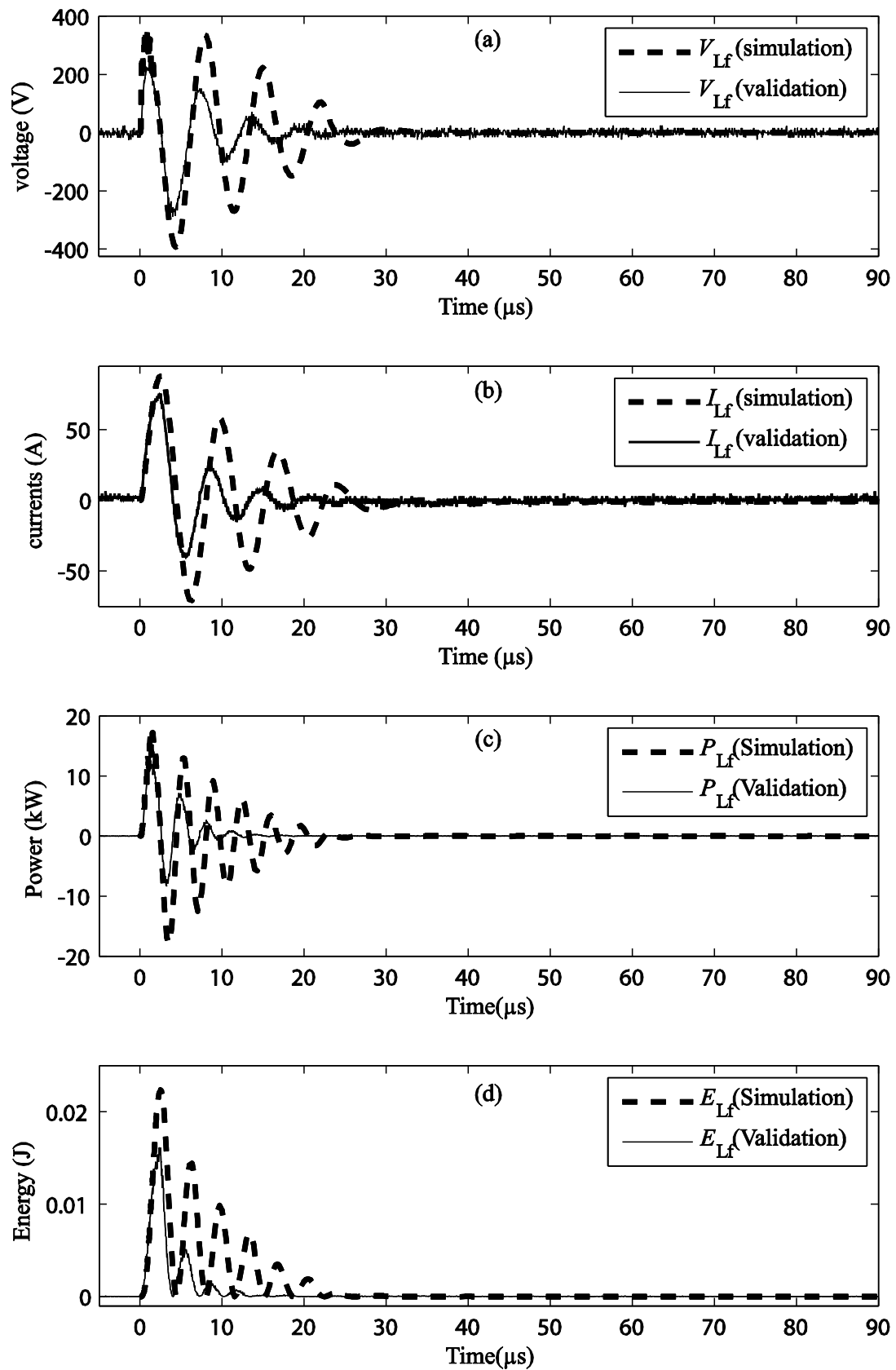


Figure 6-15: Numerical simulation and validations for the inductor  $L_f$  of the TVSS (a) Inductor current (b) Inductor voltage (b) Power variation in the inductor (c) Energy absorption in the inductor

## 6.4 Investigation of surge propagation through a complete 2-wire category A/B TVSS

Having successfully investigated a two-stage TVSS consisting of both linear and nonlinear components in the last section, we will now take this investigation a step further by adding a second nonlinear element: a TVS diode. This provides a second level of protection, thereby making a superior protector having two nonlinear and two linear components (the two resistors, small in value, are added only for current measuring purposes) as shown in Figure 6-16.

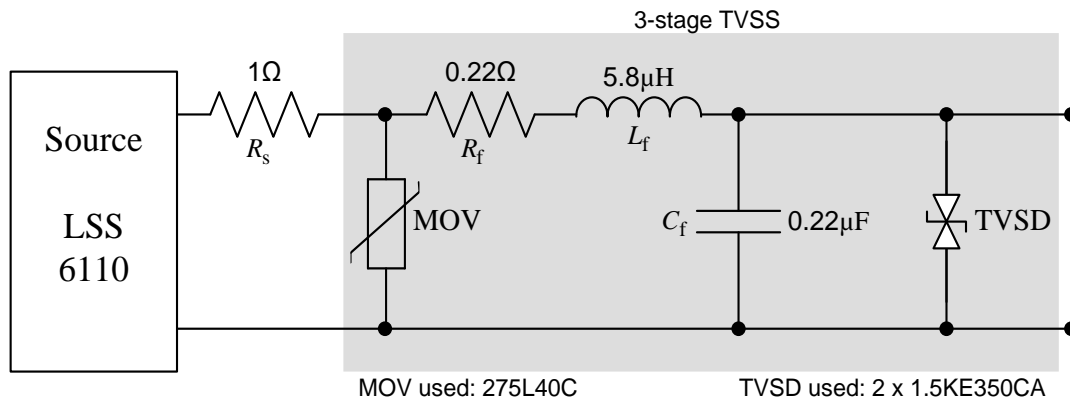


Figure 6-16: LSS driving a complete 3-stage category A/B protection unit. The protection unit is shown in the shaded area.

In order to appreciate the investigation of surge propagation through the circuit shown in Figure 6-16, it is important that we understand how this circuit operates whenever a HV surge arrives at its input terminals. While the operation is similar to the operation of the 3-wire version of this circuit discussed briefly in Section 2.6, it must be mentioned that the nonlinear surge protective devices used must be properly coordinated for effective functioning of the overall circuit in the case of a HV surge; if properly coordinated the MOV will always conduct before the TVS diode.

In this 2- protective-level TVSS, the first level of protection is provided by the MOV; because of its relatively high transient energy absorption capability most of the surge energy is absorbed by this component in the case of a HV transient. As we saw in the previous section, the sudden rush of current through the MOV gives rise to a ringing voltage and current in the line-filter elements  $L_f$  and  $C_f$ . As a result, a HV

surge can develop damagingly high voltage peaks across the filter-capacitor that may be let through to the “protected” equipment. This is where the second-level protector, the TVS diode comes into play, by conducting whenever the voltage across  $C_f$  attempts to go beyond the *clamping voltage* of the TVS diode. This situation will prevail for all stress currents up to the failure point of the TVSD. If this level is reached, the TVSD will fail to a short circuit, clearing the protection fuse that would be present in a commercial or industrial setup [5]. If the transient energy is very large and of short duration like in the case of an extra high voltage lightning transient, there can be an open circuit due to the silicon chip itself exploding [69].

For the reasons indicated above, for this 2-level protector to function correctly, the breakdown voltage of the TVSD must be higher than the firing voltage of the MOV. In the design we have considered here the 275L40C MOV has a clamping voltage just over 600 V and we used two 1.5KE350CA type TVS diodes in series to get a breakdown voltage around the 700 V mark.

Let us now develop the equivalent circuit for the setup given in Figure 6-16 in order to develop the set of differential equations required to numerically simulate the propagation of an HV transient through it. The equivalent circuit resulting from replacing the MOV and the TVS diode by their nonlinear resistance models is shown in Figure 6-17. The first two loops belonging to the equivalent circuit of the LSS are not explicitly shown here since they result in the same two state equations as developed in the earlier cases.

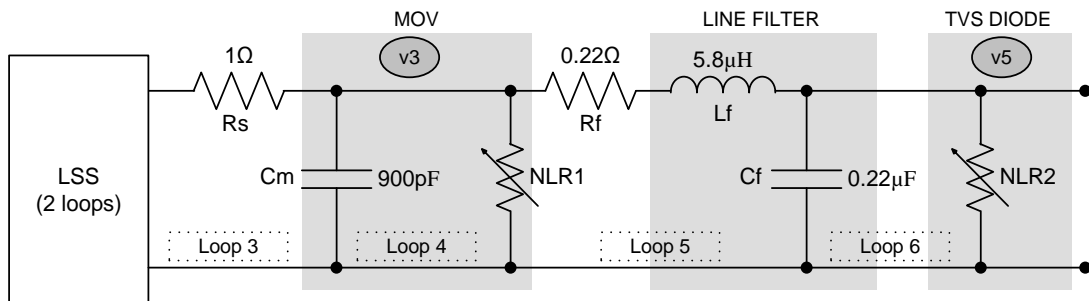


Figure 6-17: MOV and TVS diode models used to redraw the circuit of Figure 6-16

In order to formulate the set of state equations required to simulate the above circuit, we will consider six loop currents  $i_1, i_2, i_3, i_4, i_5$  and  $i_6$ . The first two loop

currents  $i_1$  and  $i_2$  are flowing within the LSS equivalent circuit and are not explicitly shown in Figure 6-17. In addition we will consider the nodal voltages  $v_3$  and  $v_5$  across the nonlinear resistances  $NLR_1$  and  $NLR_2$ . We will use the power-law based mathematical model for the MOV and TVSD nonlinear resistances. For the current and voltage variables of Figure 6-17, these models can be represented by Eq. (6-16) for the MOV and by Eq. (6-17) for the TVS diode.

$$i_4 - i_5 = k_m v_3^{\alpha_m} \quad (6-16)$$

$$i_6 = k_t v_5^{\alpha_t} \quad (6-17)$$

We will now present the set of state equations formulated for the simulation of the circuit of Figure 6-17. The loop currents  $i_1$ ,  $i_2$ ,  $i_3$  and  $i_5$ , the nodal voltages  $v_3$  and  $v_5$ , and the derivatives of the loop currents  $i_1$  and  $i_5$  were selected to be the state variables. The complete derivation of the state equations (6-18) - (6-25) is included in Appendix D-6.

$$\frac{di_1}{dt} = j_1 \quad (6-18)$$

$$\frac{dj_1}{dt} = -aj_1 - (b - ac)i_1 - adi_2 + aei_3 \quad (6-19)$$

$$\frac{di_2}{dt} = ci_1 - di_2 + ei_3 \quad (6-20)$$

$$\frac{di_3}{dt} = cf i_1 - df i_2 + (ef - g)i_3 + gi_5 + gk_m v_3^{\alpha_m} \quad (6-21)$$

$$\frac{dv_3}{dt} = h(i_3 - i_5 - k_2 v_3^{\alpha_2}) \quad (6-22)$$

$$\frac{di_5}{dt} = j_5 \quad (6-23)$$

$$\frac{dj_5}{dt} = ki_3 - (k + l)i_5 - kk_m v_3^{\alpha_m} + lk_t v_5^{\alpha_t} - nj_5 \quad (6-24)$$

$$\frac{dv_5}{dt} = mi_5 - mk_t v_5^{\alpha_t} \quad (6-25)$$

where  $a = R_1/L_1$ ,  $b = 1/L_1 C_1$ ,  $c = R_1/L_2$ ,  $d = (R_1 + R_2 + R_3)/L_2$ ,  $e = R_3/L_2$ ,  $f = R_3/(R_3 + R_S)$ ,  $g = 1/C_m (R_3 + R_S)$ ,  $h = 1/C_m$ ,  $k = 1/L_f C_m$ ,  $l = 1/L_f C_f$ ,  $m = 1/C_f$  and  $n = R_f/L_f$ .

The initial conditions for the simulation are  $i_1(0) = 0$ ,  $j_1(0) = V_{C1}(0+)/L$ ,  $i_2(0) = i_3(0) = v_3(0) = i_5(0) = j_5(0) = v_5(0) = 0$ . As before, the value given for  $j_1(0)$  results due to the initial voltage  $V_{C1}(0+)$  of the capacitor  $C_1$ . A complete listing of the code used for the simulation LSS\_TVSS.m is given in Appendix D.7. The values of  $K_m = 2.4496 \times 10^{-50.15}$  and  $\alpha_m = 18.3338$  for the “on” model of the *nonlinear resistance of the 275L40C MOV* are taken from the improved model discussed in Section 6.2. The values of  $K_t = 4.0638 \times 10^{-161}$  and  $\alpha_t = 56.3468$  for the “on” model of the series combination of two 1.5KE350CA TVS diodes were obtained as discussed in Sections 4.3.2 and 4.3.3. The “off” models of the MOV and the TVS diode have not been considered here due to the nature of the HV input transients.

We will use the simulation to study the propagation of the transient through various levels of the TVSS and compare the simulations with results obtained experimentally.

Again most of the energy delivered by the HV transient to this circuit will be absorbed by the MOV, which provides the first level of protection. The simulated voltage across the MOV and the current through it are presented in Figure 6-18(a) and Figure 6-18(b) respectively. We see that the simulations compare well with the validations with respect to both shape and magnitude. The ringing that was present, in the absence of the TVS diode Figure 6-13 has almost disappeared. In Figure 6-18(b) and Figure 6-18(c) we have shown the power variation and energy absorption of the MOV during the period of surge propagation. Again there is good agreement between

the simulation and validation for the total energy absorbed by the MOV, the percentage error being approximately 12%.

Next we will look at how the same surge propagates through the TVS diode. An observation of the voltage and current curves for this device will clearly explain how this device operates and provides a second level of protection for downstream electronics that would be connected to a TVSS. The simulations and experimental validations for the voltage across the diode and the current through this component are presented in Figure 6-19(a) and (b) respectively for a surge of 1 kV. Again we see that the simulations compare well with the validations with respect to both shape and magnitude in spite of a minor mismatch in the current curves. It must be noted that the TVS diode voltage gets clipped as soon as the filter capacitor tries to charge beyond the breakdown voltage of the TVS diodes. Further evidence to this fact can be seen if we compare the TVS voltage curve with the line-filter capacitor voltage curve shown in Figure 6-14(a), where it rises to almost 900 – 1000 V. Both the simulation and the validation show the same time instant (around the 3  $\mu$ s mark) for the point of switching of the TVS diode from its “off” state to its “on” state.

In Figure 6-19(c) and (d) we have shown the power variation and energy absorption in the TVS diode during the period of surge propagation. Approximately a 20% error is observed between the simulation and validation for the energy absorbed by the TVS diode. This energy, which is less than 100 mJ, is much smaller than the energy absorbed by the MOV, which is in the range of 1 J.

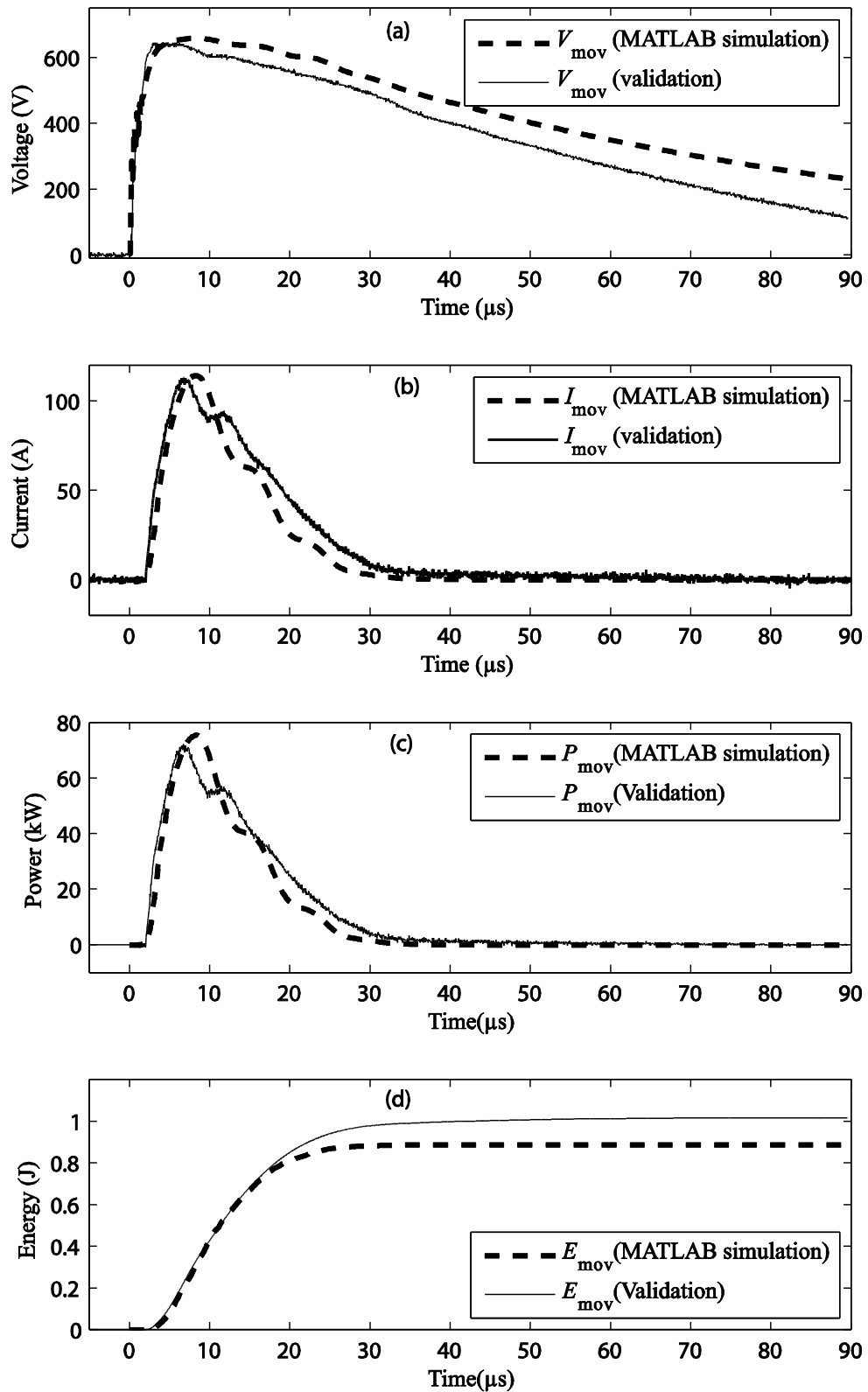


Figure 6-18: Numerical simulation and validations for the MOV of the TVSS (a) MOV voltage (b) MOV current (b) Power variation for the MOV (c) Energy absorption in the MOV

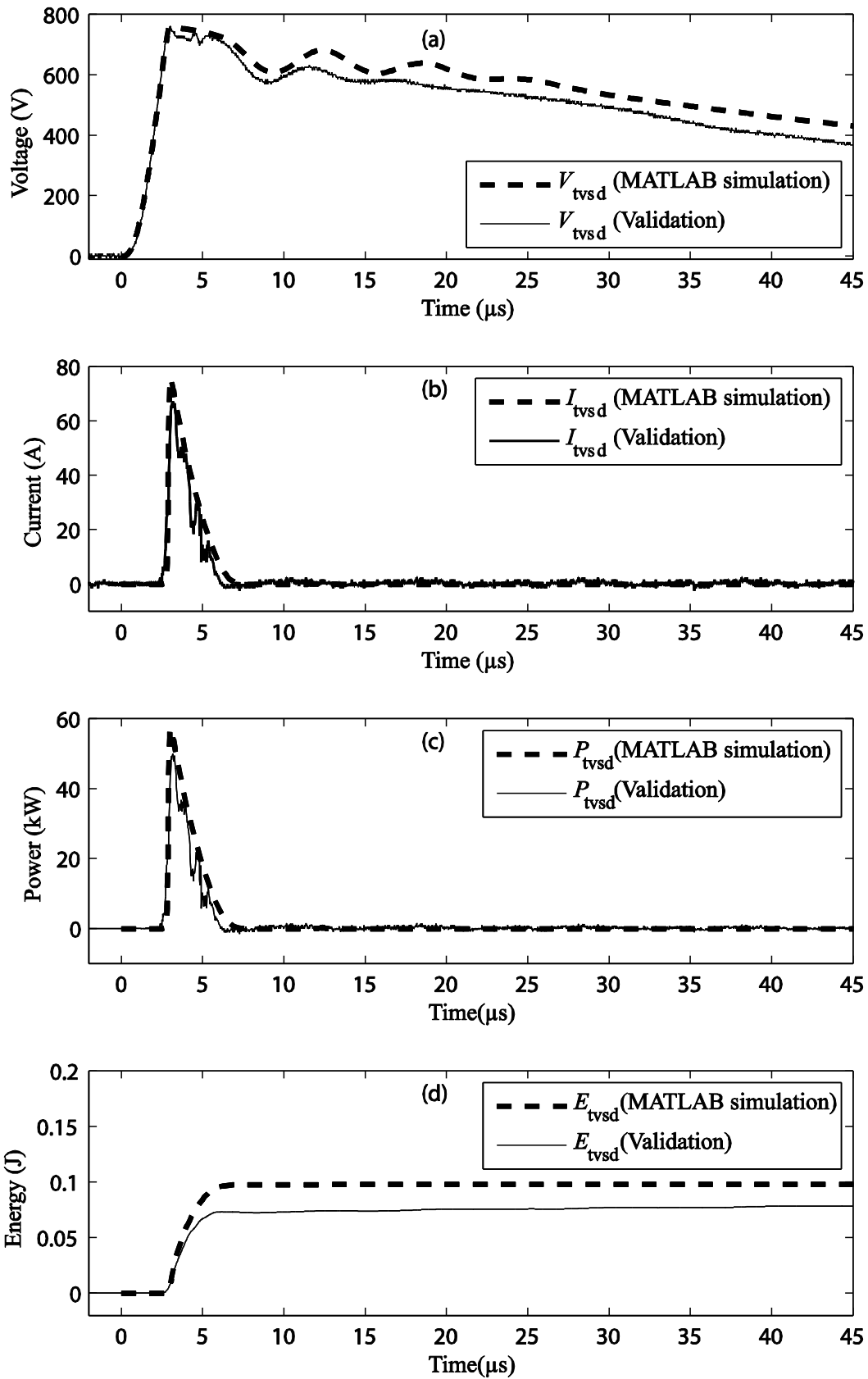


Figure 6-19: Numerical simulation and validations for the TVS diode of the TVSS (a) TVS diode voltage (b) TVS diode current (c) Power variation in the TVS diode (d) Energy absorption in the TVS diode

## Chapter 7: Conclusions and Recommendations

---

The computer simulations developed in this research using MATLAB are a unique endeavour in investigating transient propagation through a power electronics interface: class B transient voltage surge suppressor (TVSS). The flexibility made available in using mathematical models developed for nonlinear devices is an advantage in using this method to study the energy distribution among individual components within the interface. Writing state equations to describe the overall system and then using specialized ODE solvers to solve for all the chosen variables provides insight to the working of the system under stress conditions.

The idea behind the project was to develop a mathematical approach suitable for computer simulation to study the transient propagation within a power electronic interface. This method is useful for predicting incipient failure of individual components through power and energy studies.

### 7.1 General conclusions

This thesis described the development and application of a novel computer simulation technique to investigate transient surge propagation in a transient voltage surge suppressor (TVSS) unit. Initially the nonlinear devices within the TVSS were studied and suitable mathematical models were developed. The overall circuit containing a combination of linear and nonlinear devices was described by state equations that were evaluated using ordinary differential equation (ODE) solvers available in MATLAB. By using the simulations to study the power and energy patterns in individual components, incipient failure due to high voltage (HV) transients can be predicted.

#### 7.1.1 Nonlinear device modelling

The metal oxide varistor (MOV) and the transient voltage suppressor (TVS) diode, both of which are strongly nonlinear, were used in the TVSS design. Both devices were modelled using the power-law relationship between voltage and current. Initially a two-term power-law expression was used to describe each device, although

the term describing the leakage current was dropped due to the insignificant amount of power dissipated during this phase. The coefficient of nonlinearity  $\alpha$  and the constant  $k$  for each device were found by curve fitting.

### **7.1.2 Describing the problem with state equations and solving**

The overall equivalent circuit to be analysed was constructed by combining the equivalent circuit of the lightning surge simulator (LSS) with different stages of the TVSS. The state equations were written for the combined circuit using suitable current and voltage variables. The set of state equations, consisting of linear and nonlinear terms, was solved using specialized Matlab ODE solvers designed for “stiff” problems. The solvers `ode15s` and `ode23tb` were able to solve all the circuit configurations including the one with two nonlinear devices.

### **7.1.3 Validation of the numerical simulations**

All computer simulation results were validated experimentally with the use of the LSS model 6110 by Noiseken laboratories, Japan. This LSS delivers a combination wave to perform surge immunity testing of category B protectors conforming to IEC publication 61000-4-5 and to ANSI/IEEE 62.31 standard. The equivalent circuit supplied by the manufacturer was used to simulate the prescribed outputs of the LSS. These results were validated using actual outputs of the LSS and the comparisons were presented in Chapter 5.

The results on simulations on the TVSS were performed in three different stages: (a) MOV (b) MOV and line filter (c) MOV, line filter and TVS diode. Results were presented in Chapter 6. In each case the current and voltage waveforms for the MOV compared well with the validations with regard to shape and peak value. The percentage error for the total energy absorbed by the MOV was typically less than 13%. The propagation through the line filter capacitor and the inductor were investigated for case (b), which comprised the MOV and the line filter: again the voltage and current waveshapes compared well. The peak energy absorption by the capacitor differed by approximately 20% although this energy level was 10 times smaller than the energy dissipation in the MOV. The peak energy absorption by the inductor differed by approximately 25%, but then again the energy level was even

smaller: 50 times smaller than the energy dissipation in the MOV. In the final part of the simulations we had the complete category B TVSS consisting of the MOV, the line filter and the TVS diode. The voltage and current waveshapes compared well. Here we have a very good match for the time of switch-on for both the TVS diode and the MOV, the simulations and validations showing the same instants of switching. The percentage error for the total energy absorbed by the TVS diode was approximately 20%. The level of this energy was 10 times smaller than the total energy absorbed by the MOV.

## **7.2 Recommendations**

Computer simulations performed in this thesis using numerical methods for surge propagation studies of a TVSS is by no means complete in its development. Consideration of different surge propagation conditions, improvement of the equivalent circuits used and extending the investigation to study surge propagation in downstream electronics could be done to consolidate the work presented here.

### **7.2.1 Surge propagation conditions**

At the time of occurrence of a transient surge, the equipment to be protected could be powered or non-powered; in other words, connected or disconnected from the alternating current (AC) power supply line. In this work we have assumed that the TVSS under investigation was not powered. Although the maximum voltage that will be added to the transient would be approximately 325 V ( $230 \times \sqrt{2}$  V), this could be significant when the transient peak is around 1 kV. A simple application of the superposition theorem, where the effects due to the surge and the supply line are analysed separately and added, will not work in this instance because the overall circuit is nonlinear. Laboratory LSS units usually provide the facility for surging equipment under test (EUT) for either condition. In the case of powered testing, the surge would be superimposed on the line input fed to the LSS, to give the required test output. The work presented here can be continued with investigations of surge propagation under powered conditions.

### **7.2.2 Equivalent circuits used**

The equivalent circuits adapted for both the LSS and the TVSS could be improved. As we saw in Chapter 5, there were minor differences between the simulations and validations of LSS output short-circuit current. Complete elimination of this difference could bring our final simulations closer to the validations. Also in our construction of the equivalent circuit of the TVSS for simulation purpose the passive components such as resistance, inductance and capacitance were included as ideal elements without considering their realistic models. A more accurate simulation could result if such models along with cable and circuit parasitic element values of the experimental setup were also included in the equivalent circuit of the test setup.

Also the mathematical models used for the nonlinear electronic components can be improved for better accuracy; inclusion of other complex models suggested, such as the MOV model which could account for its hysteresis effect should improve accuracy. Some manufacturers provide SPICE based models for some of their nonlinear surge absorbing components; a study of their adoptability to these simulations should be investigated. Also as an alternative for comparison, SPICE based software such as PSpice could be used with user developed models as well as manufacturer supplied models.

### **7.2.3 Investigation of surge propagation in downstream electronics**

A TVSS such as the one investigated for surge propagation in this project usually sits at the front end of a modern power conversion interface such as a switched mode power supply (SMPS) or an uninterruptible power supply (UPS). As such, there is a considerable amount of downstream electronics between a TVSS and a sensitive electronic load that needs to be investigated for HV surge propagation study, if we are to protect the expensive and sensitive electronic loads. The challenge of such an investigation using the methodologies considered in this project would be interesting as more nonlinear electronic devices will have to be accurately modelled and more complex networks analysed.

## References

---

- [1] Global Hydrology and Climate Center. (2012). *Global lightning image*. Retrieved October, 2013, from <http://thunder.nsstc.nasa.gov/data/query/mission.png>
- [2] "Electromagnetic Compatibility (EMC) - Part 4-5: Testing and Measurement Techniques - Surge Immunity Test," in *IEC 61000-4-5: 2005*, ed. Geneva: International Electrotechnical Commission, 2005.
- [3] "IEEE Recommended Practice on Characterization of Surges in Low-Voltage (1000 V and Less) AC Power Circuits," in *IEEE C62.41.2-2002*, ed, 2003.
- [4] ITRS Committee, "Executive summary," in *International Technology Roadmap for Semiconductors*, USA, 2011 Update, p. 5.
- [5] K. H. Billings, *Switchmode Power Supply Handbook*. New York: McGraw-Hill, 1999.
- [6] N. Kularatna, "Protection of Systems from Surges and Transients," in *DC Power Supplies Power Management and Surge Protection for Power Electronic Systems*, Boca Raton: CRC press, 2012, Chap. 9.
- [7] S. Gunther, F. Binns, D. M. Carmean, and J. C. Hall, "Managing the impact of increasing microprocessor power consumption," *Intel Technology Journal*, vol. 5, pp. 1-9, 2001.
- [8] N. Kularatna, "Powering systems based on complex ICs and the quality of Utility AC source: an end to end approach to protection against transients," in *Proc. of Power Quality*, 2005.
- [9] J. Douglas, "Power quality solutions," *Power Engineering Review, IEEE*, vol. 14, pp. 3-7, 1994.
- [10] "IEEE Guide for Surge Voltages in Low-Voltage Ac Power Circuits," *ANSI/IEEE Std C62.41-1980*, p. 8, 1981.
- [11] N. Kularatna, "Digital and Analogue Instrumentation: Testing and Measurement," London, UK: Institution of Electrical Engineers, 2003, Chap. 2.
- [12] Intel corporation. (2011). *Intel 22nm 3-D Tri-Gate Transistor Technology*. Retrieved June, 2012, from <http://newsroom.intel.com/docs/DOC-2032>

- [13] S. Duety, et al, "The key for processor performance beyond a GHz is clean power," *Proceedings of PCIM*, pp. 68-74, 2000.
- [14] P. Dautriche, "Analog design trends and challenges in 28 and 20nm CMOS technology," in *Solid-State Device Research Conference (ESSDERC), 2011 Proceedings of the European*, pp. 1-4.
- [15] N. Kularatna, "Off-the-line switchmode power supplies," in *Power Electronics Design Handbook: Low-Power Components and Applications*, Boston: Newnes, 1998, Chap. 4.
- [16] G. Chryssis, *High-frequency switching power supplies: theory and design*: McGraw-Hill New York, 1984.
- [17] Littelfuse. (1998). *Transient Suppression Devices and Principles: Application Note AN9768*. Retrieved November, 2012, from [http://www.digikey.co.nz/Web%20Export/Supplier%20Content/Littelfuse\\_18/PDF/LF\\_TransientSuppressionDevices.pdf?redirected=1](http://www.digikey.co.nz/Web%20Export/Supplier%20Content/Littelfuse_18/PDF/LF_TransientSuppressionDevices.pdf?redirected=1)
- [18] R. Chundru, L. Zhen, D. Pommerenke, K. Keong, L. Cheung-Wei, F. Centola, and R. Steinfeld, "An evaluation of TVS devices for ESD protection," in *Electromagnetic Compatibility (EMC), 2011 IEEE International Symposium on*, pp. 62-67.
- [19] L. M. Levinson and H. R. Philipp, "The physics of metal oxide varistors," *Journal of Applied Physics*, vol. 46, pp. 1332-1341, 1975.
- [20] B. van Beneden, "Varistors: Ideal solution to surge protection," *Power Electronics Technology*, vol. 29, pp. 26-32, 2003.
- [21] Littlefuse. (1998). *Littelfuse Varistors - Basic Properties, Terminology and Theory: Application Note AN9767.1*. Retrieved November, 2012, from [http://www.digikey.co.nz/Web%20Export/Supplier%20Content/Littelfuse\\_18/PDF/LF\\_Varistors.pdf?redirected=1](http://www.digikey.co.nz/Web%20Export/Supplier%20Content/Littelfuse_18/PDF/LF_Varistors.pdf?redirected=1)
- [22] B. Zitnik, M. Babuder, M. Muhr, and R. Thottappillil, "Numerical modelling of metal oxide varistors," in *Proceedings of the XIVth International Symposium on High Voltage Engineering*, Tsinghua University, Beijing, China, 2005, pp. 1-6.
- [23] G. Z. Zang, J. F. Wang, H. C. Chen, W. B. Su, C. M. Wang, and P. Qi, "Nonlinear electrical behaviour of the WO<sub>3</sub>-based system," *Journal of Materials Science*, vol. 39, pp. 4373-4374, 2004.

- [24] Littelfuse. (2003). *Varistor SPICE models*. Retrieved May, 2013, from <http://www.littelfuse.com/technical-resources/spice-models/varistor-spice-models.aspx>
- [25] Littelfuse. (1999). *The ABCs of MOVs: Application Note AN9311.6*. Retrieved November, 2012, from <http://www.secomtel.com/UpFiles/Attach/0/2007/5/17/141245.pdf>
- [26] D. Tidey. (1999). *The ABCs of Littelfuse Multilayer Suppressors: Application Note AN9671.2*. Retrieved November, 2012, from [http://dev.littelfuse.com/data/en/Application\\_Notes/an9671.pdf](http://dev.littelfuse.com/data/en/Application_Notes/an9671.pdf)
- [27] G. D. Mahan, L. M. Levinson, and H. R. Philipp, "Theory of conduction in ZnO varistors," *Journal of Applied Physics*, vol. 50, pp. 2799-2812, 1979.
- [28] B. Walaszczyk, "Multiple protection devices guard against transients," *Power Electronics Technology*, vol. 28, pp. 55-65, 2002.
- [29] D. Dunlap, "Thermally protected MOVs resist overvoltage failures," *PCIM Power Electronic Systems*, vol. 27, pp. 64-68, 2001.
- [30] STMicroelectronics. (2004). *Transil / Trisil comparison*. Retrieved June, 2013, from <http://pdf1.alldatasheet.com/datasheet-pdf/view/97696/STMICROELECTRONICS/AN574.html>
- [31] ON Semiconductor. (2001). *Transient Voltage Suppression Devices: Data sheet for IN6267A series*. Retrieved November, 2012, from <http://www.icbase.com/file/pdf/add/on/DG-106-001en.pdf>
- [32] M. Clark, "Expand the data sheet on silicon transient voltage protection devices," *PCIM Power Electronic Systems*, vol. 26, pp. 42-44, 2000.
- [33] K. Walters. (2011). *Failure mechanisms for transient voltage suppressors: MicroNote 135*. Retrieved June, 2013, from <http://www3.microsemi.com/micnotes/135.pdf>
- [34] J. Lepkowski and W. Lepkowski, "Evaluating TVS protection circuits with SPICE," *Power Electronics Technology*, vol. 32, pp. 44-49, 2006.
- [35] H. Satoh, "Study on increasing the surge capability of a lightning surge protection, semiconductor device," *Electromagnetic Compatibility, IEEE Transactions on*, vol. 35, pp. 311-315, 1993.

- [36] K. Walters and M. Clark. *What is a thyristor surge protective device and how does it work?* Retrieved June, 2013, from <http://www.microsemi.com/sites/default/files/micnotes/105.pdf>
- [37] ON Semiconductor. (2005). *Thyristor Surge Protectors, Data sheet for MMT08B310T3 - Rev. 3*. Retrieved November, 2012, from [http://www.onsemi.com/pub\\_link/Collateral/MMT08B310T3-D.PDF](http://www.onsemi.com/pub_link/Collateral/MMT08B310T3-D.PDF)
- [38] K. Samaras, C. Sandberg, C. J. Saimas, and A. Koulaxouzidis, "Electrical surge protection devices for industrial facilities - a tutorial review," in *Petroleum and Chemical Industry Conference, 2005. Industry Applications Society 52nd Annual*, 2005, pp. 165-175.
- [39] O. M. Clark and R. E. Gavender, "Lightning protection for microprocessor based electronic systems," in *Industry Applications Society Annual Meeting, 1990., Conference Record of the 1990 IEEE*, 1990, pp. 1460-1466 vol.2.
- [40] R. Rosen, W. Simendinger, C. Debbault, H. Shimoda, L. Fleming, B. Stoner, and O. Zhou, "Application of carbon nanotubes as electrodes in gas discharge tubes," *Applied Physics Letters*, vol. 76, pp. 1668-1670, 2000.
- [41] W. Russell, "Transients vs Electronic Circuits: Survival of the Fittest-Part I: The Need for Transient Protection," *Powerconversion and Intelligent Motion*, vol. 22, pp. 66-71, 1996.
- [42] O. M. Clark, "Transient voltage suppressor types and applications," *Powerconversion and Intelligent Motion*, vol. 16, pp. 19-21, 1990.
- [43] "Approved Draft Revision to Recommended Practice for Powering and Grounding Electronic Equipment. (Color Book Series - Emerald Book)," *IEEE Std P1100/D2*, 2005.
- [44] Eaton. (2009). *Eaton's guide to surge suppression: What you need to know about surge protection devices*. Retrieved June, 2013, from <http://www.eaton.com/ecm/groups/public/@pub/@electrical/documents/content/sa01005003e.pdf>
- [45] R. D. Winters, "Power Supply Voltage Transient Analysis & Protection," in *Powercon III, Power Conversion Conference*, Tempe, Arizona, June 1976.
- [46] Semtech International. (2002). *Surging ideas: TVS diode application note AN96-07*. Retrieved June, 2013, from [http://www.semtech.com/images/datasheet/transient\\_immunity\\_standards\\_iec\\_61000-4-x\\_ag.pdf](http://www.semtech.com/images/datasheet/transient_immunity_standards_iec_61000-4-x_ag.pdf)

- [47] "IEEE Recommended Practice on Surge Voltages in Low-Voltage AC Power Circuits," *IEEE C62.41-1991*, 1991.
- [48] Littelfuse. (2013). *UL 1449 3rd edition overview*. Retrieved July, 2013, from <http://www.littelfuse.com/Technical%20Resources/Education%20Center/UL1449.aspx#Overview>
- [49] F. Bohac. (2010). *UL 1449 - 3rd Edition: Effects of lightning protection systems*. Retrieved July, 2013, from <http://www.geindustrial.com/publibrary/checkout/UL-1449?TNR=White%20Papers|UL-1449|generic>
- [50] Siemens Industry Inc. (2009). *UL 1449 Third Edition: SPD/TVSS Changes Effective*. Retrieved July, 2013, from [http://w3.usa.siemens.com/us/internet-dms/btlv/PowerDistributionComm/PowerDistribution/docs\\_EABU%20docs/UL1449\\_3rd\\_Edition%20Revised.pdf](http://w3.usa.siemens.com/us/internet-dms/btlv/PowerDistributionComm/PowerDistribution/docs_EABU%20docs/UL1449_3rd_Edition%20Revised.pdf)
- [51] C. R. Wylie and L. C. Barrett, *Advanced engineering mathematics*, 5th ed.: McGraw-Hill New York, 1985.
- [52] C. B. Moler, *Numerical computing with MATLAB*: Society for Industrial and Applied Mathematics, 2004.
- [53] Mathworks. (2012). *How Do I Obtain an Impulse Response?* Retrieved November, 2012, from <http://www.mathworks.com/support/tech-notes/1900/1901.html>
- [54] Laser analytics group, The University of Cambridge. (2008). *Using the MATLAB ODE solvers*. Retrieved December, 2012, from [http://laser.cheng.cam.ac.uk/wiki/images/e/e5/NumMeth\\_Handout\\_7.pdf](http://laser.cheng.cam.ac.uk/wiki/images/e/e5/NumMeth_Handout_7.pdf)
- [55] The MathWorks, *The student edition of MATLAB: Student user guide*: Prentice Hall, 1992.
- [56] "High Voltage Test Techniques - Part 1: General Definitions and Test Requirements," in *IEC 60060-1: 2010*, ed, 2010.
- [57] "IEEE Recommended Practice on Characterization of Surges in Low-Voltage (1000 V and Less) AC Power Circuits," in *IEEE C62.41.2-2002*, ed, 2003, p. 17.
- [58] Littelfuse. (2012). *Littelfuse - UltraMOV Varistor Series*. Retrieved December, 2012, from [www.littelfuse.com/data/en/Data\\_sheets/Littelfuse\\_MOV\\_UltraMOV.pdf](http://www.littelfuse.com/data/en/Data_sheets/Littelfuse_MOV_UltraMOV.pdf)

- [59] Littelfuse. (1998). *Varistor Testing: Application Note AN9773*. Retrieved November, 2012, from [http://www.littelfuse.com/data/en/Application\\_Notes/an9773.pdf](http://www.littelfuse.com/data/en/Application_Notes/an9773.pdf)
- [60] Littelfuse. (2012). *Littelfuse: C-III Varistor Series*. Retrieved December, 2012, from [www.littelfuse.com/~media/Files/Littelfuse/Technical%20Resources/Documents/Data%20sheets/LittelfuseVaristorCIII.pdf](http://www.littelfuse.com/~media/Files/Littelfuse/Technical%20Resources/Documents/Data%20sheets/LittelfuseVaristorCIII.pdf)
- [61] D. C. Tayal, *Electricity and Magnetism*: Global media, 2009.
- [62] I. Kim, T. Funabashi, H. Sasaki, T. Hagiwara, and M. Kobayashi, "Study of ZnO arrester model for steep front wave," *IEEE Transactions on Power Delivery*, vol. 11, pp. 834-841, 1996.
- [63] R. A. Jones, P. R. Clifton, G. Grotz, M. Lat, F. Lembo, D. J. Melvold, D. Nigol, J. P. Skivtas, A. Sweetana, D. F. Goodwin, J. L. Koepfinger, D. W. Lenk, Y. Latour, R. T. Leskovich, Y. Musa, J. Adinzh, K. Stump, and E. R. Taylor, "Modeling of metal oxide surge arresters," *IEEE Transactions on Power Delivery*, vol. 7, pp. 302-309, 1992.
- [64] C. Chrysanthou and J. Boksiner, "Analysis of coordination between primary and secondary protectors," *IEEE Transactions on Power Delivery*, vol. 12, pp. 1501-1507, 1997.
- [65] "IEEE Standard Test Specifications for Varistor Surge-Protective Devices," in *IEEE C62.33-1982*, ed, 1982, p. 2.
- [66] Littelfuse. (2008). *Transient Voltage Suppression (TVS) Diode Products*. Retrieved November, 2012, from [http://www.newark.com/pdfs/techarticles/littelfuse/TVS\\_Diodes.pdf](http://www.newark.com/pdfs/techarticles/littelfuse/TVS_Diodes.pdf)
- [67] Littelfuse. (2012). *Littelfuse: 1.5KE Transient Voltage Suppression Diode Series*. Retrieved September, 2013, from [http://www.mouser.com/ds/2/240/Littelfuse\\_TV5-Diode\\_1.5KE-41903.pdf](http://www.mouser.com/ds/2/240/Littelfuse_TV5-Diode_1.5KE-41903.pdf)
- [68] Fairchild. (2002). *Transient Voltage Suppressors 1V5KE6V8(C)A - 1V5KE440(C)A*. Retrieved September, 2013, from [http://projects.uniprecision.com/sc\\_upload/images/1.5KE36A-FAIRCHILD%20%20%20%20KE07575.pdf?PHPSESSID=a36c5ef09508bcb11d43195f4e5dc211](http://projects.uniprecision.com/sc_upload/images/1.5KE36A-FAIRCHILD%20%20%20%20KE07575.pdf?PHPSESSID=a36c5ef09508bcb11d43195f4e5dc211)
- [69] Vishay General Semiconductor. (2007). *Failure modes and fusing of TVS devices: Application Note 88440*. Retrieved October, 2013, from <http://www.vishay.com/docs/88440/failurem.pdf>

- [70] S. James, K. Nihal, A. Steyn-Ross, A. Pandey, R. Kunnemeyer, and D. Tantrigoda, "Investigation of failure patterns of desktop computer power supplies using a lightning surge simulator and the generation of a database for a comprehensive surge propagation study," in *IECON 2010 - 36th Annual Conference on IEEE Industrial Electronics Society*, pp. 1275-1280.
- [71] D. K. Cheng, *Analysis of Linear Systems*. Reading, Mass.: Addison-Wesley, 1959.
- [72] C. H. Edwards and D. E. Penney, *Differential Equations and Linear Algebra*, 3rd ed. Upper Saddle River, NJ: Pearson Education, 2010.



# Appendices

---

## Appendix A: MATLAB code used for Chapter 3

### A.1 Euler simulation of LCR circuit driven by a charged capacitor

– MATLAB code used to produce Figure 3-3

(Name of file: RLC\_simulations\_4\_methods.m)

```
%-----  
function RLC_simulations_4_methods  
% Solve for RLC current using Euler. "switch" command set to  
% METHOD 1.  
% Assume capacitor is fully charged at time zero.  
  
R = 7;  
C = 10e-6;  
L = 2.7e-6;  
Vc0 = 100;  
  
a = R/L; b = 1/(L*C);  
w = sqrt(a^2/4 - b);  
  
i_theory = @(t) Vc0/L * sinh(w*t)/w .* exp(-a*t/2);  
  
t = linspace(0, 0.5e-3, 1000);  
  
%-----  
% DE definition for RLC circuit  
function xdot = RLC_dot(t, x, flag, params)  
    [x1 x2] = deal(x(1), x(2));  
    x1_dot = x2;  
    x2_dot = -a*x2 - b*x1;  
    xdot = [x1_dot; x2_dot];    % return column vector  
end  
  
% Euler solution of DEs: I = current; J = dI/dt  
Nsteps = 4000;  
[I, J] = deal(zeros(Nsteps,1));  
dt = 0.125e-6;  
time = [0: Nsteps-1]*dt;  
  
% choose integration method  
% 1 = Euler; 2 = improved Euler; 3 = Euler with RLC_dot; 4 = RK4  
METHOD = 1  
  
switch METHOD  
% old Euler method: use explicit approximation for delta-function  
case 1  
    I(1) = 0;
```

```

    J(1) = 0;
    for n = 1 : Nsteps-1
        I(n+1) = I(n) + J(n)*dt;
        J(n+1) = J(n) + (-a*J(n) - b*I(n) + Vc0/(L*dt)*(n==1)) * dt;
    end

% new Euler: integrate delta-function to give initial condition for
% J
    case 2
        I(1) = 0;
        J(1) = Vc0/L;
        for n = 1 : Nsteps-1
            I(n+1) = I(n) + J(n)*dt;
            J(n+1) = J(n) + (-a*J(n) - b*I(n)) * dt;
        end

% new Euler using RLC_dot function
    case 3
        X = zeros(2, Nsteps);
        X(:,1) = [0; Vc0/L];
        for n = 1 : Nsteps-1
            X(:, n+1) = X(:, n) + RLC_dot([], X(:, n), '', [])*dt;
        end
        I = X(1,:); J = X(2,:);

% RK4 with fixed timesteps
    case 4
        X0(:,1) = [0; Vc0/L]; flag = ''; params = [];
        [t_out, X_out] = rk4fixed(@RLC_dot, time, X0, flag, params);
        I = X_out(:,1); J = X_out(:,2);
end

i_theory_s = @(time) Vc0/L * sinh(w*time)/w .* exp(-a*time/2);
err_curve = I'- i_theory_s(time);

fignum = 3;
figure(fignum); clf;

subplot(211)
    plot(t*1e6, i_theory(t),'--', 'linewidth', 3);
    zoom on; grid on; hold on;
    plot(time*1e6, I, '-r', 'linewidth', 1);
    legend('Laplace','Euler simulation');
    xlabel('Time (us)'); ylabel('Loop current (A)');
    title('(a)')
    axis ([-5 500 0 15])

subplot(212)
    plot(time*1e6, err_curve, 'o-k', 'linewidth', 1);grid on;
    axis ([-1 5 -5 1]);
    legend('Euler Error','Location','SouthEast');
    xlabel('Time (us)'); ylabel('Discrepancy (A)');
    title('(b)')
end

```

## A.2 Improved Euler simulation (using initial conditions that arise from the impulse input) of LCR circuit driven by a charged capacitor – MATLAB code used to produce Figure 3-4

(Name of file: RLC\_simulations\_4\_methods.m)

```

%-----
function RLC_Euler_4_methods
% Solve for RLC current using improved Euler. "switch" command set
% to METHOD 2.
% Assume capacitor is fully charged at time zero.

R = 7;
C = 10e-6;
L = 2.7e-6;
Vc0 = 100;

a = R/L; b = 1/(L*C);
w = sqrt(a^2/4 - b);

i_theory = @(t) Vc0/L * sinh(w*t)/w .* exp(-a*t/2);

t = linspace(0, 0.5e-3, 1000);

%-----
% DE definition for RLC circuit
function xdot = RLC_dot(t, x, flag, params)
    [x1 x2] = deal(x(1), x(2));
    x1_dot = x2;
    x2_dot = -a*x2 - b*x1;
    xdot = [x1_dot; x2_dot]; % return column vector
end

% Euler solution of DEs: I = current; J = dI/dt
Nsteps = 4000;
[I, J] = deal(zeros(Nsteps,1));
dt = 0.125e-6;
time = [0: Nsteps-1]*dt;

% choose integration method
% 1 = Euler; 2 = improved Euler; 3 = Euler with RLC_dot; 4 = RK4
METHOD = 2

switch METHOD
% old Euler method: use explicit approximation for delta-function
case 1
    I(1) = 0;
    J(1) = 0;
    for n = 1 : Nsteps-1
        I(n+1) = I(n) + J(n)*dt;
        J(n+1) = J(n) + (-a*J(n) - b*I(n) + Vc0/(L*dt)*(n==1)) *
dt;

```

```

end

% new Euler: integrate delta-function to give initial condition for
J
case 2
    I(1) = 0;
    J(1) = Vc0/L;
    for n = 1 : Nsteps-1
        I(n+1) = I(n) + J(n)*dt;
        J(n+1) = J(n) + (-a*J(n) - b*I(n)) * dt;
    end

% new Euler using RLC_dot function
case 3
    X = zeros(2, Nsteps);
    X(:,1) = [0; Vc0/L];
    for n = 1 : Nsteps-1
        X(:, n+1) = X(:, n) + RLC_dot([], X(:, n), '', [])*dt;
    end
    I = X(1,:); J = X(2,:);

% RK4 with fixed timesteps
case 4
    X0(:,1) = [0; Vc0/L]; flag = ''; params = [];
    [t_out, X_out] = rk4fixed(@RLC_dot, time, X0, flag, params);
    I = X_out(:,1); J = X_out(:,2);

end

i_theory_s = @(time) Vc0/L * sinh(w*time)/w .* exp(-a*time/2);
err_curve = I'- i_theory_s(time);

fignum = 3;
figure(fignum); clf;

subplot(211)
plot(t*1e6, i_theory(t),'--', 'linewidth', 2);
zoom on; grid on; hold on;
plot(time*1e6, I, '-r', 'linewidth', 1);
legend('Laplace','improved Euler simulation');
xlabel('Time (us)'); ylabel('Loop current (A)');
title('a')
axis ([-5 500 0 15])

subplot(212)
plot(time*1e6, err_curve, 'o-k', 'linewidth', 1);grid on;
axis ([-1 10 -0.2 1.2]);
legend('improved Euler Error','Location','best');
xlabel('Time (us)'); ylabel('Discrepancy (A)');
title('b')

end

```

### A.3 rk4fixed: General-purpose 4<sup>th</sup>-order Runge-Kutta ODE used by simulation listed in Appendix A.4

(Name of file: rk4fixed.m)

```
function [t_out, y_out] = rk4fixed(FUN, tspan, y0, flag, params)

% rk4fixed is a 4th-order Runge-Kutta integration routine with fixed
% time-steps. Requires 4 function evaluations per step.
% 4th-order RK methods have a local error estimate of O(h^5).
%
%   FUN - String containing function name of differential eqn
%   tspan - Vector of fixed time-points for integration
%   y0 - Initial values (column-vector)
%   flag - (not used: required for compatability with ODE45)
%   params - Vector of parameters to be passed to FUN
%
%   t_out - Returned integration time points (column-vector)
%   y_out - Returned solution, one row-vector per t_out value
%
% rk4fixed calls the differential eqn FUN as follows:
%   ydot = FUN(t, y, flag, params)
%       t - Present time value (scalar)
%       y - Present y-value (scalar or column-vector)
%       flag - String constant (usually empty: '')
%       params - Vector of input parameters
%       ydot - Computed derivative (column-vector)

% Marc Compere <CompereM@asme.org> 06-Oct-1999, 19-May-2001
% ASR: 21-Mar-2004 Tuned for PHYS315 use
% ASR: 26-Mar-2007 Tidied up time-increments

% Initialization
Npts = length(tspan);
t_out = zeros(Npts, 1);
y_out = zeros(Npts, length(y0));

dt = tspan(2) - tspan(1);

t_out(1) = tspan(1);
y_out(1,:) = y0.'; % use row-vector for output
y = y0(:); % use column-vector for calculations

half_dt = dt/2;

for i = 2: Npts
    t_now = tspan(i-1);
    t_half = t_now + half_dt;
    t_full = t_now + dt;

    K1 = feval(FUN, t_now, y, flag, params);
    K2 = feval(FUN, t_half, y + half_dt*K1, flag, params);
    K3 = feval(FUN, t_half, y + half_dt*K2, flag, params);
    K4 = feval(FUN, t_full, y + dt*K3, flag, params);

    y = y + dt/6*(K1 + 2*K2 + 2*K3 + K4);
end
```

```
        t_out(i) = tspan(i);  
        y_out(i,:) = y.';  
end  
  
return
```

## A.4 RK4 simulation of LCR circuit driven by a charged capacitor

– MATLAB code used to produce Figure 3-5

(Name of file: RLC\_simulations\_4\_methods.m)

```
%-----  
-----  
function RLC_simulations_4_methods  
% Solve for RLC current using rk4fixed general-purpose ODE solver.  
"switch" command set to METHOD 4.  
% Assume capacitor is fully charged at time zero.  
  
R = 7;  
C = 10e-6;  
L = 2.7e-6;  
Vc0 = 100;  
  
a = R/L; b = 1/(L*C);  
w = sqrt(a^2/4 - b);  
  
i_theory = @(t) Vc0/L * sinh(w*t)/w .* exp(-a*t/2);  
  
t = linspace(0, 0.5e-3, 1000);  
  
%-----  
% DE definition for RLC circuit  
function xdot = RLC_dot(t, x, flag, params)  
    [x1 x2] = deal(x(1), x(2));  
    x1_dot = x2;  
    x2_dot = -a*x2 - b*x1;  
    xdot = [x1_dot; x2_dot];    % return column vector  
end  
  
% Euler solution of DEs: I = current; J = dI/dt  
Nsteps = 4000;  
[I, J] = deal(zeros(Nsteps,1));  
dt = 0.125e-6;  
time = [0: Nsteps-1]*dt;  
  
% choose integration method  
% 1 = Euler; 2 = improved Euler; 3 = Euler with RLC_dot; 4 = RK4  
METHOD = 4;  
  
switch METHOD  
% old Euler method: use explicit approximation for delta-function  
case 1  
    I(1) = 0;  
    J(1) = 0;  
    for n = 1 : Nsteps-1  
        I(n+1) = I(n) + J(n)*dt;
```

```

        J(n+1) = J(n) + (-a*J(n) - b*I(n) + Vc0/(L*dt)*(n==1)) *
dt;
    end

% new Euler: integrate delta-function to give initial condition for
J
    case 2
        I(1) = 0;
        J(1) = Vc0/L;
        for n = 1 : Nsteps-1
            I(n+1) = I(n) + J(n)*dt;
            J(n+1) = J(n) + (-a*J(n) - b*I(n)) * dt;
        end

% new Euler using RLC_dot function
    case 3
        X = zeros(2, Nsteps);
        X(:,1) = [0; Vc0/L];
        for n = 1 : Nsteps-1
            X(:, n+1) = X(:, n) + RLC_dot([], X(:, n), '', [])*dt;
        end
        I = X(1,:); J = X(2,:);

% RK4 with fixed timesteps
    case 4
        X0(:,1) = [0; Vc0/L]; flag = ''; params = [];
        [t_out, X_out] = rk4fixed(@RLC_dot, time, X0, flag, params);
        I = X_out(:,1); J = X_out(:,2);
end

i_theory_s = @(time) Vc0/L * sinh(w*time)/w .* exp(-a*time/2);
err_curve = I'- i_theory_s(time);

fignum = 3;
figure(fignum); clf;

subplot(211)
    plot(t*1e6, i_theory(t),'--','linewidth', 3);
    zoom on; grid on; hold on;
    plot(time*1e6, I,'-r', 'linewidth', 1);
    legend('Laplace solution','RK4 simulation','Location','Best');
    xlabel('Time (us)'); ylabel('Loop current (A)');
    title('(a)')
    axis ([-5 500 0 15])

subplot(212)
    plot(time*1e6, err_curve*1e3, 'o-k', 'linewidth', 1);grid on;
    axis ([-0.5 5 -2 2]);
    legend('RK4 Error','Location','Best');
    xlabel('Time (us)'); ylabel('Discrepancy (mA)');
    title('(b)')
end

```

## A.5 ode45 simulation of LCR circuit driven by a charged capacitor

– MATLAB code used to produce Figure 3-6

(Name of file: RLC\_circuit\_simulation\_ode45.m)

```
%-----  
function RLC_circuit_simulation_ode45  
% Solve for RLC current using ode45 variable-step ODE solver.  
% Assume capacitor is fully charged at time zero.  
  
R = 7;  
C = 10e-6;  
L = 2.7e-6;  
Vc0 = 100;  
  
a = R/L; b = 1/(L*C);  
w = sqrt(a^2/4 - b);  
  
i_theory = @(t) Vc0/L * sinh(w*t)/w .* exp(-a*t/2);  
  
t = linspace(0, 0.1e-3, 1000);  
  
%-----  
% DE definition for RLC circuit  
function xdot = RLC_dot(t, x, flag, params)  
    [x1 x2] = deal(x(1), x(2));  
    x1_dot = x2;  
    x2_dot = -a*x2 - b*x1;  
    xdot = [x1_dot; x2_dot];    % return column vector  
end  
  
% ode45 solution of DEs: I = current; J = dI/dt  
time = [0 100e-6];  
  
METHOD = 1;  
  
switch METHOD  
  
% ode45 with variable timesteps  
case 1  
    X0(:,1) = [0; Vc0/L]; flag = ''; params = [];  
%    [t_out, X_out] = rk4fixed(@RLC_dot, time, X0, flag, params);  
    [t_out, X_out] = ode45(@RLC_dot, time, X0, flag, params);  
    time=t_out;  
    I = X_out(:,1); J = X_out(:,2);  
end  
  
fignum = 1;  
figure(fignum); clf;  
  
subplot(211)
```

```

    plot(t*1e6, i_theory(t),'--', 'linewidth', 3);
    zoom on; grid on; hold on;
    plot(time*1e6, I, 'r', 'linewidth', 1);
    legend('Laplace solution','ode45
simulation','Location','Southeast');
    xlabel('Time (us)'); ylabel('Loop current (A)');
    title('a')
    axis ([-1 20 0 15])

subplot(212)
    plot(time(1:end-1)*1e6, diff(time)*1e6, 'o-k', 'linewidth',
1);grid on;
    axis ([-1 20 -0.1 0.5]);
    legend('Time-step','Location','Southeast');
    xlabel('Time (us)'); ylabel('Time-step t (us)');
    title('b')

end

```

## Appendix B: MATLAB code used in the compilation of Chapter 4

### B.1 Calculation of the slope ( $\alpha$ ) and intercept ( $\log k$ ) of the “off” and “on” models for the varistor 275L40C

```
% Calculation of the slope(alpha) and intercept(log k) of the "off"
model
% and the "on" model using "polyfit"

Res_on = [ 397      4.1E-05
           446      7.2E-04
           452      1.9E-03
           457      3.0E-03
           458      3.5E-03
           600         2
           640      21
           660      46
           680      72
           700     104      ];

I_on = Res_on(:,2);
V_on = Res_on(:,1);

% extract slope of log-log graph for "on" model
pf_on = polyfit(log(V_on), log(I_on), 1)
alpha_on = pf_on(1)
k_on = exp(pf_on(2))

Res_off = [ 100.3   1.5E-07
            199.4   1.1E-06
            300.3   8.8E-06
            397     4.1E-05      ];

I_off = Res_off(:,2);
V_off = Res_off(:,1);

% extract slope of log-log graph for "off" model
pf_off = polyfit(log(V_off), log(I_off), 1)
alpha_off = pf_off(1)
k_off = exp(pf_off(2))
```

## B.2 Development of the combined model for the MOV 275L40C

– MATLAB code used to produce Figure 4-16

```
% Development of a combined model for the leakage and normal regions
of
% operations for a 275L40C varistor
%-----
function MOV_curve_fit

data = [
    100.3    1.5E-07
    199.4    1.1E-06
    300.3    8.8E-06
    397      4.1E-05
    397      4.1E-05
    446      7.2E-04
    452      1.9E-03
    457      3.0E-03
    458      3.5E-03
    600      2
    640      21
    660      46
    680      72
    700      104      ];

I_mov = data(:,2); V_mov = data(:,1);

figure(1); clf;

V_lo = [100 750]; I_lo = 9.3231*10^-16*V_lo.^4.0413;

V_hi = [300 750]; I_hi = 3.5040*10^-73*V_hi.^26.2396;

V_fit = linspace(100, 750, 100);

I_fit = 9.3231*10^-16*V_fit.^4.0413
        + 3.5040*10^-73*V_fit.^26.2396;

plot(V_lo, I_lo, '-k', 'linewidth', 2, 'color', 0.7*[1 1 1]);
hold on;

plot(V_hi, I_hi, '-k', 'linewidth', 2, 'color', 0.7*[0 1 0]);

plot(V_fit, I_fit, '-k', 'linewidth', 2, 'color', 1*[1 0 0]);

legend('K_1V^?', 'K_2V^?', 'K_1V^?^1 +
        K_2V^?^2', 'Location', 'NorthWest');

I, V] = deal(I_mov, V_mov);
plot(V(1:9), I(1:9), 'o', V(10:14), I(10:14), '+k', 'linewidth', 2.5);
zoom on; grid on; hold on;
```

```
set(gca,'xtick',100:100:800);  
  
set(gca, 'xscale', 'log', 'yscale', 'log');  
  
xlabel('Voltage (V)');  
ylabel('Current (A)');  
  
end
```

### B.3 Verification of the combined model developed for the MOV 275L40C

– MATLAB code used to produce Figure 4-18 and Figure 4-19

```
function MOV_model_verification

% i1 - input current; i2 - MOV current; v1 - input voltage; v2 -
output
% voltage

v1_set = [20: 10: 1000];

graph_flag = 0;
[i1, i2, v1, v2] = MOV_suppressor(v1_set, graph_flag);

% Experimental readings

results = [
    95      95  0.10    0
    200    200  0.20    0
    300    300  0.30    0
    400    400  0.40    0
    500    500  0.50    0
    610    610  0.61    2
    670    660  0.66   22
    730    680  0.68   49
    760    690  0.69   79
    810    700  0.70  111
    860    710  0.71  152
    900    713  0.72  188
    938    718  0.72  222
];

v1_res = results(:,1); v2_res = results(:,2);
i2_res = results(:,4); i3_res = results(:,3);

figure(1); clf;
subplot(311);

    plot(v1_set, v2, '--','linewidth',2); zoom on; hold on;
    plot(v1_res,v2_res,'xk','linewidth',2);
    legend('Simulation','Validation','Location','NorthWest')
    xlabel('Input voltage (V)');
    ylabel('Load voltage (V)');
    text(400, 800, '(a)')

subplot(312);

    plot(v1_set, i2, '-g','linewidth',2); zoom on; hold on;
    plot(v1_res,i2_res,'xk','linewidth',2);
    xlabel('Input voltage (V)');
    ylabel('MOV current (A)');
    text(500, 300, '(b)');
```

```

        legend('Simulation','Validation','Location','NorthWest');

subplot(313);

    plot(v1_set, i1-i2, '--r','linewidth',2);zoom on; hold on;
    plot(v1_res,i3_res,'xb','linewidth',2);
    xlabel('Input voltage (V)');
    ylabel('Load current (A)');
    legend('Simulation','Validation','Location','NorthWest')
    text(500, 0.8, '(c)')

end

%-----
-----
function [i1, i2, v1, v2] = MOV_suppressor(v1_set, graph_flag)
% Solve loop equations for MOV-only surge suppressor
% Given input voltage v1 (scalar or vector), compute corresponding
values
% of i1 (input current), i2 (MOV current), and v2 (output voltage).

if nargin == 0
    v1_set = 680;    % input line voltage
    graph_flag = 1;
end

% circuit values
[r1 rL] = deal(1, 1000);    % line resistance; load resistance (ohms)

i1_span = linspace(0.01, 600, 3000)';

% MOV fit parameters and V --> I function
% (the low-voltage currents are wrong!!)
[k1, alpha] = deal(2.4611*10^-15.4, 4.0413);
[k2, beta] = deal(1.4628*10^-72.65, 26.2396);
i_MOV = @(v) k1*v.^alpha + k2*v.^beta;

for j = 1 : length(v1_set)
    v1 = v1_set(j);

    % attempt to solve for input current i1
    eqn_MOV = @(i) (i * (r1 + rL) - v1) / rL - i_MOV(v1 - i*r1);

    % look for zero-crossings of eqn_MOV
    eq = eqn_MOV(i1_span);
    zc = find(eq(1:end-1) .* eq(2:end) < 0);
    Num_roots = length(zc);
    if Num_roots == 0
        warning('\n MOV solver returned %d roots for v1 = %d
volts', Num_roots, v1);
        [i1(j),i2(j),v2(j)] = deal(NaN);
    else
        i1(j) = fzero(eqn_MOV, [i1_span(zc) i1_span(zc+1)]);
        i2(j) = i_MOV(v1 - i1(j)*r1);
        v2(j) = (i1(j) - i2(j)) * rL;
    end
end
if graph_flag

```

```
        figure(2); clf;
        plot(i1_span, eq); hold on;
        plot(i1, 0, 'ro');
        zoom on; grid on;
        xlabel('i1 span (amps)');
        drawnow;
        hold off;
    end

end

v1 = v1_set;

end
```

## Appendix C: Development of state equations and the MATLAB code used for the work presented in Chapter 5

### C.1 Laplace solution for the open-circuit voltage of the LSS validated with a SPICE simulation

– Matlab code used to produce Figure 5-3

```
function LSS_open_circuit_voltage_analysis
% LSS equivalent circuit
% Laplace solution for the open-circuit voltage of the LSS validated
with a SPICE simulation (SPICE data included)
% Capacitor initial charge = 100V

L1 = 2.7e-6;
C = 10e-6;
R1 = 7;
R2 = 1.1;
L2 = 6e-6;
R3 = 1e6;

A = R1+R2+R3 ;
B = R1^2 ;

format short e

a0 = 1000*C*R1
b3 = L1*L2*C
b2 = C*R1*L2 + A*L1*C
b1 = A*C*R1 + L2 - C*B
b0 = A

p = [b3 b2 b1 b0]

r = roots(p)

t = linspace (0,200e-6,10001);

f = @(a) a0*exp(a*t)/(3*b3*a^2+2*b2*a+b1);

% setup current I in output loop
I = zeros(size(t));

for j = 1:3
    I = I + f(r(j));
    Voc = I*1e6;
end

% SPICE data is read from a comma-separated values (CSV) file

M = csvread('LSS_OCV_2loops_spice.csv', 1,1); %reads data from the
% csv formatted file starting at row 1 and column 1
```

```
time_spice = M(:,2);      % takes all rows of column three
Voc_spice = M(:,3);      % takes all rows of column four

figure(1);clf;
plot (t*1e6,Voc,'linewidth', 2);hold on;
plot(time_spice*1e6, Voc_spice, 'xr','linewidth', 1);
legend('Laplace','Spice');
axis ([-10 200 0 1000])

xlabel('Time (us)'); ylabel('Voltage (V)');

end
```

## C.2 SPICE input file to trace the open-circuit voltage of the LSS

(The results obtained were included in the MATLAB code to validate the Laplace solution – Appendix C.1)

```
** LSS - Open-circuit Voltage **
```

```
** Circuit Description **
```

```
C1 1 0 10UF IC=1000V          ; Capacitance of 10µF with  
                               initial voltage of 1000 volts  
L1 1 2 2.7UH                 ; Inductor of 2.7 micro-henries  
R1 2 0 7                     ; Resistance of 7 ohms  
R2 2 3 1.1                   ; Resistance of 1.1 ohms  
L2 3 4 6UH                   ; Inductor of 6 micro-henries  
R3 4 0 1MEG                  ; Resistance of 1 meg-ohm
```

```
** Output Requests **
```

```
* Transient analysis from 0 to 100 us with a 1 us time  
increment and using initial conditions (UIC)
```

```
.TRAN 1US 100US UIC
```

```
* Plot the result of the transient analysis with the voltage  
at node 4
```

```
.PLOT TRAN V(4)
```

```
.PROBE V(4)
```

```
.END                          ; End of circuit file
```

### C.3 Laplace solution for the open-circuit voltage of the LSS validated with numerical simulations based on Euler and RK4 method

- MATLAB code LSS\_OCV\_Euler\_RK4 used to produce Figure 5-6(a)

```

%-----
-----
function LSS_OCV_Euler_and_RK4
% Solve for open-circuit voltage of the two loop LSS
% equivalent circuit using Euler and RK4 methods.
% Assume the capacitor is fully charged at time zero

R1 = 7;
C = 10e-6;
L1 = 2.7e-6;
R2 = 1.1;
L2 = 6e-6;
R3 = 1e6;
Vc0 = 1000;

a = R1/L1; b = 1/(L1*C);
c = R1/L2; d = (R1+R2+R3)/L2;
tic
A = R1+R2+R3 ;
B = R1^2 ;

format short e

a0 = 1000*C*R1
b3 = L1*L2*C
b2 = C*R1*L2 + A*L1*C
b1 = A*C*R1 + L2 - C*B
b0 = A

p = [b3 b2 b1 b0]

r = roots(p)

t = linspace (0,100e-6,10001);

f = @(h) a0*exp(h*t)/(3*b3*h^2+2*b2*h+b1);

% setup current I in output loop
I = zeros(size(t));

for j = 1:3
    I = I + f(r(j));
    Voc = I*1e6;
end
%
fignum = 3;
figure(fignum); clf;
plot(t*1e6, Voc, 'linewidth', 1);
zoom on; hold on;
toc

```

```

%-----
% DE definition for LSS circuit
function xdot = RLC_dot(t, x, flag, params)
    [x1 x2 x3] = deal(x(1), x(2), x(3));
    x1_dot = x2;
    x2_dot = -a*x2 - (b-a*c)*x1 - (a*d)*x3;
    x3_dot = c*x1-d*x3;
    xdot = [x1_dot; x2_dot; x3_dot];    % return column vector
end

% Euler solution of DEs: I = current; J = dI/dt
Nsteps = 1e6;
[I1, J, I2] = deal(zeros(Nsteps,1));
dt = 1e-11;
time = [0: Nsteps-1]*dt;

% choose integration method
% 1 = Euler; 2 = improved Euler; 3 = Euler with RLC_dot; 4 = RK4
METHOD = 2;
tic
switch METHOD

% Euler with fixed timesteps
case 1
    I1(1) = 0;
    J(1) = Vc0/L1; % integrate delta-function to give initial
condition
    I2(1) = 0;
    for n = 1 : Nsteps-1
        I1(n+1) = I1(n) + J(n)*dt;
        J(n+1) = J(n) + (-a*J(n) - (b-a*c)*I1(n) - a*d*I2(n)) *
dt;
        I2(n+1) = I2(n)+(c*I1(n)-d*I2(n))*dt;
    end

% RK4 with fixed timesteps
case 2
    X0(:,1) = [0; Vc0/L1; 0]; flag = ''; params = [];
    [t_out, X_out] = rk4fixed(@RLC_dot, time, X0, flag, params);
    time=t_out;
    I1 = X_out(:,1); J = X_out(:,2); I2 = X_out(:,3);
end

figure(fignum);
plot(time*1e6, I2*1e6, '--r', 'linewidth', 2);
axis ([-2 100 0 1000]);
legend('Laplace solution','Simulation with rk4fixed solver');
xlabel('Time (us)'); ylabel('Voltage (V)');
toc
end

```

## C.4 Development of state equations (5-13) - (5-17) for the MOV “off” state driven by the LSS

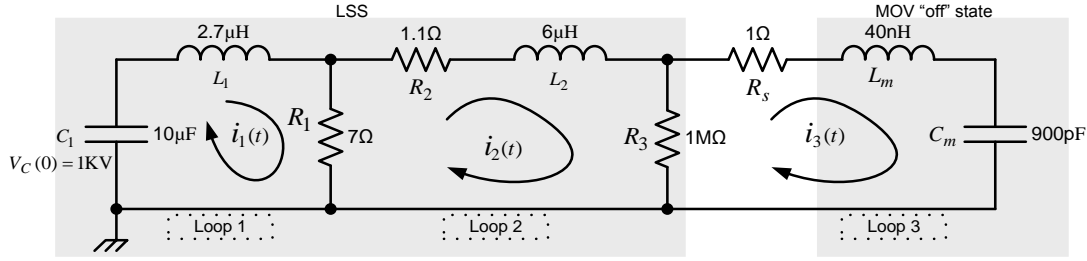


Figure C.4-1: MOV “off” state driven by the LSS (Combined equivalent circuit)

In order to solve this 3-loop circuit we will assume that the loop currents are  $i_1$ ,  $i_2$ , and  $i_3$ . The Laplace transformed network representation of Figure C.4-1 is given in Figure C.4- 2.

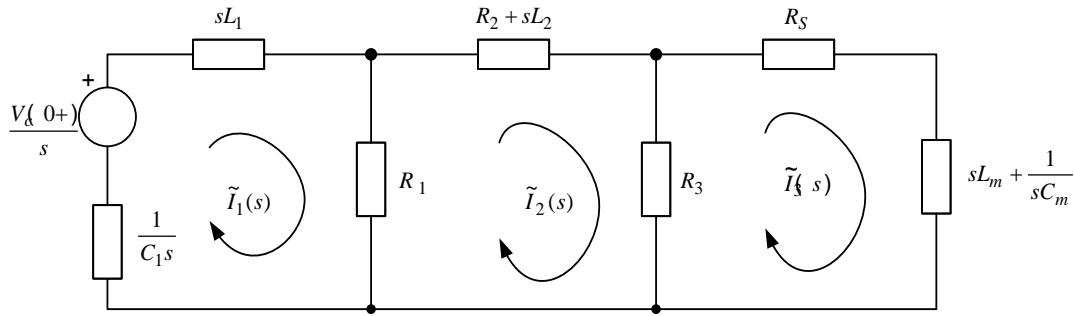


Figure C.4- 2: Transformed network for the circuit in Figure C.4-1

The loop equations for the circuit shown in Figure C.4- 2 are given by

$$\left(sL_1 + R_1 + \frac{1}{sC_1}\right)\tilde{I}_1(s) - R_1\tilde{I}_2(s) = -\frac{V_{c1}(0+)}{s} \quad (\text{C.4-1})$$

$$-R_1\tilde{I}_1(s) + (R_1 + R_2 + R_3 + sL_1)\tilde{I}_2(s) - R_3\tilde{I}_3(s) = 0 \quad (\text{C.4-2})$$

$$\left(R_3 + R_s + sL_m + \frac{1}{sC_m}\right)\tilde{I}_3(s) - R_3\tilde{I}_2(s) = 0 \quad (\text{C.4-3})$$

Let us first consider the first loop Eq. (C.4-1). Multiplying Eq (C.4-1) by  $sC_1$

$$(s^2L_1C_1 + sR_1C_1 + 1)\tilde{I}_1(s) - (sR_1C_1)\tilde{I}_2(s) = C_1V_{c1}(0+) \quad (\text{C.4-4})$$

Taking the inverse Laplace transform of Eq. (C.4-4)

$$\frac{d^2 i_1}{dt^2} L_1 C_1 + \frac{di_1}{dt} R_1 C_1 + i_1 - R_1 C_1 \frac{di_2}{dt} = C_1 V_{c1}(0+). \delta(t) \quad (\text{C.4-5})$$

Dividing Eq. (C.4-5) by  $L_1 C_1$ , we get

$$\frac{d^2 i_1}{dt^2} + \frac{R_1}{L_1} \frac{di_1}{dt} + \frac{1}{L_1 C_1} i_1 - \frac{R_1}{L_1} \frac{di_2}{dt} = \frac{V_{c1}(0+)}{L_1} . \delta(t) \quad (\text{C.4-6})$$

In order to solve this second-order DE numerically, we recast it into normal form: a system with two interacting first-order DEs. Let

$$\frac{di_1}{dt} = j_1 \quad (\text{C.4-7})$$

Then

$$\frac{dj_1}{dt} = -\frac{R_1}{L_1} j_1 - \frac{1}{L_1 C_1} i_1 - \frac{R_1}{L_1} \frac{di_2}{dt} + \frac{V_{c1}(0+)}{L_1} . \delta(t) \quad (\text{C.4-8})$$

Now let us consider the second-loop Eq. (C.4-2). Taking the inverse Laplace transform of Eq. (C.4-2), we get

$$i_2(R_1 + R_2 + R_3) + L_2 \frac{di_2}{dt} - i_1 R_1 - i_3 R_3 = 0 \quad (\text{C.4-9})$$

Dividing by  $L_2$  and rearranging

$$\frac{di_2}{dt} = \frac{R_1}{L_2} i_1 + \frac{R_3}{L_2} i_3 - \frac{R_1 + R_2 + R_3}{L_2} i_2 \quad (\text{C.4-10})$$

Substituting Eq. (C.4-10) in Eq. (C.4-8), we get

$$\frac{dj_1}{dt} = -\frac{R_1}{L_1} j_1 - \frac{1}{L_1 C_1} i_1 - \frac{R_1}{L_1} \left( \frac{R_1}{L_2} i_1 + \frac{R_3}{L_2} i_3 - \frac{R_1 + R_2 + R_3}{L_2} i_2 \right) + \frac{V_{c1}(0+)}{L_1} . \delta(t) \quad (\text{C.4-11})$$

Rearranging Eq. (C.4-11)

$$\frac{dj_1}{dt} = -\frac{R_1}{L_1}j_1 - \left( \frac{1}{L_1C_1} - \frac{R_1^2}{L_1L_2} \right) i_1 - \frac{R_1(R_1 + R_2 + R_3)}{L_1L_2} i_2 - \frac{R_1R_3}{L_1L_2} i_3 + \frac{V_{c1}(0+)}{L_1} \cdot \delta(t) \quad (\text{C.4-12})$$

Now let us consider the third-loop Eq. (C.4-3). Multiplying Eq. (C.4-3) by  $sC_m$

$$\tilde{I}_3(s)[1 + s(R_3 + R_S)C_m + s^2L_mC_m] - \tilde{I}_2(s)sR_3C_m = 0 \quad (\text{C.4-13})$$

Taking the inverse Laplace transform of Eq. (C.4-13), we get

$$\frac{d^2i_3}{dt^2}L_mC_m + \frac{di_3}{dt}(R_3 + R_S)C_m + i_3 - R_3C_m \frac{di_2}{dt} = 0 \quad (\text{C.4-14})$$

Dividing Eq. (C.4-14) by  $L_mC_m$

$$\frac{d^2i_3}{dt^2} + \frac{(R_3 + R_S)}{L_m} \frac{di_3}{dt} + \frac{1}{L_mC_m} i_3 - \frac{R_3}{L_m} \frac{di_2}{dt} = 0 \quad (\text{C.4-15})$$

In order to solve the second-order DE (C.4-15) numerically, we recast it into normal form: Let

$$\frac{di_3}{dt} = j_3 \quad (\text{C.4-16})$$

Then Eq. (C.4-15) can be written as

$$\frac{dj_3}{dt} = -\frac{(R_3 + R_S)}{L_m} j_3 - \frac{1}{L_mC_m} i_3 + \frac{R_3}{L_m} \left( \frac{R_1}{L_2} i_1 + \frac{R_3}{L_2} i_3 - \frac{R_1 + R_2 + R_3}{L_2} i_2 \right) \quad (\text{C.4-17})$$

Rearranging Eq. (C.4-17) gives

$$\frac{dj_3}{dt} = -\frac{(R_3 + R_S)}{L_m}j_3 + \frac{R_1R_3}{L_2L_m}i_1 - \frac{R_3(R_1 + R_2 + R_3)}{L_2L_m}i_2 + \left(\frac{R_3^2}{L_2L_m} - \frac{1}{L_mC_m}\right)i_3 \quad (\text{C.4-18})$$

Now the equations (C.4-7), (C.4-10), (C.4-12), (C.4-16) and (C.4-18) make up the set of state equations required to simulate Figure C.4-1 (same as Figure 5-9). These five equations can be written as state equations (5-13) - (5-17) provided we make the following substitutions:

$$a = R_1/L_1, \quad b = 1/L_1C, \quad c = R_1/L_2, \quad d = (R_1 + R_2 + R_3)/L_2, \quad e = R_3/L_2, \\ f = (R_3 + R_S)/L_m, \quad g = R_3/L_m, \quad \text{and} \quad h = 1/L_mC_m.$$

The impulse response that results from the delta function input in Eq. (C.4-12) can be taken care of by using the initial condition that arises from the impulse input, and making the input itself equal to zero. Hence the initial conditions would be  $i_1(0) = 0, j_1(0) = V_{C1}(0+)/L_1, i_2(0) = i_3(0) = j_3(0) = 0$ .

## C.5 Numerical simulation of the “off” state current in a MOV validated with a SPICE based simulation

– Matlab code used to produce Figure 5-10

```

%-----
function LSS_MOV_three_loops_ODE15S
% Solve for third loop current thru the "off" state of the MOV.

R1 = 7;
C = 10e-6;
L1 = 2.7e-6;
R2 = 1.1;
L2 = 6e-6;
R3 = 1e6
Rs = 1;
Lm = 40e-9;
Cm = 900e-12;
Vc0 = 100;

a = R1/L1, b = 1/(L1*C)
c = R1/L2, d = (R1+R2+R3)/L2
e = R3/L2, f = (R3+Rs)/Lm
g = R3/Lm, h = 1/(Lm*Cm)

fignum = 1;

%-----
% SPICE data is read from a comma-separated values (CSV) file

M = csvread('LSS_MOV_3loops_spice.csv', 1,1); %reads data from
% the csv formatted file starting at row 1 and column 1

time_spice = M(:,2); % takes all rows of column three
I3_spice = M(:,3); % takes all rows of column four

%-----
% DE definition for RLC circuit
function xdot = RLC_dot(t, x, flag, params)
[x1 x2 x3 x4 x5] = deal(x(1), x(2), x(3), x(4), x(5));
x1_dot = x2;
x2_dot = -a*x2 - (b-a*c)*x1 - a*d*x3 + a*e*x4;
x3_dot = c*x1 - d*x3 + e*x4;
x4_dot = x5;
x5_dot = -f*x5 + c*g*x1 - g*d*x3 + (e*g-h)*x4;
xdot = [x1_dot; x2_dot; x3_dot; x4_dot; x5_dot]; % return
% column vector
end

time = [0 1e-5];

tic

% ode15s with variable timesteps

```

```

X0(:,1) = [0; Vc0/L1; 0; 0; 0]; flag = ''; params = [];
options = odeset('RelTol', 1e-3);
[t_out, X_out] = ode15s(@RLC_dot, [time(1) time(end)], X0, options);
I1 = X_out(:,1); J = X_out(:,2); I2 = X_out(:,3); I3 = X_out(:,4); K
= X_out(:,5);

figure(fignum);
    subplot(211)

    plot(time*1e6, I3, '--r', 'linewidth', 2);hold on;
    plot(time_spice*1e6, I3_spice, '-k', 'linewidth', 1);
    legend('ode15s based simulation','SPICE based simulation');
    axis ([0 10 -0.13 0.4])
    title('(a)')
    xlabel('Time (us)'); ylabel('MOV "off" state current (A)');

    subplot(212)

    plot(diff(time)*1e6,'+-k');
    xlabel('Index number'); ylabel('Time step (us)');
    title('(b)')

toc
end

```

## C.6 Development of state equations (5-18) - (5-23) for the assumed fixed states of the MOV driven by the LSS

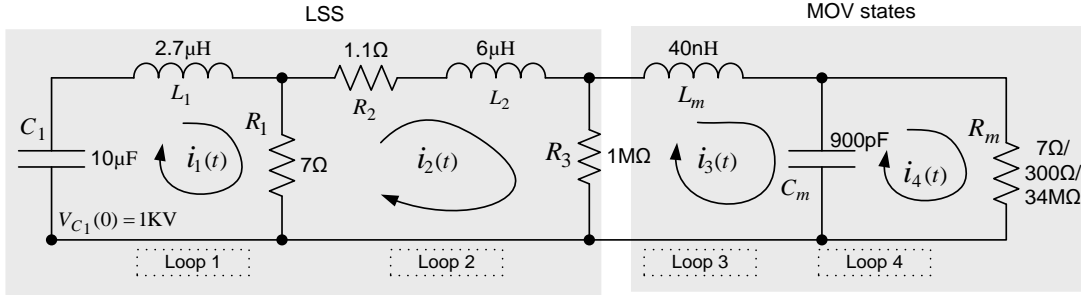


Figure C.6- 1: Fixed MOV states driven by transients from the LSS

In order to solve this 4-loop circuit we will assume that the loop currents are  $i_1$ ,  $i_2$ ,  $i_3$  and  $i_4$ . The Laplace transformed network representation of Figure C.6- 1 is given in Figure C.6- 2.

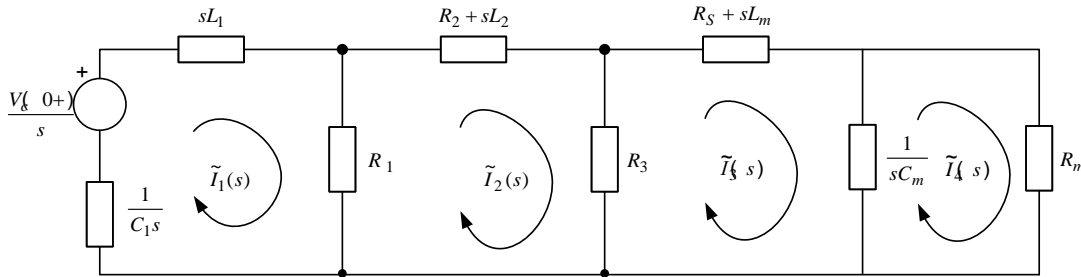


Figure C.6- 2: Transformed network for the circuit in Figure C.6- 1

$$\left(sL_1 + R_1 + \frac{1}{sC_1}\right)\tilde{I}_1(s) - R_1\tilde{I}_2(s) = -\frac{V_{c1}(0+)}{s} \quad (\text{C.6-1})$$

$$-R_1\tilde{I}_1(s) + (R_1 + R_2 + R_3 + sL_1)\tilde{I}_2(s) - R_3\tilde{I}_3(s) = 0 \quad (\text{C.6-2})$$

$$\left(R_3 + R_5 + sL_m + \frac{1}{sC_m}\right)\tilde{I}_3(s) - R_3\tilde{I}_2(s) - \frac{1}{sC_m}\tilde{I}_4(s) = 0 \quad (\text{C.6-3})$$

$$\left(R_m + \frac{1}{sC_m}\right)\tilde{I}_4(s) - \frac{1}{sC_m}\tilde{I}_3(s) = 0 \quad (\text{C.6-4})$$

Let us first consider the first loop Eq.(C.6-1). Multiplying Eq (C.6-1) by  $sC_1$

$$(s^2L_1C_1 + sR_1C_1 + 1)\tilde{I}_1(s) - (sR_1C_1)\tilde{I}_2(s) = C_1V_{c1}(0+) \quad (\text{C.6-5})$$

Taking the inverse Laplace transform of Eq. (C.6-5)

$$\frac{d^2 i_1}{dt^2} L_1 C_1 + \frac{di_1}{dt} R_1 C_1 + i_1 - R_1 C_1 \frac{di_2}{dt} = C_1 V_{c1}(0+). \delta(t) \quad (\text{C.6-6})$$

Dividing Eq. (C.6-6) by  $L_1 C_1$ , we get

$$\frac{d^2 i_1}{dt^2} + \frac{R_1}{L_1} \frac{di_1}{dt} + \frac{1}{L_1 C_1} i_1 - \frac{R_1}{L_1} \frac{di_2}{dt} = \frac{V_{c1}(0+)}{L_1} . \delta(t) \quad (\text{C.6-7})$$

In order to solve this second-order DE numerically, we recast it into normal form: a system with two interacting first-order DEs. Let

$$\frac{di_1}{dt} = j_1 \quad (\text{C.6-8})$$

Then

$$\frac{dj_1}{dt} = -\frac{R_1}{L_1} j_1 - \frac{1}{L_1 C_1} i_1 - \frac{R_1}{L_1} \frac{di_2}{dt} + \frac{V_{c1}(0+)}{L_1} . \delta(t) \quad (\text{C.6-9})$$

Now let us consider the second-loop Eq. (C.6-2). Taking the inverse Laplace transform of Eq. (C.6-2), we get

$$i_2(R_1 + R_2 + R_3) + L_2 \frac{di_2}{dt} - i_1 R_1 - i_3 R_3 = 0 \quad (\text{C.6-10})$$

Dividing by  $L_2$  and rearranging

$$\frac{di_2}{dt} = \frac{R_1}{L_2} i_1 + \frac{R_3}{L_2} i_3 - \frac{R_1 + R_2 + R_3}{L_2} i_2 \quad (\text{C.6-11})$$

Substituting Eq. (C.6-11) in Eq. (C.6-9), we get

$$\frac{dj_1}{dt} = -\frac{R_1}{L_1} j_1 - \frac{1}{L_1 C_1} i_1 - \frac{R_1}{L_1} \left( \frac{R_1}{L_2} i_1 + \frac{R_3}{L_2} i_3 - \frac{R_1 + R_2 + R_3}{L_2} i_2 \right) + \frac{V_{c1}(0+)}{L_1} . \delta(t) \quad (\text{C.6-12})$$

Rearranging Eq. (C.6-12)

$$\frac{dj_1}{dt} = -\frac{R_1}{L_1}j_1 - \left( \frac{1}{L_1C_1} - \frac{R_1^2}{L_1L_2} \right) i_1 - \frac{R_1(R_1 + R_2 + R_3)}{L_1L_2} i_2 - \frac{R_1R_3}{L_1L_2} i_3 + \frac{V_{c1}(0+)}{L_1} \cdot \delta(t) \quad (\text{C.6-13})$$

Now let us consider the third-loop Eq. (C.6-3). Multiplying it by  $sC_m$

$$\tilde{I}_3(s)[1 + s(R_3 + R_S)C_m + s^2L_mC_m] - \tilde{I}_2(s)sR_3C_m - \tilde{I}_4(s) = 0 \quad (\text{C.6-14})$$

Taking the inverse Laplace transform of Eq. (C.6-14), we get

$$\frac{d^2i_3}{dt^2}L_mC_m + \frac{di_3}{dt}(R_3 + R_S)C_m + i_3 - R_3C_m \frac{di_2}{dt} - i_4 = 0 \quad (\text{C.6-15})$$

Dividing Eq. (C.6-15) by  $L_mC_m$

$$\frac{d^2i_3}{dt^2} + \frac{(R_3 + R_S)}{L_m} \frac{di_3}{dt} + \frac{1}{L_mC_m} i_3 - \frac{R_3}{L_m} \frac{di_2}{dt} - \frac{1}{L_mC_m} i_4 = 0 \quad (\text{C.6-16})$$

In order to solve the second-order DE, Eq. (C.6-16) numerically, we recast it into normal form: Let

$$\frac{di_3}{dt} = j_3 \quad (\text{C.6-17})$$

Then Eq. (C.6-16) can be written as

$$\frac{dj_3}{dt} = -\frac{(R_3 + R_S)}{L_m} j_3 - \frac{1}{L_mC_m} i_3 + \frac{R_3}{L_m} \left( \frac{R_1}{L_2} i_1 + \frac{R_1}{L_2} i_3 - \frac{R_1 + R_2 + R_3}{L_2} i_2 \right) + \frac{1}{L_mC_m} i_4 \quad (\text{C.6-18})$$

Rearranging Eq. (C.6-18) gives

$$\frac{dj_3}{dt} = -\frac{(R_3 + R_S)}{L_m} j_3 + \frac{R_1 R_3}{L_2 L_m} i_1 - \frac{R_3(R_1 + R_2 + R_3)}{L_2 L_m} i_2 + \left( \frac{R_3^2}{L_2 L_m} - \frac{1}{L_m C_m} \right) i_3 + \frac{1}{L_m C_m} i_4 \quad (\text{C.6-19})$$

Now let us consider the fourth loop Eq. (C.6-4). Multiplying it by  $sC_m$

$$(sR_m C_m - 1)\tilde{I}_4(s) - \tilde{I}_3(s) = 0 \quad (\text{C.6-20})$$

Taking the inverse Laplace transform of Eq. (C.6-14), we get

$$R_m C_m \frac{di_4}{dt} + i_4 - i_3 = 0 \quad (\text{C.6-21})$$

Dividing Eq. (C.6-21) by  $R_m C_m$

$$\frac{di_4}{dt} = \frac{1}{R_m C_m} i_3 - \frac{1}{R_m C_m} i_4 \quad (\text{C.6-22})$$

Now the equations (C.6-8), (C.6-11), (C.6-13), (C.6-17), (C.6-19) and (C.6-22) make up the set of six state equations required to simulate the working of Figure C.6- 1 (same as Figure 5-12). These six equations can be written as state equations (5-18) - (5-23) provided we make the following substitutions:

$$a = R_1/L_1, \quad b = 1/L_1 C, \quad c = R_1/L_2, \quad d = (R_1 + R_2 + R_3)/L_2, \quad e = R_3/L_2, \\ f = g = R_3/L_m, \quad h = 1/L_m C_m, \quad \text{and } k = 1/C_m R_m.$$

The impulse response that results from the delta function input in Eq. (C.6-13) can be taken care of by using the initial condition that arises from the impulse input, and making the input itself equal to zero. Hence the initial conditions would be  $i_1(0) = 0$ ,  $j_1(0) = V_{C1}(0+)/L$ ,  $i_2(0) = i_3(0) = j_3(0) = i_4(0) = 0$ , where  $V_{C1}(0+)$  is the initial voltage of the LSS capacitor or the amplitude of the surge voltage generated by the LSS.

## C.7 Numerical simulation of an assumed fixed state of an MOV validated with a SPICE based simulation

– MATLAB code used to produce Figure 5-13(c)

```

%-----
function LSS_MOV_four_loops_Rm_7ohms

% Solve for the third loop current (out of 4) thru Rm.
%
% ODE15s (with jacobian). Works well with RelTol = 1e-3 & 1e-4.

% Change Rm =300 ohms and Rm = 34 Mohms for the other two
simulations;
% respective SPICE data has to be imported for validation

R1 = 7;
C = 10e-6;
L1 = 2.7e-6;
R2 = 1.1;
L2 = 6e-6;
R3 = 1e6;
Rs = 0;
Lm = 40e-9;
Cm = 900e-12;
Rm = 7;
Vc0 = 1000;

a = R1/L1; b = 1/(L1*C);
c = R1/L2; d = (R1+R2+R3)/L2;
e = R3/L2; f = (R3+Rs)/Lm;
g = R3/Lm; h = 1/(Lm*Cm);
k = 1/(Cm*Rm);

fignum = 1;

%-----

% SPICE data is read from a comma-separated values (CSV) file

M = csvread('LSS_MOV_4loops_spice.csv', 1,1); %reads data from the
csv
% formatted file starting at row 1 and column 1

time_spice = M(:,2); % takes all rows of column three
I3_spice = M(:,3); % takes all rows of column four

%-----
% DE definition for RLC circuit
function xdot = RLC_dot(t, x, flag, params)
    [x1 x2 x3 x4 x5 x6] = deal(x(1), x(2), x(3), x(4), x(5),
x(6));
    x1_dot = x2;
    x2_dot = -a*x2 - (b-a*c)*x1 - a*d*x3 + a*e*x4;

```

```

x3_dot = c*x1 - d*x3 + e*x4;
x4_dot = x5;
x5_dot = -f*x5 + c*g*x1 - g*d*x3 + (e*g-h)*x4 + h*x6;
x6_dot = k*x4 - k*x6;
xdot = [x1_dot; x2_dot; x3_dot; x4_dot; x5_dot; x6_dot]; %
return column vector
end

time = [0 0.2e-4];

% set initial conditions
X0(:,1) = [0; Vc0/L1; 0; 0; 0; 0]; flag = ''; params = [];

% define Jacobian matrix
J = [ 0      1  0      0      0  0
      (a*c-b) -a -a*d  a*e    0  0
      c      0 -d     e     0  0
      0      0  0     0     1  0
      c*g    0 -g*d  (e*g-h) -f  h
      0      0  0     k     0 -k];

options = odeset('RelTol', 1e-4 , 'Stats', 'on', 'Jac', J);

tic
[t_out, X_out] = ode15s(@RLC_dot, [time(1) time(end)], X0,
options);
toc

time = t_out;
I1 = X_out(:,1); J1 = X_out(:,2); I2 = X_out(:,3); I3 =
X_out(:,4); J3 = X_out(:,5); I4 = X_out(:,6);

figure(fignum);
plot(time*1e6, I3, '--r', 'linewidth', 2);hold on;
plot(time_spice*1e6, I3_spice, '-k', 'linewidth', 1);
legend('ode15s based simulation','SPICE based simulation');
title('(c)')
xlabel('Time (us)'); ylabel('Loop 3 / MOV current (A)');

figure(2);
plot(time(1:end-1)*1e6,diff(time)*1e6,'-+k');
title('Diff(time) Vs Index - (ode23tb - with Jac: Rm = 500 ohms;
RelTol = 1e-4)')
xlabel('Time (us)'); ylabel('Time difference (us)');

end

```

[By changing  $R_m$  to  $300 \Omega$  and  $34 M\Omega$  in the code, the other two simulations can be performed to produce Figure 5-13 (a) and (b) respectively; the respective SPICE data has to be imported for validation]

## Appendix D: Development of state equations and the MATLAB code used for the work presented in Chapter 6

### D.1 Development of state equations(6-2) - (6-7) for an MOV driven by the LSS

The complete equivalent circuit for this situation was given in Figure 6-3 and is repeated here for convenience as Figure D.1-1.

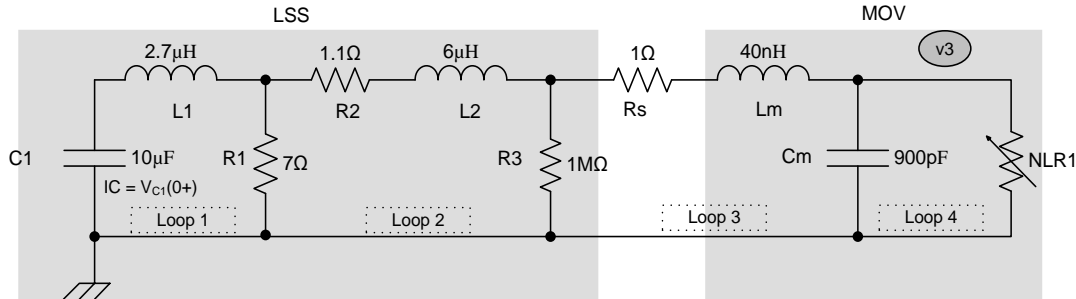


Figure D.1-1: Overall equivalent circuit for an MOV driven by an LSS

In order to solve this 4-loop circuit we will assume that the loop currents are  $i_1$ ,  $i_2$ ,  $i_3$  and  $i_4$ .

Considering loop 1 and writing the KVL equation,

$$V_{C1}(0+) \theta(t) - \frac{1}{C_1} \int i_1 dt - L_1 \frac{di_1}{dt} - R_1(i_1 - i_2) = 0 \quad (D.1-1)$$

where  $\theta(t)$  is the Heaviside function and  $V_{C1}(0+) \theta(t)$  is the initial voltage of the capacitor  $C_1$ .

Differentiating Eq. (D.1-1), we get

$$V_{C1}(0+) \delta(t) - \frac{1}{C_1} i_1 - L_1 \frac{d^2 i_1}{dt^2} - R_1 \left( \frac{di_1}{dt} - \frac{di_2}{dt} \right) = 0 \quad (D.1-2)$$

Rearranging Eq. (D.1-2)

$$\frac{d^2 i_1}{dt^2} = \frac{V_{C1}(0+)}{L_1} \delta(t) - \frac{1}{L_1 C_1} i_1 - \frac{R_1}{L_1} \left( \frac{di_1}{dt} - \frac{di_2}{dt} \right) \quad (D.1-3)$$

Considering the auxiliary:

$$\frac{di_1}{dt} = j_1 \quad (D.1-4)$$

Now Eq. (D.1-3) can be written as

$$\frac{dj_1}{dt} = -\frac{R_1}{L_1}j_1 - \frac{1}{L_1C_1}i_1 - \frac{R_1}{L_1}\frac{di_2}{dt} \quad (\text{D.1-5})$$

where the exposed  $\delta$ -function has been eliminated by making the initial condition  $j_1(0) = V_{C1}(0+)/L_1$ .

Let us consider loop-2 now; taking KVL results in

$$i_2(R_1 + R_2 + R_3) + L_2\frac{di_2}{dt} - i_1R_1 - i_3R_3 = 0 \quad (\text{D.1-6})$$

Dividing by  $L_2$  and rearranging

$$\frac{di_2}{dt} = \frac{R_1}{L_2}i_1 - \frac{R_1 + R_2 + R_3}{L_2}i_2 + \frac{R_3}{L_2}i_3 \quad (\text{D.1-7})$$

By substituting Eq. (D.1-7) in Eq. (D.1-5), we get

$$\frac{dj_1}{dt} = -\frac{R_1}{L_1}j_1 - \frac{1}{L_1C_1}i_1 - \frac{R_1}{L_1}\left(\frac{R_1}{L_2}i_1 - \frac{R_1 + R_2 + R_3}{L_2}i_2 + \frac{R_3}{L_2}i_3\right) \quad (\text{D.1-8})$$

Rearranging Eq. (D.1-8)

$$\frac{dj_1}{dt} = -\frac{R_1}{L_1}j_1 - \left(\frac{1}{L_1C_1} - \frac{R_1^2}{L_1L_2}\right)i_1 - \frac{R_1(R_1 + R_2 + R_3)}{L_1L_2}i_2 - \frac{R_1R_3}{L_1L_2}i_3 \quad (\text{D.1-9})$$

Moving on to loop-3, let us take KVL again

$$(R_3 + R_S)i_3 + L_m\frac{di_3}{dt} + \frac{1}{C_m}\int i_3 dt - R_3i_2 - \frac{1}{C_m}\int i_4 dt = 0 \quad (\text{D.1-10})$$

Differentiating Eq. (D.1-10), we get

$$\frac{di_3}{dt}(R_3 + R_S) + \frac{d^2i_3}{dt^2}L_m + \frac{1}{C_m}i_3 - R_3\frac{di_2}{dt} - \frac{1}{C_m}i_4 = 0 \quad (\text{D.1-11})$$

Rearranging Eq. (D.1-11),

$$\frac{d^2i_3}{dt^2} + \frac{(R_3 + R_S)}{L_m}\frac{di_3}{dt} + \frac{1}{L_mC_m}i_3 - \frac{R_3}{L_m}\frac{di_2}{dt} - \frac{1}{L_mC_m}i_4 = 0 \quad (\text{D.1-12})$$

Introducing auxiliary,

$$\frac{di_3}{dt} = j_3 \quad (\text{D.1-13})$$

Converting Eq. (D.1-12) into a first-order DE, we get

$$\frac{dj_3}{dt} = -\frac{(R_3 + R_S)}{L_m} j_3 - \frac{1}{L_m C_m} i_3 + \frac{R_3}{L_m} \frac{di_2}{dt} + \frac{1}{L_m C_m} i_4 \quad (\text{D.1-14})$$

The current  $i_4$  is the current through the nonlinear resistance of the MOV model and is assumed to be governed by Eq. (6-1) which is repeated here as Eq. (D.1-15).

$$i_4 = K_1 v_3^{\alpha_1} + K_2 v_3^{\alpha_2} \quad (\text{D.1-15})$$

By substituting Eqs. (D.1-15) and (D.1-7) in Eq. (D.1-14), we get

$$\begin{aligned} \frac{dj_3}{dt} = & -\frac{(R_3 + R_S)}{L_m} j_3 + \frac{R_3}{L_m} \left( \frac{R_1}{L_2} i_1 - \frac{R_1 + R_2 + R_3}{L_2} i_2 + \frac{R_3}{L_2} i_3 \right) - \frac{1}{L_m C_m} i_3 \\ & + \frac{1}{L_m C_m} (K_1 v_3^{\alpha_1} + K_2 v_3^{\alpha_2}) \end{aligned} \quad (\text{D.1-16})$$

Rearranging Eq. (D.1-16)

$$\begin{aligned} \frac{dj_3}{dt} = & -\frac{(R_3 + R_S)}{L_m} j_3 + \frac{R_1 R_3}{L_2 L_m} i_1 - \frac{R_3 (R_1 + R_2 + R_3)}{L_2 L_m} i_2 \\ & + \left( \frac{R_3^2}{L_2 L_m} - \frac{1}{L_m C_m} \right) i_3 + \frac{1}{L_m C_m} (K_1 v_3^{\alpha_1} + K_2 v_3^{\alpha_2}) \end{aligned} \quad (\text{D.1-17})$$

Let us consider the nodal voltage  $v_4$  now; since this is the voltage across the capacitor  $C_m$ , we have

$$v_4 = \frac{1}{C_m} \int (i_3 - i_4) dt \quad (\text{D.1-18})$$

Differentiating Eq.(D.1-18), we get

$$\frac{dv_4}{dt} = \frac{1}{C_m} (i_3 - i_4) \quad (\text{D.1-19})$$

Substituting Eq. (D.1-15) in Eq. (D.1-19)

$$\frac{dv_4}{dt} = \frac{1}{C_m} (i_3 - K_1 v_3^{\alpha_1} - K_2 v_3^{\alpha_2}) \quad (\text{D.1-20})$$

Now the equations (D.1-4), (D.1-9), (D.1-7), (D.1-13), (D.1-17) and (D.1-20) make up the set of six state equations corresponding to the state variables  $i_1, j_1, i_2, i_3, j_3$  and  $v_3$ . This set of six state equations were successfully used to simulate the working of Figure D.1-1 (same as Figure 6-3). These six equations can be written as state equations (6-2) - (6-7) provided we make the following substitutions:

$$a = R_1/L_1, \quad b = 1/L_1 C, \quad c = R_1/L_2, \quad d = (R_1 + R_2 + R_3)/L_2, \quad e = R_3/L_2, \\ f = (R_3 + R_S)/L_m, \quad g = R_3/L_m, \quad h = 1/L_m C_m, \quad \text{and} \quad k = 1/C_m.$$

The initial conditions for this simulation are  $i_1(0) = 0, j_1(0) = V_{C1}(0+)/L, i_2(0) = i_3(0) = j_3(0) = v_4(0) = 0$ , where  $V_{C1}(0+)$  is the initial voltage of the LSS capacitor or the amplitude of the surge voltage generated by the LSS.

## D.2 Numerical simulation and validations of an MOV (1<sup>st</sup> stage of an TVSS/SPD) driven by an LSS

– MATLAB code (LSS\_MOV\_with\_nonlinearR.m ) used to produce figures from Figure 6-4 to Figure 6-7.

```

%-----
function LSS_MOV_ODE15S

% Comparison of simulated MOV current and voltage
% (with Lm & Cm & nonlinear R) with those obtained using the LSS.
% MOV used; 275L40C : MOV model used; Power-law based model
% ODE solver used: ode15s (with routine to return jacobian).

R1 = 7;
C = 10e-6;
L1 = 2.7e-6;
R2 = 1.1;
L2 = 6e-6;
R3 = 1e6;
Rs = 1;
Lm = 40e-9;
Cm = 900e-12;

Vc0 = 1000;

a = R1/L1; b = 1/(L1*C);
c = R1/L2; d = (R1+R2+R3)/L2;
e = R3/L2; f = (R3+Rs)/Lm;
g = R3/Lm; h = 1/(Lm*Cm);
k = 1/Cm;

% values from polynomial fit
[k1, alpha] = deal(0, 4.0413);
[k2, beta] = deal(3.4628*10^-72.65, 26.2396);

% changed to obtain a reduced error in energy absorbed by the MOV
% [k2, beta] = deal(2.4496*10^-50.15, 18.3338);

fignum = 1;

% DE definition for RLC circuit
function xdot = RLC_dot(t, x, flag, params)...
    [x1 x2 x3 x4 x5 x6] = deal(x(1), x(2), x(3), x(4), x(5), x(6));
    x1_dot = x2;
    x2_dot = -a*x2 - (b-a*c)*x1 - a*d*x3 + a*e*x4;
    x3_dot = c*x1 - d*x3 + e*x4;
    x4_dot = x5;
    x5_dot = -f*x5 + c*g*x1 - g*d*x3 + (e*g-h)*x4 + ...
        h*(k1*x6^alpha + k2*x6^beta);
    x6_dot = k*x4 - k*(k1*x6^alpha + k2*x6^beta);

% return column vector
xdot = [x1_dot; x2_dot; x3_dot; x4_dot; x5_dot; x6_dot];

```

```

end

% The function that returns the Jacobian matrix

function J = FJac(t,x)

    J(6,6)=0;

    J(1,2)=1;

    J(2,1)=(a*c-b);
    J(2,2)=-a;
    J(2,3)=-a*d;
    J(2,4)=a*e;

    J(3,1)=c;
    J(3,3)=-d;
    J(3,4)=e;

    J(4,5)=1;

    J(5,1)=c*g;
    J(5,3)=-g*d;
    J(5,4)=(e*g-h);
    J(5,5)=-f;
    J(5,6)=h*(k1*alpha*x(6)^(alpha-1)+ k2*beta*x(6)^(beta-1));

    J(6,4)=k;
    J(6,6)=-k*(k1*alpha*x(6)^(alpha-1)+ k2*beta*x(6)^(beta-1));

end

time = [0 1e-4];

X0(:,1) = [0; Vc0/L1; 0; 0; 0; 0]; flag = ''; params = [];
options = odeset('RelTol', 1e-3,'Stats','on','Jac',@FJac);

tic
[t_out, X_out] = ode15s(@RLC_dot, [time(1) time(end)], X0, options);
toc

time = t_out;
I1 = X_out(:,1); J1 = X_out(:,2); I2 = X_out(:,3); I3 = X_out(:,4);
J3 = X_out(:,5); V3 = X_out(:,6);

% LSS data (start)

%reads data from the csv formatted file starting at row 17 and
column 1
M = csvread('1KV_Surge_275L40C.csv', 17,1);

% just to see the first few lines (prints the first five rows and
all the columns of the current M)
M(1:5,:)

```

```

t = M(:,4);
I = M(:,3);      % takes all rows of column three
V = M(:,2);      % takes all rows of column two

% LSS data (end)

figure(fignum);

subplot(311)

plot(time*1e6, I3*10,'--r', 'linewidth', 2);hold on;
plot (t*1e6,I*10,'-r');hold on;

plot(time*1e6, (Lm*J3)+V3,'--b', 'linewidth', 2);hold on;
plot (t*1e6,V,'-b');hold on;

axis([-5 90 -40 1200])
legend('I_m_o_v(Simulation)', 'I_m_o_v(Validation)',...
      'V_m_o_v(Simulation)', 'V_m_o_v(Validation)')
title(' (a) ');
xlabel('Time (us)'); ylabel('Current (x10) (A) / Voltage (V)');

subplot(312)

Pcs = V3.*(I3/1e3);
plot (time*1e6,Pcs,'--g', 'linewidth', 2);hold on;
Plss = V.*(I/1e3);
plot (t*1e6,Plss,'k');

legend('P_m_o_v(Simulation)', 'P_m_o_v(Validation)')
xlabel('time(us)');
ylabel('Power (kW)');
zoom on; axis tight;
axis([-5 90 0 70]);
title(' (b) ');

subplot(313)

Ecs = (cumsum(Pcs(1:end-1).*diff(time)))*1e3;
plot (time(1:end-1)*1e6,Ecs,'--g', 'linewidth', 2);hold on;

t1 = M(11,4);
t2 = M(12,4);
dt = t2-t1;
Elss = cumsum(Plss*1e3)*dt;
plot (t*1e6,Elss,'k');hold on;

xlabel('time(us)');
ylabel('Energy (J)');
zoom on; axis tight;
axis([-5 90 0 1.2]);
title(' (c) ');
legend('E_m_o_v(Simulation)', 'E_m_o_v(Validation)',...
      'Location', 'SouthEast')

figure(2);

```

```

plot(time(1:end-1)*1e6,diff(time)*1e6,'-+k');
title('Diff(time) Vs Index - ...
(ode23t - with Jac routine: RelTol = 1e-3)')
xlabel('Time (us)'); ylabel('Time difference (us)');

figure(3);

plot(V, I,'--k', 'linewidth', 2);grid on;hold on;
plot(V3, I3,'-m', 'linewidth', 1);grid on;hold on;
plot(V3, I3,'-m', 'linewidth', 2);grid on;hold on;

legend('Validation','Initial simulation',...
'Improved simulation','Location','Best');
xlabel('MOV voltage (V)'); ylabel('MOV current (A)');

end

```

### D.3 PSpice source file for simulating an MOV (1<sup>st</sup> stage of a TVSS) driven by an LSS

\*\* MOV output voltage \*\*

\*\* Circuit Description \*\*

C1 1 0 10UF IC=1000V ; Capacitance of 10  $\mu$ F with initial voltage of 1000 V  
L1 1 2 2.7UH ; Inductor of 2.7  $\mu$ H  
R1 2 0 7 ; Resistance of 7  $\Omega$   
R2 2 3 1.1 ; Resistance of 1.1  $\Omega$   
L2 3 4 6UH ; Inductor of 6  $\mu$ H  
R3 4 0 1MEG ; Resistance of 1 M $\Omega$   
R4 5 6 1 ; Resistance 1 ohm  
X 6 0 V20E275 ; Call to sub circuit V20E275

\*\* Analysis Requests \*\*

VX 4 5 DC 0V ; Measures current through R4

\*\* Output Requests \*\*

\* Transient analysis from 0 to 100  $\mu$ s with a 0.1  $\mu$ s time increment and using initial conditions (UIC)

.TRAN 0.1US 100US 0US 0.1US UIC

\* Print the result of the transient analysis with the voltage at node 6 and current through R4

.PRINT TRAN V(6) I(VX)

\*\*\*\*\*

\*Varistor PSpice Model Netlist\*

\*\*\*\*\*

\* Littelfuse Inc.  
\* March 25, 2003  
\* Version 4.2

\* Representing typical characteristics for the following UltraMOV series varistor:  
\* V20E275

\*

.SUBCKT V20E275 1 2 PARAMS: TOL=0

X1 1 2 UMOV PARAMS: T=[1+TOL/100] L=12nH C=900pF a1=2.726

+ a2=5.574E-2 a3=1.837E-2 a4=-3.412E-3 a5=1.362E-2 a6=-3.772E-2

.ENDS V20E275

\*

\* Part of the code common to all UltraMOV series varistors

.SUBCKT UMOV 1 2 PARAMS: T=1 C=1pF L=1nH a1=1 a2=0 a3=0 a4=0 a5=0

```

+      a6=100u a7=100u
E_non_lin      3 1      VALUE [T*(
+      10^(
+      +a1+a2*(log10(limit(v(4),a7,1g))-3)
+      +a3*2^(-log10(limit(v(4),a7,1g))+3)
+      +a4*exp(-log10(limit(v(4),a7,1g))+3)
+      +a5*exp(log10(limit(v(4),a7,1g))-3)
+      +a6*2^(log10(limit(v(4),a7,1g))-3)
+      )
+      -10^(
+      a1+a2*(log10(-limit(v(4),-1g,-a7))-3)
+      +a3*2^(-log10(-limit(v(4),-1g,-a7))+3)
+      +a4*exp(-log10(-limit(v(4),-1g,-a7))+3)
+      +a5*exp(log10(-limit(v(4),-1g,-a7))-3)
+      +a6*2^(log10(-limit(v(4),-1g,-a7))-3)
+      )
+      +limit(v(4)/a7*v(8),-v(8),v(8))
+      )]
L_series      5 6 [L]
H_H1      4 0 VH_H1 1k
VH_H1      5 70 0V
R_R2      0 4 1G
R_series      6 2 100u
V_V1      3 70 0V
E_x_zero      8 0      VALUE [10^(
+      a1+a2*(log10(a7/1e3))
+      +a3*2^(-log10(a7/1e3))
+      +a4*exp(-log10(a7/1e3))
+      +a5*exp(log10(a7/1e3))
+      +a6*2^(log10(a7/1e3))
+      )]
R_x_zero      8 0 1G
C_parallel      1 5 [C]
.ENDS UMOV

*
.END ; End of circuit file

```

#### D.4 Development of state equations (6-9) - (6-15) for a 2-stage (MOV followed by a line-filter) TVSS driven by an LSS

The complete equivalent circuit for this situation was given in Figure 6-12 and is repeated here for convenience as Figure D.4-1.

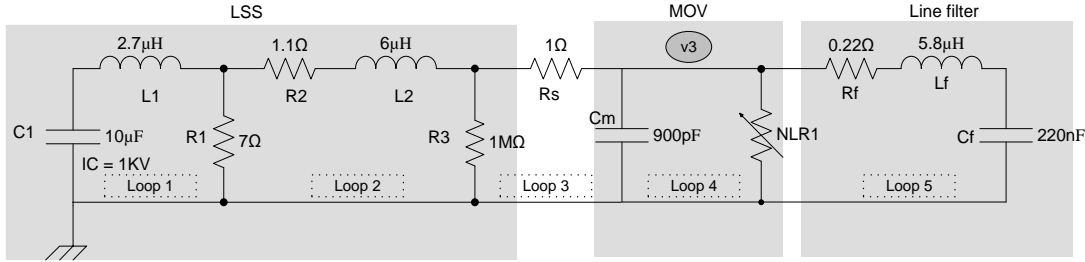


Figure D.4-1: LSS driving the first two stages of a category B protection unit

We will consider five loop currents  $i_1$ ,  $i_2$ ,  $i_3$ ,  $i_4$  and  $i_5$  for the loops shown in Figure D.4-1 and also the nodal voltage  $v_3$  across the nonlinear resistance  $NLR_1$ , as the current through it is a function of this voltage.

Since the first two loops of this circuit (the LSS) are identical to the one given in the 4-loop circuit of Figure D.1-1, the following three state equations remain unchanged.

$$\frac{di_1}{dt} = j_1 \quad (D.4-1)$$

$$\frac{dj_1}{dt} = -\frac{R_1}{L_1}j_1 - \left( \frac{1}{L_1C_1} - \frac{R_1^2}{L_1L_2} \right) i_1 - \frac{R_1(R_1 + R_2 + R_3)}{L_1L_2} i_2 - \frac{R_1R_3}{L_1L_2} i_3 \quad (D.4-2)$$

$$\frac{di_2}{dt} = \frac{R_1}{L_2}i_1 - \frac{R_1 + R_2 + R_3}{L_2}i_2 + \frac{R_3}{L_2}i_3 \quad (D.4-3)$$

Considering loop-3 and writing the KVL equation, we get

$$(R_3 + R_5)i_3 + \frac{1}{C_m} \int i_3 dt - R_3i_2 - \frac{1}{C_m} \int i_4 dt = 0 \quad (D.4-4)$$

Differentiating Eq.(D.4-4), we get

$$\frac{di_3}{dt}(R_3 + R_S) + \frac{1}{C_m}i_3 - R_3\frac{di_2}{dt} - \frac{1}{C_m}i_4 = 0 \quad (\text{D.4-5})$$

Rearranging Eq.(D.4-5), we get

$$\frac{di_3}{dt} = \frac{R_3}{(R_3 + R_S)}\frac{di_2}{dt} - \frac{1}{C_m(R_3 + R_S)}i_3 + \frac{1}{C_m(R_3 + R_S)}i_4 \quad (\text{D.4-6})$$

The current  $(i_4 - i_5)$  is the current through the nonlinear resistance of the MOV model and is assumed to be governed by Eq. (6-8), which is repeated here as Eq. (D.4-7)

$$i_4 - i_5 = K_2v_3^{\alpha_2} \quad (\text{D.4-7})$$

By substituting Eqs. (D.4-3) and (D.4-7) in Eq.(D.4-6), we get

$$\begin{aligned} \frac{di_3}{dt} = \frac{R_3}{(R_3 + R_S)} \left( \frac{R_1}{L_2}i_1 - \frac{R_1 + R_2 + R_3}{L_2}i_2 + \frac{R_3}{L_2}i_3 \right) - \frac{1}{C_m(R_3 + R_S)}i_3 \\ + \frac{1}{C_m(R_3 + R_S)}(i_5 + K_2v_3^{\alpha_2}) \end{aligned} \quad (\text{D.4-8})$$

Rearranging Eq. (D.4-8), we get

$$\begin{aligned} \frac{di_3}{dt} = \frac{R_3R_1}{L_2(R_3 + R_S)}i_1 - \frac{R_3(R_1 + R_2 + R_3)}{L_2(R_3 + R_S)}i_2 + \frac{1}{(R_3 + R_S)} \left( \frac{R_3^2}{L_2} - \frac{1}{C_m} \right) i_3 \\ + \frac{K_2}{C_m(R_3 + R_S)}v_3^{\alpha_2} + \frac{1}{C_m(R_3 + R_S)}i_5 \end{aligned} \quad (\text{D.4-9})$$

Let us consider the nodal voltage  $v_3$  now; since this is the voltage across the capacitor  $C_m$ , we have

$$v_3 = \frac{1}{C_m} \int (i_3 - i_4) dt \quad (\text{D.4-10})$$

Differentiating and substituting for  $i_4$  from Eq. (D.4-7), we get

$$\frac{dv_3}{dt} = \frac{1}{C_m}(i_3 - i_5 - K_2 v_3^{\alpha_2}) \quad (\text{D.4-11})$$

Considering loop-5 and writing the KVL equation, we get

$$v_3 = R_f i_5 + L_f \frac{di_5}{dt} + \frac{1}{C_f} \int i_5 dt \quad (\text{D.4-12})$$

Differentiating and substituting for  $\frac{dv_3}{dt}$  from Eq. (D.4-11), we get

$$\frac{1}{C_m}(i_3 - i_5 - K_2 v_3^{\alpha_2}) = R_f \frac{di_5}{dt} + L_f \frac{d^2 i_5}{dt^2} + \frac{1}{C_f} i_5 \quad (\text{D.4-13})$$

Rearranging Eq. (D.4-13), we get

$$\frac{d^2 i_5}{dt^2} = \frac{1}{L_f C_m} i_3 - \frac{1}{L_f} \left( \frac{1}{C_m} + \frac{1}{C_f} \right) i_5 - \frac{1}{L_f C_m} K_2 v_3^{\alpha_2} - \frac{R_f}{L_f} \frac{di_5}{dt} \quad (\text{D.4-14})$$

Introducing the auxiliary

$$\frac{di_5}{dt} = j_5 \quad (\text{D.4-15})$$

Now Eq. (D.4-14) can be written as

$$\frac{dj_5}{dt} = \frac{1}{L_f C_m} i_3 - \frac{1}{L_f} \left( \frac{1}{C_m} + \frac{1}{C_f} \right) i_5 - \frac{R_f}{L_f} j_5 - \frac{1}{L_f C_m} K_2 v_3^{\alpha_2} \quad (\text{D.4-16})$$

Now the equations (D.4-1), (D.4-2), (D.4-3), (D.4-9), (D.4-11), (D.4-15) and (D.4-16) make up the set of seven state equations corresponding to the state variables  $i_1, j_1, i_2, i_3, v_3, i_5$  and  $j_5$ . This set of seven state equations were successfully used to simulate the working of Figure D.4-1 (same as Figure 6-12). These seven equations can be written as state equations (6-9) - (6-15) provided we make the following substitutions:

$a = R_1/L_1$  ,  $b = 1/L_1C$  ,  $c = R_1/L_2$  ,  $d = (R_1 + R_2 + R_3)/L_2$  ,  $e = R_3/L_2$  ,  $f = R_3/(R_3 + R_S)$  ,  $g = 1/C_m (R_3 + R_S)$  ,  $h = 1/L_f C_m$  ,  $k = 1/L_f C_f$  ,  $l = 1/C_m$  and  $m = R_f/L_f$

The initial conditions for the simulation are  $i_1(0) = 0$  ,  $j_1(0) = V_{C_1}(0+)/L$  ,  $i_2(0) = i_3(0) = v_3(0) = i_5(0) = j_5(0) = 0$  . As before, the value given for  $j_1(0)$  results due to the initial voltage  $V_{C_1}(0+)$  of the capacitor  $C_1$  , which is the amplitude of the surge voltage generated by the LSS.

## D.5 Numerical simulation and validations of a 2-stage (MOV and a line-filter) TVSS/SPD driven by an LSS

– Matlab code (LSS\_MOV\_LineFilter.m) used to produce figures from Figure 6-13 to Figure 6-15.

```
%-----  
function LSS_MOV_LineFilter_ODE15S  
  
% Simulated voltage, current, power and energy plots for a TVSS  
% with an MOV and line-filter elements (Cf and Lf) compared with LSS  
% validations.  
  
% MOV used - 275L40C  
% ODE solver used: ode15s (with routine to return jacobian)  
% LSS used: Noiseken LSS-6110  
  
R1 = 7;  
C1 = 10e-6;  
L1 = 2.7e-6;  
R2 = 1.1;  
L2 = 6e-6;  
R3 = 1e6;  
Rs = 1;  
Rf = 0.22;  
Cm = 900e-12;  
Lf = 5.8e-6;  
Cf = 0.22e-6;  
  
Vc0 = 1000;  
  
a = R1/L1; b = 1/(L1*C1);  
c = R1/L2; d = (R1+R2+R3)/L2;  
e = R3/L2; f = R3/(R3+Rs);  
g = 1/(Cm*(R3+Rs)); h = 1/(Lf*Cm);  
k = 1/(Lf*Cf); l = 1/Cm;  
m = Rf/Lf;  
  
[k2, beta] = deal(2.4496*10^-50.15, 18.3338);  
  
fignum = 1;  
  
% DE definition for RLC circuit  
function xdot = RLC_dot(t, x, flag, params)  
[x1 x2 x3 x4 x5 x6 x7] = deal(x(1), x(2), x(3), x(4), x(5),  
x(6), x(7));  
  
x1_dot = x2;  
x2_dot = -a*x2 - (b-a*c)*x1 - a*d*x3 + a*e*x4;  
x3_dot = c*x1 - d*x3 + e*x4;  
x4_dot = c*f*x1 - d*f*x3 + (e*f-g)*x4 + g*x6 + g*k2*x5^beta;  
x5_dot = l*x4 - l*x6 - l*k2*x5^beta;  
x6_dot = x7;  
x7_dot = h*x4 - (h+k)*x6 - h*k2*x5^beta - m*x7;
```

```

        xdot = [x1_dot; x2_dot; x3_dot; x4_dot; x5_dot; x6_dot;
        x7_dot]; % return column vector
end

% The function that returns the Jacobian matrix
function J = FJac(t,x)

    J(7,7)=0;

    J(1,2)=1;

    J(2,1)=(a*c-b);
    J(2,2)=-a;
    J(2,3)=-a*d;
    J(2,4)=a*e;

    J(3,1)=c;
    J(3,3)=-d;
    J(3,4)=e;

    J(4,1)=c*f;
    J(4,3)=-d*f;
    J(4,4)=e*f-g;
    J(4,5)=g*k2*beta*x(5)^(beta-1);
    J(4,6)=g;

    J(5,4)=1;
    J(5,5)=-1*k2*beta*x(5)^(beta-1);
    J(5,6)=-1;

    J(6,7)=1;

    J(7,4)=h;
    J(7,5)=-h*k2*beta*x(5)^(beta-1);
    J(7,6)=-(h+k);
    J(7,7)=-m;

end

time = [0 0.9e-4];
X0(:,1) = [0; Vc0/L1; 0; 0; 0; 0; 0]; flag = ''; params = [];
options = odeset('RelTol', 1e-3, 'Stats', 'on', 'Jac', @FJac);
tic
[t_out, X_out] = ode15s(@RLC_dot, [time(1) time(end)], X0,
options);
toc

time = t_out;
I1 = X_out(:,1); J1 = X_out(:,2); I2 = X_out(:,3);
I3 = X_out(:,4); V4 = X_out(:,5); I5 = X_out(:,6);
J5 = X_out(:,7);

% LSS data (start)

M = csvread('1KV_275L40C_RFIF_6230.csv', 17,1); %reads data from the
csv formatted file starting at row 17 and column 1

```

```

t = M(:,5);           % takes all rows of column 5
I = M(:,4);           % takes all rows of column 4
VCf = M(:,3);         % takes all rows of column 3
Vmov = M(:,2);        % takes all rows of column 2
ICf = M(:,6);         % takes all rows of column 6
VRf = M(:,7);         % takes all rows of column 7

% LSS data (end)

% plots for MOV
figure(fignum);

subplot(411)

plot(time*1e6, V4,'--k', 'linewidth', 2);hold on;
plot (t*1e6,Vmov,'-k');

legend('V_m_o_v (MATLAB simulation)','V_m_o_v (validation)');
xlabel('Time (us)'); ylabel('Voltage (V) ');
axis([-5 90 -10 750])
title(' (a) ');

subplot(412)

plot(time*1e6, (I3-I5),'--k', 'linewidth', 2);hold on;
plot (t*1e6,((I-ICf)-1),'-k','linewidth', 1);hold on;

legend('I_m_o_v (MATLAB simulation)','I_m_o_v (validation)');
xlabel('Time (us)'); ylabel('Current (A)');
axis([-5 90 -20 200])
title(' (b) ');

subplot(413)

Pcs = V4.*((I3-I5)/1e3);
plot (time*1e6,Pcs,'--k','linewidth', 2);hold on;

Plss = Vmov.*(((I-ICf)-1)/1e3);
plot (t*1e6,Plss,'k');

legend('P_m_o_v (MATLAB simulation)','P_m_o_v (Validation)')
xlabel('time (us)');
ylabel('Power (kW)');
zoom on;
axis([-5 90 -10 130]);
title(' (c) ');

subplot(414)

Ecs = (cumsum(Pcs(1:end-1).*diff(time)))*1e3;
plot (time(1:end-1)*1e6,Ecs,'--k','linewidth', 2);hold on;

t1 = M(11,5);
t2 = M(12,5);
dt = t2-t1;

```

```

Elss = cumsum(Plss*1e3)*dt;
plot (t*1e6,Elss,'k');

xlabel('time(us)');
ylabel('Energy (J)');
zoom on; axis([-5 90 0 1.2])
title('c');
legend('E_m_o_v(MATLAB simulation)','E_m_o_v(Validation)',
      'Location','SouthEast')

% Plots for the line-filter capacitor Cf
figure(2);

subplot(411)

plot(time*1e6, V4-Lf*J5-Rf*I5,'--k', 'linewidth', 2);hold on;
plot (t*1e6,VCf,'-k');hold on;grid on;

legend('V_C_f (MATLAB simulation)','V_C_f (validation)')
xlabel('Time (us)'); ylabel('voltage (V)');
axis([-5 90 -10 1100])
title('a');

subplot(412)

plot(time*1e6, I5,'--k', 'linewidth', 2);hold on;
plot(t*1e6, ICf,'-k', 'linewidth', 1);hold on;grid on;

legend('I_C_f (MATLAB simulation)','I_C_f (validation)')
xlabel('Time (us)'); ylabel('currents (A)');
axis([-5 90 -80 100])
title('b');

subplot(413)

Pcs = (V4-Lf*J5-Rf*I5).*(I5)/1e3;
plot (time*1e6,Pcs,'--k','linewidth', 2);hold on;grid on;

Plss = VCf.*(ICf)/1e3;
plot (t*1e6,Plss,'k');

legend('P_C_f(MATLAB simulation)','P_C_f(Validation)')
xlabel('time(us)');
ylabel('Power (kW)');
zoom on; axis([-5 90 -60 65]);
title('c');

subplot(414)

Ecs = (0.5*Cf*(V4-Lf*J5-Rf*I5).*(V4-Lf*J5-Rf*I5));
plot (time*1e6,Ecs,'--k','linewidth', 2);hold on;grid on;

Elss =0.5*Cf*VCf.*VCf;
plot (t*1e6,Elss,'k');

legend('E_C_f(MATLAB simulation)','E_C_f(Validation)',

```

```

        'Location','NorthEast');
xlabel('time(us)');
ylabel('Energy (J)');
zoom on; axis([-5 90 0 0.13])
title('(d)');

% Plots for line-filter inductor Lf
figure(3);

subplot(411)

plot(time*1e6, Lf*J5,'--k', 'linewidth', 2);hold on;
plot (t*1e6,Vmov-VCf-VRf,'-k');hold on;

legend('V_L_f (simulation)','V_L_f (validation)')
xlabel('Time (us)'); ylabel(' voltage (V)');
axis([-5 90 -425 400]);
title('(a)');

subplot(412)

plot(time*1e6, I5,'--k', 'linewidth', 2);hold on;
plot(t*1e6, (ICf+1.0),'-k', 'linewidth', 1);hold on;

legend('I_L_f (simulation)','I_L_f (validation)')
xlabel('Time (us)'); ylabel('currents (A)');
axis([-5 90 -75 95]);
title('(b)');

subplot(413)

Pcs = (Lf*J5).*I5/1e3;
plot (time*1e6,Pcs,'--k','linewidth', 2);hold on;

Plss = (Vmov-VCf-VRf).*(ICf+1.0)/1e3;
plot (t*1e6,Plss,'k');

legend('P_L_f(Simulation)','P_L_f(Validation)')
xlabel('time(us)'); ylabel('Power (kW)');
zoom on; axis([-5 90 -20 20]);
title('(c)');

subplot(414)

Ecs = (0.5*Lf*(I5).*(I5));
plot (time*1e6,Ecs,'--k','linewidth', 2);hold on;

Elss = 0.5*Lf*(VRf/Rf).*(VRf/Rf);
plot (t*1e6,Elss,'k');

legend('E_L_f(Simulation)','E_L_f(Validation)')
xlabel('time(us)'); ylabel('Energy (J)');
zoom on; axis([-5 90 -0.001 0.025])
title('(d)');

```

end

## D.6 Development of state equations (6-18) - (6-25) for a 3-stage (MOV followed by a line-filter and a TVS diode) TVSS driven by an LSS

The complete equivalent circuit for this situation was given in Figure 6-17 and is repeated here for convenience as Figure D.6-1.

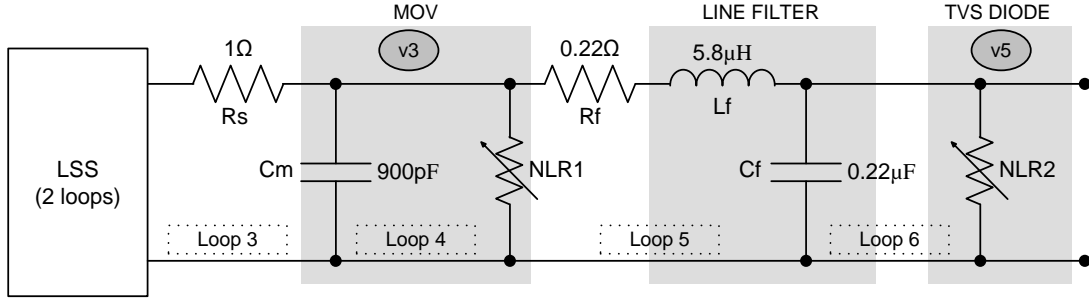


Figure D.6-1: Equivalent circuit for the LSS driving a 3-stage 2-level TVSS

We will consider six loop currents  $i_1$ ,  $i_2$ ,  $i_3$ ,  $i_4$ ,  $i_5$  and  $i_6$ . The first two loop currents  $i_1$  and  $i_2$  are flowing within the LSS equivalent circuit and are not explicitly shown in Figure D.6-1. In addition we will consider the nodal voltages  $v_3$  and  $v_5$  across the nonlinear resistances  $NLR_1$  and  $NLR_2$ .

Since the first four loops of this circuit (2 loops in the LSS, loop-3 and loop-4) are identical to the one given in the 5-loop circuit of Figure D.4-1, the following five state equations remain unchanged.

$$\frac{di_1}{dt} = j_1 \quad (\text{D.6-1})$$

$$\frac{dj_1}{dt} = -\frac{R_1}{L_1}j_1 - \left(\frac{1}{L_1C_1} - \frac{R_1^2}{L_1L_2}\right)i_1 - \frac{R_1(R_1 + R_2 + R_3)}{L_1L_2}i_2 - \frac{R_1R_3}{L_1L_2}i_3 \quad (\text{D.6-2})$$

$$\frac{di_2}{dt} = \frac{R_1}{L_2}i_1 - \frac{R_1 + R_2 + R_3}{L_2}i_2 + \frac{R_3}{L_2}i_3 \quad (\text{D.6-3})$$

$$\begin{aligned} \frac{di_3}{dt} = & \frac{R_3R_1}{L_2(R_3 + R_5)}i_1 - \frac{R_3(R_1 + R_2 + R_3)}{L_2(R_3 + R_5)}i_2 + \frac{1}{(R_3 + R_5)}\left(\frac{R_3^2}{L_2} - \frac{1}{C_m}\right)i_3 \\ & + \frac{K_m}{C_m(R_3 + R_5)}v_3^{\alpha_m} + \frac{1}{C_m(R_3 + R_5)}i_5 \end{aligned} \quad (\text{D.6-4})$$

$$\frac{dv_3}{dt} = l(i_3 - i_5 - k_mv_3^{\alpha_m}) \quad (\text{D.6-5})$$

Considering loop-5 and writing the KVL equation, we get

$$v_3 = R_f i_5 + L_f \frac{di_5}{dt} + \frac{1}{C_f} \int (i_5 - i_6) dt \quad (\text{D.6-6})$$

Differentiating and substituting for  $\frac{dv_3}{dt}$  from Eq.(D.6-5), we get

$$\frac{1}{C_m} (i_3 - i_5 - K_m v_3^{\alpha_m}) = R_f \frac{di_5}{dt} + L_f \frac{d^2 i_5}{dt^2} + \frac{1}{C_f} (i_5 - i_6) \quad (\text{D.6-7})$$

Rearranging Eq. (D.6-7), we get

$$\frac{d^2 i_5}{dt^2} = \frac{1}{L_f C_m} i_3 - \frac{1}{L_f} \left( \frac{1}{C_m} + \frac{1}{C_f} \right) i_5 - \frac{1}{L_f C_m} K_m v_3^{\alpha_m} - \frac{R_f}{L_f} \frac{di_5}{dt} + \frac{1}{L_f C_f} i_6 \quad (\text{D.6-8})$$

Introducing the auxiliary

$$\frac{di_5}{dt} = j_5 \quad (\text{D.6-9})$$

Now Eq. (D.6-8) can be written as

$$\frac{dj_5}{dt} = \frac{1}{L_f C_m} i_3 - \frac{1}{L_f} \left( \frac{1}{C_m} + \frac{1}{C_f} \right) i_5 - \frac{R_f}{L_f} j_5 - \frac{1}{L_f C_m} K_m v_3^{\alpha_m} + \frac{1}{L_f C_f} i_6 \quad (\text{D.6-10})$$

Let us consider the nodal voltage  $v_5$  now; since this is the voltage across the capacitor  $C_f$ , we have

$$v_5 = \frac{1}{C_f} \int (i_5 - i_6) dt \quad (\text{D.6-11})$$

Differentiating Eq.(D.6-11), we get

$$\frac{dv_5}{dt} = \frac{1}{C_f} (i_5 - i_6) \quad (\text{D.6-12})$$

The current  $i_6$  is the current through the nonlinear resistance of the TVS diode model and is assumed to be governed by Eq. (6-17) which is repeated here as Eq. (D.6-13).

$$i_6 = K_t v_5^{\alpha_t} \quad (\text{D.6-13})$$

Substituting Eq.(D.6-13) in equations (D.6-10) and (D.6-12), we get Eq. (D.6-14) and Eq. (D.6-15) respectively.

$$\begin{aligned} \frac{dj_5}{dt} = \frac{1}{L_f C_m} i_3 - \frac{1}{L_f} \left( \frac{1}{C_m} + \frac{1}{C_f} \right) i_5 - \frac{R_f}{L_f} j_5 - \frac{1}{L_f C_m} K_m v_3^{\alpha_m} \\ + \frac{1}{L_f C_f} K_t v_5^{\alpha_t} \end{aligned} \quad (\text{D.6-14})$$

$$\frac{dv_5}{dt} = \frac{1}{C_f} (i_5 - K_t v_5^{\alpha_t}) \quad (\text{D.6-15})$$

Now the equations (D.6-1), (D.6-2), (D.6-3), (D.6-4), (D.6-5), (D.6-9), (D.6-14) and (D.6-15) make up the set of eight state equations corresponding to the state variables  $i_1, j_1, i_2, i_3, v_3, i_5, j_5$  and  $v_5$ . This set of eight state equations were successfully used to simulate the working of Figure D.6-1 (same as Figure 6-17). These seven equations can be written as state equations (6-18) - (6-25) provided we make the following substitutions:

$$a = R_1/L_1, \quad b = 1/L_1 C_1, \quad c = R_1/L_2, \quad d = (R_1 + R_2 + R_3)/L_2, \quad e = R_3/L_2, \quad f = R_3/(R_3 + R_S), \\ g = 1/C_m (R_3 + R_S), \quad h = 1/C_m, \quad k = 1/L_f C_m, \quad l = 1/L_f C_f, \quad m = 1/C_f \text{ and } n = R_f/L_f.$$

The initial conditions for the simulation are  $i_1(0) = 0, j_1(0) = V_{C1}(0+)/L, i_2(0) = i_3(0) = v_3(0) = i_5(0) = j_5(0) = v_5(0) = 0$ . As before, the value given for  $j_1(0)$  results due to the initial voltage  $V_{C1}(0+)$  of the capacitor  $C_1$ , which is the amplitude of the surge voltage generated by the LSS.

## D.7 Numerical simulation and validations of a 3-stage (MOV followed by a line-filter and a TVS diode) TVSS/SPD driven by an LSS

– MATLAB code (LSS\_MOV\_LineFilter\_TVS\_Diode.m) used to produce figures from Figure 6-18 to Figure 6-19.

```
%-----  
-----  
function LSS_TVSS_ODE15S  
% Simulated voltage, current, power and energy plots for a TVSS  
% with an MOV (for level-1 protection), a line-filter and a TVS  
% diode (for level-2 protection, compared with LSS validations.  
  
% LSS used: Noiseken LSS-6110  
% MOV used - 275L40C  
% TVS diode used - 2 X 1.5KE350CA  
  
% ODE solver used: ode15s (with routine to return jacobian)  
  
R1 = 7;  
C1 = 10e-6;  
L1 = 2.7e-6;  
R2 = 1.1;  
L2 = 6e-6;  
R3 = 1e6;  
Rs = 1;  
Rf = 0.22;  
Cm = 900e-12;  
Lf = 4.0e-6;  
Cf = 0.22e-6;  
  
Vc0 = 1000;  
  
a = R1/L1; b = 1/(L1*C1);  
c = R1/L2; d = (R1+R2+R3)/L2;  
e = R3/L2; f = R3/(R3+Rs);  
g = 1/(Cm*(R3+Rs)); h = 1/Cm;  
k = 1/(Lf*Cm); l = 1/(Lf*Cf);  
m = 1/Cf; n=Rf/Lf;  
  
% original PL model for 275L40C  
[km, alpham] = deal(2.4496*10^-50.15, 18.3838);  
% PL model for 2x1.5KE350CA  
[kt, alphas] = deal(4.0638e-161, 56.3468);  
  
fignum = 1;  
  
% DE definition for RLC circuit  
function xdot = RLC_dot(t, x, flag, params)  
    [x1 x2 x3 x4 x5 x6 x7 x8] = deal(x(1), x(2), x(3), x(4), ...  
    x(5), x(6), x(7), x(8));  
    x1_dot = x2;  
    x2_dot = -a*x2 - (b-a*c)*x1 - a*d*x3 + a*e*x4;  
    x3_dot = c*x1 - d*x3 + e*x4;
```

```

x4_dot = c*f*x1 - d*f*x3 + (e*f-g)*x4 + g*x6 + g*km*x5^alphan;
x5_dot = h*x4 - h*x6 - h*km*x5^alphan;
x6_dot = x7;
x7_dot = k*x4 - (k+1)*x6 - k*km*x5^alphan + ...
        1*kt*x8^alphan-n*x7;
x8_dot = m*x6 - m*kt*x8^alphan;

xdot = [x1_dot; x2_dot; x3_dot; x4_dot; x5_dot; x6_dot; ...
        x7_dot; x8_dot]; % return column vector
end

% The function that returns the Jacobian matrix
function J = FJac(t,x)

    J(8,8)=0;

    J(1,2)=1;

    J(2,1)=(a*c-b);
    J(2,2)=-a;
    J(2,3)=-a*d;
    J(2,4)=a*e;

    J(3,1)=c;
    J(3,3)=-d;
    J(3,4)=e;

    J(4,1)=c*f;
    J(4,3)=-d*f;
    J(4,4)=e*f-g;
    J(4,5)=g*km*alphan*x(5)^(alphan-1);
    J(4,6)=g;

    J(5,4)=h;
    J(5,5)=-h*km*alphan*x(5)^(alphan-1);
    J(5,6)=-h;

    J(6,7)=1;

    J(7,4)=k;
    J(7,5)=-k*km*alphan*x(5)^(alphan-1);
    J(7,6)=- (k+1);
    J(7,8)=1*kt*alphan*x(8)^(alphan-1);
    J(7,7)=-n;

    J(8,6)=m;
    J(8,8)=-m*kt*alphan*x(8)^(alphan-1);

end

time = [0 0.9e-4];
X0(:,1) = [0; Vc0/L1; 0; 0; 0; 0; 0; 0]; flag = ''; params = [];
options = odeset('RelTol', 1e-3, 'Stats', 'on', 'Jac', @FJac);
tic
[t_out, X_out] = ode23t(@RLC_dot, [time(1) time(end)], X0, options);
toc

```

```

time = t_out;
I1 = X_out(:,1); J1 = X_out(:,2); I2 = X_out(:,3);...
I3 = X_out(:,4); V4 = X_out(:,5); I5 = X_out(:,6);...
J5 = X_out(:,7); V6 = X_out(:,8);

% LSS data (start)

M = csvread('1kV_Surge_275L40CpRFIFp_2x350V_TVSD_031013_0041.csv',...
17,1);
%reads data from the csv formatted file starting at row 17 and
column 1

t = M(:,5);
Vmov = M(:,4); % takes all rows of column 4
Iprot = M(:,3); % takes all rows of column 3
IRf = M(:,2); % takes all rows of column 2
Imov= M(:,6);

N = csvread('1kV_Surge_275L40CpRFIFp_2x350V_TVSD_081013_0047.csv',...
17,1);
%reads data from the csv formatted file starting at row 17 and
column 1

tt = N(:,4);
Vtvdsd = N(:,2); % takes all rows of column 4
Itvdsd = N(:,3); % takes all rows of column 3

% LSS data (end)

% Plots for the MOV
figure(fignum);

subplot(411)

plot(time*1e6, V4,'--k', 'linewidth', 2);hold on;
plot (t*1e6,Vmov,'-k');

legend('V_m_o_v (MATLAB simulation)','V_m_o_v (validation)');
xlabel('Time (us)'); ylabel('Voltage (V) ');
axis([-5 90 -10 750])
title('(a)');

subplot(412)

plot(time*1e6, km*(V4.^alphan),'--k', 'linewidth', 2);hold on;
plot (t*1e6,Imov,'-k','linewidth', 1);hold on;

legend('I_m_o_v (MATLAB simulation)','I_m_o_v (validation)');
xlabel('Time (us)'); ylabel('Current (A)');
axis([-5 90 -20 120])
title('(b)');

subplot(413)

Pcs = V4.*(km*(V4.^alphan)/1e3);
plot (time*1e6,Pcs,'--k','linewidth', 2);hold on;

```

```

Plss = Vmov.*(Imov/1e3);
plot (t*1e6,Plss,'k');

legend('P_m_o_v(MATLAB simulation)','P_m_o_v(Validation)')
xlabel('time(us)');
ylabel('Power (kW)');
zoom on;
axis([-5 90 -10 80]);
title('(c)');

subplot(414)

Ecs = (cumsum(Pcs(1:end-1).*diff(time)))*1e3;
plot (time(1:end-1)*1e6,Ecs,'--k','linewidth', 2);hold on;

t1 = M(11,5);
t2 = M(12,5);
dt = t2-t1;
Elss = cumsum(Plss*1e3)*dt;
plot (t*1e6,Elss,'k');

xlabel('time(us)');
ylabel('Energy (J)');
zoom on; axis([-5 90 0 1.2])
title('(c)');
legend('E_m_o_v(MATLAB
simulation)','E_m_o_v(Validation)','Location','SouthEast')

% Plots for the TVS diode
figure(3);

subplot(411)

plot(time*1e6, V6,'--k', 'linewidth', 2);hold on;
plot (tt*1e6,Vtvsd,'-k');

legend('V_t_v_s_d (MATLAB simulation)','V_t_v_s_d
(Validation)','Location','SouthEast');
xlabel('Time (us)'); ylabel('Voltage (V) ');
axis([-2 45 -10 800])
title('(a)');

subplot(412)

plot(time*1e6, kt*(V6.^alphan),'--k', 'linewidth', 2);hold on;
plot (tt*1e6,Itvsd,'-k','linewidth', 1);hold on;

legend('I_t_v_s_d (MATLAB simulation)','I_t_v_s_d (Validation)');
xlabel('Time (us)'); ylabel('Current (A)');
axis([-2 45 -10 80])
title('(b)');

subplot(413)

Pcst = V6.*(kt*(V6.^alphan)/1e3);

```

```

plot (time*1e6,Pcst,'--k','linewidth', 2);hold on;

Plsst = Vtvsd.*(Itvsd/1e3);
plot (tt*1e6,Plsst,'k');

legend('P_t_v_s (MATLAB simulation)', 'P_t_v_s (Validation)')
xlabel('time (us)');
ylabel('Power (kW)');
zoom on; axis([-2 45 -10 60]);
title('(c)');

subplot(414)

Ecst = (cumsum(Pcst(1:end-1).*diff(time)))*1e3;
plot (time(1:end-1)*1e6,Ecst,'--k','linewidth', 2);hold on;

tt1 = N(11,4);
tt2 = N(12,4);
dtt = tt2-tt1;
Elsst = cumsum(Plsst*1e3)*dtt;
plot (tt*1e6,Elsst,'k');

xlabel('time (us)');
ylabel('Energy (J)');
zoom on; axis([-2 45 -0.02 0.2]);
title('(c)');
legend('E_t_v_s (MATLAB
simulation)', 'E_t_v_s (Validation)', 'Location', 'northeast')

figure(2);
plot(time(1:end-1)*1e6,diff(time)*1e6,'-+k');
title('Diff(time) Vs Index - (ode23t - with Jac routine: RelTol =
1e-3)')
xlabel('Time (us)'); ylabel('Time difference (us)');

end

```

## Appendix E: Transient analysis in linear networks by Laplace methods; some examples

For excitation functions of the more general type, the classical method of solving ordinary differential equations is difficult to apply and the Laplace transform method proves to be superior.

### E.1 Series RC circuit with a biexponential input voltage

The series  $RC$  circuit in Figure E.1-1(a) is excited by a biexponential voltage source which resembles a standard open circuit voltage transient from a lightning surge simulator.

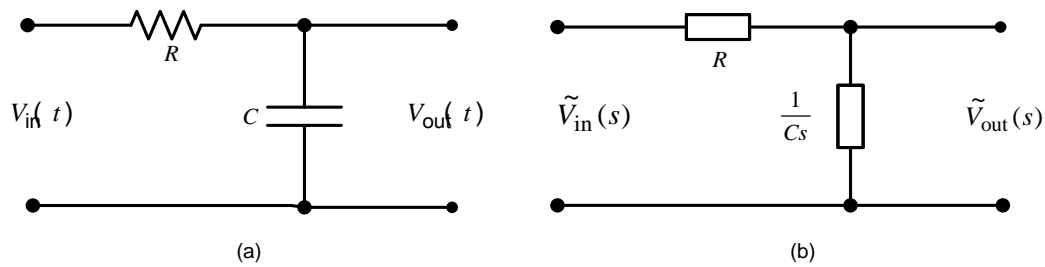


Figure E.1-1: (a) Series RC circuit; (b) Transformed network of circuit in (a)

Assuming that the initial charge in the capacitor is zero, the transformed network of the circuit in Figure E.1-1(a) is shown in Figure E.1-1(b). By the application of the voltage divider rule to Figure E.1-1(b), we get

$$\tilde{V}_{out}(s) = \frac{\frac{1}{Cs}}{\frac{1}{Cs} + R} \tilde{V}_{in}(s) = \frac{1}{1 + RCs} \tilde{V}_{in}(s) \quad (\text{E.1-1})$$

Here, the over-tilde ( $\sim$ ) symbol denotes a Laplace transformed quantity, for example,  $\mathcal{L}[V_{in}(t)] = \tilde{V}_{in}(s)$ .

Let  $V_{in}(t)$  be a normalized transient function modelled by a biexponential curve with  $\alpha$  being the rate constant for slow decay and  $\beta$  being the rate constant for fast rise,

$$V_{in}(t) = N(e^{-\alpha t} - e^{-\beta t}) \quad (\text{E.1-2})$$

where  $N$  is the normalization constant used to give unity height.

The Laplace transform of equation (E.1-2) is

$$\mathcal{L}[V_{in}(t)] = N[\mathcal{L}(e^{-\alpha t}) - \mathcal{L}(e^{-\beta t})]$$

By the use of Laplace transform tables

$$\tilde{V}_{in}(s) = N\left(\frac{1}{s - \alpha} - \frac{1}{s - \beta}\right) \quad (\text{E.1-3})$$

Rewriting equation (E.1-1) in terms of the circuit rate constant,  $\gamma = 1/RC$

$$\tilde{V}_{out}(s) = \frac{\gamma}{s + \gamma} \tilde{V}_{in}(s)$$

where  $\tilde{V}_{in}(s)$  is given by equation (E.1-3). Thus

$$\tilde{V}_{out}(s) = N\gamma \left[ \frac{1}{(s + \gamma)(s + \alpha)} - \frac{1}{(s + \gamma)(s + \beta)} \right] \quad (\text{E.1-4})$$

Each term within the square brackets of equation (E.1-4) can be decomposed by the partial fraction expansion. Expressing the first term as a sum of terms

$$\frac{1}{(s + \gamma)(s + \alpha)} = \frac{A}{s + \gamma} + \frac{B}{s + \alpha} \quad (\text{E.1-5})$$

The partial-fraction expansion in equation (E.1-5) indicates that LHS consists of a sum of terms, each of which is a factor of the denominator. The values of  $A$  and  $B$  are determined by combining the individual fractions by means of the lowest common denominator and comparing the resultant numerator coefficients with those in LHS of equation (E.1-5). Thus,

$$\frac{1}{(s + \gamma)(s + \alpha)} = \frac{A(s + \alpha) + B(s + \gamma)}{(s + \gamma)(s + \alpha)} = \frac{s(A + B) + A\alpha + B\gamma}{(s + \gamma)(s + \alpha)}$$

Equating powers of  $s$  in numerator:  $A + B = 0$  and  $A\alpha + B\gamma = 1$

from which

$$A = \frac{1}{\alpha - \gamma} \quad \text{and} \quad B = \frac{-1}{\alpha - \gamma}$$

Substitution of these values in equation (E.1-5) results in

$$\frac{1}{(s + \gamma)(s + \alpha)} = \frac{1}{\alpha - \gamma} \left( \frac{1}{s + \gamma} - \frac{1}{s + \alpha} \right) \quad (\text{E.1-6})$$

Similarly,

$$\frac{1}{(s + \gamma)(s + \beta)} = \frac{1}{\beta - \gamma} \left( \frac{1}{s + \gamma} - \frac{1}{s + \beta} \right) \quad (\text{E.1-7})$$

Substitution of equation (E.1-6) and (E.1-7) in (E.1-4) results in

$$\begin{aligned} \tilde{V}_{\text{out}}(s) = N\gamma \left[ \frac{1}{\alpha - \gamma} \left( \frac{1}{s + \gamma} - \frac{1}{s + \alpha} \right) \right. \\ \left. - \frac{1}{\beta - \gamma} \left( \frac{1}{s + \gamma} - \frac{1}{s + \beta} \right) \right] \quad (\text{E.1-8}) \end{aligned}$$

The development which leads from Eq. (E.1-4) to Eq. (E.1-8) is the basis for the partial-fraction expansion of an arbitrary function.

Taking the inverse Laplace transform of Eq. (E.1-8)

$$\begin{aligned} V_{\text{out}}(t) = N\gamma \left\{ \frac{1}{\alpha - \gamma} \left[ \mathcal{L}^{-1} \left( \frac{1}{s + \gamma} \right) - \mathcal{L}^{-1} \left( \frac{1}{s + \alpha} \right) \right] \right. \\ \left. - \frac{1}{\beta - \gamma} \left[ \mathcal{L}^{-1} \left( \frac{1}{s + \gamma} \right) - \mathcal{L}^{-1} \left( \frac{1}{s + \beta} \right) \right] \right\} \end{aligned}$$

Hence the output voltage across the capacitor is

$$V_{\text{out}}(t) = V_C(t) = N\gamma \left[ \frac{1}{\alpha - \gamma} (e^{-\gamma t} - e^{-\alpha t}) - \frac{1}{\beta - \gamma} (e^{-\gamma t} - e^{-\beta t}) \right]$$

Similarly the output voltage across the resistor can be shown to be

$$V_R(t) = N\gamma \left[ \frac{1}{\alpha - \gamma} (\alpha e^{-\alpha t} - \gamma e^{-\gamma t}) - \frac{1}{\beta - \gamma} (\beta e^{-\beta t} - \gamma e^{-\gamma t}) \right]$$

Figure E.1- 2 shows the plots for the input and output voltages of circuit in Figure E.1-1. The  $\alpha = 0.01425 \times 10^6 \text{ s}^{-1}$  and  $\beta = 4.85 \times 10^6 \text{ s}^{-1}$  values used, correspond to a standard open circuit voltage generated by a lightning surge simulator (LSS). For

normalization of the input voltage,  $N=1.02032$  [70]. The values used for the resistor and the capacitor were  $R=1\Omega$  and  $C=220\mu\text{F}$ .

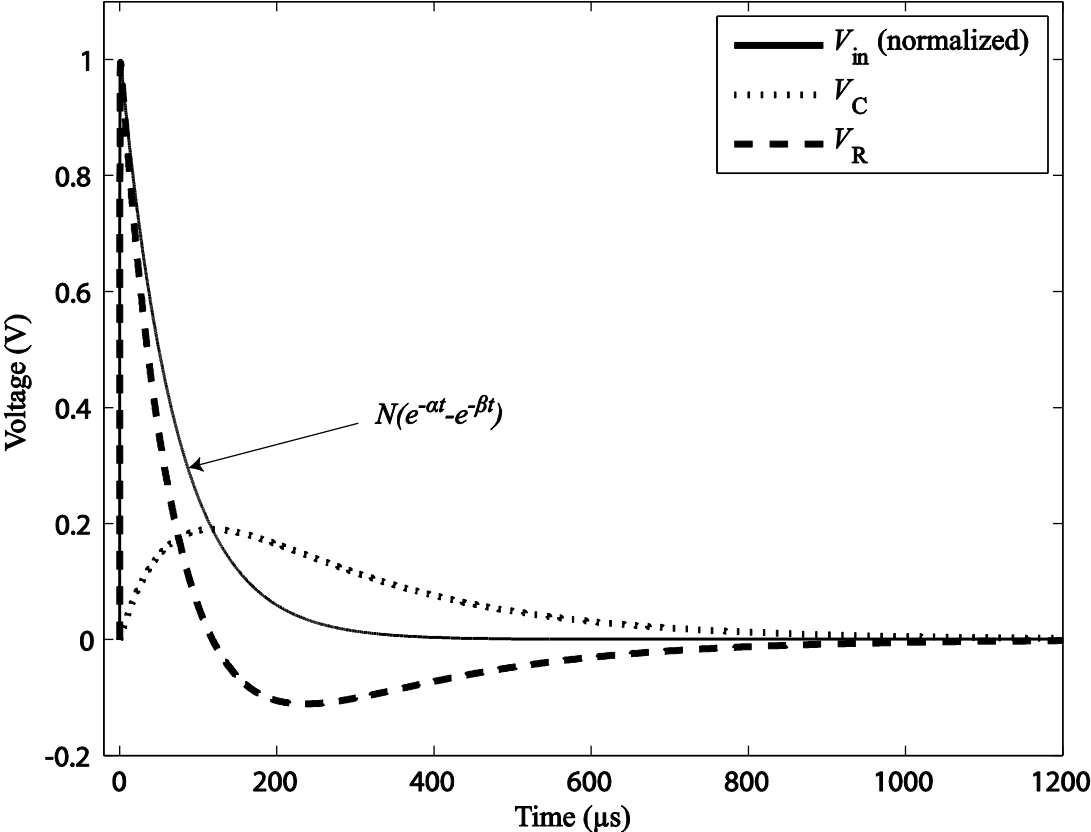


Figure E.1- 2: Input and output voltages of circuit in Figure E.1-1

**E.2 RLC circuit driven by a charged capacitor**

The current in the *RLC* circuit shown in Figure E.2- 1 can be easily deduced using the transformed network representations for R, L and C. The initial charge of the capacitor  $v_c(0)$  has been taken into account in the transformed-network representation of the capacitance.

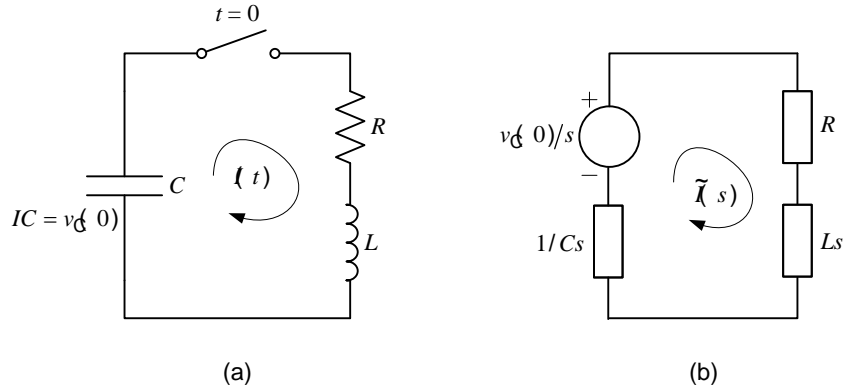


Figure E.2- 1: (a) RLC circuit driven by a charged capacitor; (b) Transformed network for circuit in (a)

For the transformed network,

$$\begin{aligned} \frac{v_C(0)}{s} &= I(s) \left( \frac{1}{sC} + R + sL \right) \\ (1 + sCR + s^2CL)I(s) &= Cv_C(0) \\ I(s) &= \frac{Cv_C(0)}{(1 + sCR + s^2CL)} = \frac{v_C(0)}{L} \frac{1}{s^2 + \frac{R}{L}s + \frac{1}{LC}} \\ I(s) &= \frac{v_C(0)}{L} \frac{1}{s^2 + as + b} \end{aligned} \quad (\text{E.3-1})$$

where  $a = R/L$ ,  $b = 1/LC$ .

Taking the inverse Laplace transform of Eq.(E.3-1)

$$i(t) = \frac{v_C(0)}{L} \frac{1}{\omega} \sinh(\omega t) \cdot e^{-at/2}, \quad \text{for } t \geq 0 \quad (\text{E.3-2})$$

where  $\omega = \sqrt{\frac{a^2}{4} - b}$

### E.3 An occurrence of the unit impulse function; discharging of an initially charged capacitor

In Chapter 5 of this thesis, the equivalent circuit of a lightning surge simulator (used for experimental validations) is analysed. Here, the behaviour of a discharging capacitor, which had been initially charged to a known voltage, is studied. The

following example [71], which is similar to such an analysis shows how the function  $\delta(t)$  may arise in such a situation and the reason for it.

Example: Two capacitors ( $C_1 = 1 \text{ F}$ ,  $C_2 = 2 \text{ F}$ ) and a resistor ( $R = 3 \Omega$ ) are arranged in a circuit as shown in Figure E.3-1(a).  $C_1$  is initially charged to a voltage  $E$  volts with polarity as shown. The switch is closed at  $t = 0$ . Let us determine the current in  $C_1$  as a function of time.

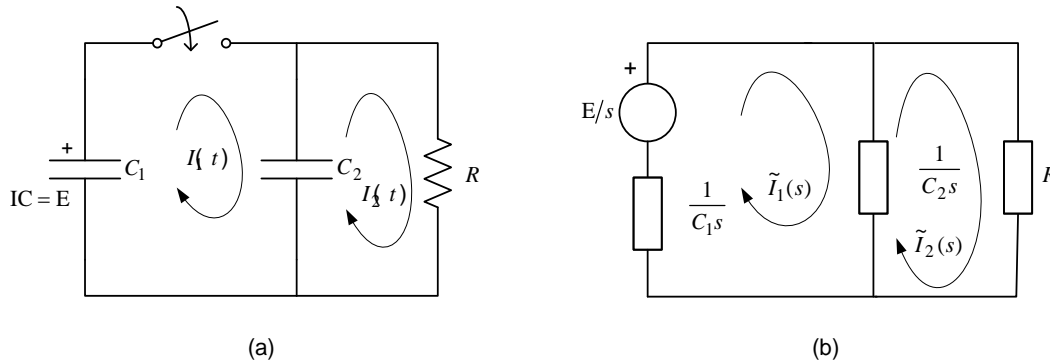


Figure E.3-1: (a) Circuit for example (b) Transformed circuit

Applying loop analysis to the transformed circuit shown in Figure E.3-1(b) and inserting the given numerical values for  $C_1$ ,  $C_2$ , and  $R$  we have

$$\frac{3}{2s} \tilde{I}_1(s) - \frac{1}{2s} \tilde{I}_2(s) = \frac{E}{s} \quad (\text{E.3-1})$$

$$-\frac{1}{2s} \tilde{I}_1(s) + \left(\frac{1}{2s} + 3\right) \tilde{I}_2(s) = 0 \quad (\text{E.3-2})$$

The desired response transform  $I_1(s)$  can be obtained from Eqs. (E.3-1) and (E.3-2):

$$\tilde{I}_1(s) = \left(\frac{6s + 1}{9s + 1}\right)$$

Dividing the improper fraction out,

$$\tilde{I}_1(s) = \frac{2E}{3} \left[ \frac{s + 1/6}{s + 1/9} \right] = \frac{2E}{3} \left[ 1 + \frac{1/18}{s + 1/9} \right] \quad (\text{E.3-3})$$

The inverse transformation of equation (E.3-3) gives the required current:

$$I_1(t) = \mathcal{L}^{-1}[\tilde{I}_1(s)] = \frac{2E}{3} \left[ \delta(t) + \frac{1}{18} e^{-t/9} \right]$$

An explanation for the appearance of  $\delta(t)$  in the above current can be given from a physical point of view as follows. We know that the voltage across a capacitor cannot change instantaneously. But when the switch in Figure E.3-1(a) is closed,  $C_1$  and  $C_2$  are in parallel, and must have equal voltages. This demand of instantaneous equalization of voltages across  $C_1$  and  $C_2$  is met by an impulsive current  $(2E/3)\delta(t)$  which represents an instantaneous charge transfer.

#### E.4 MATLAB symbolic toolbox

Whenever the inverse Laplace cannot be easily found in available tables, we could turn to the MATLAB Symbolic Toolbox, an excellent resource for finding the Laplace and the inverse Laplace transforms of a wide range of functions. Fourier transforms and Z-transforms and their inverse transforms can also be found here. Apart from the availability of symbolic functions for transforms, this toolbox provides symbolic functions for differentiation, integration, simplification, and equation solving as well.

If  $f(t) = t \cos 3t$ , then the definition of the Laplace transform gives the improper integral

$$F(s) = \mathcal{L}\{f(t)\} = \int_0^{\infty} t e^{-st} \cos 3t dt$$

whose evaluation would require a tedious integration by parts [72]. The Symbolic Toolbox commands

```
syms t s
f = t*cos(3*t)
F = laplace(f, t, s)
```

yield immediately the Laplace transform  $F(s) = (s^2 - 9)/(s^2 + 9)^2$ .

We can recover the original function  $f(t) = t \cos 3t$  with the symbolic toolbox command

```
ilaplace(F, s, t)
```

The order of  $s$  and  $t$  in the preceding commands must be noted – first  $t$ , then  $s$  when transforming; first  $s$ , then  $t$  when inverse transforming.

**Appendix F: A provisionally accepted journal paper to be published in the *IET Power Electronics* journal**

**Estimation of transient surge energy transferred with associated time delays for individual components of surge protector circuits**

Sisira James, Nihal Kularatna, Alistair Steyn-Ross, Rainer Künnemeyer  
School of Engineering, University of Waikato, Hamilton, New Zealand  
[sj74@students.waikato.ac.nz](mailto:sj74@students.waikato.ac.nz)

***Abstract*** – Modern semiconductor technology, where the feature size is reaching sub 25 nm levels, is vulnerable to transient surges such as lightning. Transient voltage suppressor systems (TVSSs) which are installed to protect modern electronics use nonlinear components such as varistors and transient voltage suppressor diodes in their design. In the case of low-voltage (1000 V and less) AC power circuits, there is no clear approach to estimate the energy absorption and associated time delays in individual components in relation to the propagated transient surge.

Numerical simulation techniques using MATLAB can be used to analyse the phenomenon of surge propagation within a TVSS and estimate the transient surge energy transferred to each component with associated time delays. In this approach, suitable mathematical models must be used for the nonlinear components, such as varistors and transient voltage suppressor diodes. This study presents the development of reasonably accurate models for the nonlinear circuit elements and formulation of state equations for the TVSS, together with simulation results; results are experimentally validated using a lightning surge simulator. The method of analyzing surge propagation presented here could be extended to analyse the phenomenon of surge propagation within power conversion stages which buffer the complex electronic circuits and the power source. Results discussed in the paper indicate that the theoretical energy calculations are within 10% of the experimental results for the individual circuit elements.

***Keywords*** - transient propagation, surge protection, varistor modelling, power quality

## **I. Introduction**

Proliferation of complex multi-million transistor semiconductor devices into a wide range of equipment from automated industrial assembly lines to sophisticated computer systems, has increased the vulnerability of such equipment to power quality problems[1]; these complex devices which are ultra large- scale integrated (ULSI) circuits have progressed towards advanced system-on-chip concepts with feature size dropping towards 22 nm [2-4]. The switch mode power

supplies (SMPS) that sit between the utility AC and processor-based equipment also carry complex circuitry. Both the power supply and the processor-based load are prone to damage by very short duration high-voltage transients such as lightning. Hence an end-to-end approach on transient propagation studies from the utility AC to final DC rails is of utmost importance.

An appropriate point to begin a transient propagation study would be at the TVSS that usually sits between the utility AC and the SMPS. Our objective here is to analyze the phenomenon of surge propagation in a TVSS and estimate the energy transferred to each one of its components. A representative schematic of a TVSS with two levels of protection, suitable for operation in the location categories A and B, is shown in Figure 1(a). The varistors M2 and M3 along with TVS diodes T2 and T3 would act in the case of a common-mode transient such as lightning, while the varistor M1 and TVS diode T1 would protect the load from a difference-mode transient. Category of the protector refers to the location category for which the protector is designed. These locations are defined within the IEEE C62.41 standard [5] and are depicted in Figure 1(b).

In the work presented here we have performed numerical simulations to analyse the energy transfer to individual components and associated time delays for a simplified 2-wire version of a TVSS in the event of a lightning transient occurrence. As the TVSS represents a typical power electronic interface with a combination of linear and nonlinear electronic components, we believe that this work can be continued to encompass downstream electronics that would be encountered in power electronic systems. Appropriate mathematical models had to be used for the nonlinear metal oxide varistor (MOV) and the transient voltage suppressor (TVS) diode. A lightning surge simulator (LSS) that conforms to IEC 61000-4-5 and IEEE C62.41 standards, capable of generating transient waveforms up to a maximum peak voltage of 6.6 kV, was used to validate the analysed results.

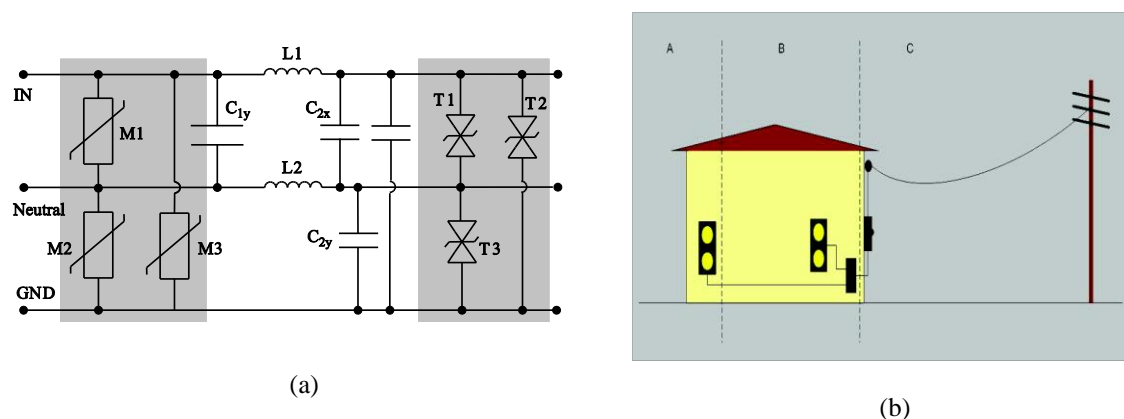


**Figure 1:** (a) A typical TVSS designed for AC mains operation with two levels (shaded areas) of protection (b) Location categories as per IEEE/ANSI C62.41, where category A is more than 20 m from category C; category B extends between categories C and A; category C is outside and service entrance

A TVSS is based on nonlinear bidirectional break-over components such as MOVs and TVS diodes in combination with capacitors and inductors. The quality of the TVSS and the protection it provides is governed by the test procedures adopted by the manufacturers, the energy absorbent capacity of the nonlinear protection components and their speed of response [6-11]. Over ninety

percent of the contemporary TVSSs designated for protection of low-voltage ac power circuitry are of parallel type with an MOV being the major component responsible for the suppression of surges and transient voltages. MOVs across the input wires are responsible for first-level protection from transients expected through the line-input. In order to handle extended transient stress, TVS diodes are connected as shown to provide a second level of protection. If the output capacitors are charged by the extended stress up to the breakdown voltage of the diodes, heavy conduction will occur in the diodes instantly [12].

In Section II a basic approach to modeling nonlinear devices used in a TVSS is discussed. Approximate power-law models will be used in the development of the differential equations which will represent the total system to be analysed. Section III provides information pertaining to the Lightning Surge Simulator Noiseken LSS-6230 which was used to experimentally validate the numerical results. In Section IV we discuss step-by-step MATLAB based numerical simulations which helped us analyze component-wise energy transfers to the TVSS with reasonable error margins and experimental procedures adopted using an LSS to validate the computer simulation predictions. Such simulations will allow us to predict the incipient failure of particular electronic components in the TVSS due to the propagation of a transient voltage across it.

## **II. Development of models for the nonlinear transient suppression components**

The electrical equivalent circuit for the varistor that could relate to the three regions of its operation is shown in Figure 2(a). At low current levels, the nonlinear resistance is in a high resistance mode (approaching  $10^9 \Omega$ ) and approximates an open circuit which is represented by the leakage resistance  $R_{OFF}$ . At high currents, approaching the maximum rating, the nonlinear resistance is in a low resistance mode and approximates a short circuit. This is represented by  $R_{ON}$  and would be in the range  $1 - 10 \Omega$  [13]. A simplified version of this circuit was employed for our simulations and the same is shown in Figure 2(b).  $R_{OFF} \infty$  and  $R_{ON}$  has been neglected.

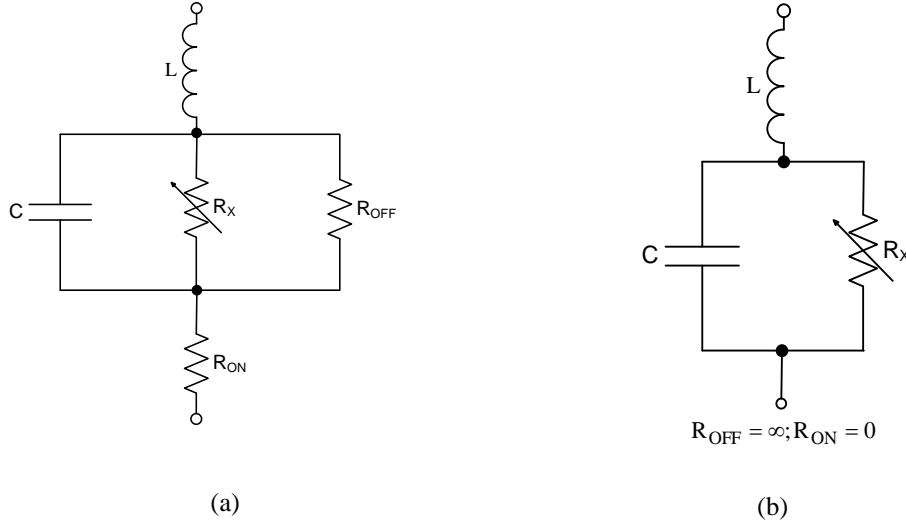


**Figure 2:** (a) Varistor equivalent circuit model [13] (b) the simplified varistor equivalent circuit used for the simulations

Different mathematical models are used for the nonlinear resistance  $R_X$ , which plays the major role in surge absorption by the varistor [13, 14]. The relationship that we use for the work presented here is given by Eq. (1)

$$i(v) = kv^\alpha \quad (1)$$

where  $i$  is the current through and  $v$  is the voltage across the varistor. The parameters  $k$  and  $\alpha$  of Eq(1) are unique to each varistor type. Exponent  $\alpha$  defines the degree of nonlinearity in the normal varistor region of operation. Eq (1) represents the MOV only in its ‘normal varistor operation’ region [13, 15, 16] and provides fairly accurate results when used in computer simulations as shown in Section IV.

We use Eq. (1) to model the nonlinear resistance of the varistor. We evaluated the constants  $k$  and  $\alpha$  for two medium-power varistors used by estimating the *slope* and the *intercept* of the log-log curve of Eq. (1), which is given by Eq.(2).

$$\log i = \alpha \log v + \log k \quad (2)$$

Although an analysis of a circuit representation containing a nonlinear model based on a power-law would be mathematically complex using Laplace methods, we demonstrate in Section IV that computer simulation employing numerical methods can be used successfully in the presence of such a model.

We also modeled two TVS diodes using a power-law relationship similar to Eq. (1). The two characteristics that were used to develop the models for 275L40C varistor and the 1.5KE170CA TVS diode are displayed side-by-side in Figure 3 for comparison. The line plots are the best curve

fits for the points shown. The degree of nonlinearity  $\alpha$ , and the leakage current can be easily compared using these plots.

It is clear from these plots that the value of  $\alpha$  (slope of the device for the “on” part of the characteristic) is much greater for the TVS diode than the MOV. The almost linear leakage regions of both models can be ignored in our investigation of surge propagation since these currents are very small and do not contribute significantly to the energies absorbed by the components. Typical  $\alpha$  values, obtained for several break-over components by means of a curve fit, are given in Table 1.

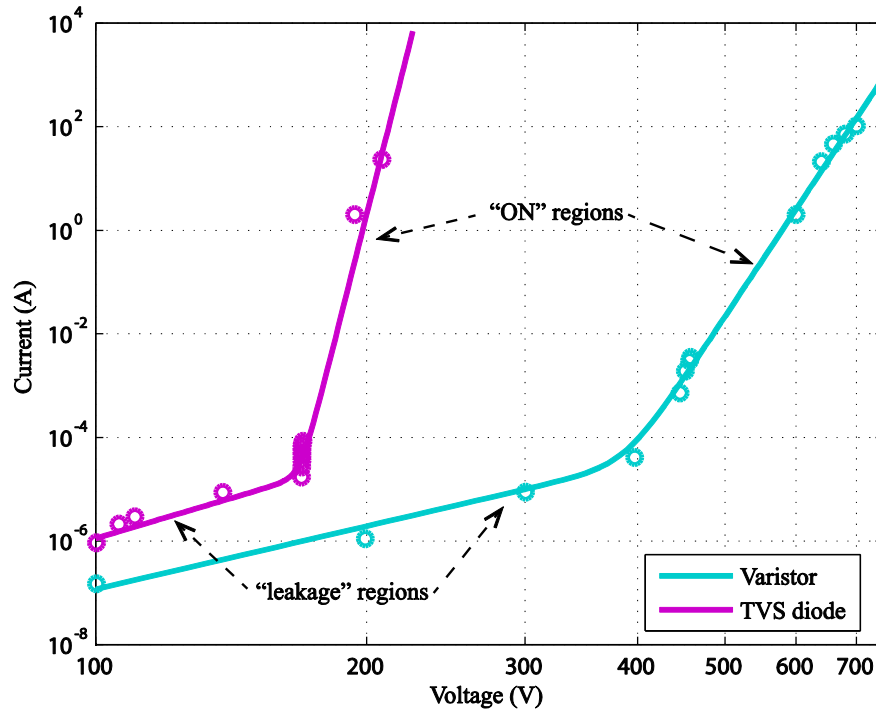


**Figure 3:** MOV and TVS diode V-I characteristics drawn on log-log graph for the determination of power-law exponent  $\alpha$ . (“ON” region points were obtained by detecting the transient peaks and the “leakage” region points were obtained in the steady state)

**Table 1:** Degree of nonlinearity ( $\alpha$ ) for some of the devices characterized [17]

Device	Type	Continuous maximum $V_{RMS}$ rating (V)	Maximum transient energy (2ms) (J)	Exponent $\alpha$
Varistor	V271HA32	275	360	$16.9 \pm 5\%$
Varistor	275L40C	275	320	$26.2 \pm 5\%$
		<b>Minimum breakdown voltage (V)</b>	<b>Peak power dissipation (1ms) (W)</b>	
TVS diode	1.5KE170CA	162	1500	$68.8 \pm 3\%$
TVS diode	1.5KE400CA	380	1500	$65.2 \pm 3\%$

Leakage current can be an area of misconception when comparing a varistor and a TVS diode. For example, we see from Figure 3 that the TVS diode leakage current is about 100 times higher, at 100V, than the varistor. This difference is greatly reduced if the TVS diode is a higher voltage device [18].

### III. Lightning surge simulator model

The results, obtained through the process of simulation and analysis for the surge propagation study, are validated using a lightning surge simulator (LSS) in the laboratory. Since the validating voltage and current waveforms during surge testing of TVSSs are governed by the LSS characteristics, an accurate surge simulator model should be an integral part of the circuit being analyzed or simulated [14,19,20]. The LSS characteristics are governed by the requirements set by the surge immunity testing standards IEEE/ANSI C62.41 and the IEC publication 61000-4-5. The equivalent circuit given in Figure 4, which was used in our analysis and computer simulations, was supplied by the manufacturer (Noise Laboratory Co., Japan) of the lightning surge simulator Noiseken LSS 6230.

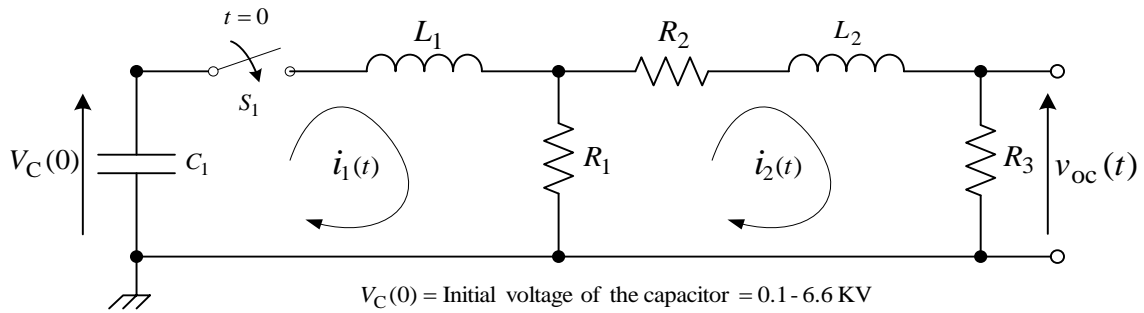


**Figure 4:** Equivalent circuit of the Noiseken LSS 6230 lightning surge generator for the generation of the combination wave (Noise Laboratory Co., Japan)

The initial voltage of the discharging capacitor  $C_1$  of the impulse source can be set to voltages in the range 100 V to 6.6 kV, in 100 V steps. In order to match the standards above, the model parameters given in Table 2 are specified by the manufacturer.

The Laplace solutions for open-circuit voltage and short-circuit current of this linear circuit with parameter values given in Table 2 were validated with experimental results of the LSS open-circuit voltage and short-circuit current. These results are shown in Figures 5(a) and 5(b).

**Table 2: Parameters for the Noiseken LSS-6230**

Parameter	Value	Parameter	Value
$C_1$	10 $\mu\text{F}$	$R_1$	7 $\Omega$
$L_1$	2.7 $\mu\text{H}$	$R_2$	1.1 $\Omega$
$L_2$	6 $\mu\text{H}$	$R_3$	1 M $\Omega$

The waveforms in Figure 5(a) and 5(b) corresponds to the 1.2/50  $\mu\text{s}$  open-circuit voltage and the 8/20  $\mu\text{s}$  short-circuit current specified in the IEEE/ANSI C62.41 and the IEC publication 61000-4-5 standards, respectively.

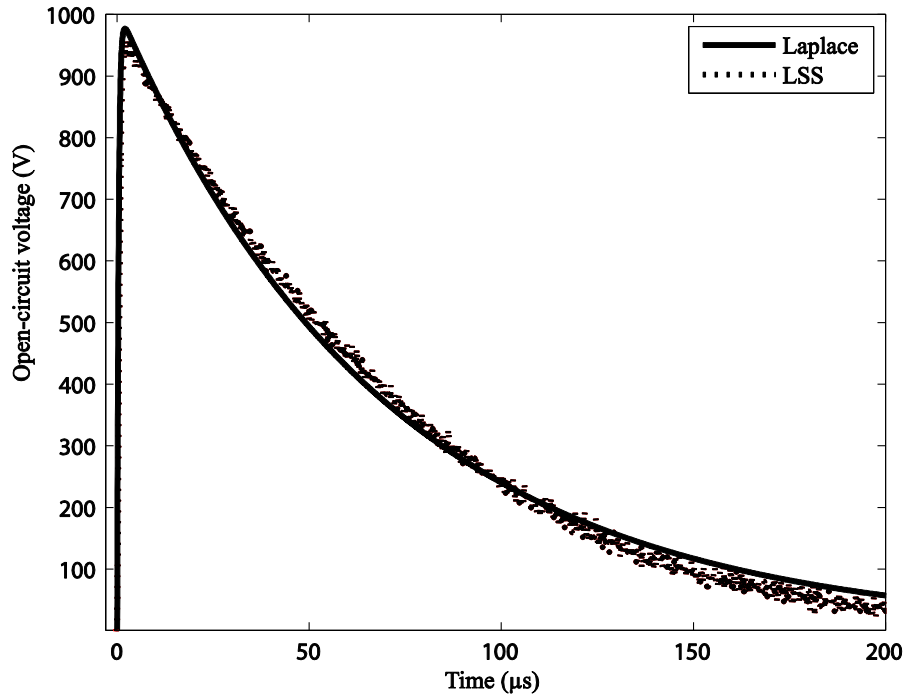
The network equations in the time-domain were formulated as a system of coupled first-order differential equations (DEs) which govern the dynamic behavior of the network. These first-order

## Appendix F: A provisionally accepted journal paper

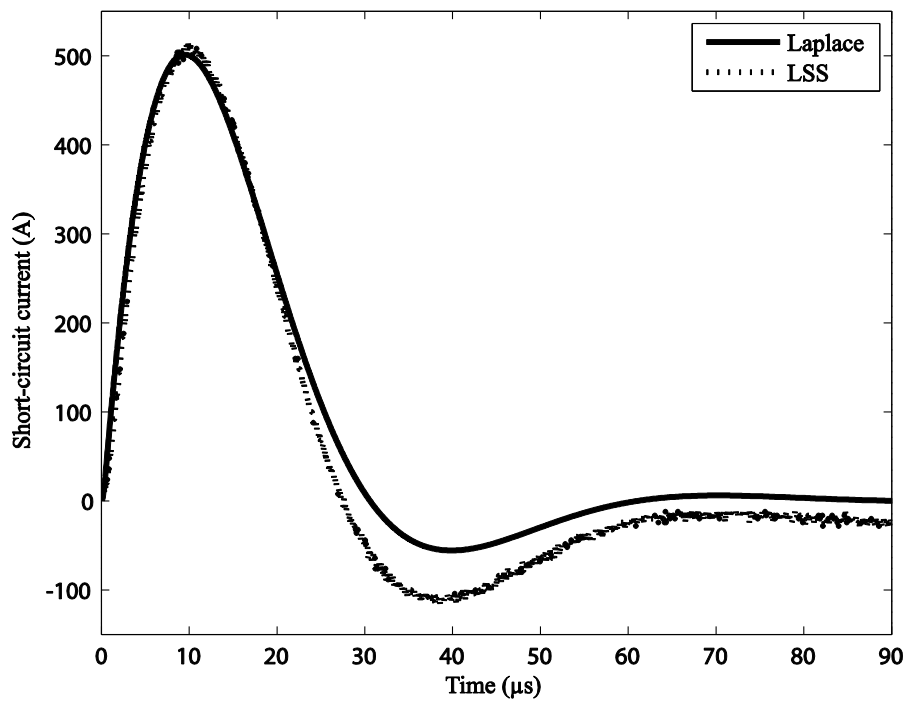
DEs (state equations), which fit the universal format given in Eq. (3) were programmed using MATLAB. Three state variables (two loop currents and one derivative of a loop current) are required for the LSS circuit

$$\frac{d}{dt}\mathbf{x} = A\mathbf{x} + B\mathbf{u} \quad (3)$$

where  $\mathbf{x}$  is the statevector and  $\mathbf{u}$  is the input vector;  $A$  is the state matrix and  $B$  is the input matrix.



(a)



(b)

**Figure 5:** Numerical simulations validated with the Laplace solutions; (a) LSS open-circuit voltage (b) LSS short-circuit current

Due to the presence of the initial charge in LSS capacitor  $C_1$ , the DE for the first loop gives rise to an exposed delta function as seen in Eq. (4).

$$\frac{d^2 i_1}{dt^2} + \frac{R_1}{L_1} \frac{di_1}{dt} + \frac{1}{L_1 C_1} i_1 - \frac{R_1}{L_1} \frac{di_2}{dt} = \frac{V_{C_1}(0)}{L_1} \delta(t) \quad (4)$$

This can be resolved for accurate MATLAB coding by using the initial condition that arises from the impulse input [21] (see Appendix I).

#### IV. Numerical simulation of surge propagation

Our goal is to simulate and predict power and energy dissipations in individual components of a 2-wire version of the TVSS shown in Figure 1(a). In order to build robust code for our numerical simulations a step-by-step approach was followed [17]. The first two circuits that we simulate here are purely linear in nature. These simulations were helpful to eliminate certain difficulties that arose in coding such circuits where the stimulus is a high energy transient.

The first circuit attempted, given in Figure 6(a) simulates the “off” state of the varistor. This could be done by considering the equivalent circuit given in Figure 2(b) and taking the series  $LC$  combination as the “off” state of the varistor since the nonlinear resistance  $R_X$  can be approximated to an open-circuit in this state. To write the set of state equations in the form of Eq. 3, five state variables (3 loop currents and 2 derivatives of loop currents) had to be used. The loop currents are denoted by  $i_n$ , where  $n$  is the loop number. The first two loop currents circulate within the LSS and the third one  $i_3(t)$  is seen flowing through the “off” state of the MOV. The resulting plot of the decaying MOV current shown in Figure 6(b) has high frequency ringing at the start. This kind of waveform with multiple timescales presents a stiff problem especially when one of the processes has a very small time constant. As a consequence we found that the fixed-step differential equation (DE) solver, the fourth-order RK (Runge-Kutta) and the variable-step MATLAB DE solver ode45 both failed to perform this simulation. This problem can be overcome by using the ode15s or ode23t MATLAB solvers which are designed for solving stiff problems [22].

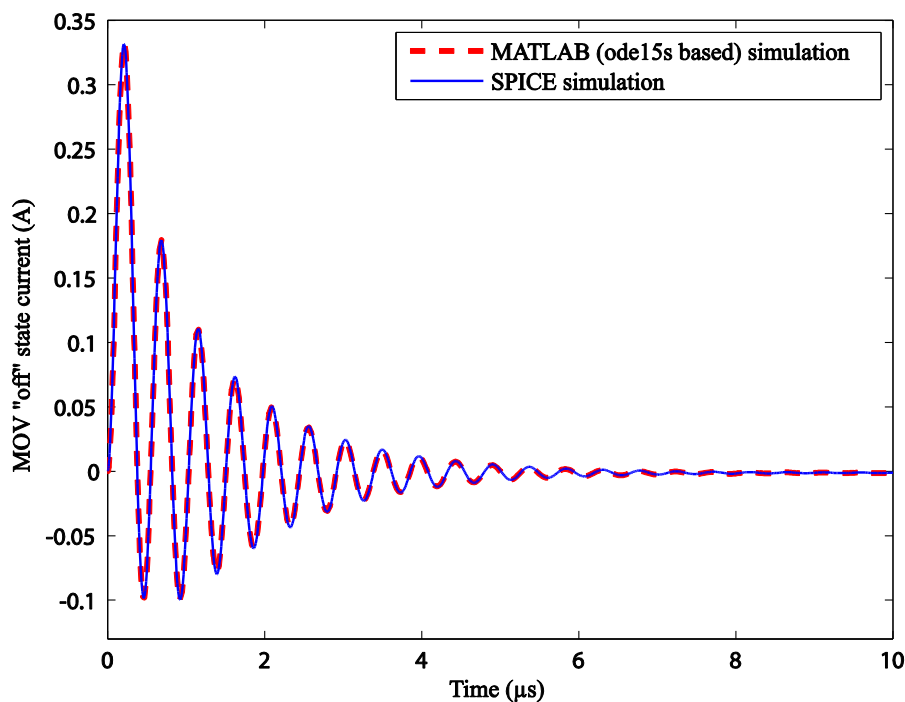
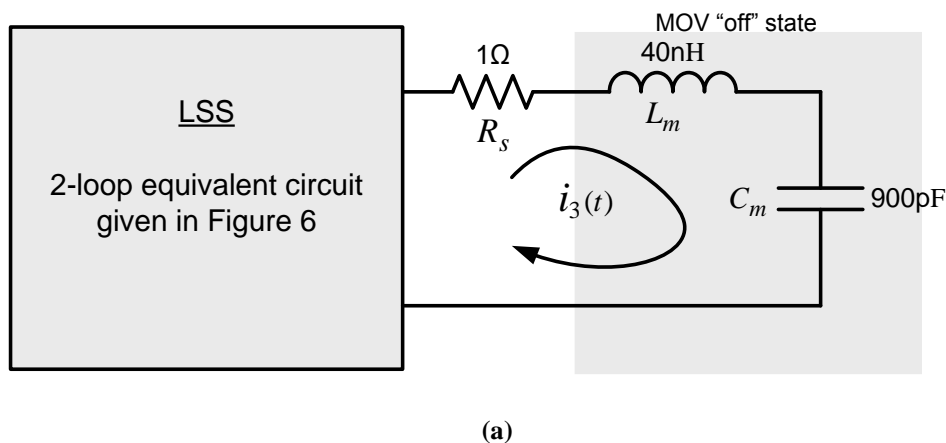


**Figure 6:** “OFF” state of the MOV pulsed by the LSS (a) test circuit; (b) simulation of the 3<sup>rd</sup> loop current

The second circuit we present here is also linear in nature and the simulation would give us an opportunity to study static instances in the operation of the nonlinear varistor. We have used three different values (7Ω, 500Ω and 30MΩ) for the static varistor resistor  $R_m$  and these values correspond to the “leakage”, “knee” and “breakdown” regions of the varistor  $V-I$  characteristic. The circuit simulated is shown in Figure 7(a). Here we require six state variables to complete the state equations. In the MATLAB coding it was important to provide the Jacobian matrix of the state equations to the ODE solver, in order to obtain uncompromised performance. This provision removes the need for the solver to estimate the Jacobian elements numerically [23]. Simulations of varistor currents for two assumed static instances of varistor resistance are shown in Figure 7(b) and (c). The SPICE simulations used to validate the numerical simulations are also shown.

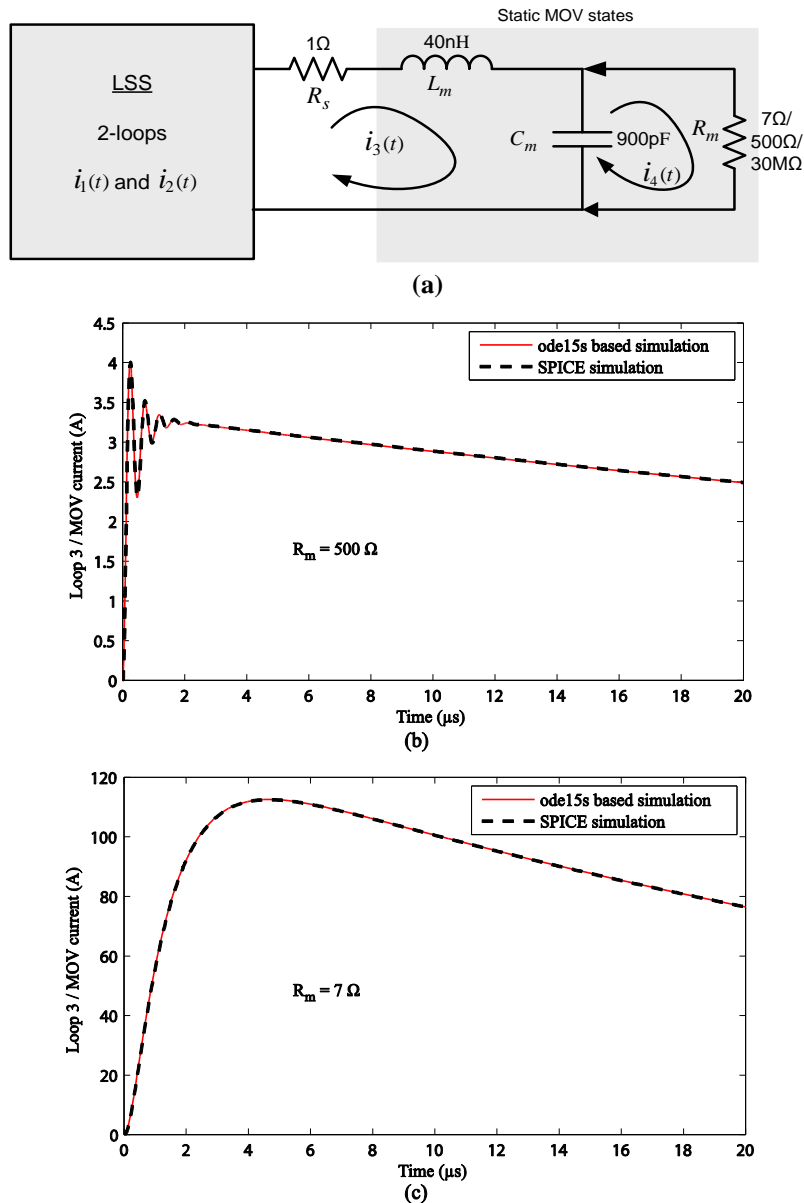


**Figure 7:** Static states of the MOV pulsed by the LSS (a) simulated circuit (b) static varistor current for  $R_m = 500\Omega$  (c) static varistor current for  $R_m = 7\Omega$

In this paper our interest is to estimate the energies delivered to individual components of a TVSS block and determine the respective time delays in the event of a lightning transient. We have been able to adapt the robust code developed for the earlier circuits to do this successfully. As we have seen earlier a TVSS consists of both linear and nonlinear elements. We have worked with the power-law model given by Eq. (1) for both the MOV and the TVS diode in formulating the state equations. Simulations based on the above were carried out for circuit blocks containing (a) an MOV, and (b) an MOV and a noise filter. Circuit diagrams and simulation/experimental validation comparison plots for (a) are shown in Figure 8 and for (b) in Figure 9 respectively. A similar simulation was also compared with a PSpice simulation; the results were almost identical [24]. The model for the MOV used in PSpice was available from the manufacturer.

The set of state equations developed for the circuit of Figure 8(a) is presented in Appendix II.

## Appendix F: A provisionally accepted journal paper

As can be seen in Figure 8(b), the current peak in the simulation coincides with the voltage peak although for a real varistor as seen in the validation, the current peak lags the voltage peak by about 2  $\mu\text{s}$ . This discrepancy could be attributed to the approximate nature of the model used for the nonlinear resistance of the MOV. Despite this, we see that the maximum energy absorbed by the varistor given in Figure 8(d) is within 10% of the validation. This difference in energies absorbed by the varistor could be minimized by using more accurate models for the varistor. Improvements to varistor modeling are discussed in Section V. The energy delivered to the varistor gets dissipated as heat within a short period of time.

Next we introduce the second stage of the TVSS, which is an  $LC$  line filter connected in parallel with the varistor and the circuit is shown in Figure 9(a). While the winding resistance and the inductance provide a series impedance to limit the transient current, it also prevents voltage switching transients generated on the load side from feeding back into the supply [12].

In figures 9(b) we see that the varistor current tends to ring for a few cycles at the oscillation frequency of the line-filter components, in the process of clamping the incoming surge. This simulation compares well with the validation in spite of the ringing in the simulation current not being damped as much as the validation. The reason for this discrepancy is clear as we have not accounted for the bulk resistance of the MOV during conduction and also have neglected parasitic resistances arising from device leads, etc. The simulated energy absorption by the varistor also given in Figures 9(b) is within 6% of the validation. This difference in energies could be minimized by using more accurate models for the varistor and the passive inductor and capacitor elements.

A primary task of the project is to find the energy absorption in each component of the TVSS and also to study the time lags of the maximum energy instances with respect to the occurrence of the lightning surge. We have addressed this by also studying the surge propagation through the line filter capacitor  $C_f$  and the inductor  $L_f$ . The results and validations are illustrated in Figures 9(c) and 9(d).

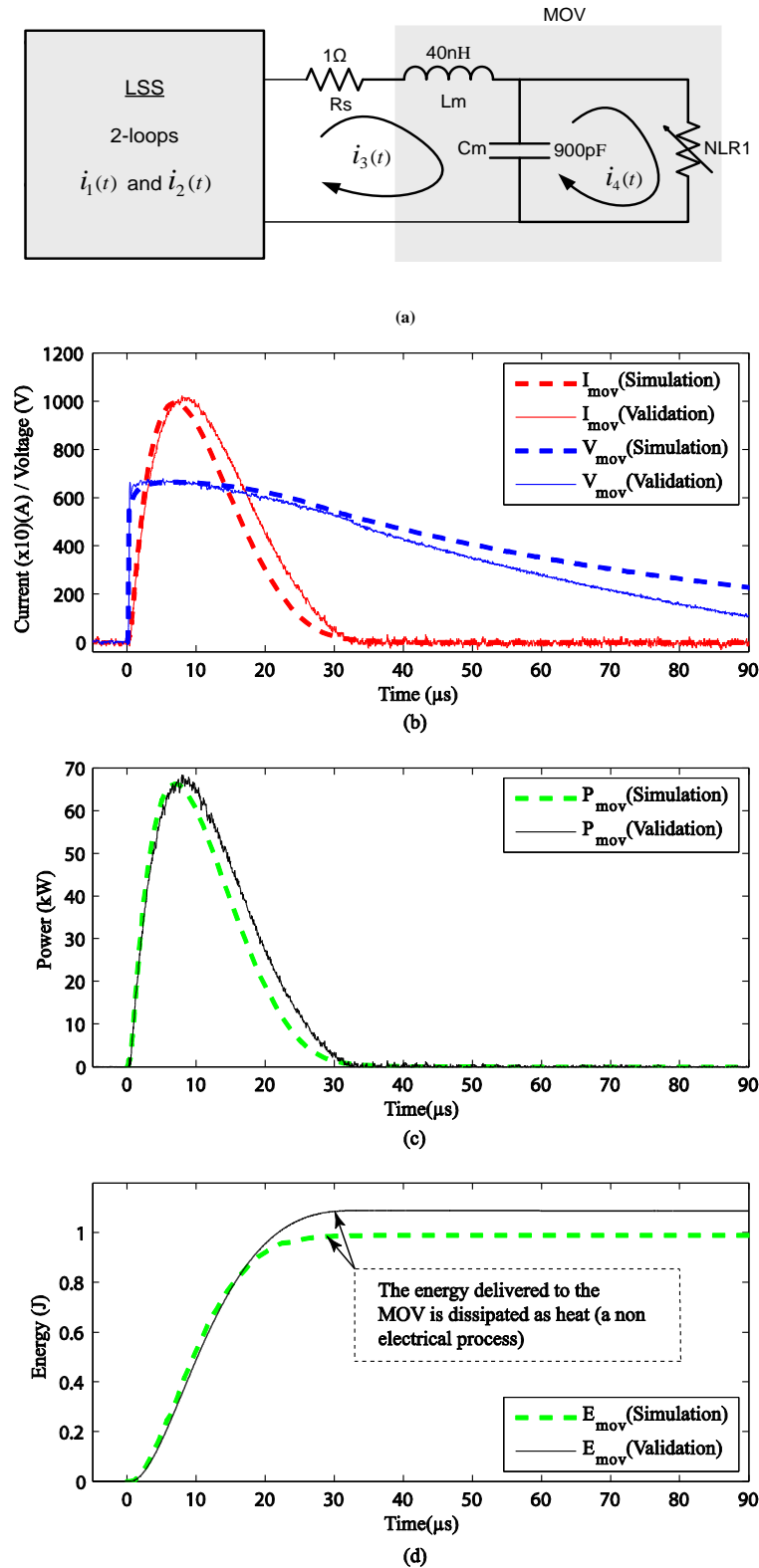


**Figure 8:** MOV pulsed by the LSS (a) circuit simulated using MATLAB; (b) varistor current and voltage (c) power delivered to the varistor (d) energy absorbed by the varistor.

It is seen that the energy stored in the capacitor  $C_f$  falls as the voltage across it falls as expected. Again the energy simulation compares well with the experimental validation except that the simulation for the energy absorption in the capacitor is slightly higher than the validation; the reason for this discrepancy is clear since we have not accounted for the resistive parts of the filter

## Appendix F: A provisionally accepted journal paper

inductor and capacitor and also other stray circuit resistances. These resistive components do absorb a bit of the energy leaving less energy for the filter capacitor and the inductor.

The approximate time delays to transfer maximum energies to each component of the TVSS are also shown clearly in Figure 10.

These simulations allow us to predict the power dissipation and energy patterns in each of the components of a TVSS unit. The methodology indicated here can be put to detailed analytical use in future research projects to predict the failures in downstream power electronic blocks, provided the nonlinear electronic devices can be represented by suitable mathematical models.

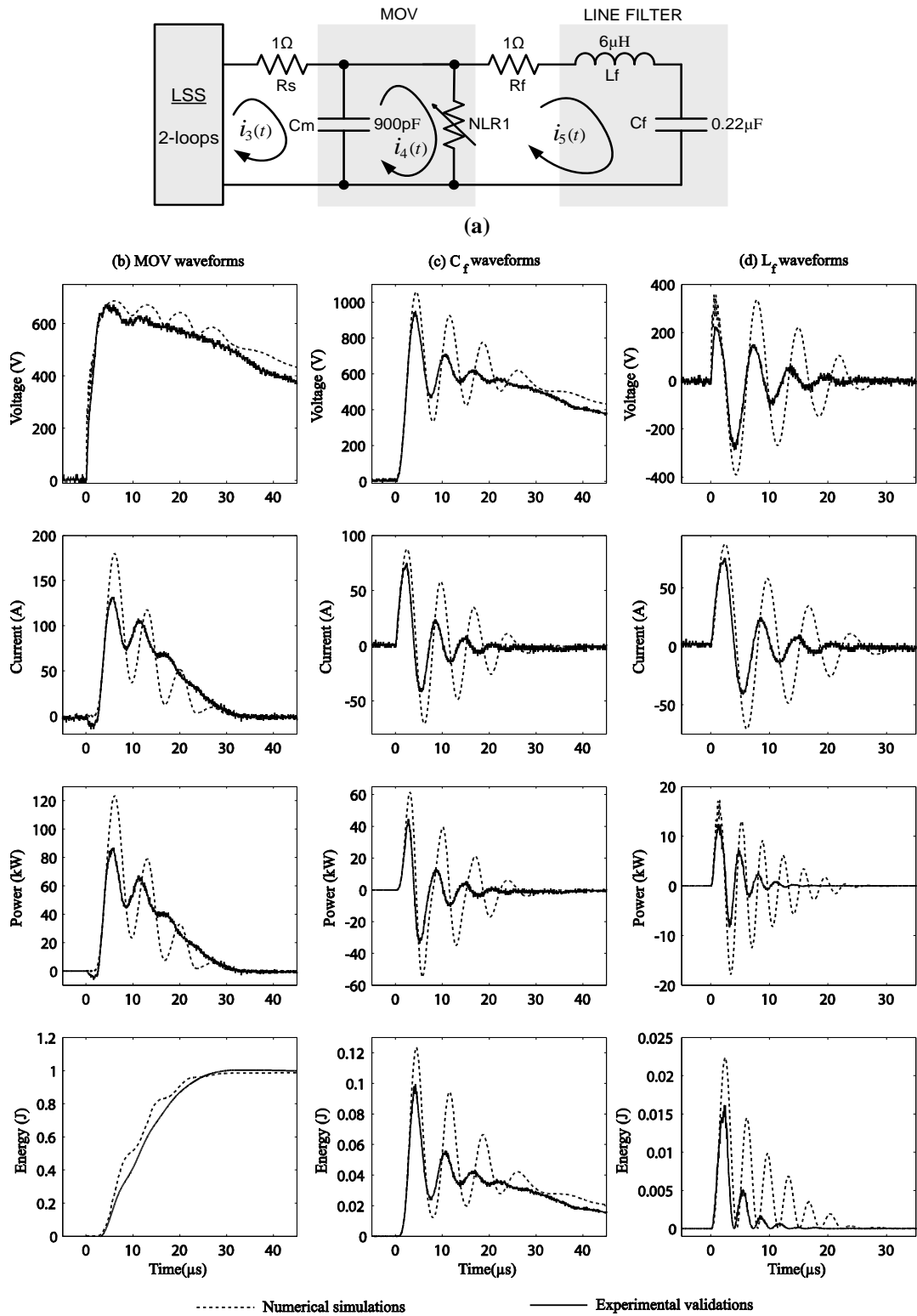


**Figure 9:** TVSS with a varistor and a line filter pulsed with the LSS (a) simulated circuit with typical line filter values; (b) varistor waveforms (c)  $C_f$  waveforms (d)  $L_f$  waveforms

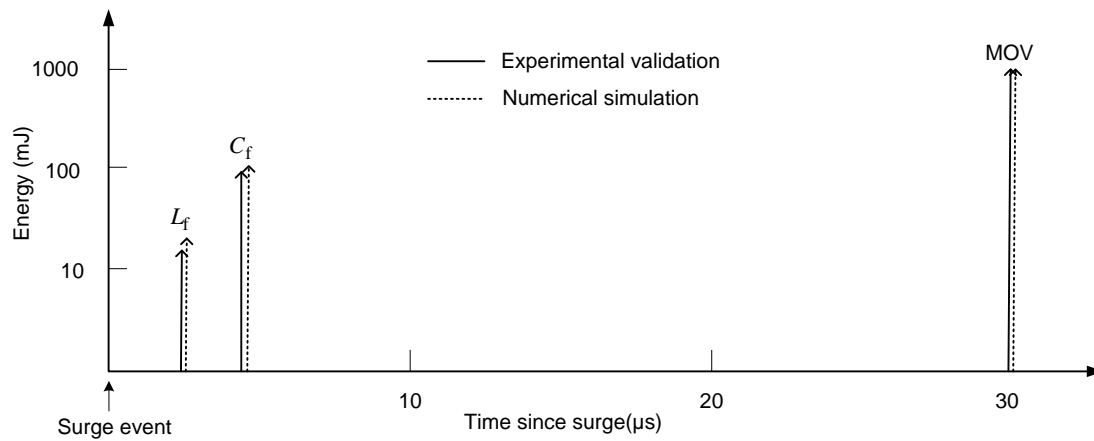


**Figure 10:** Maximum energies handled by each component of the TVS with associated time delays. (Note the logarithmic scale on the y-axis)

## V. Improvements to nonlinear device modeling

Figure 11(a) shows experimental plots for voltage and current of a varistor, driven by a 1kV surge, along with the corresponding simulations. We also show the associated measured dynamic hysteresis curve in Figure 11(b). The associated dynamic  $I$ - $V$  curve for the simulation based on the power-law fit, which is also shown in Figure 11(b), does not account for the hysteresis seen in the measured curve.

The hysteresis effect needs to be accounted for if the modeling of the varistor is to be completely accurate [14]. Although the curve-fitting, according to the power-law given by Eq. (1), is not a very accurate model of the varistor dynamics, it is adequate for the purpose of predicting energy absorption by various components of the protector circuit.

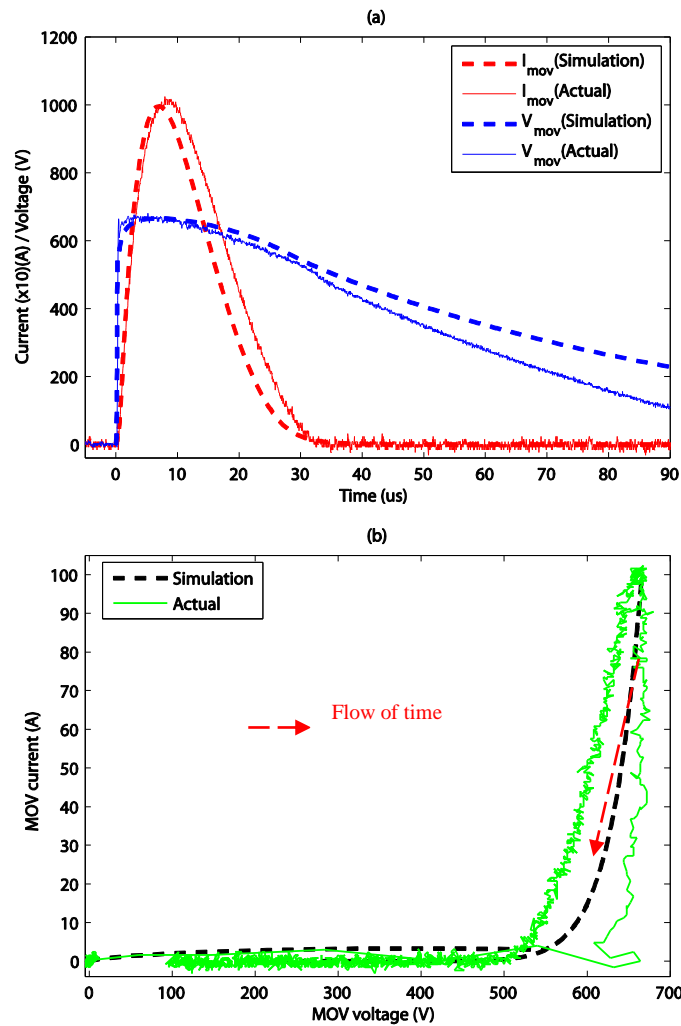


**Figure 11:** (a) Current and voltage in a 275L40C varistor driven by a 1kV surge; simulation and actual plots (b) Associated dynamic I-V curves of traces shown in (a)

## VI Conclusion

This paper shows that MATLAB-based numerical simulation which solves appropriately chosen sets of state equations is suitable for predicting the actual energy transfers into individual components of surge protector circuits. The approach presented also gives clear indication of the approximate time delays associated with the energy transfers. These predictions will assist in designing effective surge protectors and also the approach could be extended to general power converters in the power conversion interface of an electronic system. The development of sufficiently accurate models for the nonlinear devices encountered is essential for these predictions. All numerical simulations presented here have been validated experimentally using a lightning surge simulator. Error margins for simulations with significant levels of energy were found to be within 10%.

## Appendix I

We will use Eq. (3) to provide the resolution that justifies the use of the initial condition that arises from an impulse input. Integrating Eq. (3)

$$\mathbf{x} = \int (A\mathbf{x} + B\mathbf{u}) dt \quad (5)$$

$$\mathbf{x} = A \int (\mathbf{x}) dt + B \int (\mathbf{u}) dt \quad (6)$$

For the impulse response,  $\mathbf{u}$  is a delta function which has an area of one from  $-\infty$  to  $+\infty$ . Therefore,

$$\mathbf{x} = A \int (\mathbf{x}) dt + B \cdot 1 = A \int (\mathbf{x}) dt + B \quad (7)$$

In order to determine the initial conditions that corresponds to an impulse, we need to determine the value of  $\mathbf{x}$  at  $t = 0$ . Assuming that  $\mathbf{x} = 0$  from  $t = -\infty$  to  $t = 0$ , the integral can be evaluated from 0 to time  $t$ . Since we are interested in the initial condition at  $t = 0$ , we need to evaluate the integral from  $t = 0$  to  $t = 0$ . Hence the result is,

$$\mathbf{x}(t = 0) = A \int_{t=0}^{t=0} (\mathbf{x}) dt + B = 0 + B = B \quad (8)$$

Therefore, an impulse may be simulated by using an input of all zeros and initial conditions of  $B$ .

Resolving the second-order DE given by Eq. (4) into a couple of first-order DEs, we get

$$\frac{di_1}{dt} = j_1 \quad (9)$$

$$\frac{dj_1}{dt} = -aj - (b - ac)i_1 - adi_2 + \frac{V_C(0)}{L}\delta(t) \quad (10)$$

where  $a = R_1/L_1$ ,  $b = 1/L_1C$ ,  $c = R_1/L_2$ , and  $d = R_1 + R_2 + R_3/L_2$

Hence from Eqs. (8) and (10), we get the initial condition

$$j_1(t = 0) = \frac{V_C(0)}{L} \quad (11)$$

which will be used in all our simulations.

## Appendix II

Equations (5) to (10) make up the set of six state equations for the circuit of Figure 9(a). The subscript  $n$  in the loop currents  $i_n$  and in the derivatives of loop currents  $j_n$  refers to the loop number. The voltage across the nonlinear resistance is given by  $v_4$ .

$$\frac{di_1}{dt} = j_1 \quad (12)$$

$$\frac{dj_1}{dt} = -aj_1 - (b - ac)i_1 - adi_2 + aei_3 \quad (13)$$

$$\frac{di_2}{dt} = ci_1 - di_2 + ei_3 \quad (14)$$

$$\frac{di_3}{dt} = j_3 \quad (15)$$

$$\frac{dj_3}{dt} = -fj_3 + cgi_1 - gdi_2 + (eg - h)i_3 + h(kv_4^\alpha) \quad (16)$$

$$\frac{dv_4}{dt} = m(i_3 - kv_4^\alpha) \quad (17)$$

where,

$a = R_1/L_1$ ,  $b = 1/L_1C$ ,  $c = R_1/L_2$ ,  $d = R_1 + R_2 + R_3/L_2$ ,  $e = R_3/L_2$ ,  $f = (R_3 + R_S)/L_m$ ,  $g = R_3/L_m$ ,  $h = 1/L_mC_m$  and  $m = 1/C_m$

## References for the above journal paper

- [1] J. Douglas, "Power quality solutions," *Power Engineering Review, IEEE*, vol. 14, pp. 3-7, 1994.
- [2] ITRS Committee, "International Technology Road Map for Semiconductors", 2006 Update , USA, 89 pages
- [3] N. Kularatna, "Powering systems based on complex ICs and the quality of utility AC source: an end to end approach to protection against transients," in *Proc. of Power Quality*, 2005, (Session PQS02).
- [4] S. Gunther, F. Binns, D. M. Carmean, and J. C. Hall, "Managing the impact of increasing microprocessor power consumption," *Intel Technology Journal*, vol. 5, pp. 1-9, 2001.

## Appendix F: A provisionally accepted journal paper

- [5] "IEEE recommended practice on characterization of surges in low-voltage (1000 V and less) AC power circuits," *IEEE Std C62.41.2-2002*, pp. 9-10, 2003.
- [6] Greim, M.C.: "High end digital systems give a thumbs down to rules of thumb"; EDN, June 5, 2000, pp 100-108.
- [7] Kularatna, N.: "Power electronics design handbook- low power components and applications"; Butterworth-Heinemann, 1998. (Chapter 4).
- [8] "IEEE guide for surge voltages in low-voltage ac power circuits," *ANSI/IEEE Std C62.41-1980*, 1981.
- [9] Holland, A.F.: "Behavior of solid state technology in transient and surge protection systems"; IEE colloquium on Lightning and EMC, Jan 1996, pp 8/1-8/8.
- [10] Drabkin, M.M.: "Surge protection of low voltage AC power by MOV based SPDs"; 10<sup>th</sup> Intl Conf on Harmonics and Quality of Power, Oct 2002, pp 6-9
- [11] Baran, M.E.; Warong Tocharoenchai; Craven, K.; Reitfort, D.; , "Surge protection capabilities of uninterruptible power supplies," *Harmonics and Quality of Power, 2000. Proceedings. Ninth International Conference on* , vol.1, no., pp.284-288 vol.1, 2000
- [12] Billings, K.: "Switch mode power supply handbook", 2<sup>nd</sup> edition, McGraw Hill, 1999. (Part 1, Chapter 2).
- [13] "Littlefuse Varistors – Basic Properties, Terminology and Theory", Application Note, July 1999, AN9767.1
- [14] Zitnik, B., Vidmar, M.: "Numerical modeling of metal oxide varistors", Proceedings of the XIVth International Symposium on High Voltage Engineering, August 25-29, 2005
- [15] L. M. Levinson and H. R. Philipp, "The physics of metal oxide varistors," *Journal of Applied Physics*, vol. 46, pp. 1332-1341, 1975.
- [16] G. Z. Zang, J. F. Wang, H. C. Chen, W. B. Su, C. M. Wang, and P. Qi, "Nonlinear electrical behaviour of the WO<sub>3</sub>-based system," *Journal of Materials Science*, vol. 39, pp. 4373-4374, 2004.
- [17] S. James, N. Kularatna, D. A. Steyn-Ross, and R. Kunnemeyer, "Numerical simulation of surge protection circuits and experimental verification using a lightning surge simulator," in *IECON 2012 - 38th Annual Conference on IEEE Industrial Electronics Society*, pp. 615-620.

## Appendix F: A provisionally accepted journal paper

- [18] Littelfuse. (1998). *Transient Suppression Devices and Principles: Application Note AN9768*. Retrieved November, 2012, from [http://www.digikey.co.nz/Web%20Export/Supplier%20Content/Littelfuse\\_18/PDF/LF\\_TransientSuppressionDevices.pdf?redirected=1](http://www.digikey.co.nz/Web%20Export/Supplier%20Content/Littelfuse_18/PDF/LF_TransientSuppressionDevices.pdf?redirected=1)
- [19] Chrysanthou, C.; Boksiner, J.; "Analysis of coordination between primary and secondary protectors," *IEEE Transactions on Power Delivery*, vol.12, no.4, pp.1501-1507, Oct 1997
- [20] IEEE Working Group 3.4.11, "Modeling of metal oxide surge arresters", *IEEE Transactions on Power Delivery*, vol. 7, No. 1, January 1992.
- [21] Mathworks, "How do I obtain an impulse response?". Retrieved June, 2013, from: <http://www.mathworks.com/support/tech-notes/1900/1901.html>
- [22] S. James; N. Kularatna; D. A. Steyn-Ross; R. Künnemeyer.; "Modeling of surge protection circuits for the study of transient propagation in power conversion interfaces," *Proceedings of the 18<sup>th</sup> Electronics New Zealand Conference* , pp.113-117, Nov 2011
- [23] Laser analytics group, The University of Cambridge. (2008). *Using the MATLAB ODE solvers*. Retrieved December, 2012, from [http://laser.cheng.cam.ac.uk/wiki/images/e/e5/NumMeth\\_Handout\\_7.pdf](http://laser.cheng.cam.ac.uk/wiki/images/e/e5/NumMeth_Handout_7.pdf)
- [24] S. James: "*Investigation of surge propagation in transient voltage surge suppressors and experimental verification*," PhD thesis, The University of Waikato, Section 6.2.2, pp.126-128, 2014